New states of matter in one- and twodimensional lattice models

Zur Erlangung des akademischen Grades eines
DOKTORS DER NATURWISSENSCHAFTEN
von der Fakultät für Physik der
Universität (TH) Karlsruhe

genehmigte

DISSERTATION

von

Dipl.-Phys. Stephan Rachel

aus Rastatt

Referent: Prof. Dr. Peter Wölfle, TKM

Korreferent: Prof. Dr. Alexander Shnirman, TKM

Datum der Prüfung: 12. Dezember 2008

Acknowledgement

To my wife Marion

Contents

Chapter 1

Introduction

The search for new states of matter is one of the oldest motives to conduct physical research. For instance, the realization of low temperature laboratories at the beginning of the previous century has led to the discovery of superconductivity and superfluidity. In the last two decades, the combination of atomic physics and quantum optics has led to pioneering discoveries by searching for new states of matter. The development of cold atom experiments and the achievement of optical lattices have opened a wide perspective for the discovery of new states of matter. The successful generation of a Bose–Einstein condensate of rubidium [18] and sodium atoms [41], respectively, was certainly the most prominent example. Meanwhile, also molecules consisting of two fermionic lithium atoms were demonstrated to form a Bose–Einstein condensate [158]. Even more spectacular was the experimental confirmation of the so–called BEC–BCS crossover at which the interactions between the lithium atoms was continuously varied from repulsive to attractive [157]. In another remarkable experiment, the quantum phase transition from a bosonic superfluid to a Mott insulating state was observed in a gas of rubidium atoms loaded into a three–dimensional optical lattice [59].

In this thesis, we follow the motive to search for new states of matter. We consider physical situations which have not been observed so far, neither experimentally nor theoretically. In fact, we will consider different lattice models which exhibit exotic states of matter. Although both systems seem to be different, they are interrelated by the hope that we can experience their experimental realization by cold atom experiments within the next decade.

In the first part of this thesis, we consider bosonic atoms in a two–dimensional optical lattice. The uncharged, bosonic atoms are assumed to be exposed to an artificial magnetic field. This magnetic field might be realized through rotation of the optical lattice. Recently, it was demonstrated how to co–rotate an optical lattice to a rotating gas of atoms [146]. The effect of the rotation to the neutral atoms is comparable to the effect of a magnetic field to Bloch electrons. In case, the effective magnetic field is very strong, we will meet situations of *fragmented* Bose–Einstein condensation – situations where not only a single condensate is present. One of these scenarios is even associated with an antiferromagnetically ordered current pattern on the lattice [63].

In the second part of this thesis, we deal with low–dimensional antiferromagnetism. A long–standing theory about the properties of one–dimensional spin models leads us to spin chains where the symmetry group SU(2) of the quantum mechanical spin is replaced by the symmetry groups SU(3) and SU(4). While the projected electron spin is characterized by two different values, say "↑" and "↓", the spin can take three different values in case of the symmetry group SU(3), say "blue", "red", and "green". Such antiferromagnets have so far never been observed in nature. The availability of cold atom "engineering", however, might principally provide the chance to observe an SU(3) antiferromagnet. Thereby, the atoms might be prepared in three different internal states and loaded into an optical lattice. The fine–tuning of interactions could realize an approximate SU(3) symmetry. Very recently, the trapping of a three component degenerate Fermi gas was realized [74, 118] and the stabilization of an SU(3) Fermi gas seems now to be feasible. This success supports the hope for the realization of SU(3) and SU(4) antiferromagnetism in the future. Our investigation of SU(3) and SU(4) spin chains will bring a new kind of topological phase transition to light. This phase transition is characterized by an abrupt change of the confinement forces between the elementary spin excitations: from free elementary spin excitations to strongly confined spin excitations [62, 122].

Chapter 2

Ultracold bosons in a π–flux lattice

2.1   Introduction

The original observation of the phenomenon known as "superfluidity" was made simultaneously in liquid ^{4}He in 1938 by two groups, Kapitza in Moscow [82] and Allen and Misener in Cambridge [16]. At this time, it was already known that liquid helium[1] was not observed to freeze under its own vapor pressure. During the 1930s it became clear that curious things happened at and below a characteristic temperature (~ 2.17 K) which was called "lambda temperature". Both experimental groups found that below the lambda temperature the liquid flowed so easily that the viscosity would have to be at least a factor of 1500 smaller than in the phase above the lambda temperature. It was this tremendous difference in the viscosity (or even the possible absence of viscosity) that brought Kapitza to coin this phenomenon "superfluidity". A few months after the experimental observation of superfluidity, Fritz London came up with a qualitative explanation [99] that is nowadays still valid. The isotope ^{4}He is composed of an even number of elementary particles (two protons, two neutrons, two electrons) and thus, the many particle wavefunction of the system should be symmetric under the exchange of two He atoms. In the language of statistical physics, ^{4}He atoms obey "Bose–Einstein statistics". London realized that the "lambda transition" of ^{4}He might be related with the phase transition of the noninteracting Bose gas predicted in 1925 by Einstein [45, 46]. Motivated by a paper by Satyendra N. Bose from 1924 [32], Einstein had studied the thermodynamic behavior of the noninteracting Bose gas, and had shown that below a certain temperature (depending on the mass and density of the gas) a macroscopic number of atoms should occupy a single one–particle state. This peculiar phenomenon is nowadays called "Bose–Einstein condensation" (BEC). But at the time of Einstein's suggestion, the revailing view was that BEC is a pathology of the noninteracting gas which would disappear in the presence of interactions. Very soon thereafter, Laszlo Tisza acted on London's suggestion by proposing the "two–fluid" model [144]. While the "condensate" behaves completely without friction, the rest of the system

---

[1]The production of the light isotope ^{3}He started in the early 1950s, prior liquid helium was synonymous with ^{4}He.

behaves like an ordinary liquid. Tisza's "two–fluid" model contained one remarkable prediction: the two fluids, i.e., the condensate and the rest, should oscillate out of phase, which can be seen as a so far unknown type of collective excitations. In 1941, Lev Landau worked out the two–fluid model quantitatively [92]. In his paper, which is a milestone in condensed matter theory, he introduced the concept of "quasiparticles". He identified the quasiparticles of a Bose liquid as of two types: phonons and rotons. While Landau's two–fluid hydrodynamics provides the conceptual framework of superfluidity, it is purely phenomenological in the sense that the superfluidity itself and the excitations are postulated rather than derived rigorously from a microscopic theory. Nikolai N. Bogoliubov was the first who investigated in 1947 the interacting Bose system within a microscopic theory [31] introducing the field of research known today as the "many body problem". Bogoliubov assumed a weakly interacting, dilute Bose gas and made a few well–justified approximations, based on the assumption that the Bose gas undergoes a phase transition into the Bose–condensed phase. He derived easily the sound wave like excitations for small momenta, while for large momenta he found the behavior of free particles (instead of the roton branch postulated by Landau)[2]. In the 1950s, a better understanding of the relationship between superfluidity and BEC was developed and Landau's predictions for the excitations spectrum of ^{4}He was verified. First successful measurements of the condensate fraction was done.

Much later, the experimental field of dilute atomic gases, starting in the 1970s, were developed. This field benefited from the new techniques of atomic physics, magnetical and optical trapping mechanism, and advanced cooling processing. Spin–polarized hydrogen was the first element which was considered experimentally due to its light mass. In these experiments, the hydrogen were cooled very close to (but not below) the BEC transition temperature. In the 1980s laser–based cooling techniques were used to trap and cool neutral atoms. Alkali atoms were very good candidates, as their optical transition frequencies are in the range of available lasers. By combining the various cooling and trapping methods being available, the experimental teams of Eric Cornell and Carl Wieman at Boulder and Wolfang Ketterle at MIT eventually succeeded in 1995 in observing BEC in vapors of ^{87}Rb [18] and ^{23}Na [41]. While the field of *cold atomic gases* experienced an unprecedented hype, we wish to report from a particular progress within this field, the achievement of optical lattices [78]. Two counter–propagating laser beams build a standing laser wave which cause an effective periodic potential for neutral atoms with periodicity of half the laser wavelength. Applying three of such laser pairs (one for each space direction) yields a three–dimensional periodic potential, an optical lattice. In 2002, Markus Greiner *et al.* demonstrated that a gas of ^{87}Rb atoms, trapped in such an optical lattice and cooled below the BEC–phase transition, can be driven from the superfluid phase to a Mott insulator phase by tuning the interaction strength [50,59]. The phenomenon of BEC turned out to be very robust and is nowadays well–established in atomic gases both in magneto–optical traps and in optical lattices.

---

[2]This problem was later fixed by Lee, Huang, and Yang [96], and Girardeau [57] by extending Bogoliubov's original work.

In certain situations, however, a system does not condense into a *single* condensate. The physics of condensation can lead to the formation of several condensates, to situations of *fragmented* condensation. As we reported above, the very concept of BEC is the macroscopic occupation of a single–particle state, usually the single–particle ground state. How does the condensation occur when the single–particle ground state is degenerate, with two or more states competing for condensation? How do the bosons distribute themselves in these competing levels? The best possible answer is that the condensation process, or more precise, the fragmentation process highly depends on the interplay of degeneracies and interactions [110].

A system which generically possesses degeneracies in the single particle spectrum is a simple hopping model, i.e., a kinetic energy term in the tight–binding approximation, on a square lattice subject to a strong magnetic field. For the first time, the single particle spectrum of this model was discovered by Douglas R. Hofstadter [73]. He considered crystal electrons in a uniform magnetic field and discovered a recursive or fractal structure in the single particle spectrum. The magnetic flux which passes through a lattice cell, divided by a *Dirac flux quantum*, yields a dimensionless parameter α whose rationality or irrationality strongly influences the nature of the spectrum. For instance, the spectrum for irrational magnetic fields, i.e., irrational values of α, is a Cantor set, i.e., it is an uncountable but measure–zero set of points. For rational values of $\alpha = p/q$, however, the single particle spectrum is q–fold degenerate. In the following we will call a lattice, where the flux in units of the Dirac flux quantum through every lattice cell is of strength α, a "$2\pi\alpha$ flux lattice". The *Hofstadter butterfly*, the energy–magnetic field phase diagram for single particle states, is shown in Fig. 2.1.

Hofstadter originally considered crystal electrons, i.e., fermions, but a single particle property never depends on statistics[3]. Thus we know that the single particle ground state of bosons on a $2\pi\alpha$ flux lattice is degenerate for certain rational values of α. It will be the main concern of this thesis chapter to resolve the following question which we can formulate in a fundamental and in a more specific way:

- What happens to bosons on a lattice subject to a magnetic field?

- How does the condensation or fragmentation process occur?

Before we will start to resolve these questions [63] in Sec. 2.3 we have to deal with a very practical problem. The Hofstadter butterfly has so far never been observed experimentally, as magnetic fields of the order of $\alpha = 1$ are impossible to realize in real crystals. For atoms loaded into an optical lattice with lattice constants 1000 times larger than in a real crystal this problem seems to be sorted out. However, the atoms used in optical lattice experiments must be neutral. The use of charged atoms would never be stable, any experimental setup would be destroyed by huge Coulomb forces between the atoms. In a realistic situation, we remain, hence, with uncharged bosons which do not feel the presence of a uniform magnetic field in the sense of the

---

[3]One should always keep in mind that the concept of statistics makes sense not until more than one particle is considered, even though we are used to speak about one boson or one fermion...

$$\alpha = 1/q = \Phi a^2/\Phi_0$$
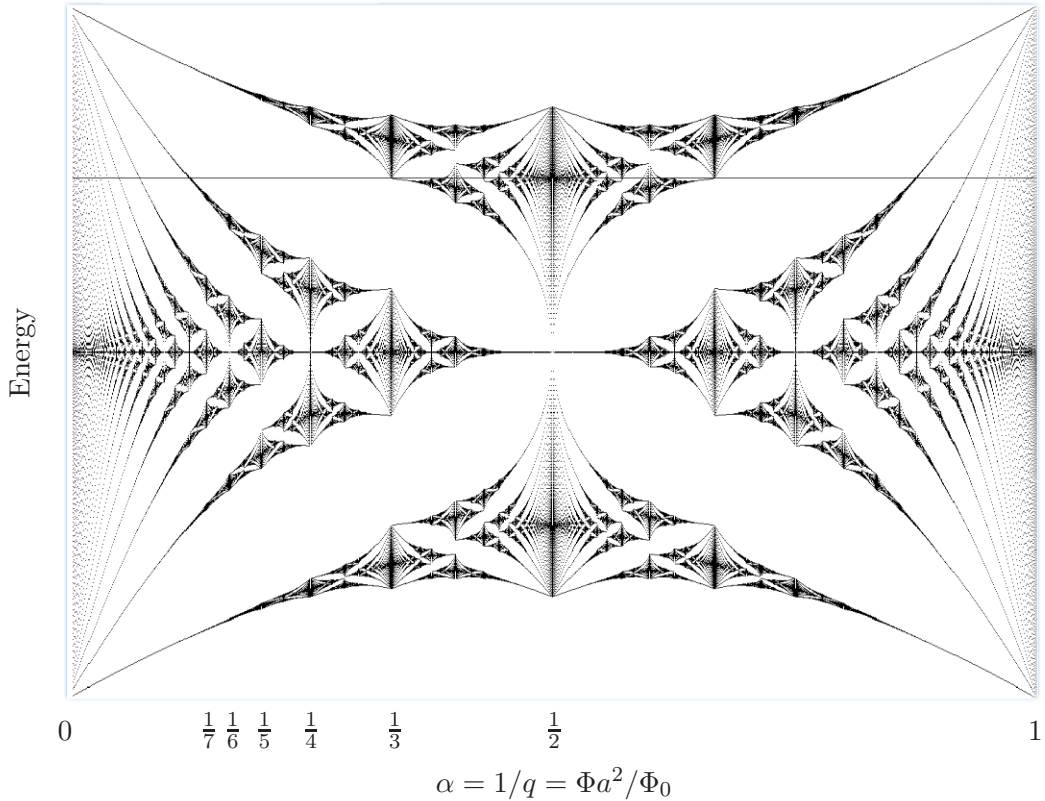
Figure 2.1: The Hofstadter butterfly: the single particle energies are plotted as a function of the magnetic field (in dimensionless units α) as explained in the text.

quantum mechanical principle of "minimal coupling". Confronted with this blind alley, the field of "cold atoms" were responsive to it very creatively. In Sec. 2.2, we briefly list the most promising proposals how to realize an artificial magnetic field for bosons in an optical lattice.

This thesis chapter is organized as follows[4]: after reviewing the experimental proposals for an artificial magnetic field in Sec. 2.2, we introduce in Sec. 2.3 the microscopic model which describes bosons in a flux lattice. In the following, we discuss as a paradigm the case of $\alpha = 1/2$, i.e., a π–flux lattice. As the interacting model is not analytically soluble, we aim to derive in Sec. 2.4 an effective model which we are able to solve. It turns out that this effective model is a realization of Noziéres Hamiltonian. For repulsive interactions, we find, as a main result, the many particle ground state to be two–fold degenerate. Each ground state is associated with an antiferromagnetically ordered current pattern in real space. We confirm in Sec. 2.4.2, 2.4.3, and 2.6 the validity of this effective model numerically. It turns out to be an exact description of the microscopic model in the weakly interacting regime. The current patterns, however, remain for arbitrary filling and repulsive interaction strength. We briefly review in Sec. 2.5 the phenomenon of fragmentation in BEC

---

[4]The main part of the presented results of this thesis chapter ("Cold bosonic atoms in a π–flux lattice") is contained in Ref. [63].

and its relevance to the presented work. In particular, we show that the considered model with attractive interactions exhibits a fragmented condensate, while the model with repulsive interactions realizes a Schrödinger–cat. In the conclusion, Sec. 2.7, we discuss after a concise summary the generalization from π–flux to arbitrary flux.

2.2 Experimental realization of artificial magnetic fields

A major impediment to study models such as those describing the quantum Hall effect, is the lack couplings to the neutral atoms in the same way as the electric and magnetic fields couple to charged particles. In the late 1990s, there were already several, somewhat limited, implementations of electrical and magnetic fields for neutral atoms. Experimentalists routinely use the Earth's gravitational field as an analog of a uniform electric field [17]. They also study systems in non-inertial frames: uniform acceleration is equivalent to a constant electric field [102], while circular motion corresponds to a uniform magnetic field [1, 69, 72, 103]. With the rise of optical lattice experiments, the creation of artificial magnetic fields available to neutral atoms loaded into optical lattices has been of great interest. So far, an artificial magnetic field was not realized in optical lattice experiments. Nonetheless, in the last years there have been a few promising proposals from theorists which have shown a path to engineer such magnetic fields. The first proposal goes back to Jaksch and Zoller [79] and makes use of laser–induced hopping of atoms with two distinct internal states. Mueller [109] has developed this approach to atoms with three distinct internal states. A completely different scheme to engineer effective magnetic fields was suggested by Sørensen, Demler, and Lukin [138]. That work uses time–dependent hopping matrix elements along with a large oscillating quadrupolar potential. Meanwhile, the idea of realizing artificial magnetic fields was even extended to non–Abelian gauge potentials [117]. Most recently, the first experiment with a rotating optical lattice succeeded. Even though the goal of this experiment was the demonstration of vortex pinning in an optical lattice, a similar setup could be used to realize *flux lattices*, as discussed in this thesis. In the following, we will focus onto the relation of rotation and availability of a vector potential to neutral atoms.

2.2.1 Rotation of the optical lattice

As mentioned above, a circular motion corresponds to a uniform magnetic field. Consider the many–particle Hamiltonian of an atomic gas with arbitrary interaction in a rotating frame,

$$H \;=\; \sum_{\boldsymbol{p}} \frac{\boldsymbol{p}^2}{2m} + \sum_{\boldsymbol{r}_i, \boldsymbol{r}_j} V(\boldsymbol{r}_i, \boldsymbol{r}_j) - \Omega L_z \qquad\qquad (2.1)$$

where Ω is the rotation frequency and the rotation axis is assumed to be parallel to $\hat{\boldsymbol{z}}$. By use of the identity

$$-\Omega L_z = -\boldsymbol{\Omega}\boldsymbol{L} = -\boldsymbol{\Omega}(\boldsymbol{r}\times\boldsymbol{p}) = -\boldsymbol{p}(\boldsymbol{\Omega}\times\boldsymbol{r}) \equiv -\boldsymbol{p}\boldsymbol{A}, \qquad (2.2)$$

the Hamiltonian (2.1) is equivalent to

$$\sum_{\boldsymbol{p}} \frac{(\boldsymbol{p}-\boldsymbol{A})^2}{2m} + \sum_{\boldsymbol{r}_i,\boldsymbol{r}_j} V(\boldsymbol{r}_i,\boldsymbol{r}_j) - \frac{m}{2}\Omega^2\left(x^2+y^2\right) \qquad (2.3)$$

where $\boldsymbol{r} = (x,y,z)^{\mathrm{t}}$ and the effective vector potential is defined as

$$\boldsymbol{A} = \Omega\, m \begin{pmatrix} -y \\ x \\ 0 \end{pmatrix} = m(\boldsymbol{\Omega}\times\boldsymbol{x}).$$

It corresponds to a magnetic field in symmetric gauge, $\boldsymbol{B} = \tilde{B}\boldsymbol{z}$ with $\tilde{B} = 2\Omega m$. The essence is that $\tilde{B} \propto \Omega$. To compensate the additional last term in Eq. (2.3) which represents the centrifugal effects of rotation, one assumes an applied confining potential $V_{\mathrm{conf}} = m/2\,\omega^2(x^2+y^2)$. For $\omega = \Omega$, the centrifugal effect cancels. We shall therefore use "rotation" and "magnetic field" interchangeably.

In the presence of a lattice, one additionally has to regard lattice potential, trapping potential, and a proper way of expanding the bosonic field operators. In the following, we will sketch the way from the continuum Hamiltonian to the lattice Hamiltonian [27, 28] which turns out to be similar to a magnetic Bose–Hubbard Hamiltonian.

The system we wish to describe is an atomic cloud with fixed number of bosons rotating with an angular velocity or rotation frequency Ω about the z axis. This cloud is trapped in a two–dimensional optical lattice corotating with the same frequency in the presence of an additional superimposed two–dimensional harmonic confining potential with characteristic frequency ω. The non–rotating Hamiltonian H_0 consists of the kinetic energy term, the harmonic confining potential $V^{\mathrm{t}}(\boldsymbol{x})$, the optical lattice $V^{\mathrm{latt}}(\boldsymbol{x})$, and a contact interaction with coupling constant g. The effect of rotation is included by time–independent rotating–frame coordinates. This is done by the transformation $H = H_0 - \int d\boldsymbol{x}\Phi^\dagger\Omega L_z\Phi$, where Φ is a bosonic annihilation field operator. The Hamiltonian in the rotating frame coordinates is then given by

$$H = \int d\boldsymbol{x}\Phi^\dagger\left(-\frac{\hbar^2}{2m}\nabla^2 + V^{\mathrm{latt}}(\boldsymbol{x}) + V^{\mathrm{t}}(\boldsymbol{x}) + \frac{g}{2}\Phi^\dagger\Phi - \Omega L_z\right)\Phi, \qquad (2.4)$$

where m is the mass of a single boson. We assume a square lattice potential described by $V^{\mathrm{latt}}(\boldsymbol{x}) = V_0(\sin^2(\pi x/d) + \sin^2(\pi y/d))$, the trapping potential has to be rotationally invariant under rotations around the z axis, $V^{\mathrm{t}}(\boldsymbol{x}) = m/2\omega^2 r^2$, where $r = |\boldsymbol{x}|$. Now Eq. (2.4) becomes

$$H = \int d\boldsymbol{x}\Phi^\dagger\left(\frac{\boldsymbol{\Pi}^2}{2m} + V^{\mathrm{latt}}(\boldsymbol{x}) + \frac{1}{2}m\left(\omega^2 - \Omega^2\right)r^2 + \frac{g}{2}\Phi^\dagger\Phi\right)\Phi, \qquad (2.5)$$

where $\boldsymbol{\Pi} = -i\hbar\boldsymbol{\nabla} + m\boldsymbol{A}(\boldsymbol{x})$ is the covariant momentum and $\boldsymbol{A}(\boldsymbol{x}) = \boldsymbol{x} \times \boldsymbol{\Omega}$ is the equivalent of a magnetic vector potential in symmetric gauge stemming from the rotation. The important step is now to expand the field operators Φ such that it meets the requirements of large angular velocities, i.e., $\hbar\Omega \sim 0.1E_R$ with the recoil energy $E_R = \hbar^2\pi^2/2md^2$. For lower angular velocities it is sufficient to retain only Wannier orbitals $W_S^{l=0}(\boldsymbol{x} - \boldsymbol{x}_i)$ constructed from the lowest Bloch band $l = 0$ [151]. Due to this approximation, the phase description of the single particle wave function is flat within a particular lattice site with sharp gradients at site boundaries. For larger rotation frequencies, however, the ΩL_z term mixes into higher bands to a non-negligible extent. This mixing causes the modification of phase structure within sites. We are able to overcome this problem by using a modified Wannier basis given by

$$W_R(\boldsymbol{x} - \boldsymbol{x}_i) = \exp\left(-i\frac{m}{\hbar}\int_{\boldsymbol{x}_i}^{\boldsymbol{x}} \boldsymbol{A}(\boldsymbol{x}')d\boldsymbol{x}\right)W_S^0(\boldsymbol{x} - \boldsymbol{x}_i)\,, \qquad (2.6)$$

where the azimuthal phase gradient within a site is proportional to Ω. We have chosen $\boldsymbol{x}_i$ to coincide with the site center in order to ensure that at $\boldsymbol{x} = \boldsymbol{x}_i$ the Wannier orbital is real, $W_R(0) = W_S(0)$[5]. By means of the modified Wannier basis set we can express the field operators as

$$\Phi(\boldsymbol{x}) = \sum_i a_i W_R(\boldsymbol{x} - \boldsymbol{x}_i) \qquad (2.7)$$

where a_i is a bosonic annihilation operator at site i. When substituting (2.7) in the Hamiltonian (2.5) we obtain by use of the tight–binding approximation the following Bose–Hubbard Hamiltonian which can be seen analogously to that of Bloch electrons in a magnetic field:

$$H = -\sum_{\langle i,j\rangle} \tilde{t}(\Omega,\omega)\left(a_i^\dagger e^{-i\phi_{ij}}a_j + \text{h.c.}\right) + \sum_i \epsilon_i(\Omega,\omega)n_i + \frac{U}{2}n_i(n_i - 1) \qquad (2.8)$$

The essence is that the *magnetic phases* ϕ_{ij} are connected with the rotation as

$$\phi_{ij} = \frac{m}{\hbar}\int_{\boldsymbol{x}_j}^{\boldsymbol{x}_i} \boldsymbol{A}(\boldsymbol{x}')d\boldsymbol{x}' = \frac{m\Omega}{\hbar}(x_iy_j - x_jy_i) \propto \Omega. \qquad (2.9)$$

The definitions for $\tilde{t}$ and ϵ_i are evaluated [28] as

$$\tilde{t}(\Omega,\omega) = t + \frac{m(\Omega^2 - \omega^2)}{2}A_1\,,$$

$$\epsilon_i(\Omega,\omega) = \varepsilon - \frac{m(\Omega^2 - \omega^2)}{2}(r_i^2 + A_2)\,.$$

---

[5]In Ref. [29] it was shown by means of imaginary–time propagation techniques that the modified Wannier basis set W_R describes the phase gradient within a site better than the regular Wannier basis W_S and captures the for our purposes important parts of the Hilbert space satisfyingly.

The parameters t and ε are identical to the hopping and onsite zero–point energies associated with the standard Bose–Hubbard model [50], and are obtained by evaluating the integrals

$$t \;=\; \int d\boldsymbol{x}\, W_S^{\star}(\boldsymbol{x} - \boldsymbol{x}_i) \left(-\frac{\hbar^2}{2m}\nabla^2 + V^{\text{latt}}(\boldsymbol{x}) \right) W_S(\boldsymbol{x} - \boldsymbol{x}_j),$$

$$\varepsilon \;=\; \int d\boldsymbol{x}\, W_S^{\star}(\boldsymbol{x} - \boldsymbol{x}_i) \left(-\frac{\hbar^2}{2m}\nabla^2 + V^{\text{latt}}(\boldsymbol{x}) \right) W_S(\boldsymbol{x} - \boldsymbol{x}_i).$$

The modifications to these terms coming from the rotation are proportional to $(\Omega^2 - \omega^2)$ and to the overlap parameters defined as

$$A_1 \;\equiv\; \int dx\, W_S^{\star}(x - x_i)(x - x_i)^2 W_S(x - x_j),$$

$$A_2 \;\equiv\; 2\int dx\, W_S^{\star}(x - x_i)(x - x_i)^2 W_S(x - x_i),$$

where $W_S(x - x_i)$ is a one–dimensional Wannier function. Finally, the onsite energy U is for an s-wave scattering length a_s given by [78]

$$U = \frac{4\pi a_s \hbar^2}{m} \int d\boldsymbol{x}\, |W_S(\boldsymbol{x} - \boldsymbol{x}_i)|^4.$$

Note that the scattering length a_s can be tuned to negative values by means of a Feshbach resonance [30, 55, 126] which results in an attractive onsite potential. For the discussion of the stability of an attractive bosonic gas see Sec. 2.4.

So far we have shown that the rotation of the optical lattice would realize an effect to the neutral atoms which is identical to the effect of a magnetic field to charged particles. It sounds impossible to rotate an optical lattice. Nonetheless, in a recent experiment the JILA group has demonstrated the rotation of an optical lattice [146]. The experimental setup is shown in Fig. 2.2 (a). A mask with a set of holes is mounted onto a motor–driven rotary stage, and a laser beam (532nm) is expanded, collimated, and passed through the mask. After the mask, there are three beams which are focussed by a convex lens onto the Bose–condensed rotating cloud of ^{87}Rb.

The interference pattern at the focus constructs a quasi-2D optical lattice. The geometry and spatial extent of the triangular or the square optical lattice is determined by the size and layout of the holes of the mask and the focal length of the second lens. The diameter of the holes in Fig. 2.2 (b) and (c) is $\phi_1 = \phi_2 = 2.5$mm and $d_1 = 11.5$mm, and $d_2 = 13.5$mm. This results in a lattice constant for the triangular lattice of 7.8μm and for the square lattice of 7μm [146]. Note that the goal of this experiment was the pinning of vortices of the vortex lattice (i.e., the rotating BEC) to columnar sites of the corotating optical lattice. This goal of this experiment is, hence, very different from our purpose. Nonetheless, in this experiment the rotation
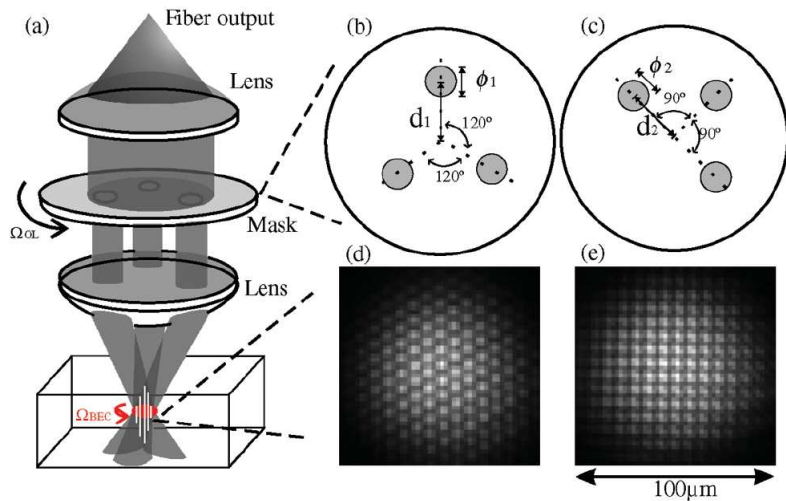
Figure 2.2: (a) Schematic diagram of the setup for the rotating quasi-2D optical lattice. Layouts for the masks for a triangular (b) and square (c) optical lattices. (d) and (e) are pictures of triangular and square optical lattices, respectively. The figure is taken from Ref. [146].

of an optical lattice is realized. Hence, with the results obtained above we can consider this experiment as the first successful creation of an artificial magnetic field. The regime which was obtained in this experiment is $\alpha \sim 1$, i.e., a flux lattice with a Dirac flux quantum per lattice cell was realized [135]. The "Bose–Hubbard physics" breaks down at lattice constants larger than $1 \sim 2\mu$m, i.e., in this experiment the Bose–Hubbard model was not realized. In principle, by modifying the mask and the lens shown in Fig. 2.2, within this experimental setup a lattice constant of about 1μm might be feasible [135]. In this case, however, α is fifty times smaller than one as the flux per lattice cell scales obviously with the square of the lattice constant. A fifty times faster rotation is technically extremely hard to stabilize and control. Imperfections of the rotation, e.g., vibrations, have to be controlled much better than in this experiment. Additionally, the laser intensity V_0 has to be increased drastically to obtain adequate tunneling rates. We wish to emphasize that there are no fundamental reasons why an experiment in the Bose–Hubbard regime with sufficiently fast rotations could not be realizable. There are, however, purely technical reasons why we have to wait for those experiments.

2.3 Magnetic Bose–Hubbard model

In the previous sections we have mentioned several possibilities how an artificial magnetic field or vector potential may be realized in optical lattice experiments. We have figured out that the realization of the *magnetic* phases Λ in the kinetic energy,

$$\mathcal{H}_{\mathrm{kin}} = \sum_{\langle i,j \rangle} -t \left(c_i^{\dagger} \; e^{i\Lambda_{ij}} \; c_j + \mathrm{h.c.} \right), \tag{2.10}$$

which represent the artificial magnetic field, could be achieved in principle[6]. We further assume a contact or on–site (Hubbard) interaction for the bosons with amplitude U which is the natural interaction in optical lattice experiments. Note that U might be tuned continuously from large negative values to large positive values by means of a Feshbach resonance [30, 55, 126]. Altogether we arrive the magnetic Bose–Hubbard model (mBHM) on the square lattice,

$$\mathcal{H}_{\mathrm{mBHM}} = \sum_{\langle i,j \rangle} -t \left(c_i^\dagger \, e^{i\Lambda_{ij}} \, c_j + \mathrm{h.c.} \right) + \frac{U}{2} \sum_i n_i \left(n_i - 1 \right), \qquad (2.11)$$

where the brackets under the sum indicate nearest neighbor hopping. The bosonic creation and annihilation operators fulfill the standard commutation relation, $[c_j, c_i^\dagger] = \delta_{ij}$, and $n_i = c_i^\dagger c_i$ counts the boson number on site i. The magnetic phases Λ_{ij} are related with the vector potential $\boldsymbol{A}$ as

$$\Lambda_{ij} = \frac{2\pi}{\Phi_0} \int_j^i \boldsymbol{A} \, d\boldsymbol{s} \qquad (2.12)$$

where $\Phi_0 = hc/e$ is the Dirac flux quantum. We assume an applied vector potential $\boldsymbol{A}$ of strength $\alpha = 1/q$ being the number of Dirac flux quanta per lattice cell chosen in Landau gauge,

$$\boldsymbol{A}(\boldsymbol{r}) = \frac{\Phi_0}{q} \frac{1}{a^2} \, y \, \hat{\boldsymbol{x}}, \qquad (2.13)$$

which corresponds to a magnetic field $\boldsymbol{B}(\boldsymbol{r}) = -\Phi_0/(qa^2)\hat{\boldsymbol{z}}$ in z–direction. This causes a total phase of $2\pi/q$, when integrating around a plaquette, $\oint \boldsymbol{A} d\boldsymbol{s} = 2\pi/q$, and thus gives rise to the name $2\pi/q$–flux lattice. In the following we set the lattice spacing a to unity. While the ordinary Bose–Hubbard model (BHM) [50, 78] has only one free parameter t/U, the mBHM has two free parameters, besides t/U the magnetic field represented by q. In what follows, we focus onto the special case $q = 2$ where the magnetic field reaches its maximum value[7]. In Sec. 2.7, we discuss possible paths to generalize the results we obtained for $q = 2$ to arbitrary q.

Ultracold bosonic atoms in a π–flux lattice

In the following, we assume the vector potential (2.13) of the strength of half a Dirac flux quantum per lattice cell, $q = 2$,

$$\boldsymbol{A}(\boldsymbol{r}) = \frac{\Phi_0}{2} \frac{1}{a^2} \, y \, \hat{\boldsymbol{x}}. \qquad (2.14)$$

Substituting the vector potential (2.14) in the magnetic phases (2.12) , we find in vertical direction vanishing magnetic phases, $\Lambda^v = 0$, whereas in horizontal direction

---

[6]In what follows we do not specify the origin of the magnetic phases and assume that their realization does not cause additional problems or peculiarities.

[7]As the magnetic field is proportional to a phase in the Hamiltonian, it possesses a natural 2π periodicity. In this sense, the magnetic field represented by $q = 2$, which corresponds to a phase of π in the Hamiltonian, is the "maximum" magnetic field.

we find the phases alternating between $\Lambda^{h,1} = 0$ and $\Lambda^{h,2} = \pi$. This yields in every second "row" a sign–change of the hopping amplitude t as illustrated in Fig. 2.3. The alternation of the sign of the hopping amplitude in horizontal direction explicitly
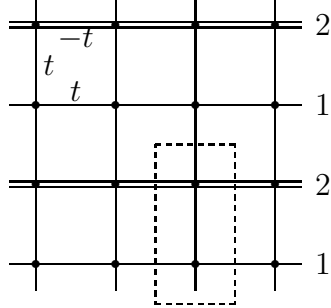
Figure 2.3: The dots correspond to the sites, the lines between the dots to nearest neighbor bonds. A simple line denotes the hopping amplitude t with positive sign, while a double line the hopping amplitude with negative sign, $-t$. The applied magnetic field causes explicit breaking of translational symmetry in y–direction (depending on the chosen gauge). We label the sublattice with horizontal hopping t by 1 and with horizontal hopping $-t$ by 2. The dashed box indicates a primitive unit cell.

breaks translation symmetry in y-direction[8]. In order to restore translational invariance, we introduce two sublattices $\alpha = 1$ and $\alpha = 2$ and, hence, double the primitive unit cell. The new primitive unit cell is illustrated by a dashed box in Fig. 2.3. In the following we label the primitive unit cell by i and thus an individual site by $i\alpha$. Note that a doubled primitive unit cell causes a halved Brioullin zone (BZ). Depending on the chosen gauge (2.13) the BZ is halved in k_y–direction (as illustrated in Fig. 2.4) and, as a consequence, k_y is not a good quantum number anymore. In the following we denote the in k_y–direction halved Brioullin zone as $\text{BZ}^\star = [-\pi, \pi[\times [-\frac{\pi}{2}, \frac{\pi}{2}[$.

The Hamiltonian now reads

$$H_{\text{kin}} = \sum_{\langle \alpha i, \alpha' j \rangle} t_{\alpha\alpha'} \, c_{i\alpha}^\dagger c_{j\alpha'} + \frac{U}{2} \sum_{i\alpha} n_{i\alpha}(n_{i\alpha} - 1) \qquad (2.15)$$

where $t_{11} = t_{12} = t$ and $t_{22} = -t$. Before we concentrate on the many particle Hamiltonian, we wish to get some insides by studying the single particle Hamiltonian. In particular, we should recover its spectrum as the vertical line at $\alpha = 1/2$ in the Hofstadter butterfly Fig. 2.1. In order to diagonalize the single particle Hamiltonian, i.e., the kinetic energy term in (2.15), we Fourier transform it to momentum space by means of

$$c_{i\alpha} = \sqrt{\frac{2}{N_s}} \sum_{\boldsymbol{k} \in \text{BZ}^\star} e^{-i\boldsymbol{k}\boldsymbol{R}_{i\alpha}} \, c_{\boldsymbol{k}\alpha}. \qquad (2.16)$$

---

[8]Note that this explicit symmetry breaking depends on the chosen gauge (2.14). Thus we should think of a broken symmetry in our description rather than in the model itself. As we will see later, the applied (artificial) magnetic field breaks certain symmetries. We will continue this discussion when we have have found the ground state of the model.
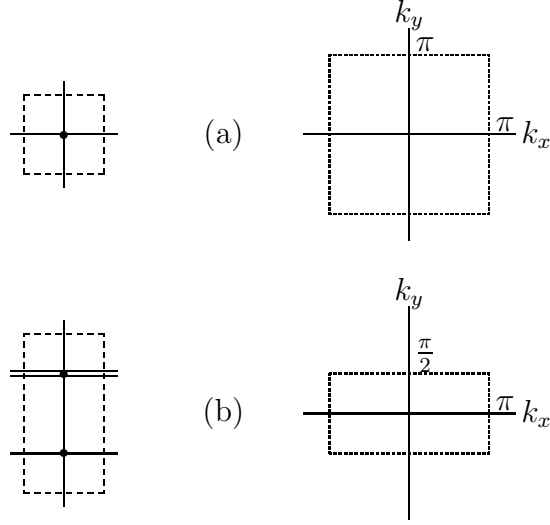
Figure 2.4: (a) Primitive unit cell and the Brillouin zone (BZ) of an ordinary square lattice. (b) π–flux square lattice where the applied magnetic field causes a doubled primitive unit cell and a halved Brioullin zone (BZ*). See the discussion in the text.

Here N_s is the number of lattice sites and, hence, $N_s/2$ the number of primitive unit cells. $\boldsymbol{R}_{i\alpha}$ is the coordinate of the lattice site in the ith unit cell on sublattice α. Using the relations

$$\sum_j e^{i(\boldsymbol{k}-\boldsymbol{k}')\boldsymbol{R}_{j\alpha}} = \frac{N_s}{2}\,\delta_{\boldsymbol{k}\boldsymbol{k}'} \quad \text{and} \quad \sum_{\boldsymbol{k}\in\mathrm{BZ}^\star} = \frac{N_s}{2} \tag{2.17}$$

we obtain

$$H_{\mathrm{kin}} = -2t\sum_{\boldsymbol{k}} \left(c_{\boldsymbol{k}1}^\dagger, c_{\boldsymbol{k}2}^\dagger\right) H_{\boldsymbol{k}} \begin{pmatrix} c_{\boldsymbol{k}1} \\ c_{\boldsymbol{k}2} \end{pmatrix} \tag{2.18}$$

with

$$H_{\boldsymbol{k}} = \hat{\sigma}_z \cos\left(ak_x\right) + \hat{\sigma}_x \cos\left(ak_y\right), \tag{2.19}$$

where σ_x and σ_z are Pauli matrices. Whereas for an ordinary hopping model without applied magnetic field the Fourier transform diagonalizes the Hamiltonian, here we end up with a block–diagonal form of the Hamiltonian. Each block is the two–dimensional matrix $H_{\boldsymbol{k}}$ reflecting the fact that the primitive unit cell contains two lattice sites. We are able to transform from the crystal momentum operators $c_{\boldsymbol{k}\alpha}$ to band operators $b_{\boldsymbol{k}\pm}$ belonging to an upper (+) and lower band (−) by a unitary transformation $\mathcal{U}$ such that

$$H_{\mathrm{kin}} = -2t\sum_{\boldsymbol{k}\in\mathrm{BZ}^\star} \left(c_{\boldsymbol{k}1}^\dagger, c_{\boldsymbol{k}2}^\dagger\right) \mathcal{U}^{\mathrm{t}}\mathcal{U}\,H_{\boldsymbol{k}}\,\mathcal{U}^{\mathrm{t}}\mathcal{U} \begin{pmatrix} c_{\boldsymbol{k}1} \\ c_{\boldsymbol{k}2} \end{pmatrix} =$$

$$\sum_{\boldsymbol{k}\in\mathrm{BZ}^\star} \left(b_{\boldsymbol{k}+}^\dagger, b_{\boldsymbol{k}-}^\dagger\right) \hat{\sigma}_z 2t\sqrt{\cos^2 ak_x + \cos^2 ak_y} \begin{pmatrix} b_{\boldsymbol{k}+} \\ b_{\boldsymbol{k}-} \end{pmatrix}.$$

The unitary operator $\mathcal{U}$ contains in its rows both eigenvectors of the matrix (2.19). It is explicitly given by

$$\mathcal{U} = \begin{pmatrix} u_1^-(\boldsymbol{q}) & u_1^+(\boldsymbol{q}) \\ u_2^-(\boldsymbol{q}) & u_2^+(\boldsymbol{q}) \end{pmatrix} \qquad (2.20)$$

where

$$u_1^-(\boldsymbol{q}) = \frac{\cos(aq_x) - \sqrt{\cos^2(aq_x) + \cos^2(aq_y)}}{\sqrt{X(\boldsymbol{q})}} \qquad (2.21)$$

$$u_1^+(\boldsymbol{q}) = \frac{\cos(aq_x) + \sqrt{\cos^2(aq_x) + \cos^2(aq_y)}}{\sqrt{X(\boldsymbol{q})}} \qquad (2.22)$$

$$u_2^-(\boldsymbol{q}) = \frac{\cos(aq_y)}{\sqrt{X(\boldsymbol{q})}} \qquad (2.23)$$

$$u_2^+(\boldsymbol{q}) = \frac{\cos(aq_y)}{\sqrt{X(\boldsymbol{q})}} \qquad (2.24)$$

and

$$X(\boldsymbol{q}) = \cos^2(aq_y) + \left(\cos(aq_x) + \sqrt{\cos^2(aq_x) + \cos^2(aq_y)}\right)^2. \qquad (2.25)$$

Finally we obtain the diagonalized single particle Hamiltonian,

$$H = \sum_{\boldsymbol{k} \in \mathrm{BZ}^\star} \sum_{\nu \in \{+,-\}} (\varepsilon_{\boldsymbol{k}}^\nu - \mu) \; b_{\boldsymbol{k}\nu}^\dagger b_{\boldsymbol{k}\nu} \qquad (2.26)$$

with eigenenergies

$$\varepsilon_{\boldsymbol{k}}^\pm = \pm 2t\sqrt{\cos^2(k_x) + \cos^2(k_y)}. \qquad (2.27)$$

Note that a π–flux lattice has a continuous single particle spectrum between $\varepsilon_{\min} = -2\sqrt{2}t$ and $\varepsilon_{\max} = 2\sqrt{2}t$. At $\varepsilon = 0$ there are Dirac points where the upper band $\varepsilon_{\boldsymbol{k}}^+$ and the lower band $\varepsilon_{\boldsymbol{k}}^-$ touch each other, see Fig. 2.5. As the single particle spectrum behaves in $k_x = k_y = k$ direction as $\varepsilon_{(k,k)} \sim |\boldsymbol{k} - \boldsymbol{k}_D|$ the spectrum is sometimes called relativistic or Dirac spectrum.

As a main result, the lower band has two minima, one at $\boldsymbol{k}_{\min} = (0,0)$ and the other at $\boldsymbol{k}_{\min} = (\pi, 0)$ in the Brioullin zone BZ*. We have illustrated the two minima in the following figure with black dots, in the reduced BZ (left) as well as in the lower single particle band (right):
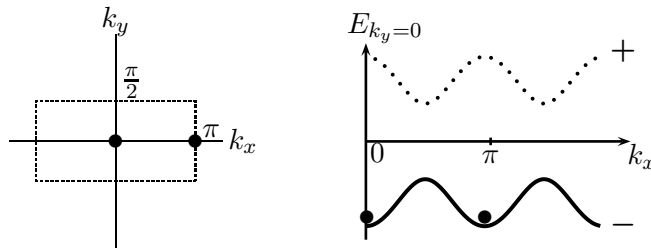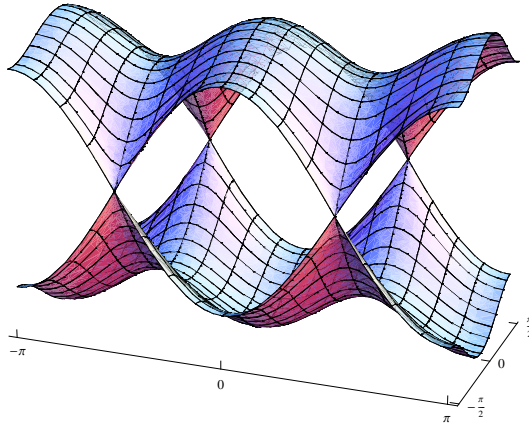
Figure 2.5: (Color online) Upper and lower band $\varepsilon_{\boldsymbol{k}}^{\pm}$ of the one–particle spectrum of the BHM on a π–flux lattice. The Brioullin zone in k_y–direction is halved as motivated in Fig. (2.4b). Upper and lower band touch each other at the Dirac points.

As stressed in the introduction, immediately the question appears how the condensation of the many boson system occurs.

As a last consideration of the single particle states, we focus onto the density distribution in real space. We expect for an ordinary (i.e., no external potential, no magnetic field etc.) single particle state a homogenous density distribution in real space. Let $|\psi_0\rangle = c^{\dagger}|0\rangle$ be such a single particle state on an arbitrary lattice, then we expect the expectation value $\langle\psi_0|\hat{n}_i|\psi_0\rangle$ to be homogenous, i.e., this expectation value is identical on every lattice site. For the Bose liquid in the condensed phase, all particles occupy the lowest single particle state macroscopically (at least at $T = 0$). This lowest single particle state is usually the momentum eigenstate with zero momentum, $|\boldsymbol{k} = 0\rangle$. All particles are, hence, localized in momentum space at $\boldsymbol{k} = 0$. Due to Heisenberg's uncertainty relation, the particles must be totally delocalized in real space associated with the "real space density" $\langle\Psi_0|\hat{n}_i|\Psi_0\rangle = \text{const.}$, where $|\Psi_0\rangle$ is the many particle ground state. We conclude that *simple* BEC is associated with a homogenous density profile in real space (at least at $T = 0$). In presence of π–flux, the density profile of the single particle ground state changes drastically. The two-fold degenerate ground state of the π–flux lattice is

$$b_0^{\dagger}|0\rangle \equiv b_{k_x=0,-}^{\dagger}|0\rangle = \left(-u\, c_{k_x=0,1}^{\dagger} + v\, c_{k_x=0,2}^{\dagger}\right)|0\rangle \qquad (2.28)$$

$$b_{\pi}^{\dagger}|0\rangle \equiv b_{k_x=\pi,-}^{\dagger}|0\rangle = \left(-v\, c_{k_x=\pi,1}^{\dagger} + u\, c_{k_x=\pi,2}^{\dagger}\right)|0\rangle\ , \qquad (2.29)$$

where the crystal momentum operators $c_{\boldsymbol{k}\alpha}$ (defined in Eq. (2.16)) and the band operators $b_{\boldsymbol{k}\pm}$ are connected by the unitary transformation (2.20). The coefficients are explicitly given by $u = (1 - \sqrt{2})/\mathcal{N}$ and $v = 1/\mathcal{N}$ with the normalization constant $\mathcal{N}^2 = 2(2 - \sqrt{2})$. As the single particle groundstates $b_0^{\dagger}|0\rangle$ and $b_{\pi}^{\dagger}|0\rangle$,

(a) $b_0^\dagger \,|\,0\,\rangle$ (b) $b_\pi^\dagger \,|\,0\,\rangle$
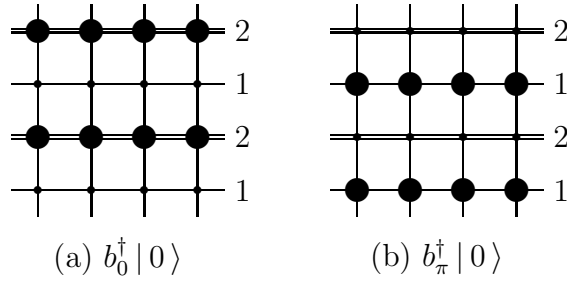
Figure 2.6: Density distributions of the one–particle ground states (a) $b_0^\dagger \,|\,0\,\rangle$ and (b) $b_\pi^\dagger \,|\,0\,\rangle$ in position space for the π–flux lattice. The density is strongly varying between both sublattices. The area of the dots corresponds to $|u|^2 \approx 0.15/(N_\mathrm{s}/2)$ or $|v|^2 \approx 0.85/(N_\mathrm{s}/2)$, respectively.

respectively, are linear combinations of the crystal momentum operators belonging to the sublattices $\alpha = 1$ and $\alpha = 2$, we expect a non–uniform density distribution in real space. In fact, we find

$$\langle\, 0\, |\, b_0 \; n_{i,\alpha=1} \; b_0^\dagger \,|\,0\,\rangle = |u|^2 \approx 0.15/(N_\mathrm{s}/2)$$
$$\langle\, 0\, |\, b_0 \; n_{i,\alpha=2} \; b_0^\dagger \,|\,0\,\rangle = |v|^2 \approx 0.85/(N_\mathrm{s}/2) \;. \tag{2.30}$$

For the second single particle ground state, $b_\pi^\dagger \,|\,0\,\rangle$, we find for the expectation values the same but interchanged results. The density patterns are illustrated in Fig. 2.6.

As we have seen, in momentum space the kinetic energy term can be diagonalized by an additional unitary transformation according to the doubled primitive unit cell. Indeed, the Brioullin zone is halved but we have a lower and an upper band. In order to investigate the full interacting many body Hamiltonian, we have to transform the Hubbard interaction into the band operators $b_{\boldsymbol{k}\pm}^\dagger$. First, we Fourier transform it to momentum space via (2.16):

$$\mathcal{H}_{\mathrm{int}} \;=\; \frac{U}{2} \sum_{i=1}^{N_\mathrm{s}/2} \sum_{\alpha=1,2} n_{i\alpha}\,(n_{i\alpha} - 1)$$

$$=\; \frac{U}{N_\mathrm{s}} \sum_{\alpha=1,2} \sideset{}{'}\sum_{\boldsymbol{k},\boldsymbol{k}',\boldsymbol{q}} c_{\boldsymbol{k}+\boldsymbol{q},\alpha}^\dagger c_{\boldsymbol{k}'-\boldsymbol{q},\alpha}^\dagger c_{\boldsymbol{k}',\alpha} c_{\boldsymbol{k},\alpha} \tag{2.31}$$

The prime at the sum indicates that the summation is restricted to momenta of the halved Brioullin zone $\mathrm{BZ}^\star$. Now, we have to transform the crystal momentum operators to band operators by means of the transformation

$$\begin{pmatrix} c_{\boldsymbol{k},1} \\ c_{\boldsymbol{k},2} \end{pmatrix} = \mathcal{U}^{\mathrm{t}} \begin{pmatrix} b_{\boldsymbol{k},+} \\ b_{\boldsymbol{k},-} \end{pmatrix}. \tag{2.32}$$

where $\mathcal{U}$ was defined in (2.20). The Hubbard interaction (2.31) in terms of the band operators is already an expression with many terms and, hence, very unpractical to

handle. As we are interested in the low–energy behavior of the mBHM, we drop all terms containing $b_{\boldsymbol{k},+}^{\dagger}$ operators, i.e., all operators belonging to the upper band. Then we end up with an effective interaction,

$$\mathcal{H}_{\mathrm{int}}^{\mathrm{eff}} = \frac{U}{N_{\mathrm{s}}} \sum_{\boldsymbol{k},\boldsymbol{k}',\boldsymbol{q}}' \mathcal{A}(\boldsymbol{k},\boldsymbol{k}',\boldsymbol{q})\, b_{\boldsymbol{k}+\boldsymbol{q},-}^{\dagger} b_{\boldsymbol{k}'-\boldsymbol{q},-}^{\dagger} b_{\boldsymbol{k}',-} b_{\boldsymbol{k},-} \tag{2.33}$$

The factor $\mathcal{A}(\boldsymbol{k},\boldsymbol{k}',\boldsymbol{q})$ appears due to the transformation from the crystal momentum operators to the band operators, it is explicitly given by

$$\mathcal{A}(\boldsymbol{k},\boldsymbol{k}',\boldsymbol{q}) = \sum_{\alpha=1,2} u_{\alpha}^{-}(\boldsymbol{k}+\boldsymbol{q})\, u_{\alpha}^{-}(\boldsymbol{k}'-\boldsymbol{q})\, u_{\alpha}^{-}(\boldsymbol{k}')\, u_{\alpha}^{-}(\boldsymbol{k}). \tag{2.34}$$

The effective interaction (2.33) is still too complicated and cannot solved analytically. In the following section, we will consider a more simplified version of the effective interaction. The exact solution of this effective model sheds light on the ground state properties of the many boson system in the π–flux lattice.

2.4   Effective model

In the previous section, we have investigated the single particle properties of the π–flux lattice. In this section, we are mainly interested in the properties of the many boson system. As long as we are considering the non–interacting case ($U = 0$), we expect the many particle ground state to be ($N_{\mathrm{b}} + 1$)–fold degenerate where N_{b} is the number of bosons. The $N_{\mathrm{b}} + 1$ ground states correspond to the states $|N_{\mathrm{b}},0\rangle$, $|N_{\mathrm{b}}-1,1\rangle$, $|N_{\mathrm{b}}-2,2\rangle$, ..., and $|0,N_{\mathrm{b}}\rangle$. In these kets, the first entry denotes the number of particles occupying the $k_x = 0$ single particle ground state and the second entry the number of particles occupying the $k_x = \pi$ single particle ground state. In the following, we consider the effective Hubbard interaction (2.33) and keep only the operators belonging to the macroscopically occupied states, i.e., only terms containing operators at $k_x = 0$ or $k_x = \pi$, respectively. Doing so, we find the following effective Hamiltonian

$$\tilde{\mathcal{H}} = \frac{U}{N_{\mathrm{s}}} \left[\frac{3}{4} \left(b_0^{\dagger} b_0^{\dagger} b_0 b_0 + b_{\pi}^{\dagger} b_{\pi}^{\dagger} b_{\pi} b_{\pi} \right) + b_0^{\dagger} b_0 b_{\pi}^{\dagger} b_{\pi} + \frac{1}{4} \left(b_0^{\dagger} b_0^{\dagger} b_{\pi} b_{\pi} + \mathrm{h.c.} \right) \right]. \tag{2.35}$$

An appropriate basis set is provided by the states

$$|m\rangle \equiv \frac{1}{\sqrt{(N_{\mathrm{b}}-m)!m!}} (b_0^{\dagger})^{N_{\mathrm{b}}-m} (b_{\pi}^{\dagger})^{m} |0\rangle \tag{2.36}$$

with $m = 0, \ldots, N_{\mathrm{b}}$. The first three terms in (2.35) are diagonal in this basis while the fourth and fifth term are scattering elements. The diagonal terms play the role of a potential,

$$\langle m| \left[\frac{3}{4} \left(b_0^{\dagger} b_0^{\dagger} b_0 b_0 + b_{\pi}^{\dagger} b_{\pi}^{\dagger} b_{\pi} b_{\pi} \right) + b_0^{\dagger} b_0 b_{\pi}^{\dagger} b_{\pi} \right] |m\rangle = \frac{1}{2} \left(m - \frac{N_{\mathrm{b}}}{2} \right)^2 + \frac{5N_{\mathrm{b}}(N_{\mathrm{b}}-5/6)}{8}$$

The non–diagonal term plays the role of hopping on this virtual chain with $N_{\mathrm{b}}+1$ sites. We find

$$\langle m| \left[\frac{1}{4} \left(b_0^\dagger b_0^\dagger b_\pi b_\pi + \mathrm{h.c.} \right) \right] |m \pm 2\rangle \ \approx \ \frac{1}{4}\, m\,(N_{\mathrm{b}} - m). \tag{2.37}$$

As the effective Hamiltonian (2.35) seems to be insoluble, one might approximate the hopping (2.37) to be constant. This approximation reduces the effective Hamiltonian (2.35) to a harmonic oscillator. When solving this oscillator, the study of its eigenenergies and eigenfunctions might help to understand the physical properties of the magnetic BHM at $\alpha = 1/2$.

At this point, we will dispense with the investigation of this approximate harmonic oscillator, since we have eventually found the exact solution of the effective Hamiltonian (2.35). Its spectrum and eigenstates will shed light on the underlying physical mechanism of the bose liquid in a π–flux lattice.

2.4.1   Exact solution for $U > 0$ and $U < 0$

In order to derive the exact solution of the effective model (2.35) we rewrite it as follows:

$$
\begin{aligned}
\tilde{\mathcal{H}}\frac{N_{\mathrm{s}}}{U} &= \frac{3}{4} \left(b_0^\dagger b_0^\dagger b_0 b_0 + b_\pi^\dagger b_\pi^\dagger b_\pi b_\pi \right) + b_0^\dagger b_0 b_\pi^\dagger b_\pi + \frac{1}{4} \left(b_0^\dagger b_0^\dagger b_\pi b_\pi + \mathrm{h.c.} \right) \\[2mm]
&= \frac{1}{4} \left(b_0^{\dagger\,2} + b_\pi^{\dagger\,2} \right) \left(b_0^{\,2} + b_\pi^{\,2} \right) + \frac{1}{2} \Big(\underbrace{b_0^\dagger b_0 + b_\pi^\dagger b_\pi}_{N_{\mathrm{b}}} \Big)^2 - \frac{1}{2} \Big(\underbrace{b_0^\dagger b_0 + b_\pi^\dagger b_\pi}_{N_{\mathrm{b}}} \Big) \\[2mm]
&= \left(\frac{1}{\sqrt{2}} \right)^4 \left(b_0^\dagger + i b_\pi^\dagger \right) \left(b_0^\dagger - i b_\pi^\dagger \right) \left(b_0 - i b_\pi \right) \left(b_0 + i b_\pi \right) + \frac{N_{\mathrm{b}}(N_{\mathrm{b}} - 1)}{2} \\[2mm]
&= c^\dagger d^\dagger c\, d\ + \frac{N_{\mathrm{b}}(N_{\mathrm{b}} - 1)}{2}
\end{aligned}
\tag{2.38}
$$

In the new operators c and d, the effective model becomes diagonal. For convenience, we skip the constant term in (2.38),

$$\mathcal{H}' \ = \ \frac{U}{N_{\mathrm{s}}}\, c^\dagger c\, d^\dagger d \ = \ \frac{U}{N_{\mathrm{s}}}\, n_c\, n_d\ . \tag{2.39}$$

This is exactly Noziéres model, see for a discussion Sec. 2.5.1. The new operators are defined as

$$c^\dagger \ = \ \frac{1}{\sqrt{2}} \left(b_0^\dagger + i b_\pi^\dagger \right) \tag{2.40}$$

$$c \ = \ \frac{1}{\sqrt{2}} \left(b_0 - i b_\pi \right) \tag{2.41}$$

$$d^\dagger = \frac{1}{\sqrt{2}}\left(b_0^\dagger - ib_\pi^\dagger\right) \tag{2.42}$$

$$d = \frac{1}{\sqrt{2}}\left(b_0 + ib_\pi\right). \tag{2.43}$$

They fulfill the standard commutation relations, $[c, c^\dagger] = 1$, $[d, d^\dagger] = 1$, and $[c, d^\dagger] = 0$, as they are connected with the operators $b_0^\dagger$ and $b_\pi^\dagger$ by a unitary transformation

$$\mathcal{T} = \frac{1}{\sqrt{2}}\begin{pmatrix} 1 & i \\ 1 & -i \end{pmatrix}.$$

The eigenstates of our effective model are easily given by

$$|N_\mathrm{b}, m\rangle = \frac{1}{\sqrt{m!(N_\mathrm{b} - m)!}}\, c^{\dagger m}\, d^{\dagger N_\mathrm{b} - m}\, |0\rangle \tag{2.44}$$

for $m = 0, 1, \ldots, N_\mathrm{b}$. The corresponding eigenenergies are

$$E_m = \frac{U}{N_\mathrm{s}}\, m(N_\mathrm{b} - m). \tag{2.45}$$

So far, we have not specified the sign of the interaction parameter U. All results we have obtained are independent of the sign of U. The spectrum for repulsive $U > 0$ is shown in Fig. 2.7 and for attractive $U < 0$ in Fig. 2.8. The spectrum
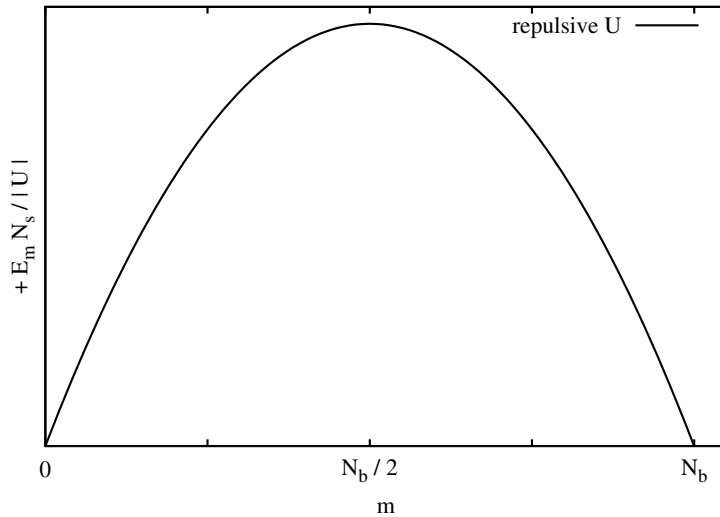
Figure 2.7: Spectrum of the effective Hamiltonian (2.35) for repulsive $U > 0$.

of the repulsive model is linear for small m and small $N_\mathrm{b} - m$. The states with lowest energy are $|N_\mathrm{b}, 0\rangle$ and $|N_\mathrm{b}, N_\mathrm{b}\rangle$. The ground state of our model is two–fold degenerate, independent of N_b being even or odd. The ground state corresponds to a simple condensate where all particles occupy the single particle state $c^\dagger |0\rangle$, $|N_\mathrm{b}, N_\mathrm{b}\rangle$, or the single particle state $d^\dagger |0\rangle$, $|N_\mathrm{b}, 0\rangle$, respectively. The ground states

of the mBHM at $\alpha = 1/2$, however, are superpositions of $|N_{\mathrm{b}}, N_{\mathrm{b}}\rangle$ and $|N_{\mathrm{b}}, 0\rangle$ in order to be momentum eigenstates:

$$|\tilde{0}\rangle \;=\; |k_x^{\mathrm{tot}} = 0\rangle = \frac{1}{\sqrt{2}} \Big(|N_{\mathrm{b}}, N_{\mathrm{b}}\rangle + |N_{\mathrm{b}}, 0\rangle \Big) \tag{2.46}$$

$$|\tilde{\pi}\rangle \;=\; |k_x^{\mathrm{tot}} = \pi\rangle = \frac{1}{i\sqrt{2}} \Big(|N_{\mathrm{b}}, N_{\mathrm{b}}\rangle - |N_{\mathrm{b}}, 0\rangle \Big) \tag{2.47}$$

The states $|\tilde{0}\rangle$ and $|\tilde{\pi}\rangle$ are superpositions of two distinct Bose–Einstein condensates. As a BEC is seen as a *macroscopic quantum object*, our ground states are superpositions of macroscopic objects or states. Therefore, $|\tilde{0}\rangle$ and $|\tilde{\pi}\rangle$ are refereed to as "Schrödinger cat states".
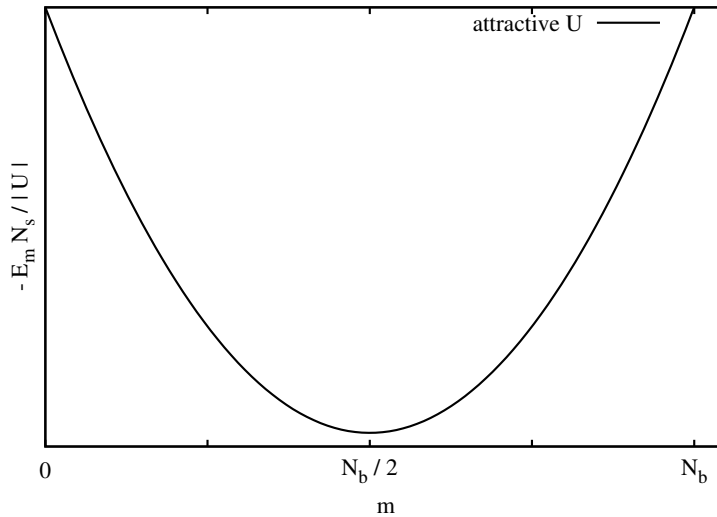
Figure 2.8: Spectrum of the effective Hamiltonian (2.35) for attractive $U < 0$.

For the effective Hamiltonian (2.35) with attractive interactions $U < 0$ the situation changes significantly. The spectrum (2.45) changes its sign, and the resulting spectrum has the shape of a parabola rather than an inverted parabola, see Fig. 2.8. The ground state of the attractive model is now given by

$$|N_{\mathrm{b}}, N_{\mathrm{b}}/2\rangle \;=\; \frac{1}{(N_{\mathrm{b}}/2)!} \, c^{\dagger N_{\mathrm{b}}/2} \, d^{\dagger N_{\mathrm{b}}/2} \, |0\rangle \, . \tag{2.48}$$

It corresponds to the evenly distributed occupation of the "c–condensate" and the "d–condensate". We will say that the attractive model possesses a *fragmented* condensate. We will stress the issue of fragmentation in Sec. 2.5.

The reader may notice that the consideration of a model with attractive interactions is principally delicate. The stability of an attractive Bose gas was discussed controversly. In the nineties, however, the stability of ^{7}Li which possesses attractive interactions was predicted for a certain parameter regime [81, 128] and eventually measured [34, 35] (attractive interactions correspond to negative scattering lengths).

A sufficiently small number of particles and sufficiently weak interactions [81, 128] are required. The instability to collapse when these conditions are not fulfilled has also been discussed by several authors [25, 120, 137]. Meanwhile, the use of a Feshbach resonance to tune the scattering length by changing the magnetic field allows atom–atom interaction from repulsive to attractive[9]. This was demonstrated in a ^{85}Rb BEC [126]. At a critical value of the scattering length $a_c < 0$, an abrupt transition was observed in which atoms were ejected from the condensate. Below a_c, the condensate remains stable. Already in 1998, it was pointed out by Wilkin, Gunn, and Smith that bosonic models with attractive interactions prefer to fragment rather than condense as repulsive models do [153]. Even though, this discussion was restricted to atomic gases, for our lattice model with effective magnetic field we find fragmentation as well. We wish to emphasize that the only requirement for the stability of attractive Bose models are weak interactions and diluteness of the gas. This should apply for the magnetic BHM as well. In the two following subsections we will test the validity of the effective model for repulsive and attractive interactions. We compare it on small clusters with the original microscopic model (2.11) by means of exact diagonalization studies.

2.4.2   Gap scaling and comparison with effective model

The effective model (2.35) is a rude approximation of the magnetic BHM (2.11) at $\alpha = 1/2$. The main assumption is that for weak interactions the many particle physics of the magnetic BHM is dominated by the interplay and interaction of the two macroscopically occupied single particle ground states. The only justification comes from the experience that a many boson system tends to occupy its single particle groundstate(s) macroscopically. In what follows, we wish to test the made approximations. The spectrum of the effective model for repulsive interactions $U > 0$ was derived in the previous section. The energy gap between the ground state and the first excited state is

$$\Delta = E_1 - E_0 = \frac{U}{N_s}\big(N_b - 1\big) \approx \frac{U N_b}{N_s} \tag{2.49}$$

where the approximation in (2.49) becomes exact for $N_b \gg 1$. The gap in the spectrum of the effective model should correspond to an energy gap in the spectrum of the magnetic BHM at $k_x^{\mathrm{tot}} = 0$ or $k_x^{\mathrm{tot}} = \pi$, respectively, if the effective model is an adequate description of the magnetic BHM. To test this prediction, we have performed numerical studies on finite clusters containing 4×4 and 6×6 sites. We have computed the gap size at $k_x^{\mathrm{tot}} = 0$ for several values of $U > 0$ and for different particle numbers N_b. In Fig. 2.9 we have plotted the gap sizes versus $U N_b / N_s$. On the first view, this seems not to fit very well. However, as we are considering particle numbers $N_b < 10$, we are far away from the limit $N_b \gg 1$. Hence the approximation in (2.49) is not valid. Instead, we use the exact result from (2.49). In Fig. 2.10, we have plotted

---

[9]Note that a uniform magnetic field is used to tune the scattering length as it is sensitive to the magnetic field. This has nothing to do with the artificial magnetic field required for the π–flux.
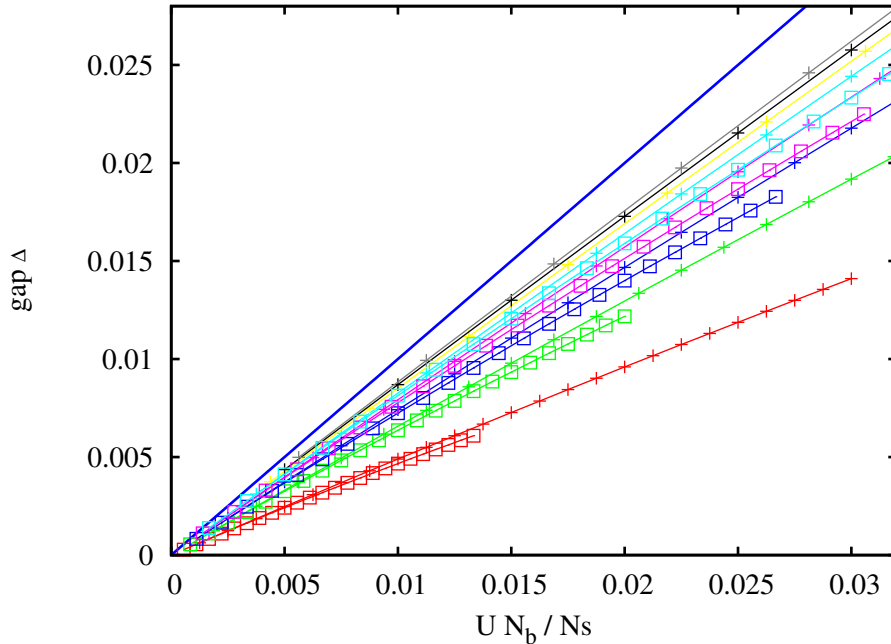
Figure 2.9: The gap size is plotted vs. interaction U times particle density $N_{\mathrm{b}}/N_{\mathrm{s}}$. The pluses corresponds to data points taken from a 4×4 lattice and the squares with the dot in the middle to data points taken from a 6×6 lattice. Red data corresponds to $N_{\mathrm{b}} = 2$, green to $N_{\mathrm{b}} = 3$, dark blue to $N_{\mathrm{b}} = 4$, pink to $N_{\mathrm{b}} = 5$, light blue to $N_{\mathrm{b}} = 6$, yellow to $N_{\mathrm{b}} = 7$, black to $N_{\mathrm{b}} = 8$, and grey to $N_{\mathrm{b}} = 9$. The blue solid line corresponds to the slope of one which is expected from the effective model, see Eq. (2.49).

the rescaled gap size $\Delta N_{\mathrm{b}}/(N_{\mathrm{b}} - 1)$ vs. interaction times density $U N_{\mathrm{b}}/N_{\mathrm{s}}$. Now the numerical data matches perfectly with the predictions of the effective model. We conclude that for weak repulsive interactions the effective model (2.35) describes at least the gap scaling at $k_x^{\mathrm{tot}} = 0$ perfectly. It is worth mentioning that this energy gap should experimentally be observable within the standard spectroscopy methods. This energy gap corresponds to a massive mode in the excitation spectrum and is a single particle excitation rather than a collective excitation. Additionally, the c–condensate as well as the d–condensate exhibit a gapless Goldstone mode. Within a Bogoliubov–like approach, we have calculated the low–lying excitation spectrum and found for small momenta $\boldsymbol{k}$ that the Goldstone mode obeys for small momenta the dispersion law $\epsilon^{\mathrm{exc}} = v_c |\boldsymbol{k}|$ with the critical velocity

$$ v_c = \left. \frac{\partial \varepsilon_{\boldsymbol{k}}}{\partial \boldsymbol{k}} \right|_{\boldsymbol{k} \to 0} = \left(\frac{\sqrt{2} t \, U \, N_c}{N_{\mathrm{s}}} \right)^{\frac{1}{2}} . \qquad (2.50) $$

The complete Bogoliubov calculation is presented in Appendix A.2.

Now we turn to the effective model with attractive interactions. Its spectrum has the minimum (or minima) around $m = N_{\mathrm{b}}$. We have to distinguish the cases of
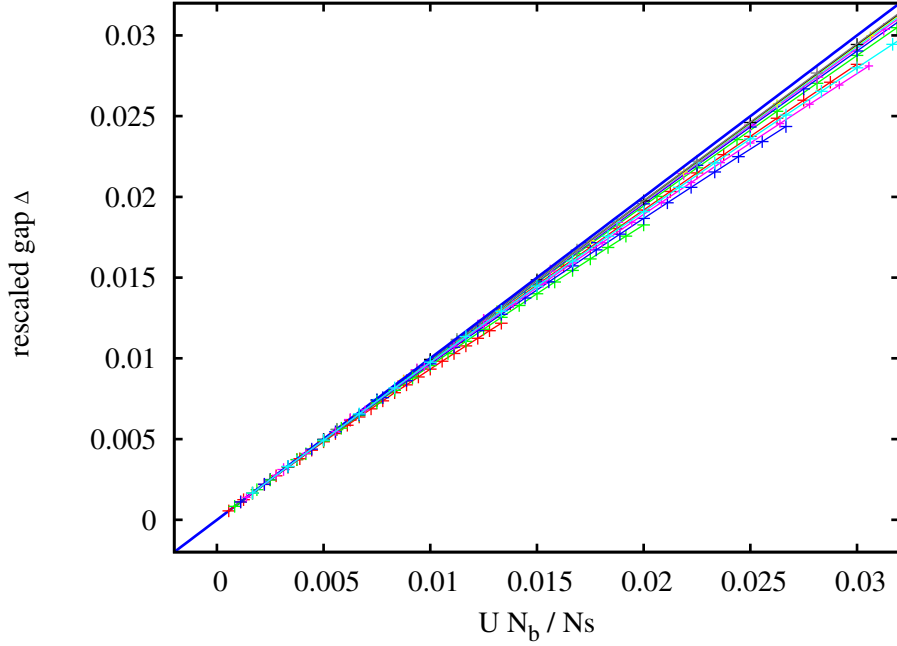
Figure 2.10: The rescaled gap size is plotted vs. interaction U times particle density $N_\mathrm{b}/N_\mathrm{s}$. The original gap size was rescaled by the factor $N_\mathrm{b}/(N_\mathrm{b} - 1)$ which comes from Eq. (2.49). The dark blue solid line corresponds to the prediction from the effective model. The data points are identical to those of Fig. 2.49.

even and odd particle numbers. For even particle numbers we find a finite size gap between ground state and first excited state as

$$\delta^{\mathrm{even}} = E_{\frac{N_\mathrm{b}}{2} \pm 1} - E_{\frac{N_\mathrm{b}}{2}} = -\frac{|U|}{N_\mathrm{s}} \left(\left(\frac{N_\mathrm{b}}{2} \pm 1 \right) \left(\frac{N_\mathrm{b}}{2} \mp 1 \right) - \left(\frac{N_\mathrm{b}}{2} \right)^2 \right)$$

$$= \frac{|U|}{N_\mathrm{s}}.$$

(2.51)

For odd particle numbers we find the finite size gap as

$$\delta^{\mathrm{odd}} = E_{\frac{N_\mathrm{b} \pm 3}{2}} - E_{\frac{N_\mathrm{b} \pm 1}{2}} = -\frac{|U|}{4N_\mathrm{s}} \big((N_\mathrm{b} \pm 3)(N_\mathrm{b} \mp 3) - (N_\mathrm{b} \pm 1)(N_\mathrm{b} \mp 1) \big)$$

$$= 2\frac{|U|}{N_\mathrm{s}}.$$

(2.52)

We notice that the gap is predicted to be independent of the particle number N_b apart from the even–odd–alternation. In Fig. 2.11, we show the numerical data taken from 4×4 clusters for various particle numbers. The numerical data fits for small interactions U perfectly the predicted values. On the 4×4 cluster, there is up to $U/t \approx 0.15$ perfect agreement between effective and microscopic model. We find for
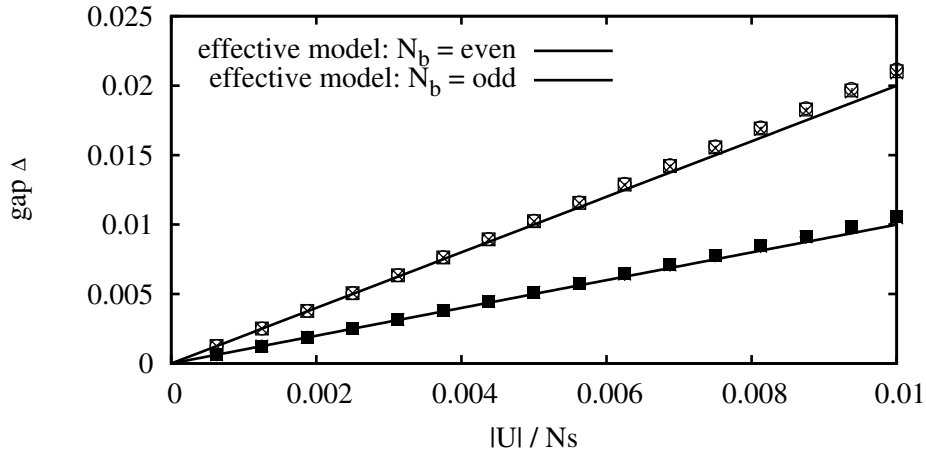
Figure 2.11: The gap size is plotted vs. interaction U/N_s. As predicted by the effective model, the gap alternates between even and odd particle numbers. The data points lay on top of each other for different particle numbers. The "even" data points correspond to $N_b = 2$, 4, and 6, and the "odd" data points to $N_b = 3$, 5, and 7. The solid lines represent the predicted values of the effective model.

6×6 clusters comparable results, in the weakly interacting regime the numerical studies confirm the prediction of the effective model perfectly. We conclude that the effective model (2.35) describes the gap scaling at $k_x^{\text{tot}} = 0$ of the magnetic BHM at $\alpha = 1/2$ not only for weak repulsive interactions very well but also for weak attractive interactions. The reader may notice that the gap would be in case of repulsive interactions observable via standard spectroscopy methods. The gap of the attractive model is, however, a finite size gap and physically meaningless. It is useful only as a test or for comparison, respectively, as it can be "measured" numerically.

2.4.3 Overlap of trial wave functions

The proposed effective model has stood the first test in the previous section. The next test is much harder. The exact solution (2.38) of the effective model provided us the eigenstates and, in particular, the ground state wavefunctions. In the following we will call these ground states of the effective model *trial wave functions* while the ground states of the full Hamiltonian *exact ground states*. We will briefly explain the explicit construction of the trial wave functions. We start with the single particle states $b_0^\dagger |0\rangle$ and $b_\pi^\dagger |0\rangle$ defined on a $\sqrt{N_s} \times \sqrt{N_s}$ square lattice and use them to construct the single particle states $\frac{1}{\sqrt{2}}(b_0^\dagger + i b_\pi^\dagger)|0\rangle \equiv |\varphi_0\rangle$ and $\frac{1}{\sqrt{2}}(b_0^\dagger - i b_\pi^\dagger)|0\rangle \equiv |\varphi_\pi\rangle$. We obtain the many–particle trial wave function as follows. First, we create the c–condensate,

$$\left| \Psi_c^{N_b} \right\rangle = \underbrace{|\varphi_0\rangle \otimes |\varphi_0\rangle \otimes \cdots \otimes |\varphi_0\rangle}_{N_b \text{ times}},$$

and d–condensate,

$$\left|\Psi_d^{N_{\mathrm{b}}}\right\rangle \;=\; \underbrace{|\varphi_\pi\rangle \otimes |\varphi_\pi\rangle \otimes \cdots \otimes |\varphi_\pi\rangle}_{N_{\mathrm{b}} \text{ times}}$$

Second, we build superpositions

$$\left|\psi_{0,N_{\mathrm{b}}}^{\mathrm{trial}}\right\rangle \;=\; \frac{1}{\sqrt{2}}\Big(\left|\Psi_c^{N_{\mathrm{b}}}\right\rangle + \left|\Psi_d^{N_{\mathrm{b}}}\right\rangle\Big), \tag{2.53}$$

$$\left|\psi_{\pi,N_{\mathrm{b}}}^{\mathrm{trial}}\right\rangle \;=\; \frac{1}{i\sqrt{2}}\Big(\left|\Psi_c^{N_{\mathrm{b}}}\right\rangle - \left|\Psi_d^{N_{\mathrm{b}}}\right\rangle\Big). \tag{2.54}$$

The exact ground states are obtained from exact diagonalization of the magnetic BHM at $\alpha = 1/2$ with repulsive interactions U on a $\sqrt{N_{\mathrm{s}}} \times \sqrt{N_{\mathrm{s}}}$ square lattice with periodic boundary conditions. We denote the two ground states for a given U by $\left|\zeta_{0,N_{\mathrm{b}}}^{U}\right\rangle$ or $\left|\zeta_{\pi,N_{\mathrm{b}}}^{U}\right\rangle$, respectively. The subscripts 0 and π correspond to the total momentum k_x^{tot}. In Tab. 2.1, we have listed a few overlaps for wavefunctions defined on a 4×4 lattice. We find grandiose overlaps: for low particle densities the trial wave

Overlaps $\left\langle\psi_{0,N_{\mathrm{b}}}\big|\zeta_{0,N_{\mathrm{b}}}^{U}\right\rangle$ for 4×4 lattice							
U/t	$N_{\mathrm{b}}=2$	$N_{\mathrm{b}}=3$	$N_{\mathrm{b}}=4$	$N_{\mathrm{b}}=5$	$N_{\mathrm{b}}=6$	$N_{\mathrm{b}}=7$	$N_{\mathrm{b}}=8$
10^{-5}	1.0	1.0	1.0	1.0	1.0	1.0	1.0
10^{-3}	1.0	1.0	1.0	1.0	1.0	1.0	1.0
10^{-2}	1.0	1.0	1.0	1.0	1.0	1.0	1.0
0.1	1.0	1.0	1.0	1.0	1.0	1.0	0.999
0.2	1.0	1.0	1.0	0.999	0.999	0.999	0.998
0.3	1.0	1.0	0.999	0.998	0.998	0.997	0.996
0.4	1.0	0.999	0.998	0.997	0.996	0.995	0.993
0.5	1.0	0.999	0.998	0.996	0.994	0.992	0.990
0.75	0.999	0.997	0.995	0.992	0.989	0.985	0.981
1.0	0.998	0.996	0.992	0.988	0.983	0.977	0.971
2.0	0.996	0.988	0.977	0.966	0.953	0.939	0.981
5.0	0.986	0.962	0.925	0.899	0.863	0.824	0.781
10.0	0.976	0.933	0.861	0.822	0.761	0.695	0.621
50.0	0.957	0.877	0.742	0.685	0.592	0.490	0.379
∞	0.950	0.854	0.697	0.633	0.531	0.423	0.306
$\nu = \frac{N_{\mathrm{b}}}{N_{\mathrm{s}}}$	0.125	0.1875	0.25	0.3125	0.375	0.4375	0.5

Table 2.1: Overlaps between trial wave functions and exact ground states of the magnetic BHM at $\alpha = 1/2$ for the 4×4 lattice.

functions are exact ground states up to interactions $U \sim 0.3$. Even for half filling,

i.e., 8 bosons on the 4×4 lattice, we find overlaps at interactions $U \sim 0.3$ which are very close to 1.0. Strong interactions, however, clearly decrease the overlaps and render the trial wave functions as insufficient description. Particularly the hard–core limit $U \to \infty$ is not described by the effective model (2.35) anymore. As overlaps decrease naturally when increasing the system size, it is important to look at larger clusters. In Tab. 2.2, we have listed the overlaps calculated on a 6×6 lattice for particle numbers $N_\mathrm{b} = 2, \ldots, 6$. We notice that the quality of overlaps remains valid

Overlaps $\langle \psi_{0,N_\mathrm{b}} | \zeta^U_{0,N_\mathrm{b}} \rangle$ for 6×6 lattice					
U/t	$N_\mathrm{b}\!=\!2$	$N_\mathrm{b}\!=\!3$	$N_\mathrm{b}\!=\!4$	$N_\mathrm{b}\!=\!5$	$N_\mathrm{b}\!=\!6$
10^{-5}	1.0	1.0	1.0	1.0	1.0
10^{-3}	1.0	1.0	1.0	1.0	1.0
10^{-2}	1.0	1.0	1.0	1.0	1.0
0.1	1.0	1.0	1.0	1.0	1.0
0.2	1.0	1.0	1.0	0.999	0.999
0.3	1.0	1.0	0.999	0.999	0.998
0.4	1.0	0.999	0.999	0.998	0.997
0.5	1.0	0.999	0.998	0.997	0.996
0.75	0.999	0.998	0.996	0.994	0.992
1.0	0.999	0.997	0.994	0.991	0.987
2.0	0.997	0.992	0.984	0.975	0.965
5.0	0.992	0.977	0.957	0.932	0.905
10.0	0.987	0.962	0.928	0.888	0.843
50.0	0.978	0.937	0.881	0.815	0.741
∞	0.975	0.928	0.862	0.786	0.702
$\nu = \frac{N_\mathrm{b}}{N_\mathrm{s}}$	0.0556	0.0833	0.111	0.1389	0.1667

Table 2.2: Overlaps between trial wave functions and exact ground states of the magnetic BHM at $\alpha = 1/2$ for the 6×6 lattice.

on the 6×6 lattice. We conclude, that the effective model (2.35) approximates not only the magnetic BHM at $\alpha = 1/2$ but also describes the ground state properties exactly in the weakly interacting regime.

We have also evaluated overlaps between the attractive models. In the weakly interacting regime we have found excellent overlaps, comparable to those of the repulsive models. In particular, in the limit of small $|U|$ the trial wave functions are the exact ground states of the magnetic BHM at $\alpha = 1/2$. For larger values of $|U|$, we have found a sudden decrease of the overlaps. In this regime where $|U| > t$, the attractive interactions become dominant and the "Bose–Hubbard physics" breaks down. Consequently, the effective model fails as a sufficient description in this regime.

2.5   Fragmentation of BEC

Penrose and Onsager generalized the concept of BEC by defining condensation in terms of the single particle density matrix [119]

$$\rho^{(1)}(\boldsymbol{r}, \boldsymbol{r}') \;=\; \langle \Psi^\dagger(\boldsymbol{r})\Psi(\boldsymbol{r}')\rangle \tag{2.55}$$

where $\Psi^\dagger(\boldsymbol{r})$ creates a scalar boson at position $\boldsymbol{r}$ and $\langle \cdots \rangle$ is the usual thermal average at temperature T. As the matrix $\rho^{(1)}(\boldsymbol{r}, \boldsymbol{r}')$ is hermitian, it can be diagonalized as

$$\rho^{(1)}(\boldsymbol{r}, \boldsymbol{r}') \;=\; \sum_i n_i \, \chi_i^\star(\boldsymbol{r}')\chi_i(\boldsymbol{r}) \tag{2.56}$$

where the functions $\chi_i(\boldsymbol{r})$ are a complete orthogonal set and $\sum_i n_i = N$, the total number of particles. The eigenvalues are ordered such that $n_0 \geq n_1 \geq n_2 \geq \ldots$. Note that the eigenfunctions $\chi_i(\boldsymbol{r})$ must not coincide with the single particle eigenstates. The wavefunctions χ_i as well as the eigenvalues n_i are in general time dependent. For simplicity, we skip the time dependence. We now state the following definitions [97, 110]:

- If all eigenvalues n_i of $\rho^{(1)}$ are of order unity then we say that the system is *normal* or not Bose–condensed.

- If there exists exactly one eigenvalue of order N and all other eigenvalues are of order unity then we say the system exhibits a *simple* BEC.

- If there are two or more than two eigenvalues of order N and all other eigenvalues are of order unity, then we say the system exhibits *fragmented* BEC.

The definition implies that in case of simple BEC we can write the single particle density matrix as

$$\rho^{(1)}(\boldsymbol{r}, \boldsymbol{r}') \;=\; n_0 \, \chi_0^\star(\boldsymbol{r}')\chi_0(\boldsymbol{r}) + \ldots$$

$$\equiv \; \Psi^{(0)^\star}(\boldsymbol{r}')\Psi^{(0)}(\boldsymbol{r}) + \ldots,$$

where $\Psi^{(0)}(\boldsymbol{r})$ is often referred to as the *macroscopic wavefunction* of the system. As the given definition seems to be abstract we discuss a simple model where both simple and fragmented BEC appear[10] depending on the interactions.

2.5.1   Nozières model

The very basic example of fragmentation goes back to Nozières [110, 113, 114]. We consider a system of N bosons which might occupy the orbitals 1 and 2. The Hamiltonian of Nozières model is simply given by

$$H = \frac{g}{2}a_1^\dagger a_1 a_2^\dagger a_2 = \frac{g}{2}n_1 n_2 \tag{2.57}$$

---

[10]In the brief review of Nozières model and scalar bosons in a double well we follow the excellent review of Baym *et al.* [110].

which is form–equivalent to the effective model (2.39). The eigenenergies of (2.57) are $E = g/2 n_1 n_2$ with $N = n_1 + n_2$, the eigenstates are given by

$$|f\rangle = \frac{1}{\sqrt{n_1! n_2!}} \, a_1^{\dagger n_1} \, a_2^{\dagger n_2} \, |0\rangle. \tag{2.58}$$

For repulsive interactions $g > 0$, the ground state is two–fold degenerate with $n_1 = N$ and $n_2 = 0$ or with $n_1 = 0$ and $n_2 = N$. The ground states are $|\psi_1\rangle = a_1^{\dagger N}/\sqrt{N!}\,|0\rangle$ and $|\psi_2\rangle = a_2^{\dagger N}/\sqrt{N!}\,|0\rangle$; these states exhibit simple condensates and the eigenvalues of the single particle density matrix are N and 0,

$$\rho^{(1)} = \langle a_\mu^\dagger a_\nu \rangle = \langle \psi_1 | a_\mu^\dagger a_\nu | \psi_1 \rangle = \begin{pmatrix} N & 0 \\ 0 & 0 \end{pmatrix} = N \begin{pmatrix} 1 \\ 0 \end{pmatrix} (1, 0).$$

The macroscopic wavefunction of this simple condensate is thus $\Psi^{(0)} = \sqrt{N}(1,0)^{\mathrm{t}}$ (the superscript t stands for transpose). The single particle density matrix of $|\psi_2\rangle$ has the interchanged eigenvalues than $|\psi_1\rangle$. It is worth emphasizing that it is the most convenient property of the single particle density matrix, that one can calculate it in any basis.

For attractive interactions $g < 0$ the state with $n_1 = n_2 = N/2$ has the lowest energy. The corresponding ground state,

$$|F\rangle = \frac{a_1^{\dagger N/2} a_2^{\dagger N/2}}{(N/2)!} \, |0\rangle,$$

has a fragmented condensate which can be seen by considering the single–particle density matrix exhibiting two macroscopic eigenvalues:

$$\rho^{(1)} = \langle a_\mu^\dagger a_\nu \rangle = \frac{N}{2} \begin{pmatrix} 1 & 0 \\ 0 & 1 \end{pmatrix}. \tag{2.59}$$

To get a better understanding of fragmentation, we consider a more realistic model: scalar bosons in a double–well.

2.5.2   Scalar bosons in a double–well

In the following, we briefly review a model with a fragmented ground state where bosons are in a double–well potential with tunneling between the wells. Note that we follow Baym's review on fragmentation [110]. The model consists of a tunneling term between the wells which we label by $i = 1, 2$. We assume that in each well is only one relevant state. Bosons within a given well have an onsite interaction U which can be positive or negative. We take the Hamiltonian to be

$$H = -t \left(a_1^\dagger a_2 + a_2^\dagger a_1 \right) + \frac{U}{2} \Big(n_1(n_1 - 1) + n_2(n_2 - 1) \Big), \tag{2.60}$$

where the bosonic creation operator $a_i^\dagger$ creates a boson in well i and $n_i = a_i^\dagger a_i$ counts the number of bosons being in well i. Note that $n_i(n_i - 1) = a_i^\dagger a_i^\dagger a_i a_i$ is the usual

contact oder Hubbard interaction. For a fixed particle number $n_1 + n_2 = N$ we rewrite the interaction term as

$$H_{\text{int}} = \frac{U}{4}\Big((n_1 - n_2)^2 + N^2 - 2N \Big).$$

Note that this model, simple as it is, has wide applicability to many physical situations: atoms in a double–well potential [15, 53], internal hyperfine states coupled by electromagnetic fields [58, 111, 141], atoms in a rotating toroidal trap [147], or wave packets in an optical lattice [108]. We now construct the exact solution of (2.60). As we will see, the interaction will cause different types of fragmented states depending on the sign of the interaction U. The single particle ground state of (2.60) is given by $(a_1^\dagger + a_2^\dagger)/\sqrt{2}$ with energy $-t$ (we assume throughout the section t to be real and positive). For the non–interacting system ($U = 0$) with N bosons, the ground state is a *coherent* state

$$|C\rangle = \frac{1}{\sqrt{2^N N!}} \left(a_1^\dagger + a_2^\dagger \right)^N |0\rangle$$

with energy $-tN$. The single particle density matrix of the non–interacting ground state $|C\rangle$ is given by

$$\rho_C^{(1)} = \langle a_\mu^\dagger a_\nu \rangle = \frac{N}{2} \begin{pmatrix} 1 & 1 \\ 1 & 1 \end{pmatrix} = N \begin{pmatrix} \frac{1}{\sqrt{2}} \\ \frac{1}{\sqrt{2}} \end{pmatrix} \left(\frac{1}{\sqrt{2}}, \frac{1}{\sqrt{2}} \right).$$

$\rho^{(1)}$ has a single macroscopic eigenvalues N. The non–interacting system exhibits, hence, a simple BEC with condensate wave function $\sqrt{N/2}(1,1)^{\text{t}}$. Note that we can rewrite the coherent state $|C\rangle$ as follows:

$$|C\rangle = \sum_{\mu=0}^{N} \frac{1}{\sqrt{2^N N!}} \binom{N}{\mu} \left(a_1^\dagger \right)^{N-\mu} \left(a_2^\dagger \right)^{\mu} |0\rangle$$

$$\overset{\ell=\frac{N}{2}-\mu}{=} \sum_{\ell=-\frac{N}{2}}^{\frac{N}{2}} \frac{1}{\sqrt{2^N N!}} \frac{N!}{\left(\frac{N}{2} - \ell\right)! \left(\frac{N}{2} + \ell\right)!} \left(a_1^\dagger \right)^{\frac{N}{2}+\ell} \left(a_2^\dagger \right)^{\frac{N}{2}-\ell} |0\rangle$$

$$= \sum_{\ell=-\frac{N}{2}}^{\frac{N}{2}} \left(\frac{N!}{2^N \left(\frac{N}{2} - \ell\right)! \left(\frac{N}{2} + \ell\right)!} \right)^{\frac{1}{2}} |N/2 + \ell, N/2 - \ell\rangle$$

$$\equiv \sum_{\ell=-\frac{N}{2}}^{\frac{N}{2}} \Psi_\ell^{(0)} |\ell\rangle.$$

The coefficients $\Psi_\ell^{(0)}$ are Gaussian distributed,

$$\Psi_\ell^{(0)} = \left(\frac{N!}{2^N \left(\frac{N}{2} - \ell\right)! \left(\frac{N}{2} + \ell\right)!} \right)^{\frac{1}{2}} \approx \frac{e^{(-\ell^2/N)}}{(\pi N/2)^{\frac{1}{4}}}. \tag{2.61}$$

Since the ground state $|C\rangle$ is a linear combination of the Fock–states

$$|n_1, n_2\rangle = \frac{1}{\sqrt{n_1! n_2!}} a_1^{\dagger n_1} a_2^{\dagger n_2} |0\rangle \tag{2.62}$$

the number of particles in each well fluctuates. We find the number fluctuations as

$$\langle (\Delta n_1)^2 \rangle = \langle (n_1 - \langle n_1 \rangle)^2 \rangle = \frac{N}{4}.$$

Now we consider the interacting case and start with $U > 0$. Repulsive interactions suppress number fluctuations, meaning that the Gaussian distribution (2.61) of the coherent state will be squeezed into an even narrower distribution. In the limit of zero number fluctuations, $\langle (\Delta n_1)^2 \rangle = \langle (\Delta n_2)^2 \rangle = 0$, the ground state of the system becomes the Fock state

$$|F\rangle = \frac{a_1^{\dagger N/2} a_2^{\dagger N/2}}{(N/2)!} |0\rangle. \tag{2.63}$$

The single particle density matrix $\rho_F^{(1)} = \langle F| a_\mu^\dagger a_\nu |F\rangle$ has two macroscopic eigenvalues $\lambda_{1,2} = N/2$, corresponding to independent condensation in each well.

For attractive interactions, $U < 0$, the potential energy in (2.60) favors a large number difference in the two wells, $|\ell = N/2\rangle \equiv |N, 0\rangle$ and $|\ell = -N/2\rangle \equiv |0, N\rangle$ while the hopping favors a Gaussian distribution of number states around $\ell = 0$. The effect of the interaction is then to split the Gaussian peak of the coherent state, (2.61), into two peaks. The ground state is then a so–called Schrödinger-cat state,

$$|\text{CAT}\rangle = \frac{1}{\sqrt{2}} \left(|N, 0\rangle + |0, N\rangle \right).$$

The Schrödinger–cat state is fragmented in the sense that its single–particle density matrix has two macroscopic eigenvalues identical to that of the Fock state $|F\rangle$. On the other hand, contrary to the Fock state, it has a huge number fluctuations,

$$\langle (\Delta n_1)^2 \rangle = \langle (\Delta n_2)^2 \rangle = \frac{N^2}{4}. \tag{2.64}$$

The double–well example should have demonstrated that the calculation of the single particle density matrix is not sufficient in order to characterize the type of fragmentation. So far we repeated parts from the excellent review on fragmentation by Baym *et al.* [110].

2.5.3 Bosons in a π–flux lattice

Now we apply the acquired knowledge to the bosons in a π–flux lattice. As the effective model (2.39) is a realization of Noziéres model, we expect a single condensate for the case of repulsive interactions and a fragmented condensate for the case of attractive interactions. First we consider repulsive interactions $U > 0$. The eigenstates

of the effective model (independent of the sign of U) have the form (2.44). Thus we can easily calculate the single particle density matrix of these states,

$$\rho^{(1)} = \langle N_{\mathrm{b}}, m | \gamma^{\dagger} \gamma' | N_{\mathrm{b}}, m \rangle = \begin{pmatrix} m & 0 \\ & \\ 0 & N_{\mathrm{b}} - m \end{pmatrix} \qquad (2.65)$$

where $\gamma^{\dagger}, \gamma'^{\dagger} \in \{c^{\dagger}, d^{\dagger}\}$. For the c–condensate ($m = N_{\mathrm{b}}$) or for the d–condensate ($m = 0$), the single particle density matrix has a single macroscopic eigenvalue N_{b}. These states ($|N_{\mathrm{b}}, N_{\mathrm{b}}\rangle$ and $|N_{\mathrm{b}}, 0\rangle$) are clearly not fragmented, they correspond to a simple BEC. As pointed out in Sec. 2.4 the physical ground states of the effective model are superpositions of the c– and d–condensate, see (2.46) and (2.47). When calculating the single particle density matrix within these Schrödinger–cat states, $\rho^{(1)}$ possesses two macroscopic eigenvalues $\lambda_{1,2} = N_{\mathrm{b}}/2$,

$$\rho^{(1)}_{\mathrm{Cat}} = \langle \tilde{0} | \gamma^{\dagger} \gamma' | \tilde{0} \rangle = \langle \tilde{\pi} | \gamma^{\dagger} \gamma' | \tilde{\pi} \rangle = \begin{pmatrix} \frac{N_{\mathrm{b}}}{2} & 0 \\ & \\ 0 & \frac{N_{\mathrm{b}}}{2} \end{pmatrix} . \qquad (2.66)$$

This coincides with numerical studies performed on finite clusters where we calculated the single particle density matrix

$$\rho^{(1)}_{\mathrm{num.}} = \langle c_i^{\dagger} c_j \rangle$$

where c_i is a bosonic creation operator in real space as defined in Eq. (2.10). Hence, $\rho^{(1)}$ is a N_{s}–dimensional matrix where N_{s} is the number of lattice sites, for our numerical studies we are restricted to $N_{\mathrm{s}} = 36$. We have found the spectrum of $\rho^{(1)}$ exhibiting two macroscopic eigenvalues $\lambda_{1,2} = N_{\mathrm{b}}/2 - \varepsilon$ and $N_{\mathrm{s}} - 2$ almost vanishing eigenvalues $\lambda_{3,...,N_{\mathrm{s}}} = \mathcal{O}(10^{-5})$. The tiny quantity ε is approximately $(N_{\mathrm{s}} - 2)\,10^{-5}$. This numerical result matches with the result of the effective model (2.66) perfectly. From the scalar bosons in the double–well, we have learned that the Schrödinger–cat state has huge number fluctuations. We calculate, hence, these fluctuations and find the expected huge value,

$$\langle (n_c)^2 \rangle = \langle (n_d)^2 \rangle = \frac{N_{\mathrm{b}}^2}{4}.$$

Now we consider attractive interactions $U < 0$. Here we will find a more subtle situation caused by an "even odd discrepancy". Analytically, we find for even particle numbers ordinary fragmentation, for odd particle numbers, however, it turns out that one fragment contains 3/4 of the particles and the other fragment only 1/4 of the particles - this somewhat strange fragmentation looks like an artefact. However, numerically we confirm this analytical prediction within exact diagonalization on clusters up to 36 sites with periodic boundary conditions (PBCs).

In case of an even particle number N_{b} the ground state is given by Eq. (2.48), $|N_{\mathrm{b}}, N_{\mathrm{b}}/2\rangle = c^{\dagger N_{\mathrm{b}}/2} d^{\dagger N_{\mathrm{b}}/2} |0\rangle / (N_{\mathrm{b}}/2)!$. The corresponding density matrix is given by

$$\rho^{(1)}_{\mathrm{even}} = \begin{pmatrix} \langle c^{\dagger} c \rangle & \langle c^{\dagger} d \rangle \\ \langle d^{\dagger} c \rangle & \langle d^{\dagger} d \rangle \end{pmatrix} = \begin{pmatrix} \frac{N_{\mathrm{b}}}{2} & 0 \\ & \\ 0 & \frac{N_{\mathrm{b}}}{2} \end{pmatrix} . \qquad (2.67)$$

Numerically we find a one–to–one correspondence to this result. The evaluated number fluctuations in case of attractive interactions are

$$\left\langle (n_c)^2 \right\rangle = \left\langle (n_d)^2 \right\rangle = 0,$$

we find the same result as for the Fock state in Eq. (2.63). This supports our statement that the attractive BHM at $\alpha = 1/2$ exhibits a fragmented condensate. In case of an odd particle number, we have two ground states. The reason is simple: if one has to evenly distribute $N =$ particles onto two condensates, one ends up with $N/2$ particles in each condensate as long as N is even. If one repeats this procedure with an odd particle number, one finds two possibilities in distributing the particles evenly onto both condensates: either $(N+1)/2$ to the first and $(N-1)/2$ particles to the second condensate or vice versa. Here we have the same situation. The physical ground states are then superpositions in order to be momentum eigenstates:

$$\left| \psi_{\mathrm{odd}}^1 \right\rangle = \frac{1}{\sqrt{2}\sqrt{\frac{N_{\mathrm{b}}+1}{2}}\sqrt{\frac{N_{\mathrm{b}}-1}{2}}} \left(c^{\dagger \frac{N_{\mathrm{b}}+1}{2}} d^{\dagger \frac{N_{\mathrm{b}}-1}{2}} + c^{\dagger \frac{N_{\mathrm{b}}-1}{2}} d^{\dagger \frac{N_{\mathrm{b}}+1}{2}} \right) | 0 \rangle \quad (2.68)$$

$$\left| \psi_{\mathrm{odd}}^2 \right\rangle = \frac{1}{i\sqrt{2}\sqrt{\frac{N_{\mathrm{b}}+1}{2}}\sqrt{\frac{N_{\mathrm{b}}-1}{2}}} \left(c^{\dagger \frac{N_{\mathrm{b}}+1}{2}} d^{\dagger \frac{N_{\mathrm{b}}-1}{2}} - c^{\dagger \frac{N_{\mathrm{b}}-1}{2}} d^{\dagger \frac{N_{\mathrm{b}}+1}{2}} \right) | 0 \rangle \quad (2.69)$$

The corresponding single particle density matrix is given by

$$\rho_{\mathrm{odd}}^{(1)} = \begin{pmatrix} \left\langle c^{\dagger}c \right\rangle & \left\langle c^{\dagger}d \right\rangle \\ \left\langle d^{\dagger}c \right\rangle & \left\langle d^{\dagger}d \right\rangle \end{pmatrix} = \begin{pmatrix} \frac{N_{\mathrm{b}}}{2} & \frac{N_{\mathrm{b}}+1}{4} \\ \frac{N_{\mathrm{b}}+1}{4} & \frac{N_{\mathrm{b}}}{2} \end{pmatrix} \rightsquigarrow \begin{pmatrix} \frac{3N_{\mathrm{b}}+1}{4} & 0 \\ 0 & \frac{N_{\mathrm{b}}-1}{4} \end{pmatrix} \quad (2.70)$$

We find for both ground states two macroscopic eigenvalues, they are, however, different. In the formal definition of fragmentation, the only requirement was to have two or more macroscopic eigenvalues. Before we continue this discussion, we look at the number fluctuations, we find

$$\left\langle (n_c)^2 \right\rangle = \left\langle (n_d)^2 \right\rangle = \frac{1}{4}.$$

Compared to the number fluctuations of a coherent state ($\left\langle (n_1)^2 \right\rangle \sim N$) or even a Schrödinger–cat state ($\left\langle (n_1)^2 \right\rangle \sim N^2$), these fluctuations are very small. Our result supports, hence, the statement that the condensate is fragmented apart from the strange "even odd behavior". We have found a situation which seems to be highly unphysical, a qualitative difference between even and odd particle numbers which survives in the thermodynamic limit. Note that this cannot be an artefact of the effective model, as we find the same discrepancy in our numerical studies on square lattices with up to 36 sites. Nonetheless, we suggest that in a realistic situation the system will behave as pointed out for the "even" case. We notice that fragmentation remains a delicate topic. Summarizing, we have found that the condensate fragments in the presence of interactions. For repulsive interactions, the ground state is a Schrödinger cat state. For attractive interactions, the system exhibits a real fragmented condensate.

2.6   The current pattern

In the previous sections we have solved an effective model which turned out to describe the original model, the magnetic BHM subject to π–flux, very well. The results obtained in Sec. 2.3 appear in the light of the exact results of Sec. 2.4 unsatisfactory. We wish to emphasize that the results are not wrong. The proceeding in Sec. 2.3 represents an educated guess and all results are correct. Nonetheless, the original proceeding has concealed the real nature of the ground state of the considered model. A priori, every other proceeding, however, would have seemed to be arbitrary. Now we will rectify a few results according to our new insights, i.e., that the physical unit cell contains a whole plaquette rather than two sites only. These rectifications, however, shed light on the hidden nature of the ground state of this model. We will see that for the ground state a global $\mathbb{Z}_2$ symmetry is spontaneously broken.

Due to the chosen gauge (2.14) the Hamiltonian (2.11) breaks translational symmetry in y–direction. To restore this problem we have doubled the primitive unit cell now containing two atoms. Consequently, we obtained a halved Brioullin zone and k_y was not a good quantum number anymore, i.e., the y–component of the momentum operator does not commute with the Hamiltonian. In Sec. 2.4, we have eventually learned that the many boson system condenses in one of the single particle states $(b_0^\dagger \pm i b_\pi^\dagger)\,|\,0\,\rangle$ rather than in $b_0^\dagger\,|\,0\,\rangle$ or $b_\pi^\dagger\,|\,0\,\rangle$, respectively. Obviously, the single particle states, which will be occupied macroscopically, mix the momenta $k_x = 0$ and $k_x = \pi$. Hence, also k_x can no longer be a good quantum number. To overcome this problem we have to double the unit cell again, now containing four atoms, i.e., a whole plaquette. In opposite to Sec. 2.3 where we introduced two sublattices $\alpha = 1$ and $\alpha = 2$, we require now four sublattices $\alpha = 1, \ldots, 4$. The Brioullin zone is, hence, a quarter of the full Brioullin zone. The single particle creation operator $c^\dagger$ (or $d^\dagger$, respectively) is a linear combination of the crystal zero–momentum operators on the four sublattices,

$$
c^\dagger \;=\; \begin{pmatrix} 1/2\,\exp\left(i\tfrac{\pi}{8}\right) \\[4pt] 1/2\,\exp\left(i\tfrac{3\pi}{8}\right) \\[4pt] 1/2\,\exp\left(-i\tfrac{\pi}{8}\right) \\[4pt] 1/2\,\exp\left(-i\tfrac{3\pi}{8}\right) \end{pmatrix}^{\mathrm{T}} \cdot \begin{pmatrix} c^\dagger_{\boldsymbol{k}=0,\alpha=1} \\[4pt] c^\dagger_{\boldsymbol{k}=0,\alpha=2} \\[4pt] c^\dagger_{\boldsymbol{k}=0,\alpha=3} \\[4pt] c^\dagger_{\boldsymbol{k}=0,\alpha=4} \end{pmatrix}. \tag{2.71}
$$

Note that all the amplitudes are equal $1/2$ corresponding to a homogenous density profile in real space as expected from a simple BEC. The phases on the four sublattices are different. On sublattice $\alpha = 4$ the phase is $\varphi_4 = -3\pi/8$, on sublattice $\alpha = 3$ it is $\varphi_3 = -\pi/8$, on sublattice $\alpha = 1$ it is $\varphi_1 = \pi/8$, and on sublattice $\alpha = 2$ the phase is $\varphi_2 = 3\pi/8$. Between sublattice $\alpha = 2$ and $\alpha = 4$ the π–flux phase is applied and one can start again on sublattice $\alpha = 4$ with $\varphi_4 = -3\pi/8$. The operator $c^\dagger$ hence creates a state with a current going clockwise around the plaquette, from 4

to 3, from 3 to 1, from 1 to 2, from 2 to 4 and so on, see the following figure:
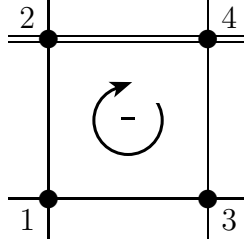
A direct consequence of this observation is that for the ground state the whole π–flux lattice has to be covered with local ring currents. The neighboring plaquettes of a plaquette with a "+" current, i.e., a current in mathematical positive direction of rotation, must have "–" currents etc. We expect, hence, a current pattern where the directions of rotation of the currents are antiferromagnetically ordered. In order to detect the expected current pattern, we have to look at the current–current correlation rather than the current itself. The ground state of the c–condensate (d–condensate), $c^{\dagger N}|0\rangle$ ($d^{\dagger N}|0\rangle$), shows this long range order in the expectation value of the current operator,

$$\langle\, \hat{j}_{\alpha\beta}\,\rangle \;=\; \frac{1}{i}\langle\, c_\alpha^\dagger c_\beta - c_\beta^\dagger c_\alpha \,\rangle. \tag{2.72}$$

For the physical ground states, however, the current has to be zero, as we have superpositions of the c– and d–condensates. By superposing the c– and the d–condensate, "+" and "–" currents cancel out. The figure of merit is the current–current correlation,

$$\langle\, \hat{j}_{\alpha'\beta'}\, \hat{j}_{\alpha\beta}\,\rangle \;=\; -\Big\langle\big(c_{\alpha'}^\dagger c_{\beta'} - c_{\beta'}^\dagger c_{\alpha'}\big)\big(c_\alpha^\dagger c_\beta - c_\beta^\dagger c_\alpha\big)\Big\rangle. \tag{2.73}$$

We apply a particle current on a reference link and detect the response of all other links. We have computed the current–current correlations within exact diagonalization on a 4×4 lattice. The result for $N_\mathrm{b} = 3$ bosons and interaction $U = 0.1$ is shown in Fig. 2.12. We find an antiferromagnetically ordered current pattern, with the same absolute value of all correlations (apart from the reference link).

In Tab. 2.3 we have listed the values of current–current correlations for various parameter settings. As value for the correlations, we have taken the value of the link which is most distant from the reference link which is normalized to have the value 1.00.

It is the main result of this thesis chapter, that the current pattern of the ground state is present for arbitrary particle densities and arbitrary repulsive interactions. We further observe that the values of the correlations start to fluctuate around a mean value when the interaction U is increased. The ground state in the weakly interacting regime has the current pattern as well as in the hard-core regime $U \to \infty$. It is one of the characteristics of these current patterns that the final value of the correlations is reached within a few sites. In Fig. 2.13 we have shown the current pattern for 6×6 π–flux lattice with $N_\mathrm{b} = 2$ and $U = 0.1$. Again we find the long range ordered pattern.
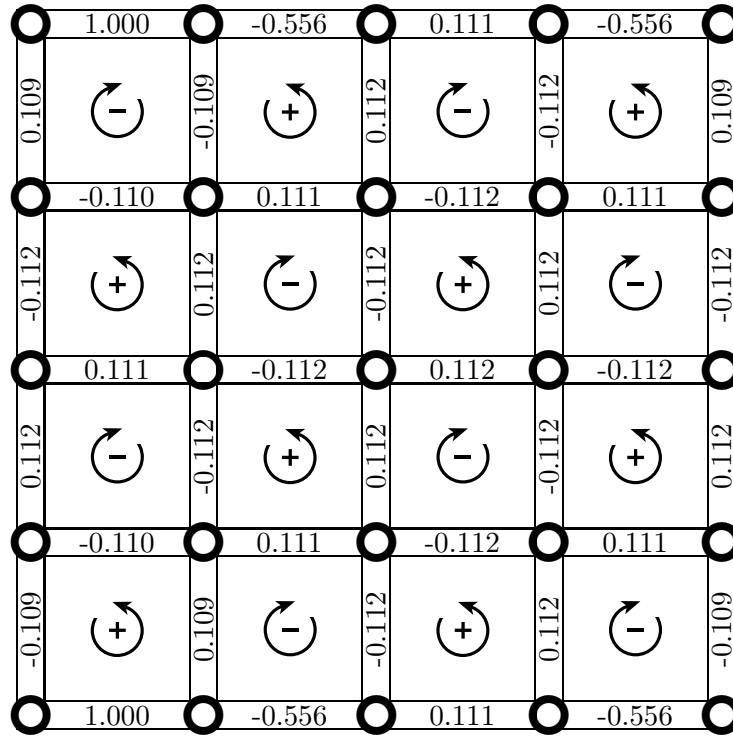
Figure 2.12: Pattern of current–current correlations of three bosons in a π–flux lattice was computed within exact diagonalization. The shown square lattice contains 16 sites with imposed PBCs. The reference link (left bottom or left top, respectively) was normalized to have the value 1.00. The absolute value of the links away from the reference link is 0.112. The current directions on the plaquettes are alternating in horizontal and vertical directions. The ground state is, hence, antiferromagnetically orbital ordered.

We can conclude that this pattern remains in the thermodynamic limit. We wish to stress again that the pattern remains stable when changing the particle density and the interaction strength. In particular, the pattern exists in the hardcore limit where double occupancy in real space is energetically suppressed. Notice that for very large interactions U the system is expected to be in the Mott insulating phase [59], i.e., superfluid order will be absent while the orbital antiferromagnetic order remains. The current pattern also resolves the question which we addressed at the beginning of this thesis chapter: which symmetry is broken? Obviously, the broken symmetry is translation symmetry modulo two lattice spacings, the corresponding group is $\mathbb{Z}_2$.

Current–current correlations

U/t	lattice	N_{b}	$\left\langle \hat{\hat{j}}_{\alpha'\beta'}\,\hat{\hat{j}}_{\alpha\beta} \right\rangle$
0.1	4×4	3	0.112
0.1	4×4	5	0.202
∞	4×4	5	0.184
0.1	4×4	8	0.308
∞	4×4	8	0.204
0.1	6×6	2	0.027
0.1	6×6	3	0.053
0.5	6×6	3	0.055
1.0	6×6	3	0.056
∞	6×6	3	0.064

Table 2.3: For various interactions strength U/t, particle number N_{b}, and lattice size N_{s} the value of the correlations are shown. The value corresponds to the absolute value of the link which is most distant from the reference link (1.00).

2.7 Conclusion and Outlook

In this thesis chapter, we have discussed the properties of the many boson system in a π–flux lattice, a square lattice which is threaded by a very strong magnetic field. As the bosonic atoms are neutral, we have given an overview of ways how to achieve artificial or effective magnetic fields for the neutral atoms. We discussed the most promising candidate, the rotation of the optical lattice in detail. In the following, we have focussed onto a magnetic field strength such that half a Dirac flux quantum goes through every plaquette. We eventually obtained an effective model which has taken into account only operators belonging to the single particle ground states which might be occupied macroscopically. We have solved this effective model exactly, the solution provided us information about the nature of this model. We worked out several properties which we could compare with the full interacting model on finite clusters by means of exact diagonalization. We have found excellent agreement between numerical results and predictions of the effective model. Amongst these predictions, most remarkable is the presence of an antiferromagnetically ordered current pattern in case of repulsive interactions. In case of attractive interactions, the net current is zero. This orbital order is stable for arbitrary particle densities and arbitrary repulsive interactions. We further could demonstrate that the bosons in a π–flux lattice are one of the rare examples of fragmentation of BEC. For attractive interactions (which we assumed to be weak to ensure stability of the system) we found the condensate to be fragmented. For repulsive interactions, however, we have shown that the ground state is a so–called Schrödinger–cat state.

Throughout the main part of this thesis chapter, we have considered a π–flux

Figure 2.13: Current–current correlations of one of the ground states of bosons in a π–flux lattice. The current pattern was evaluated within exact diagonalization of a 6×6 cluster with periodic boundary conditions. The particle density is 1/18 and the interaction is $U = 0.1$.

lattice. So far it remains an open question, what will happen for bosons on an $2\pi/q$–flux lattice. While the case of non–integer or non–rational q, respectively, is hardly treatable within our approach, we will give an outlook for what might happen when $q = 3$, 4, etc. Note that we consider only repulsive interactions $U > 0$ in the following. There are a few possibilities to generalize the $q = 2$ case to $q = 3$. We will first consider the analog of the effective model (2.35). It reads (neglecting additive

constants)

$$\mathcal{H}_{q=3} = 2\sqrt{3}\left(b_0^\dagger b_0^\dagger b_2 b_4 + b_2^\dagger b_2^\dagger b_4 b_0 + b_4^\dagger b_4^\dagger b_0 b_2 + \text{h.c.}\right)$$

$$- 4\sqrt{3}\left(b_0^\dagger b_0 b_2^\dagger b_2 + b_2^\dagger b_2 b_4^\dagger b_4 + b_4^\dagger b_4 b_0^\dagger b_0\right),$$

where the subscripts 0, 2, and 4 denote the momenta $k_x = 0$, $k_x = \frac{2\pi}{3}$, and $\frac{4\pi}{3}$. Solving this model exactly would solve the whole $q = 3$ problem. Alternatively, one could numerically solve this Hamiltonian, as it represents a special oscillator. This might shed light onto the nature of its ground state. We further evaluated the full interacting model numerically. At least for particle numbers $N_{\rm b} = 3n$ where n is integer, we found a three–fold degenerate ground state. We further calculated the one–particle density matrix and found three macroscopic eigenvalues, for $N_{\rm b} = 3n$ these macroscopic eigenvalues are $N_{\rm b}/3 = n$. Hence, the $q = 3$ model exhibits a fragmented condensate, but it remains unclear, if we have again a Schrödinger cat state or a real fragmented condensate. Nonetheless, we conjecture that again a global $\mathbb{Z}_3$ symmetry is broken. Another way of understanding the $q = 3$ model is to look at the current–current correlations. The reader might imagine as a Gedankenexperiment a current pattern which is at least invariant under translations by three lattice spacings in x and y direction. Furthermore, this pattern is three–fold degenerate only. This Gedankenexperiment remains unsolved. Nonetheless, we have computed on a 6×6 lattice (imposing PBCs) the current–current correlations for three bosons with weak interactions $U = 0.1$. The result is shown in Fig. 2.14.

As expected, there is no current pattern comparable to that of bosons in a π–flux lattice. However, we see a periodic cell containing 3×3 sites where at the edges the currents are zero. The current on the link in the center of this periodic cell has the highest absolute value. As expected, we find a physical unit cell containing $3^2 = 9$ lattice sites. Even though, we have no complete understanding of the $q = 3$ model, we can conjecture, that the model with arbitrary q will exhibit a q–fold degenerate ground state and a $q \times q$ unit cell, i.e., a global $\mathbb{Z}_q$ symmetry will be broken. We further assume the ground states to exhibit a fragmented condensate. This assumptions are supported by numerical preliminary studies for $q = 4$, 5, 6, and 7. Furthermore, there are two for experiments relevant questions. First, turning on the effective magnetic field, i.e., small values of α, has to result in a q–fold fragmentation of the condensate, which is for $q = \infty$, i.e., no magnetic field at all, clearly not–fragmented. We conjecture, that there might be any critical value α_c there the simple condensate splits into a fragmented condensate, be it a real fragmented condensate or a Schrödinger cat state. Second, by in– or decreasing the effective magnetic field from $\alpha_1 = 1/q_1$ to $\alpha_2 = 1/q_2$ where the q_i are integer, one passes a regime there a crossover between the q_1 and the q_2 phase might occur. Alternatively, there might be regions between q_1 and q_2, which are very different from the situations considered in this thesis chapter.
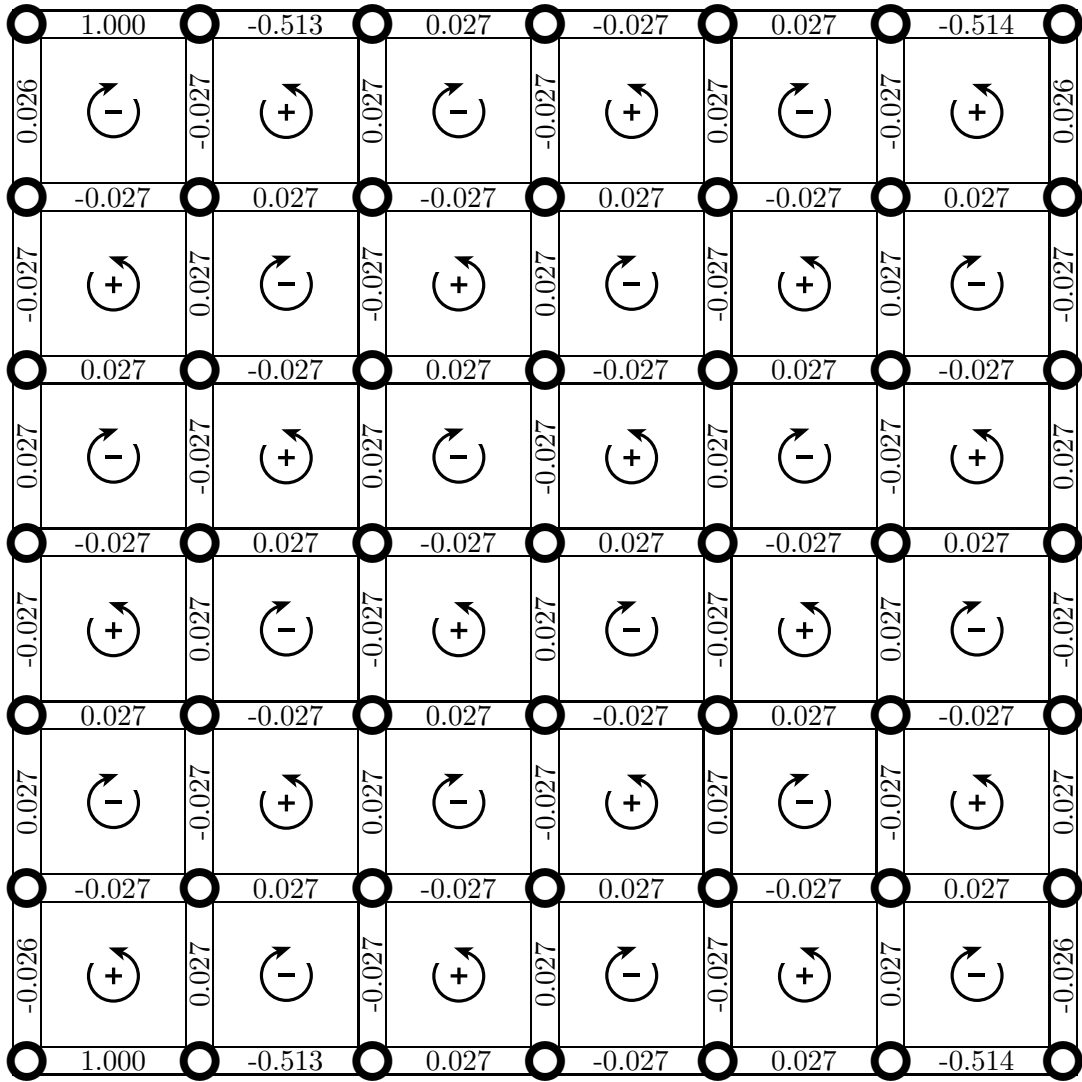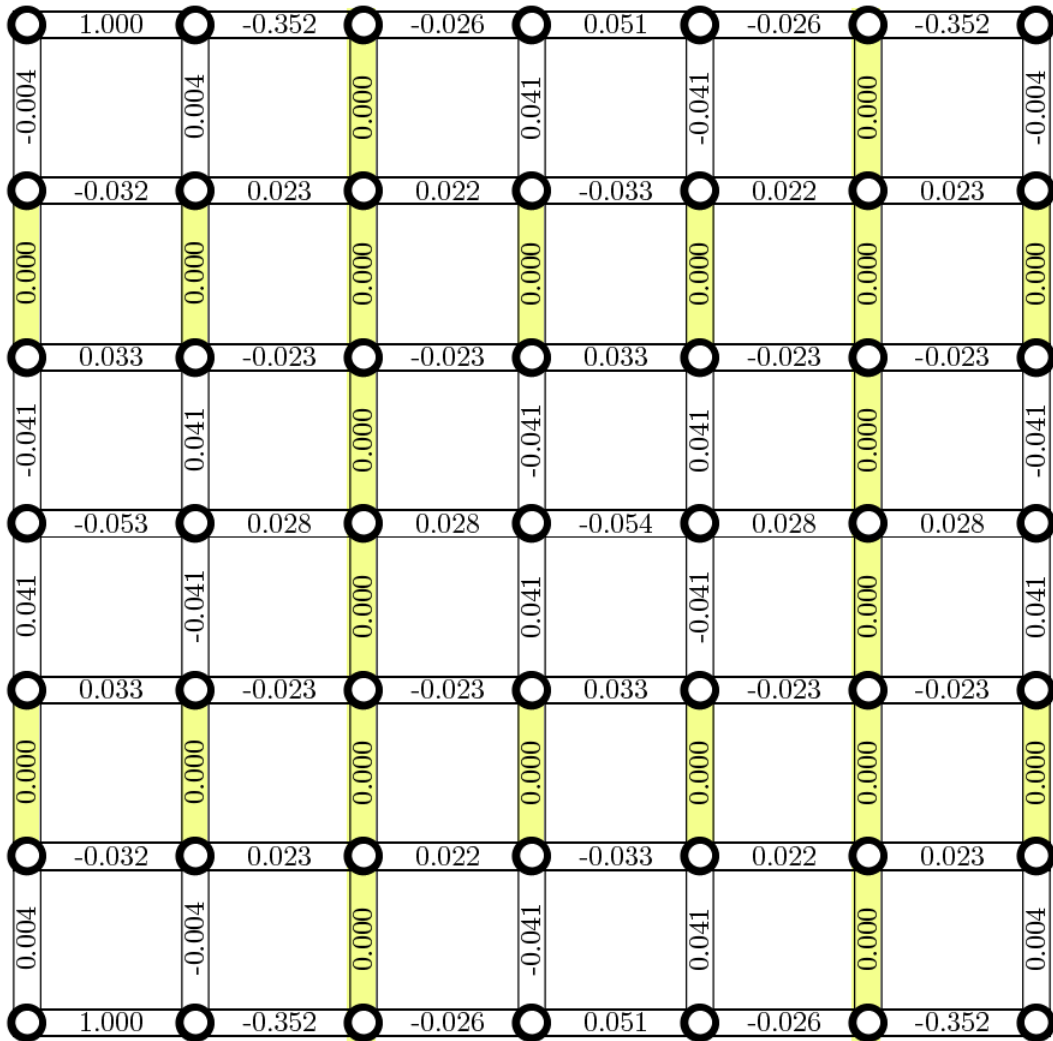
Figure 2.14: Current–current correlations of one of the ground states of bosons in a $2\pi/3$–flux lattice. The current pattern was evaluated within exact diagonalization of a 6×6 cluster with periodic boundary conditions. The particle density is $1/12$ ($N_{\mathrm{b}} = 3$) and the interaction is $U = 0.1$.

Chapter 3

Spinon confinement as origin of Haldane's gap

3.1   Introduction

With the rise of quantum mechanics in the late 20's of the last century [71,131], quantum magnetism emerged as a predominant area of research in theoretical condensed matter physics. This was to a significant part induced by the notion of the electron spin, i.e., the magnetically sensitive, internal degree of freedom of electrons, in the early 20's, which rendered the classical picture insufficient. In contrast to orbital angular momentum, which is quantized in integer units of $\hbar$ in accordance with the spatial rotation group SO(3), the internal spin is in accordance with the Lie group SU(2) quantized in integer units of $\hbar$ (the generators of both groups are identical as SU(2) is locally isomorphic to SO(3)). Ever since the invention of the Bethe ansatz in 1931 as a method to solve the $S = 1/2$ Heisenberg chain with nearest-neighbor interactions [26], spin models in (1+1) dimension, i.e., quantum spin chains, have been a most rewarding subject of study. Bethe's work eventually led to the discovery of the Yang-Baxter equation in 1967 [155] and provides the foundation of the field of integrable models. The notion of integrability rendered a plethora of models amenable to exact and often rather explicit solution [47, 90]. Quantum spin chains possess rich and deeply complex physical properties. For example, it took several decades until Faddeev and Takhtajan [48] discovered in 1981 that the elementary excitations of the $S = 1/2$ Heisenberg chain solved by Bethe carry spin 1/2 and not, as previously assumed, spin 1. The excitations of the spin 1/2 chain hence provide an instance of fractional quantization, as the Hilbert space for the chain is spanned by spin flips, which carry spin 1. It was more surprising, when Haldane conjectured in 1983 that the spin 1 Heisenberg chain has a dramatically different behavior from the spin 1/2 Heisenberg chain solved by Bethe: Haldane proposed the existence of a finite energy gap between the ground state and the lowest lying excitation. He further proposed that all half–odd–integer spin chains are generically gapless, whereas integer spin chains possess a gap in the excitation spectrum [8, 51, 67, 68]. This leads to a strikingly different behavior in the magnetic susceptibility at low temper-

atures. A gap leads to exponentially decaying spin-spin correlations and as such to a vanishing susceptibility at temperature $T = 0$. In contrast, a gapless spectrum is generically associated with correlations which decay as a power law with the distance, and a finite susceptibility at low temperatures. Haldane's at that time astonishing prediction was confirmed experimentally in the spin 1 materials $CsNiCl_3$ [37] and $Ni(C_2H_8N_2)_2NO_2(ClO_4)$ which is abbreviated NENP [14, 83, 100, 125].

Haldane's prediction based on the mapping from the Heisenberg antiferromagnet in the large–S limit to the $O(3)$ non–linear σ model which is exactly solvable. While the Heisenberg antiferromagnet is thus solvable in the large–S limit, Haldane proposed that the solution remains valid for small values of S [67, 68]. Haldane argued that chains with integral spin possess a gap in the excitation spectrum while a topological term renders half–integral spin chains gapless.

In this thesis chapter, we present a picture of the physical mechanism responsible for the *Haldane gap*. We further present a consistent approach to figure out whether or not an antiferromagnetic spin chain with a certain spin representation is critical or exhibits a gap between ground state and excitation spectrum.

As already mentioned, the elementary excitation of the spin 1/2 Heisenberg model carries spin 1/2, while the Hilbert space is spanned by spin flips which carry spin 1. As the spin quantum number s^z can be changed by any excitation in integers only, one will always create pairs of spinons in a realistic situation. The spinons of such a pair are free in the sense that they do not feel a force confining them together. The spinons are deconfined and as a consequence, the excitation spectrum is gapless. As we will see below, this holds for all spin chains with half–integer spin S. In the spin 1 Heisenberg model, the situation is fundamentally different: the elementary excitation is still a spinon pair, but now the spinons feel a linear confining force. When transforming to relative coordinates of the two spinons, one obtains a linear oscillator describing the spinon–spinon bound state (which corresponds to the spin 1 magnon). The zero point energy of this oscillator coincides with the Haldane gap. This situation applies to all spin chains with integer spin S. In order to decide whether or not a confining force between the spinons is present, we consider the valence bond solid (VBS) state, i.e., a state where the lattice is covered by local singlet bonds, of the spin representation rather than the original Heisenberg model. We use an instructive method to illustrate the VBS state and can finally decide whether the spinons are free or confined. Deconfined spinons result in a gapless excitation spectrum of the corresponding Heisenberg model, while confined spinons cause a Haldane gap in the excitation spectrum. The main advantage of this method is the straightforwardness and the predictive value. To demonstrate both, straightforwardness and predictive power, we apply our approach to arbitrary $SU(n)$ *spin* representation and generalize Haldane's conjecture which turns out to be non–trivial. In particular, we find a new type of topological phase transition from a phase with deconfined spinons to confined spinons. Finally, we confirm both the generalization of Haldane's conjecture and our whole approach numerically by calculating the low energy behavior of the Heisenberg models of all achievable $SU(n)$ spin representations.

Our results directly lead to the following observations [122]: If for a given $SU(n)$ representation (represented by a Young tableau with λ boxes) the ratio λ/n is integral then the nearest neighbor Heisenberg model is in a massive phase. The associated energy gap is the Haldane gap. If the ratio λ/n is not integral then the nearest neighbor Heisenberg model is gapless and critical, the corresponding conformal field theory (CFT) is expected to be a $SU(n)_1$ Wess–Zumino–Witten non–linear σ model. Applying a next–nearest neighbor interaction leads for a certain parameter regime J_2/J_1 to n–merization, i.e., lattice translation symmetry is broken while the ground states are invariant under translations by n lattice spacings. If λ and n have a largest common divisor $q \neq n$, the Heisenberg model with interactions to the $(1 + n/q)$-th neighboring site is expected to undergo a phase transition to a n/q–merized phase for abnormally small coupling J_2 (for the special case $n/q = 2$, the model does not n–merize at all; it directly undergoes the phase transition to the n/q–merized phase already for the J_1–J_2 model). The origin of this phase transition is, however, not a frustration effect (as in the spin 1/2 J_1–J_2 model). Instead, we have found a new type of topological phase transition: the original representation of the spins per site is changing to an effective representation placed on n/q adjacent sites. In the effective model, the representation is characterized by a Young tableau with λ' boxes, where $\lambda' = \lambda n/q$. Since the ratio λ'/n is clearly an integer, the effective model is expected to exhibit a Haldane gap.

This thesis chapter is organized as follows: In Sec. 3.2 we introduce and explain the concept of spinon confinement. We further discuss the for our purposes important properties of SU(2) spin chains and, in particular, of SU(2) VBS states. In Sec. 3.3, we discuss first the experimental relevance of spin chains with a spin symmetry group different from SU(2). Then we introduce several exact spin models with generalized spin algebra SU(3), SU(4), and SU(n) whose ground states are VBS states. At the end of this section we present and proof a general criterion for spinon confinement which depends on the spin representation only. In Sec. 3.6 we specify our predictions by studying a certain class of VBS states which yields a non–trivial categorization of three different cases: models without spinon confinement, models exhibiting spinon confinement, and models where the presence of spinon confinement depends on the range of interactions. Sec. 3.7.2 we argue that besides the obligatory gap exponentially decaying spin–spin correlations are always present when the spinons are confined. In particular, we show rigorously that there are certain VBS states breaking translational symmetry while exhibiting exponentially decaying spin–spin correlations. In Sec. 3.9 we formulate our conjecture that the Heisenberg models *follow* the constructed VBS states concerning spinon confinement, the Heisenberg model and the *corresponding* VBS state are in the same universality class. This yields the surprising situation that there are spin chains where the nearest neighbor Heisenberg model is critical and gapless, while the next–nearest neighbor Heisenberg model exhibits spinon confinement and a gap in the excitation spectrum. We will point out that the situation is totally different from the usual behavior of J_1–J_2 models. We finally confirm our approach and our conjecture by applying the density matrix renormalization group (DMRG) to all numerically achievable SU(n) Heisen-

berg models. We complete this chapter with a conclusion and a discussion about
this work.

3.2   Concept of spinon confinement and valence bond solids

In this section, we present our approach which is purely heuristic. We will see that
in certain situations a linear confining potential between spinons, the elementary
excitations in antiferromagnetic quantum spin chains, is present. These *situations*
occur when the spin representation S placed on each site is integral.

To begin with, we consider the antiferromagnetic[1] nearest neighbor Heisenberg
model with fundamental representation $S = 1/2$ which is given by the Hamiltonian

$$\mathcal{H} = \sum_{i=1}^{N} \boldsymbol{S}_i \boldsymbol{S}_{i+1} \tag{3.1}$$

where the spin $1/2$ vector operator is defined as $\boldsymbol{S} = (S^x, S^y, S^z)^{\mathrm{T}}$ and the spin
operators consists of Pauli matrices, $S_i^\alpha = \sum_{\tau,\tau'=\uparrow,\downarrow} c_{i,\tau}^\dagger \sigma_{\tau\tau'}^\alpha c_{i,\tau'}$ for $\alpha = x, y, z$. The
spin operators fulfill the angular momentum commutation relations

$$\left[S_i^\alpha \,, S_j^\beta \right] = i\delta_{ij}\epsilon^{\alpha\beta\gamma} S_i^\gamma \tag{3.2}$$

where we have set $\hbar \equiv 1$. For convenience we introduce spin flip operators $S_i^\pm = S_i^x \pm iS_i^y$ and work with $\{S^\pm, S^z\}$ rather than $\{S^x, S^y, S^z\}$. It allows to rewrite
the Heisenberg term as $\boldsymbol{S}_i \boldsymbol{S}_j = 1/2(S_i^+ S_j^- + S_i^- S_j^+) + S_i^z S_j^z$. Note that we assume
throughout the whole thesis periodic boundary conditions (PBC) unless specified oth-
erwise. Even though the Hamiltonian (3.1) is exactly solvable via Bethe ansatz [26]
and maybe the most studied spin Hamiltonian ever, we do not have an intuitive
understanding of the ground state of this model. Note that in one spatial dimension
neither long range order is present nor the classical Néel state ($\uparrow\downarrow\uparrow\downarrow\uparrow\downarrow$) is the
ground state. The Néel state is not even an eigenstate of (3.1)[2]. The ground state
is actually a quantum disordered spin liquid state.

Instead of the spin liquid state we consider a state vector where neighboring spins
tend to form a local singlet configuration. The state might be illustrated as follows:

$$\multimap \circ\!-\!\circ \quad \circ\!-\!\circ \quad \circ\!-\!\circ \quad \circ\!-\!\circ \quad \circ\!- \tag{3.3}$$

Each circle denotes a spin $1/2$ per site and the horizontal lines connecting two spins
denote the antisymmetrical coupling of the two connected spins into a singlet or a

---

[1] Throughout this thesis, we are considering antiferromagnetic spin chains only. Also when
generalizing to SU(n), we always assume the prefactor of the Heisenberg model to be positive.

[2] This can be seen easily: applying $\boldsymbol{S}_1 \boldsymbol{S}_2 = 1/2(S_1^+ S_2^- + S_1^- S_2^+) + S_1^z S_2^z$ to the spin configuration
$|\uparrow_1\downarrow_2\rangle$ on adjacent sites, one obtains $1/4|\uparrow_1\downarrow_2\rangle + 1/2|\downarrow_1\uparrow_2\rangle$. The Curie state $|\uparrow\uparrow\uparrow\uparrow \ldots\rangle$ is, however,
an exact eigenstate of the antiferromagnetic HM with eigenenergy $JN/4$.

valence bond. The cartoon is thus only an abbreviation and the valence bonds may be expressed by fermionic creation operators,

$$\circ\!\!-\!\!\circ \quad \equiv \quad \underset{i}{\circ}\!\!-\!\!\underset{i+1}{\circ} \quad = \quad c_{i,\uparrow}^{\dagger}c_{i+1,\downarrow}^{\dagger} - c_{i,\downarrow}^{\dagger}c_{i+1,\uparrow}^{\dagger}\,|\,0\,\rangle\,. \tag{3.4}$$

Note that the state (3.3) is two–fold degenerate since shifting the *cartoon* by one lattice spacing to the right (or to the left, respectively) yields a new state. Shifting by two lattice spacings to the right or to the left yields, however, the same state. We label the two ground states $|\psi_1\rangle = |\circ\!\!-\!\!\circ \;\; \circ\text{-}\rangle$ and $|\psi_2\rangle = |\text{-}\circ \;\; \circ\!\!-\!\!\circ\,\rangle$. They are explicitely given by

$$\big|\psi_{\substack{1\\(2)}}\big\rangle = \prod_{\substack{i \text{ even}\\(i \text{ odd})}} \Big(c_{i,\uparrow}^{\dagger}c_{i+1,\downarrow}^{\dagger} - c_{i,\downarrow}^{\dagger}c_{i+1,\uparrow}^{\dagger} \Big)\,|\,0\,\rangle\,. \tag{3.5}$$

Now we construct a Hamiltonian in terms of a projection operator for which $|\psi_1\rangle$ and $|\psi_2\rangle$ are the exact and unique ground states. At this point we just assume that three site interactions are sufficient. On three consecutive sites of the ground states, there will be always a singlet ($\circ\!\!-\!\!\circ$) and an individual spin $1/2$ ($\circ$), i.e., $\mathbf{0}\otimes\frac{\mathbf{1}}{\mathbf{2}} = \frac{\mathbf{1}}{\mathbf{2}}$.

The content of spin representations on three consecutive sites of the ground states is thus just the doublet representation $\frac{\mathbf{1}}{\mathbf{2}}$. For arbitrary states, however, the content on three consecutive sites is given by the tensor product $\frac{\mathbf{1}}{\mathbf{2}}\otimes\frac{\mathbf{1}}{\mathbf{2}}\otimes\frac{\mathbf{1}}{\mathbf{2}} = 2\cdot\frac{\mathbf{1}}{\mathbf{2}}\oplus\frac{\mathbf{3}}{\mathbf{2}}$. This enables us to write a Hamiltonian as the operator projecting onto the subspace with spin $3/2$,

$$\mathcal{H} = \sum_i a_i P_{\frac{3}{2}}(i, i+1, i+2)$$

with arbitrary constant $a_i > 0$. The projection operator has to fulfill $P_{\frac{3}{2}}\big|\frac{1}{2}\big\rangle = 0$ and $P_{\frac{3}{2}}\big|\frac{3}{2}\big\rangle = \big|\frac{3}{2}\big\rangle$. A proper choice for this operator is thus given in terms of spin operators by

$$P_{\frac{3}{2}}(i, i+1, i+2) = \frac{1}{3}\left((\boldsymbol{S}_i + \boldsymbol{S}_{i+1} + \boldsymbol{S}_{i+2})^2 - \frac{3}{4} \right).$$

As the eigenvalue of $\boldsymbol{S}^2$ is $S(S+1)$, one can easily convince oneself that this projector is zero for total spin $S = 1/2$ on three consecutive sites and the identity for total spin $S = 3/2$. Finally we end up with a spin Hamiltonian (for convenience we choose $a_i = 3/4$) which was first introduced by Majumdar and Ghosh [104, 105] in 1969,

$$\mathcal{H}^{\mathrm{MG}} = \sum_i \left(\boldsymbol{S}_i\boldsymbol{S}_{i+1} + \frac{1}{2}\boldsymbol{S}_i\boldsymbol{S}_{i+2} + \frac{3}{8} \right).$$

Per construction the Hamiltonian fulfills $\mathcal{H}^{\mathrm{MG}}|\psi_1\rangle = \mathcal{H}^{\mathrm{MG}}|\psi_2\rangle = 0$. Note that the Majumdar–Ghosh (MG) model is a special point in the phase diagram of the antiferromagnetic J_1–J_2 model we will discuss later (see Sec. 3.9.1). The only degree of freedom in this model is the spin. Hence, the only possibility to excite the system is to break a valence bond. Assuming that the remaining "free" spins can move we are able to draw a cartoon as follows:
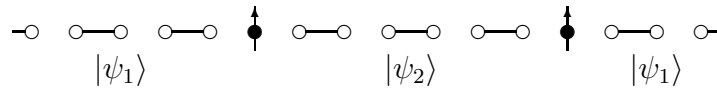
What happens is that the freely moving "spin objects" are just domain walls between the ground states $|\psi_1\rangle$ and $|\psi_2\rangle$. In the following, we call this individual spin objects *spinons*. Note that the drawn cartoon does not correspond to an exact eigenstate of the MG Hamiltonian, but we can see the essence of low–lying excitations in this model: the spinons can move freely through the system – it does not matter whether or not they are close to each other. We will say that the spinons are *deconfined* as there is no confining potential between them. It is worth emphasizing that these free (or deconfined) spinons are just domain walls between the two ground states, but domain walls which carry spin. Although the excitation spectrum of the MG model is separated from the ground states by a gap, we use the above cartoon to argue that the spectrum of the Heisenberg model (3.1) must be gapless. The gap in the MG model is due to the breaking of a valence bond which costs a finite energy and this energy cost remains in the thermodynamic limit. When a valence bond is once broken, the two resulting spinons can move independently from each other through the chain. This behavior remains valid in the HM and gives an illustrative explanation of the the *two–spinon continuum* which dominates the gapless low energy spectrum of the HM. Assume, that the first spinon has momentum q_1 and the second has momentum q_2. For fixed total momentum of the excitation, $q = q_1 + q_2$, the constituents q_1 and q_2 must not be fixed. The energy as a function of $q_1 + q_2$ is given by $\epsilon(q) = \pi|J|/2(\cos q_1 + \cos q_2)$ and provides, hence, a continuum, see Ref. [56] for details. The two–spinon continuum which is sketched in Fig. 3.1 dominates the excitation spectrum of the $S = 1/2$ HM antiferromagnet.
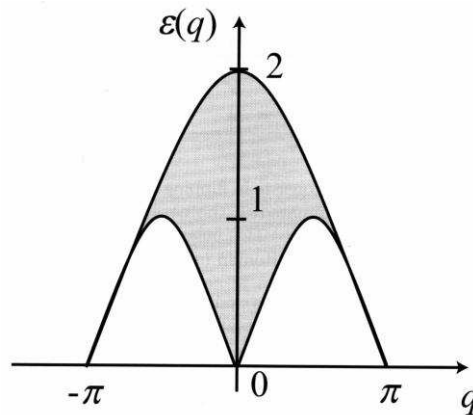
Figure 3.1: Two–spinon continuum of the antiferromagnetic HM. The spectrum is a function of $q_1 + q_2$, where q_i is the momentum of the ith spinon. The picture is taken from Ref. [56].

So far we have used our approach to argue on a heuristic level that the spin 1/2 HM has a gapless excitation spectrum. Now we present the important step how to apply our approach to higher dimensional spin representations. Again we will search

for ground states which consist of local valence bonds only. For $S = 1$, there are only two possibilities to obtain such a valence bond covering of the lattice[3]. One has to lay a $S = 1/2$ VBS state, i.e., a MG state, in top of another $S = 1/2$ VBS state and to project onto the symmetric representation on each site in order to obtain a spin 1 chain, i.e., $\mathcal{S}(\frac{1}{2} \otimes \frac{1}{2}) = \mathbf{1}$. This yields two possible states illustrated by the following cartoons.
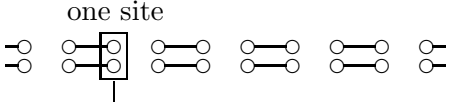
$$
\begin{array}{c}
\text{one site} \\[2pt]
\text{[cartoon]} \\[2pt]
\text{projection onto } S = 1
\end{array}
\tag{3.6}
$$

The first possibility is to take twice the same $S = 1/2$ VBS state, say ψ_1. The resulting state must be two–fold degenerate and breaks lattice translational symmetry.
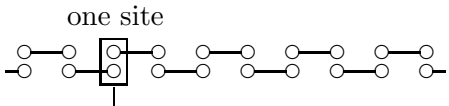
$$
\begin{array}{c}
\text{one site} \\[2pt]
\text{[cartoon]} \\[2pt]
\text{projection onto } S = 1
\end{array}
\tag{3.7}
$$

The other possibility is to glue $|\psi_1\rangle$ and $|\psi_2\rangle$ together and the resulting unique state is translational invariant. This state was introduced in 1987 by Affleck, Kennedy, Lieb, and Tasaki [11]. Meanwhile, this state is called AKLT state[4]. In the above cartoons, the circles again represent individual spins $S = 1/2$, the horizontal lines denote the antisymmetric coupling between spins and represent thus singlet bonds. The circles in top of each other mean that two spins with fundamental representation $S = 1/2$ are symmetrically coupled into a spin 1 per site. It is worth emphasizing that in our approach, one has always to consider the *most symmetric* VBS state for a given spin representation S, i.e., that the AKLT state (3.7) has to be subject of consideration rather than the two–fold degenerate dimer states (3.6).

The construction of the spin 1 VBS states was very easy in the cartoon. Now we wish to demonstrate that the explicit construction of the wave function is just as easy. For that purpose, we introduce Schwinger bosons.

Schwinger bosons [20,21,136] constitute a way to formulate spin-S representations of an SU(2) algebra. The spin operators

$$
S^+ = a^\dagger b, \qquad S^- = b^\dagger a, \qquad S^z = \frac{1}{2}(a^\dagger a - b^\dagger b),
\tag{3.8}
$$

are given in terms of boson creation and annihilation operators which obey the usual commutation relations

$$
\begin{aligned}
\left[a, a^\dagger\right] = \left[b, b^\dagger\right] = 1, \\
\left[a, b\right] = \left[a, b^\dagger\right] = \left[a^\dagger, b\right] = \left[a^\dagger, b^\dagger\right] = 0.
\end{aligned}
\tag{3.9}
$$

---

[3]The reader might convince himself that there are only the possibilities shown in the cartoons (3.6) (two–fold degenerate) and (3.7) (unique).

[4]Affleck *et al.* called this state *valence bond solid state* (VBS state). Throughout this thesis, we will call any state a VBS state as long as only local singlet bonds are present. In particular, we will consider the MG states as VBS states and also all states which breaks translational symmetry. If we call a VBS state an AKLT state then this emphasizes translational invariance.

It is readily verified with (3.9) that S^x, S^y, and S^z satisfy (3.2). The spin quantum number S is given by half the number of bosons,

$$2S = a^\dagger a + b^\dagger b, \tag{3.10}$$

and the usual spin states (simultaneous eigenstates of $\boldsymbol{S}^2$ and S^z) are given by

$$|S, s^z\rangle = \frac{(a^\dagger)^{S+s^z}}{\sqrt{(S+s^z)!}} \frac{(b^\dagger)^{S-s^z}}{\sqrt{(S-s^z)!}} |0\rangle. \tag{3.11}$$

In particular, the spin-1/2 states are given by

$$|\uparrow\rangle = c_\uparrow^\dagger |0\rangle = a^\dagger |0\rangle, \qquad |\downarrow\rangle = c_\downarrow^\dagger |0\rangle = b^\dagger |0\rangle, \tag{3.12}$$

i.e., $a^\dagger$ and $b^\dagger$ act just like the fermion creation operators $c_\uparrow^\dagger$ and $c_\downarrow^\dagger$ in this case. The difference shows up only when two (or more) creation operators act on the same site or orbital. The fermion operators create an antisymmetric or singlet configuration (in accordance with the Pauli principle),

$$|0,0\rangle = c_\uparrow^\dagger c_\downarrow^\dagger |0\rangle, \tag{3.13}$$

while the Schwinger bosons create a totally symmetric or triplet (or higher spin if we create more than two bosons) configuration,

$$|1,1\rangle = \frac{1}{\sqrt{2}}(a^\dagger)^2 |0\rangle, \qquad |1,0\rangle = a^\dagger b^\dagger |0\rangle, \qquad |1,-1\rangle = \frac{1}{\sqrt{2}}(b^\dagger)^2 |0\rangle. \tag{3.14}$$

Using the SU(2) Schwinger bosons, we may rewrite the Majumdar–Ghosh states (3.5) as

$$|\psi_{\frac{1}{(2)}}\rangle = \prod_{\substack{i \text{ even} \\ (i \text{ odd})}} \left(a_i^\dagger b_{i+1}^\dagger - b_i^\dagger a_{i+1}^\dagger\right) |0\rangle \equiv \Psi^{\overset{\text{even}}{\text{(odd)}}}[a^\dagger, b^\dagger] |0\rangle. \tag{3.15}$$

In the cartoon we could glue together two MG states and ask for the symmetric projection on each site. In terms of Schwinger bosons, we can just multiply both MG states and the Schwinger bosons ensure the symmetric projection automatically[5].

$$|\psi_{\text{AKLT}}\rangle = \prod_i \left(a_i^\dagger b_{i+1}^\dagger - b_i^\dagger a_{i+1}^\dagger\right) |0\rangle = \Psi^{\text{even}}[a^\dagger, b^\dagger] \cdot \Psi^{\text{odd}}[a^\dagger, b^\dagger] |0\rangle$$

$$= \Big| \raisebox{-0.5em}{} \Big\rangle \tag{3.16}$$

$$\text{projection onto spin } S = 1$$

---

[5] We further wish to mention that this formalism allows us to write down all SU(2) VBS states easily as $|\psi_{(m,n)}^{\text{SU}(2)}\rangle \equiv |(m,n)\rangle = (\Psi^{\text{even}}[a^\dagger, b^\dagger])^m (\Psi^{\text{odd}}[a^\dagger, b^\dagger])^n |0\rangle$ with the constraint that $m+n = 2S$. For $|(1,0)\rangle$ and $|(0,1)\rangle$ we find the MG states, while we recover the spin 1 dimer states for $|(2,0)\rangle$ and $|(0,2)\rangle$. The spin S AKLT states are given by $|(S,S)\rangle$.

AKLT also introduced a parent Hamiltonian which was constructed similarly to the MG-Hamiltonian. The idea is the following: due to the translational symmetry of the AKLT state we assume that nearest neighbor interactions are sufficient to describe this state where only the following situation occurs:

$$\text{(diagram)} \equiv \text{(diagram)} = \frac{\mathbf{1}}{\mathbf{2}} \otimes \mathbf{0} \otimes \frac{\mathbf{1}}{\mathbf{2}} = \mathbf{0} \oplus \mathbf{1}.$$

When looking at two adjacent sites of the AKLT state, only the spin representations $\mathbf{0}$ and $\mathbf{1}$ are present while on two adjacent sites of an arbitrary spin 1 state the spin representations $\mathbf{1} \otimes \mathbf{1} = \mathbf{0} \oplus \mathbf{1} \oplus \mathbf{2}$ are present. The sum over the projection operator $P_{\mathbf{2}}(i, i+1)$ which projects onto the spin 2 subspace on adjacent sites annihilates the AKLT state while all other possible states are lifted to a finite energy since the projection operator has to fulfill

$$P_{\mathbf{2}} \left| \text{(diagram)} \right\rangle = 0 \quad \text{and} \quad P_{\mathbf{2}} \left| \text{(diagram)} \right\rangle = \left| \text{(diagram)} \right\rangle.$$

A proper choice of the projection operator in terms of spin 1 operators is given by

$$P_{\mathbf{2}}(i, i+1) = \frac{1}{24} \Big((\boldsymbol{S}_i + \boldsymbol{S}_{i+1})^2 - 2 \Big) \Big((\boldsymbol{S}_i + \boldsymbol{S}_{i+1})^2 \Big).$$

Note that the spin 1 operators $S_i^{\pm}$ and S_i^z consists now of three–dimensional matrices rather than two–dimensional Pauli matrices. The parent Hamiltonian is finally given by

$$\mathcal{H}^{\text{AKLT}} = \sum_i 2 P_{\mathbf{2}}(i, i+1) = \sum_i \left(\boldsymbol{S}_i \boldsymbol{S}_{i+1} + \frac{1}{3} \left(\boldsymbol{S}_i \boldsymbol{S}_{i+1} \right)^2 + \frac{2}{3} \right) \tag{3.17}$$

and annihilates the AKLT state, $\mathcal{H}^{\text{AKLT}} \left| \text{(diagram)} \right\rangle = 0$. The only possibility to excite the system is again the breaking of a valence bond. When we do so and pull the remaining *spinons* apart we obtain the following cartoon situation[6]:

$$\underbrace{\text{(diagram)}}_{\text{distance} \propto \text{energy cost}}$$

Note that this cartoon is neither an exact eigenstate of $\mathcal{H}^{\text{AKLT}}$ nor the spinons are localized at a certain site, nonetheless, the essence what spinon confinement means can be well understood. As pointed out above, whenever the configuration $\left| \text{(diagram)} \right\rangle$ occurs, the projection operator $P_{\mathbf{2}}$ lifts the state to higher energy. In the cartoon, this situation occurs exactly once between the two spinons (apart from the two sites where the spinons are). Now it is obvious that pulling apart the two spinons from each other results in additional energy costs which are proportional to the distance of the two spinons. Between the spinons, there is a string (the AKLT-*cartoon* makes this string visible) which is energetically unfavorable. We say, hence,

---

[6]The cartoon and the corresponding idea was for the first time mentioned in Ref. [61]

that there is a linear confinement force between both spinons which cause that the two spinons are relatively close together. This total object, i.e., the two spinons and "something inbetween", is in the literature usually refered to as the spin 1 *magnon* [56]. In our understanding, however, is the magnon nothing but the two confined spinons; we say that spinon confinement is present in the AKLT chain [62]. Finally we have to explain why spinon confinement is the origin of Haldane's gap. The idea is very illustrative: we transform the coordinates of the two spinons to center–of–mass and relative coordinates. Then we consider the relative motion of the two spinons and obtain a linear oscillator, as there is a linear confining potential between the spinons. The potential is $V(x) = F_{\mathrm{conf}}|x|$ where x is the distance between the spinons, and the oscillator might be solved exactly. The zero energy of this linear oscillator corresponds to the Haldane gap. Finally we argue that the $S = 1$ HM must also have a gap in the spectrum since the spinons are still confined.

At this point, the mindful reader will have noticed that the connection between the AKLT model and the $S = 1$ HM is different from the connection between the $S = 1/2$ HM and the MG model. When adding a biquadratic term to the $S = 1$ HM, $\alpha(\boldsymbol{S}_i\boldsymbol{S}_{i+1})^2$, and increasing α from zero to $1/3$, one reaches the AKLT model. Both models are continously connected, there is no qualitative change concerning gap, spin–spin correlations etc. and, in particular, both models are in the same phase. When adding to the $S = 1/2$ HM a next–nearest neighbor term, $\beta\boldsymbol{S}_i\boldsymbol{S}_{i+2}$, and increasing β from zero to $1/2$, one reaches the MG point. While for $\beta = 0$ the system is in a critical spin liquid phase it undergoes a continous phase transition[7] to a dimerized phase at $\beta_c = 0.2411$ [44, 115]. While the correlations decay below β_c with a power law, they decay much faster above the transition and abruptly at $\beta_{\mathrm{MG}} = 1/2$. This can be understood by considering Eq. (3.3) which illustrates $\beta = 1/2$: the dimers are totally uncorrelated with each other and the correlations are zero when the distance becomes larger than two lattice sites. As we have seen, the situations between Heisenberg model and its corresponding VBS model might be very different, but presence or absence of spinon confinement remains unchanged in HM and VBS models. This statement is purely heuristic and as such it is our main conjecture.

When we apply our method to higher representations of SU(2) we recover the well–known result predicted by Haldane that spin chains with integer spin S exhibit spinon confinement while spin chains with half–integer spin S support deconfined spinon excitations. Note that this statement is fully consistent with Haldane's original work even though he never formulated his conjecture in the context of spinon confinement. About ten years ago, there were a few attempts to describe the gapped phase in spin chains within a similar concept: Affleck [9] mentioned *soliton confinement* as origin of the gapped phase in the alternating spin 1/2 chain. This concept was extended by Augier *et al.* [22] and Sørensen *et al.* [139]. A similar concept was followed in Brehmert *et al.* [36] where generalized spin 1/2 ladders and their relation to the Haldane phase was studied by means of two–spinon "composite–particles".

In the last 25 years, spin S chains were extensively studied by means of exact

---

[7]The phase transition is of Kosterlitz–Thouless type.

analytical methods, numerical simulations, and experiments. Thus it is very difficult to discover new physics related to Haldanes conjecture. One can only test whether or not a theory or an approach explaining the mechanism of Haldane's gap fits the analytical, numerical, and experimental results. Frankly speaking, a theory has only to reproduce that half–odd–integral spin chains are gapless while integral spin chains are gaped. To overcome this dilemma, we introduce several exact VBS models where the "spin group" SU(2) is replaced by SU(n), $n = 3, 4, \ldots$. We then apply our approach in order to decide whether or not the spinons are confined in these models. We predict the corresponding Heisenberg models to behave accordingly.

3.3   Exact SU(n) models

3.3.1   Motivation and Experimental relevance

The motivation to discover the wide field of SU(n) spin chains is at least two–fold. First, more than 25 years later, the generalization of Haldane's original conjecture to SU(n) spin chains is still an open problem[8]. There have been a few attempts by Affleck [4–7] and Affleck and Lieb [13], however, they never completed the classification of all SU(n) representations. Second, with the development of ultracold atom gases in the last decade, spin chains with a spin symmetry beyond SU(2) becomes experimentally relevant. The reader may notice that first experiments with three species Fermi gases have succeeded [123]. In these experiments with ^{40}K, the third state representing the third species was used for some thermometry only as a tool. In principle, the symmetry could be tuned close to the SU(3) symmetric point. This is challenging, but already an approximate SU(3) symmetry is sufficient to describe SU(3) physics [107]. It is unresolved, however, whether it is possible to have a stable enough three species mixture near a Feshbach resonance with ^{40}K [124]. Furthermore, the stability of a three species mixture was demonstrated most recently in a gas of ^{6}Li atoms [74, 118]. In these experiments, the three lowest hyperfine states were equally populated (by means of radio–frequency transitions) and the pairwise scattering lenghts between the three states were tuned across the Feshbach resonances. In the limit of large magnetic fields, all scattering lengths asymptote to the triplet scattering lengths. In this limit, the model should become invariant under global SU(3) transformations.

In the following, we wish to describe on a more sophisticated level how to realize

---

[8]The reader may notice that the group SU(2) is isomorphic to the symplectic group SP(2). The difference for $n > 2$ is that one can always couple two SP(n) spins into a singlet, while this is in general not possible for two SU(n) spins. Hence, we could generalize quantum spin chains to SP(n) rather than SU(n). In fact, we have recently proposed SP(n) dimer states as well as SP(n) VBS states [134] which reduce for $n = 2$ to the MG states and the spin 1 AKLT states, respectively. Nonetheless, the consideration of gapped and gapless models in the context of spinon confinement turned out to be trivial. We wish to refer the interested reader to Ref. [134]. As SU(2) is also locally isomorphic to SO(3), one could generalize to SO(n) spin chains [145]. In this thesis, we will restrict ourself to SU(n) generalizations, as it appears to us as the most exciting and challenging generalization.
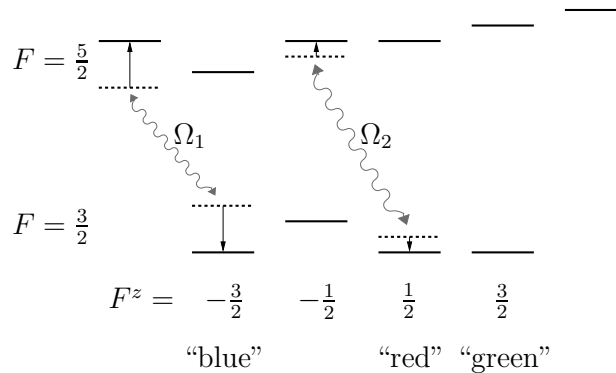
Figure 3.2: Effective lifting of the $F^z = -\frac{1}{2}$ state.

a three species Fermi gas in principle [62, 156]. In a most naive approach, one might expect to realize an SU(3) spin by using atoms with three internal states, like an atom with spin $S = 1$. If we now were to interpret the $S^z = +1$ state as SU(3) spin "blue", the $S^z = 0$ state as "red", and the $S^z = -1$ state as "green", however, the SU(3) spin would not be conserved. The SU(2) algebra would allow for the process $|+1, -1\rangle \rightarrow |0, 0\rangle$, which in SU(3) language corresponds to the forbidden process $|b, g\rangle \rightarrow |r, r\rangle$.

A more sophisticated approach is hence required. One way to obtain a system with three internal states in which the number of particles in each state (i.e., of each color) is conserved is to manipulate an atomic system with total angular momentum $F = 3/2$ (where $\boldsymbol{F} = \boldsymbol{S}_{\mathrm{el}} + \boldsymbol{L}_{\mathrm{orb}} + \boldsymbol{S}_{\mathrm{nuc}}$ includes the internal spin of the electrons, the orbital angular momentum, and the spin of the nucleus) to simulate an SU(3) spin. The important feature here is that the atoms have four internal states, corresponding to $F^z = -\frac{3}{2}, -\frac{1}{2}, +\frac{1}{2}, +\frac{3}{2}$. For such atoms, one has to suppress the occupation of one of the "middle" states, say the $F^z = -\frac{1}{2}$ state, by effectively lifting it to a higher energy while keeping the other states approximately degenerate. This can be accomplished through a combination of an external magnetic field and two carefully tuned lasers with frequencies Ω_1 and Ω_2, which effectively push down the energies of the $F^z = -\frac{3}{2}$ and the $F^z = +\frac{1}{2}$ states by coupling these states to states of (say) the energetically higher $F = 5/2$ multiplet (see Fig. 3.2). At sufficiently low temperatures, we are hence left with a system with three internal states $F^z = -\frac{3}{2}, +\frac{1}{2}, +\frac{3}{2}$, which we may identify with the colors "blue", "red", and "green" of an SU(3) spin. In leading order, the number of particles of each color is now conserved, as required by SU(3) symmetry. For example, conservation of F^z forbids processes in which a "blue" and a "green" particle turn into two "red" ones, $|b, g\rangle \rightarrow |r, r\rangle$. Higher order processes of the kind $|b, g, g\rangle \rightarrow |r, r, r\rangle$ are still possible, but negligible if the experiment is conducted at sufficiently short time scales.

If one places fermionic atoms such as ^{6}Li with an artificial SU(3) spin engineered along the lines of this or a related proposal in an optical lattice and allows for a weak hopping of the atoms on the lattice, one has developed an experimental realization

of an SU(3) Hubbard model. If the energy cost U of having two atoms on the same lattice site is significantly larger than the hopping t, and the density is one atom per site, the system will effectively constitute an SU(3) antiferromagnet. The dimension of this antiferromagnet will depend on the optical lattice, which can be one-, two-, or three-dimensional.

Apart from this idea, there was a recent proposal to realize an approximate SU(4) symmetry within cold atoms experiments with spin 3/2 atoms [150,154]. The SU(4) symmetry should be reached by fixing the ratio of four effective spin 3/2 particles per site. Assuming one would confine eight particles per site, one effectively obtained the antisymmetric representation **6** of SU(4). Replacing the SU(4) fermions in this experiment by SU(4) bosons, one would obtain an effective representation **10** on each lattice site. These proposed cold atoms experiments might sound as being far away or even unrealistic. The simple understanding of SU(3) and SU(4) spin representations, however, is definitely important for coming discussions and proposals. In the following, we will introduce several exact SU(3) and SU(n) spin models [62,64] in order to apply our approach and test whether or not the models exhibit spinon confinement.

3.3.2 SU(3) Trimer chain

Consider a chain with N lattice sites, where N has to be divisible by three, and periodic boundary conditions (PBCs). On each lattice site we place an SU(3) spin which transforms under the fundamental representation **3**, i.e., the spin can take the values (or colors) blue (b), red (r), or green (g). The trimer states are obtained by requiring the spins on each three neighboring sites to form an SU(3) singlet, which we call a trimer and sketch it by $\circ\!\!-\!\!\circ\!\!-\!\!\circ$. The three linearly independent trimer states on the chain are given by

$$
\left|\psi_{\text{trimer}}^{(\mu)}\right\rangle = \begin{cases} |\ \circ\!\!-\!\!\circ\!\!-\!\!\circ \ \ \circ\!\!-\!\!\circ\!\!-\!\!\circ \ \rangle \equiv \left|\psi_{\text{trimer}}^{(1)}\right\rangle, \\[2mm] |\ \circ \ \ \circ\!\!-\!\!\circ\!\!-\!\!\circ \ \ \circ\!\!-\!\!\circ \ \rangle \equiv \left|\psi_{\text{trimer}}^{(2)}\right\rangle, \\[2mm] |\ \circ\!\!-\!\!\circ \ \ \circ\!\!-\!\!\circ\!\!-\!\!\circ \ \ \circ \ \rangle \equiv \left|\psi_{\text{trimer}}^{(3)}\right\rangle. \end{cases} \tag{3.18}
$$

Introducing operators $c_{i\sigma}^{\dagger}$ which create a fermion of color σ ($\sigma = $ b, r, g) at lattice site i, the trimer states can be written as

$$
\left|\psi_{\text{trimer}}^{(\mu)}\right\rangle = \prod_{\substack{i \\ \left(\frac{i-\mu}{3}\ \text{integer}\right)}} \left(\sum_{\substack{(\alpha,\beta,\gamma)= \\ \pi(\text{b,r,g})}} \text{sign}(\pi)\, c_{i\,\alpha}^{\dagger}\, c_{i+1\,\beta}^{\dagger}\, c_{i+2\,\gamma}^{\dagger} \right) |\,0\,\rangle,
$$

where $\mu = 1,2,3$ labels the three degenerate ground states, and i runs over the lattice sites subject to the constraint that $\frac{i-\mu}{3}$ is integer. The sum extends over all

six permutations π of the three colors b, r, and g, i.e.,

$$\sum_{(\alpha,\beta,\gamma)=\pi(\text{b,r,g})} \text{sign}(\pi)\, c^\dagger_{i\,\alpha} c^\dagger_{i+1\,\beta} c^\dagger_{i+2\,\gamma} = c^\dagger_{i\,\text{b}} c^\dagger_{i+1\,\text{r}} c^\dagger_{i+2\,\text{g}} + c^\dagger_{i\,\text{r}} c^\dagger_{i+1\,\text{g}} c^\dagger_{i+2\,\text{b}}$$

$$+ c^\dagger_{i\,\text{g}} c^\dagger_{i+1\,\text{b}} c^\dagger_{i+2\,\text{r}} - c^\dagger_{i\,\text{b}} c^\dagger_{i+1\,\text{g}} c^\dagger_{i+2\,\text{r}} - c^\dagger_{i\,\text{g}} c^\dagger_{i+1\,\text{r}} c^\dagger_{i+2\,\text{b}} - c^\dagger_{i\,\text{r}} c^\dagger_{i+1\,\text{b}} c^\dagger_{i+2\,\text{g}}.$$

The SU(3) generators at each lattice site i are in analogy to the SU(2) case defined as

$$J_i^a = \frac{1}{2} \sum_{\sigma,\sigma'=\text{b,r,g}} c^\dagger_{i\sigma} \lambda^a_{\sigma\sigma'} c_{i\sigma'}, \quad a = 1,\ldots,8, \tag{3.19}$$

where the λ^a are the Gell-Mann matrices (see App. B.2.4). The operators (3.19) satisfy the commutation relations

$$\left[J_i^a, J_j^b \right] = \delta_{ij}\, f^{abc} J_i^c, \quad a,b,c = 1,\ldots,8, \tag{3.20}$$

(we use the Einstein summation convention) with f^{abc} the structure constants of SU(3) (see App. B.2). We further introduce the total SU(3) spin of ν neighboring sites $i,\ldots,i+\nu-1$,

$$\boldsymbol{J}_i^{(\nu)} = \sum_{j=i}^{i+\nu-1} \boldsymbol{J}_j, \tag{3.21}$$

where $\boldsymbol{J}_i$ is the eight-dimensional vector formed by its components (3.19). The parent Hamiltonian for the trimer states (3.19) is given by

$$H_{\text{trimer}} = \sum_{i=1}^{N} \left(\left(\boldsymbol{J}_i^{(4)} \right)^4 - \frac{14}{3} \left(\boldsymbol{J}_i^{(4)} \right)^2 + \frac{40}{9} \right). \tag{3.22}$$

The $\boldsymbol{J}_i \boldsymbol{J}_j$ terms appear complicated in terms of Gell-Mann matrices, but are rather simply when written out using the operator $\mathcal{P}_{ij}$, which permutes the SU(n) spins (here $n = 3$) on sites i and j,

$$\boldsymbol{J}_i \boldsymbol{J}_j = \frac{1}{2} \left(\mathcal{P}_{ij} - \frac{1}{n} \right). \tag{3.23}$$

Eq. (3.23) reduces for $n = 2$ to the famous Dirac identity [43]. Note that the Heisenberg terms is in analogy to SU(2) given by $\boldsymbol{J}_i \boldsymbol{J}_j = \sum_{a=1}^{8} J_i^a J_j^a$.

In the following, we make extensive use of SU(n) representation for $n > 2$. We will just label them "$\boldsymbol{m}$" where m is the dimension of the representation. In some cases, we give additionally the Dynkin labels of the representation, at least when we introduce a representation for the first time. We refer the reader to App. B.2 for details.

We will now proceed with the verification of the trimer Hamiltonian (3.22). Since the spins on the individual sites transform under the fundamental representation $\boldsymbol{3}$, the SU(3) content of four sites is

$$\boldsymbol{3} \otimes \boldsymbol{3} \otimes \boldsymbol{3} \otimes \boldsymbol{3} = 3 \cdot \boldsymbol{3} \oplus 2 \cdot \bar{\boldsymbol{6}} \oplus 3 \cdot \boldsymbol{15} \oplus \boldsymbol{15}', \tag{3.24}$$

i.e., we obtain representations $\mathbf{3}$, $\bar{\mathbf{6}}$, and two non-equivalent 15-dimensional representations with Dynkin coordinates $(2, 1)$ and $(4, 0)$, respectively. All these representations can be distinguished by their eigenvalues of the quadratic Casimir operator, which is given by $\left(\boldsymbol{J}_i^{(4)}\right)^2$ if the four spins reside on the four neighboring lattice sites $i, \ldots, i + 3$.

For the trimer states (3.18), the situation simplifies as we only have the two possibilities

$$
\begin{aligned}
\text{o—o—o} \quad \text{o} \quad &\hat{=} \quad \mathbf{1} \otimes \mathbf{3} = \mathbf{3}, \\
\text{o—o} \quad \text{o—o} \quad &\hat{=} \quad \bar{\mathbf{3}} \otimes \bar{\mathbf{3}} = \mathbf{3} \oplus \bar{\mathbf{6}},
\end{aligned}
$$

which implies that the total SU(3) spin on four neighboring sites can only transform under representations $\mathbf{3}$ or $\bar{\mathbf{6}}$. The eigenvalues of the quadratic Casimir operator for these representations are $4/3$ and $10/3$, respectively. The auxiliary operators

$$
H_i = \left(\left(\boldsymbol{J}_i^{(4)} \right)^2 - \frac{4}{3} \right) \left(\left(\boldsymbol{J}_i^{(4)} \right)^2 - \frac{10}{3} \right) \tag{3.25}
$$

hence annihilate the trimer states for all values of i, while they yield positive eigenvalues for $\mathbf{15}$ or $\mathbf{15'}$, i.e., all other states. Summing H_i over all lattice sites i yields (3.22). We have numerically confirmed by exact diagonalization of (3.22) for chains with $N = 9$ and 12 lattice sites that the three states (3.18) are the only ground states. In Fig. 3.3 we have shown the spectrum of the trimer model on a chain with $N = 18$ sites [121].
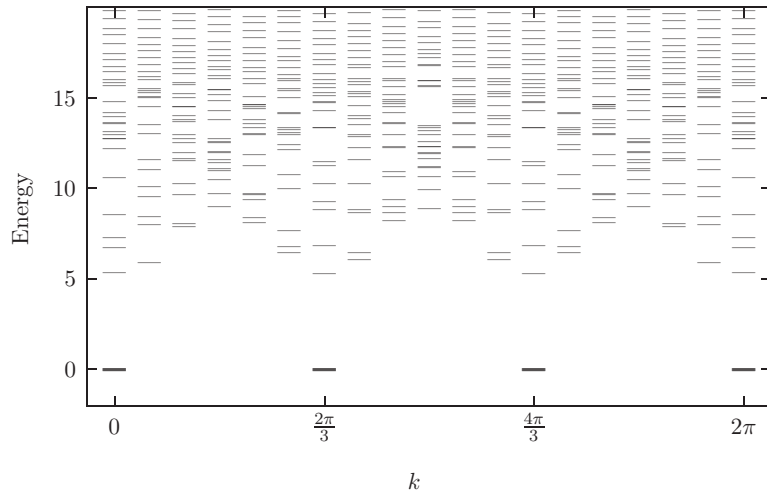
Figure 3.3: Spectrum of the trimer model (3.22) on a chain with $N = 18$ sites. The zero energy ground states (labeled by thick lines in the spectrum) are at $k = 0, \frac{2\pi}{3}$, $\frac{4\pi}{3}$ in the Brioullin zone.

Elementary excitations

Before we will consider the cartoon for the trimer model and decide whether or not spinon confinement is present, we will investigate the low–lying excitations of (3.22),

(a)   (b)

Figure 3.4: Couplings used in the numerical studies to create (a) the localized rep. **3** trial state and (b) the localized rep. $\bar{\mathbf{3}}$ trial state.

the SU(3) spinons. In analogy with the MG model, it is evident that the SU(3) spinon or "coloron" excitations correspond to domain walls between the degenerate ground states[9]. For the trimer model, however, there are two different kinds of domain walls, as illustrated by:

$$\underset{\circ\!-\!\circ\!-\!\circ}{} \;\; \overset{\mathbf{3}}{\underset{\circ}{}} \;\; \underset{\circ\!-\!\circ\!-\!\circ}{} \tag{3.26}$$

$$\underset{\circ\!-\!\circ\!-\!\circ}{} \;\; \overset{\bar{\mathbf{3}}}{\underset{\circ\!-\!\circ}{}} \;\; \underset{\circ\!-\!\circ\!-\!\circ}{} \tag{3.27}$$

The first domain wall (3.26) connects ground state μ to the left to ground state $\mu+1$ to the right, where μ is defined modulo 3 (see (3.19)), and consists of an individual SU(3) spin, which transforms under representation **3**. The second domain wall (3.27) connects ground state μ with ground state $\mu+2$. It consists of two antisymmetrically coupled spins on two neighboring sites, and hence transforms under representation $\bar{\mathbf{3}}$. As we take momentum superpositions of the localized domain walls illustrated above, we expect one of them, but not both, to constitute an approximate eigenstate of the trimer model. The reason we do not expect both of them to yield a valid excitation is that they can decay into each other, i.e., if the rep. **3** excitation is valid the rep. $\bar{\mathbf{3}}$ domain wall would decay into two rep. **3** excitations, and vice versa. The question which of the two excitations is the valid one, i.e., whether the elementary excitations transform under **3** or $\bar{\mathbf{3}}$ under SU(3) rotations, can be resolved through numerical studies. We will discuss the results of these studies now.

The rep. **3** and the rep. $\bar{\mathbf{3}}$ trial states require chains with $N = 3 \cdot \text{integer} + 1$ and $N = 3 \cdot \text{integer} + 2$ sites, respectively; we chose $N = 13$ and $N = 14$ for our numerical studies. To create the localized domain walls (3.26) and (3.27), we numerically diagonalized auxiliary Hamiltonians with appropriate couplings, as illustrated in Fig. 3.4. From these localized excitations, we constructed momentum eigenstates by superposition, and compared them to the exact eigenstates of our model Hamiltonian (3.22) for chains with the same number of sites. The results are shown in Tab. 3.1 and Fig. 3.5 for the rep. **3** trial state, and in Tab. 3.2 and Fig. 3.5 for the rep. $\bar{\mathbf{3}}$ trial state.

The numerical results clearly indicate that the rep. $\bar{\mathbf{3}}$ trial states (3.27) are valid approximations to the elementary excitations of the trimer chain, while the rep. **3** trial states (3.26) are not. We deduce that the elementary excitations of the trimer chain (3.22) transform under $\bar{\mathbf{3}}$, that is, under the representation conjugated to the

---

[9]The SU(3) spinon was in Refs. [132, 133] called *coloron*. In the following sections, we will use "coloron" and "SU(3) spinon" synonymously.

mom $[2\pi/N]$	E_{tot} exact	trial	% off	over- lap
0	2.9735	4.5860	54.2	0.9221
1, 12	6.0345	10.2804	70.4	0.5845
2, 11	9.0164	17.2991	91.9	0.0
3, 10	6.6863	13.1536	96.7	0.0
4, 9	3.0896	5.0529	63.5	0.8864
5, 8	4.8744	7.5033	53.9	0.8625
6, 7	8.5618	16.6841	94.9	0.1095

Table 3.1: Energies of the rep. **3** trial states (3.26) in comparison to the exact excitation energies of the trimer model (3.22) and their overlaps for an SU(3) spin chain with $N = 13$ sites.

mom $[2\pi/N]$	E_{tot} exact	trial	% off	over- lap
0	2.1013	2.3077	9.8	0.9953
1, 13	4.3677	4.8683	11.5	0.9864
2, 12	7.7322	8.7072	12.6	0.9716
3, 11	6.8964	7.7858	12.9	0.9696
4, 10	3.2244	3.5415	9.8	0.9934
5, 9	2.2494	2.4690	9.7	0.9950
6, 8	5.4903	6.1016	11.1	0.9827
7	7.4965	8.5714	14.3	0.9562

Table 3.2: Energies of the rep. $\bar{\mathbf{3}}$ trial states (3.27) in comparison to the exact excitation energies of the trimer model (3.22) and their overlaps for an SU(3) spin chain with $N = 14$ sites.

original SU(3) spins localized at the sites of the chain. Using the language of colors, one may say that if a basis for the original spins is spanned by blue, red, and green, a basis for the excitations is spanned by the complementary colors yellow, cyan, and magenta. This result appears to be a general feature of SU(3) spin chains, as it was recently shown explicitly to hold for the Haldane–Shastry model as well [33,132,133].

Note that the elementary excitations of the trimer chain are deconfined, meaning that the energy of two localized representation $\bar{\mathbf{3}}$ domain walls or colorons (3.27) does not depend on the distance between them. The reason is simply that domain walls connect one ground state with another, without introducing costly correlations in the region between the domain walls.
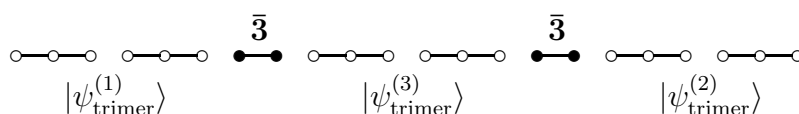
In the case of the MG model and the trimer model introduced here, however, there
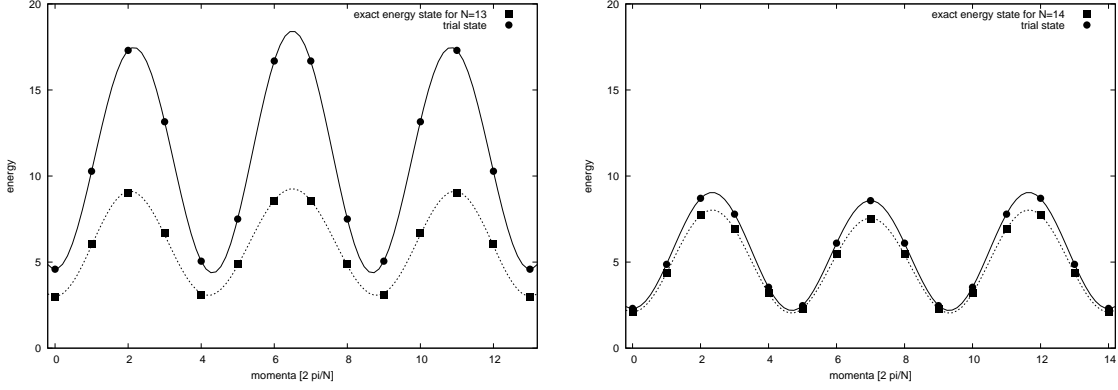
Figure 3.5: Left: Dispersion of the rep. **3** trial states (3.26) in comparison to the exact excitation energies of (3.22) for a chain with $N = 13$. Right: Dispersion of the rep. $\bar{\mathbf{3}}$ trial states (3.27) in comparison to the exact excitation energies of (3.22) for a chain with $N = 14$. The lines are in both plots a guide to the eye.

is still an energy gap associated with the creation of each coloron, which is simply the energy cost associated with the domain wall. We will consider this extensive discussion as a paradigm for $SU(n)$ spinon excitations: $SU(n)$ spinon excitations are fractionally quantized objects as the $SU(2)$ spinon is. The $SU(n)$ spin chain with fundamental representation favors the $\bar{\mathbf{n}}$ spinon rather than the $\mathbf{n}$ spinon. For higher–dimensional representations, the discussion has to be repeated carefully. Now we turn to the higher–dimensional VBS states of $SU(3)$. For that reason, we generalize Schwinger bosons introduced in Sec. 3.2 to $SU(3)$ and $SU(n)$.

SU(3) Schwinger bosons

The generalization to $SU(n)$ proceeds without incident. We content ourselves here by writing the formalism out explicitly for $SU(3)$. In analogy to (3.8), we write the $SU(3)$ spin operators (3.19)

$$
\begin{aligned}
J^1 + iJ^2 &= I^+ &&= b^\dagger r, \\
J^1 - iJ^2 &= I^- &&= r^\dagger b, \\
&\quad\; J^3 &&= \tfrac{1}{2}(b^\dagger b - r^\dagger r), \\
J^4 + iJ^5 &= V^+ &&= b^\dagger g, \\
J^4 - iJ^5 &= V^- &&= g^\dagger b, \\
J^6 + iJ^7 &= U^+ &&= r^\dagger g, \\
J^6 - iJ^7 &= U^- &&= g^\dagger r, \\
&\quad\; J^8 &&= \tfrac{1}{2\sqrt{3}}(b^\dagger b + r^\dagger r - 2g^\dagger g),
\end{aligned}
\tag{3.28}
$$

in terms of the boson annihilation and creation operators $b, b^\dagger$ (blue), $r, r^\dagger$ (red), and $g, g^\dagger$ (green) satisfying

$$
[b, b^\dagger] = [r, r^\dagger] = [g, g^\dagger] = 1 \tag{3.29}
$$

while all other commutators vanish. Again, it is readily verified with (3.29) that the operators J^a satisfy (3.20). The basis states spanning the fundamental representation **3** may in analogy to (3.12) be written using either fermion or boson creation operators:

$$|\text{b}\rangle = c_\text{b}^\dagger\,|\,0\,\rangle = b^\dagger\,|\,0\,\rangle, \quad |\text{r}\rangle = c_\text{r}^\dagger\,|\,0\,\rangle = r^\dagger\,|\,0\,\rangle, \quad |\text{g}\rangle = c_\text{g}^\dagger\,|\,0\,\rangle = g^\dagger\,|\,0\,\rangle. \quad (3.30)$$

We write this abbreviated

$$\mathbf{3} \;=\; (1,0) \;=\; \square \;\;\hat{=}\;\; c_\alpha^\dagger\,|\,0\,\rangle \;=\; \alpha^\dagger\,|\,0\,\rangle. \quad (3.31)$$

The fermion operators can be used to combine spins transforming under the fundamental representation **3** antisymmetrically, and hence to construct the representations

$$\begin{aligned}
\bar{\mathbf{3}} \;=\; (0,1) \;=\; \boxed{} \;\;&\hat{=}\;\; c_\alpha^\dagger c_\beta^\dagger\,|\,0\,\rangle, \\
\mathbf{1} \;=\; (0,0) \;=\; \boxed{} \;\;&\hat{=}\;\; c_\text{b}^\dagger c_\text{r}^\dagger c_\text{g}^\dagger\,|\,0\,\rangle.
\end{aligned} \quad (3.32)$$

The Schwinger bosons, by contrast, combine fundamental representations **3** symmetrically, and hence yield representations labeled by Young tableaux in which the boxes are arranged in a horizontal row, like

$$\begin{aligned}
\mathbf{6} \;&=\; (2,0) \;=\; \square\square \;\;&\hat{=}\;\; \alpha^\dagger\beta^\dagger\,|\,0\,\rangle, \\
\mathbf{10} \;&=\; (3,0) \;=\; \square\square\square \;\;&\hat{=}\;\; \alpha^\dagger\beta^\dagger\gamma^\dagger\,|\,0\,\rangle, \\
\mathbf{15'} \;&=\; (4,0) \;=\; \square\square\square\square \;\;&\hat{=}\;\; \alpha^\dagger\beta^\dagger\gamma^\dagger\delta^\dagger\,|\,0\,\rangle,
\end{aligned} \quad (3.33)$$

where $\alpha, \beta, \gamma, \ldots \in \{b, r, g\}$. Unfortunately, it is not possible to construct representations like

$$\mathbf{8} \;=\; (1,1) \;=\; \text{\tiny(Young tableau)}$$

by simply taking products of anti-commuting or commuting creation or annihilation operators.

Now we are prepared to rewrite the trimer states (3.19) as

$$\left|\psi_\text{trimer}^{(\mu)}\right\rangle = \prod_{\substack{i \\ \left(\frac{i-\mu}{3}\,\text{integer}\right)}} \left(\sum_{\substack{(\alpha,\beta,\gamma)= \\ \pi(b,r,g)}} \text{sign}(\pi)\, \alpha_i^\dagger\, \beta_{i+1}^\dagger\, \gamma_{i+2}^\dagger \right)|\,0\,\rangle \equiv \Psi^\mu[b^\dagger, r^\dagger, g^\dagger]\,|\,0\,\rangle, \quad (3.34)$$

where, as in (3.19), $\mu = 1, 2, 3$ labels the three degenerate ground states, i runs over the lattice sites subject to the constraint that $\frac{i-\mu}{3}$ is integer, and the sum extends over all six permutations π of the three colors b, r, and g. This formulation can be used directly to construct VBSs for SU(3) spin chains with spins transforming under totally symmetric representations as the rep. **6** and **10** on each site. These VBS states are given by

$$|\psi_{a,b,c}\rangle = \left(\Psi^1[b^\dagger, r^\dagger, g^\dagger]\right)^a \left(\Psi^2[b^\dagger, r^\dagger, g^\dagger]\right)^b \left(\Psi^3[b^\dagger, r^\dagger, g^\dagger]\right)^c|\,0\,\rangle \quad (3.35)$$

where the constraint $a + b + c = \lambda$, the number of boxes in the Young tableau, fixes the representation.

3.3.3   SU(3) representation 6 VBS model

We obtain a representation **6** VBS from two trimer states by projecting the tensor product of two fundamental representations **3** onto the symmetric subspace, i.e., onto the **6** in the decomposition $\mathbf{3} \otimes \mathbf{3} = \bar{\mathbf{3}} \oplus \mathbf{6}$. Graphically, this is illustrated as follows:

<div align="center">

one site

projection onto rep. $\mathbf{6} = (2,0)$ (3.36)

</div>

This construction yields three linearly independent **6** VBS states, as there are three ways to choose two different trimer states out of a total of three. These three VBS states are readily written out using (3.34),

$$\left| \psi_{\mathbf{6}\,\mathrm{VBS}}^{(\mu)} \right\rangle = \Psi^\mu\!\left[b^\dagger, r^\dagger, g^\dagger\right] \cdot \Psi^{\mu+1}\!\left[b^\dagger, r^\dagger, g^\dagger\right] \, |\,0\,\rangle \tag{3.37}$$

for $\mu = 1$, 2, or 3. Alternatively, we could write them as $|\psi_{1,1,0}\rangle$, $|\psi_{1,0,1}\rangle$, and $|\psi_{0,1,1}\rangle$ using the notation of Eq. (3.35) If we pick four neighboring sites on a chain with any of these states, the total SU(3) spin of those may contain the representations

$$\text{} \quad \hat{=} \quad \mathbf{3} \otimes \mathbf{3} = \bar{\mathbf{3}} \oplus \mathbf{6}$$

or the representations

$$\text{} \quad \hat{=} \quad \bar{\mathbf{3}} \otimes \bar{\mathbf{3}} \otimes \mathbf{3} = 2 \cdot \bar{\mathbf{3}} \oplus \mathbf{6} \oplus \overline{\mathbf{15}},$$

i.e., the total spin transforms under $\bar{\mathbf{3}}$, $\mathbf{6}$, or $\overline{\mathbf{15}} = (1,2)$, all of which are contained in the product

$$\mathbf{6} \otimes \mathbf{6} \otimes \mathbf{6} \otimes \mathbf{6} = 3 \cdot \bar{\mathbf{3}} \oplus 6 \cdot \mathbf{6} \oplus 7 \cdot \overline{\mathbf{15}} \oplus 3 \cdot \overline{\mathbf{15}}' \oplus 3 \cdot \mathbf{21}$$
$$\oplus \; 8 \cdot \mathbf{24} \oplus 6 \cdot \overline{\mathbf{42}} \oplus \mathbf{45} \oplus 6 \cdot \mathbf{60} \oplus 3 \cdot \mathbf{63} \tag{3.38}$$

and hence possible for a representation **6** spin chain in general. The corresponding Casimirs are given by $\mathcal{C}^2_{\mathrm{SU}(3)}(0,1) = \frac{4}{3}$, $\mathcal{C}^2_{\mathrm{SU}(3)}(2,0) = \frac{10}{3}$, and $\mathcal{C}^2_{\mathrm{SU}(3)}(1,2) = \frac{16}{3}$. This leads us to propose the parent Hamiltonian

$$H_{\mathbf{6}\,\mathrm{VBS}} = \sum_{i=1}^{N} H_i \tag{3.39}$$

with

$$H_i = \left(\left(\boldsymbol{J}_i^{(4)}\right)^2 - \frac{4}{3}\right)\left(\left(\boldsymbol{J}_i^{(4)}\right)^2 - \frac{10}{3}\right)\left(\left(\boldsymbol{J}_i^{(4)}\right)^2 - \frac{16}{3}\right). \tag{3.40}$$

Note that the operators J_i^a, $a = 1, \dots, 8$, are now given by 6×6 matrices, as the Gell-Mann matrices only provide the generators (3.19) of the fundamental representation **3**. Since the representations $\bar{\mathbf{3}}$, **6**, and $\overline{\mathbf{15}}$ possess the smallest Casimirs in the expansion (3.38), H_i and hence also $H_{\mathbf{6}\,\mathrm{VBS}}$ are positive semi-definite (i.e., have only

non-negative eigenvalues). The three linearly independent states (3.37) are zero-energy eigenstates of (3.39).

To verify that these are the only ground states, we have numerically diagonalized (3.39) for $N = 6$ and $N = 9$ sites. For $N = 9$, we find zero-energy ground states at momenta $k = 0, 3,$ and 6 (in units of $\frac{2\pi}{N}$ with the lattice constant set to unity). Note that for $N = 6$ we found two additional *finite size* zero–energy ground states. This is not surprising as the Hamiltonian involves four site interactions which is very large compared to the total chain length of $N = 6$ sites.

Excitations of the **6** VBS model are given by domain walls between two of the ground states (3.37). As in the trimer model, two distinct types of domain walls exist, which transform according to representations $\overline{\mathbf{3}}$ and $\mathbf{3}$:

$$\Psi^1 \cdot \Psi^2 \qquad \Psi^2 \cdot \Psi^3 \qquad \Psi^1 \cdot \Psi^2 \tag{3.41}$$

It is not clear which excitation has the lower energy, and it appears likely that both of them are stable against decay. Let us first look at the rep. $\overline{\mathbf{3}}$ excitation. The four-site Hamiltonian (3.40) annihilates the state for all i's except the four sites in the dashed box in (3.41), which contains the representations

$$\overline{\mathbf{3}} \otimes \overline{\mathbf{3}} \otimes \overline{\mathbf{3}} \otimes \mathbf{3} \otimes \mathbf{3} = 6 \cdot \overline{\mathbf{3}} \oplus 5 \cdot \mathbf{6} \oplus 6 \cdot \overline{\mathbf{15}} \oplus \overline{\mathbf{15}}' \oplus 2 \cdot \mathbf{24} \oplus \overline{\mathbf{42}}$$

i.e., the representations $\overline{\mathbf{15}}' = (0, 4)$, $\mathbf{24} = (3, 1)$ twice, and $\overline{\mathbf{42}} = (2, 3)$ with Casimirs $\frac{28}{3}$, $\frac{25}{3}$ and $\frac{34}{3}$, respectively, in addition to representations annihilated by H_i. For the rep. $\mathbf{3}$ excitation sketched on the right in (3.41), there are two sets of four neighboring sites not annihilated by H_i as indicated by the dashed and the dotted box. Each set contains the representations

$$\overline{\mathbf{3}} \otimes \mathbf{3} \otimes \mathbf{3} \otimes \mathbf{3} = 3 \cdot \overline{\mathbf{3}} \oplus 3 \cdot \mathbf{6} \oplus 2 \cdot \overline{\mathbf{15}} \oplus \mathbf{24}$$

i.e., only the rep. $\mathbf{24}$ in addition to representations annihilated by H_i. For our parent Hamiltonian (3.39), it hence may well be that the rep. $\mathbf{3}$ anti-coloron has the lower energy, but it is all but clear that the rep. $\overline{\mathbf{3}}$ has sufficiently higher energy to decay. For general representation **6** spin chains, it may depend on the specifics of the model which excitation is lower in energy and whether the conjugate excitation decays or not.

Since the excitations of the rep. **6** VBS chain are merely domain walls between different ground states, there is no confinement between them. We expect the generic antiferromagnetic rep. **6** chain to be gapless, even though the model we proposed here has a gap associated with the energy cost of creating a domain wall.

3.3.4   SU(3) representation 10 VBS model

Let us now turn to the **10** VBS chain, which is a direct generalization of the AKLT chain to SU(3). By combining the three different trimer states (3.34) for

$\mu = 1, 2,$ and 3 symmetrically,

$$\begin{aligned}
|\psi_{\mathbf{10}\,\text{VBS}}\rangle &= \Psi^1\big[b^\dagger, r^\dagger, g^\dagger\big] \cdot \Psi^2\big[b^\dagger, r^\dagger, g^\dagger\big] \cdot \Psi^3\big[b^\dagger, r^\dagger, g^\dagger\big]\,|\,0\,\rangle \\
&= \prod_i \Big(\sum_{\substack{(\alpha,\beta,\gamma)= \\ \pi(b,r,g)}} \text{sign}(\pi)\,\alpha_i^\dagger\,\beta_{i+1}^\dagger\,\gamma_{i+2}^\dagger \Big)\,|\,0\,\rangle,
\end{aligned} \qquad (3.42)$$

we automatically project out the rep. $\mathbf{10}$ in the decomposition $\mathbf{3}\otimes\mathbf{3}\otimes\mathbf{3} = \mathbf{1}\oplus\mathbf{2}\cdot\mathbf{8}\oplus\mathbf{10}$ generated on each lattice site by the three trimer chains. This construction yields a unique state, as illustrated:

one site
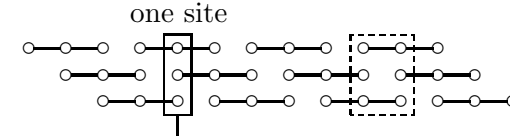
projection onto $\mathbf{10} = (3,0)$ (3.43)

In order to construct a parent Hamiltonian, note first that the total spin on two (neighboring) sites of a rep. $\mathbf{10}$ chain is given by

$$\mathbf{10} \otimes \mathbf{10} = \overline{\mathbf{10}} \oplus \mathbf{27} \oplus \mathbf{28} \oplus \mathbf{35}. \qquad (3.44)$$

On the other hand, the total spin of two neighboring sites for the $\mathbf{10}$ VBS state can contain only the representations

$$\overline{\mathbf{3}} \otimes \overline{\mathbf{3}} \otimes \mathbf{3} \otimes \mathbf{3} = 2\cdot\mathbf{1} \oplus 4\cdot\mathbf{8} \oplus \mathbf{10} \oplus \overline{\mathbf{10}} \oplus \mathbf{27}, \qquad (3.45)$$

as can be seen easily from the dashed box in the cartoon above. (Note that this result is independent of how many sites we include in the dashed box.) After the projection onto rep. $\mathbf{10}$ on each lattice site, we find that only reps. $\overline{\mathbf{10}} = (0,3)$ and $\mathbf{27} = (2,2)$ occur for the total spin of two neighboring sites for the $\mathbf{10}$ VBS state. With the Casimirs $\mathcal{C}^2_{\text{SU}(3)}(0,3) = 6$ and $\mathcal{C}^2_{\text{SU}(3)}(2,2) = 8$ we obtain the parent Hamiltonian

$$H_{\mathbf{10}\,\text{VBS}} = \sum_{i=1}^{N} \left(\boldsymbol{J}_i\boldsymbol{J}_{i+1} + \frac{1}{5}\big(\boldsymbol{J}_i\boldsymbol{J}_{i+1}\big)^2 + \frac{6}{5} \right), \qquad (3.46)$$

the operators J_i^a, $a = 1, \ldots, 8$, are now 10×10 matrices, and we have used $\boldsymbol{J}_i^2 = 6$. $H_{\mathbf{10}\,\text{VBS}}$ is positive semi-definite and annihilates the $\mathbf{10}$ VBS state (3.42).

The Hamiltonian (3.46) provides the equivalent of the AKLT model [11,12], whose unique ground state is constructed from dimer states by projection onto spin 1, for SU(3) spin chains. Note that as in the case of SU(2), it is sufficient to consider linear and quadratic powers of the total spin of only two neighboring sites. This is a general feature of the corresponding SU(n) models, as we will elaborate in Sec. 3.3.7.

Since the $\mathbf{10}$ VBS state (3.42) is unique, we cannot have domain walls connecting different ground states. We hence expect the coloron and anti-coloron excitations to be confined in pairs, as illustrated below. The state between the excitations is no longer annihilated by (3.46), as there are pairs of neighboring sites containing

higher-dimensional representations, as indicated by the dotted box below. As the number of such pairs increases linearly with the distance between the excitation, the confinement potential depends linearly on this distance.

$$(3.47)$$

In principle, it would also be possible to create three colorons (or three anti-colorons) rather than a coloron–anti-coloron pair, but as all three excitations would feel strong confinement forces, we expect the coloron–anti-coloron pair to constitute the dominant low energy excitation. The confinement force between the pair induces a linear oscillator potential for the relative motion of the constituents. The zero-point energy of this oscillator gives rise to a Haldane-type energy gap, which is independent of the model specifics. We expect this gap to be a generic feature of rep. **10** spin chains with short-range antiferromagnetic interactions.

3.3.5   SU(3) representation 8 VBS model

To construct a representation **8** VBS state, consider first a chain with alternating representations **3** and $\mathbf{\bar{3}}$ on neighboring sites, which we combine into singlets[10]. This can be done in two ways, yielding the two states

We then combine a **3**–$\mathbf{\bar{3}}$–singlet with another **3**–$\mathbf{\bar{3}}$–singlet which is shifted by one lattice spacing to the right or the left, respectively. This yields representations $\mathbf{3} \otimes \mathbf{\bar{3}} = \mathbf{1} \oplus \mathbf{8}$ at each site. The **8** VBS state is obtained by projecting onto representation **8**. Corresponding to the two **3**–$\mathbf{\bar{3}}$ states illustrated above, we obtain two linearly independent **8** VBS states, Ψ^{L} and Ψ^{R}, which may be visualized as

$$(3.48)$$

These states transform into each other under space reflection (parity) or color conjugation (interchange of **3** and $\mathbf{\bar{3}}$). Note that the representation **8** VBS state might

---

[10]We emphasize that we are not considering spin chains with alternating representations, i.e., the **3**–$\mathbf{\bar{3}}$ chain is not subject of our interest. Here we just explain that one can use these alternating singlet bonds to construct a representation **8** VBS state which is subject of our consideration.

be defined on arbitrary chain length N, i.e., for both even and odd N. To make this clear one could prefer another way of drawing the cartoon,

one site
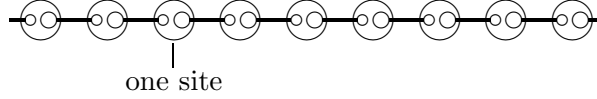
The $S = 1$ AKLT chain supports the same feature which is clearly a property of the adjoint representation $(1, 0, \dots, 0, 1)$ of SU(n): $(1, 0, \dots, 0, 1)^{\otimes N} = \text{Singlet} \oplus \dots$ for arbitrary N. Note that this is the only advantage of the alternative cartoon and, in particular, it is not convenient to get informations about spinon confinement.

We are able to write down the states by use of matrix products which allows us to calculate the static spin–spin correlation functions explicitly. We will present the matrix product states as well as the correlations in Sec. 3.8.

Let us now formulate a parent Hamiltonian for these states. If we consider two lattice sites on an SU(3) chain with a representation **8** on each lattice site in general, we find the full SU(3) content

$$\mathbf{8} \otimes \mathbf{8} = \mathbf{1} \oplus 2 \cdot \mathbf{8} \oplus \mathbf{10} \oplus \overline{\mathbf{10}} \oplus \mathbf{27} \tag{3.49}$$

with $\mathbf{10} = (3, 0)$, $\overline{\mathbf{10}} = (0, 3)$, and $\mathbf{27} = (2, 2)$. On the other hand, for the **8** VBS states only the representations $\mathbf{3} \otimes \bar{\mathbf{3}} = \mathbf{1} \oplus \mathbf{8}$ can occur for the total spin of two neighboring sites, as the two sites always contain one singlet (see dashed box in (3.48) on the right above). With the Casimirs $\mathcal{C}^2_{\text{SU}(3)}(0, 0) = 0$ and $\mathcal{C}^2_{\text{SU}(3)}(1, 1) = 3$ for representations **1** and **8**, respectively, we construct the parent Hamiltonian

$$H_{\mathbf{8}\,\text{VBS}} = \sum_{i=1}^{N} \left(\boldsymbol{J}_i \boldsymbol{J}_{i+1} + \frac{2}{9} \big(\boldsymbol{J}_i \boldsymbol{J}_{i+1} \big)^2 + 1 \right), \tag{3.50}$$

where the operators J_i^a, $a = 1, \dots, 8$, are now 8×8 matrices, and we have used the Casimir $\boldsymbol{J}_i^2 = 3$ on each site. $H_{\mathbf{8}\,\text{VBS}}$ is positive semi-definite, and annihilates the states Ψ^{L} and Ψ^{R}. We have numerically verified for chains with $N = 3$, 4, 5, and 6 lattice sites that Ψ^{L} and Ψ^{R} are the only ground states of (3.50).

Naively, one might assume the **8** VBS model to support deconfined spinons or colorons, which correspond to domain walls between the two ground states Ψ^{L} and Ψ^{R}. A closer look at the domain walls, however, shows that this is highly unlikely, as each domain wall is a bound state of either two anti-colorons or two colorons, as illustrated below.

$$\tag{3.51}$$

There is no reason to assume that the domain wall depicted above as two anti-colorons in fact corresponds to a single coloron, as it appears to be the case for the

trimer chain. There we created a domain wall corresponding to a single coloron by removing one of the rep. **3** spins from a trimer, leaving the remaining rep. **3** spins coupled antisymmetrically as in the ground state. If we were to combine the two reps. **3** into a rep. $\bar{\mathbf{3}}$ in (3.51), we would not reproduce a correlation present in the ground state, but enforce a new correlation. The correct interpretation of the domain wall between Ψ^{L} and Ψ^{R} is hence that of a bound state between two linearly confined anti-colorons. The origin of the confining potential is illustrated below.

$$
\begin{array}{cc}
\text{anti-coloron} & \text{anti-coloron} \\
\mathbf{3} & \mathbf{3}
\end{array}
$$

$$\text{(3.52)}$$
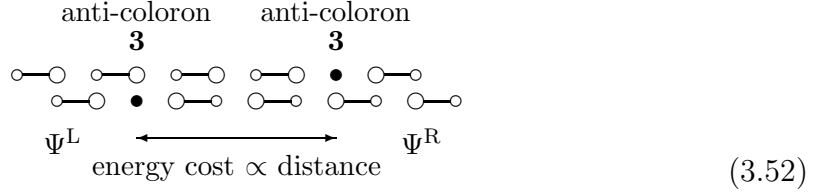
As in the **10** VBS, the confinement induces a linear oscillator potential for the relative motion of the anti-colorons. The zero-point energy of this oscillator corresponds to a Haldane-type gap in the spectrum. The ground state wave function of the oscillator is symmetric, and hence corresponds to a symmetric combination of $\mathbf{3} \otimes \mathbf{3}$, i.e., rep. **6**. The antisymmetric combination $\bar{\mathbf{3}}$ corresponds to the first excited state of the oscillator, which we expect to cost more than twice the energy of the symmetric state [60]. This statement holds for the pair of colorons in (3.51) as well.

The domain walls, however, are not the only low energy excitations. In either of the ground states, we can create coloron–anti-coloron bound states, which make no reference to the other ground state, as illustrated below.

$$
\begin{array}{cc}
\text{anti-coloron} & \text{coloron} \\
\mathbf{3} & \bar{\mathbf{3}}
\end{array}
$$

$$\text{(3.53)}$$
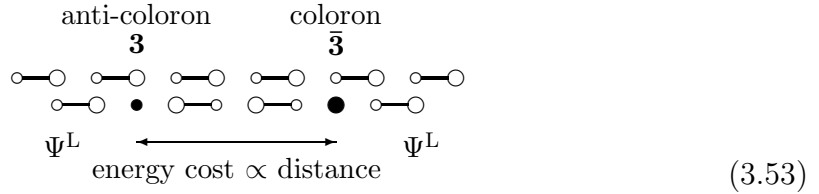
The oscillator model tells us again that the "symmetric" combination of $\mathbf{3} \otimes \bar{\mathbf{3}}$, i.e., rep. **8**, has the lowest energy, which we expect to be comparable, if not identical, to the energy required to create each of the domain walls above. The singlet **1** will have an energy comparable to that of a domain wall transforming under either $\bar{\mathbf{3}}$ or **3**. In any event, we expect the **8** VBS model to display a Haldane gap due to coloron or spinon confinement.

The excitation spectrum of (3.50) for a chain with $N = 8$ sites and PBCs is shown in Fig. 3.6. While the ground state energy is zero, the spectrum shows that the lowest excitation transforms under rep. **8**, as expected from (3.53), with a singlet and then another rep **8** following at slightly higher energies. It is tempting to interpret those three levels as the lowest levels of the coloron–anti-coloron oscillator (3.53), but then there should be another singlet at a comparable spacing above. The fact that the spacings between these excitations are significantly smaller than the energy of the first exited state, however, would be consistent with such an interpretation, as the spinons in VBS models always have a local energy cost associated with their
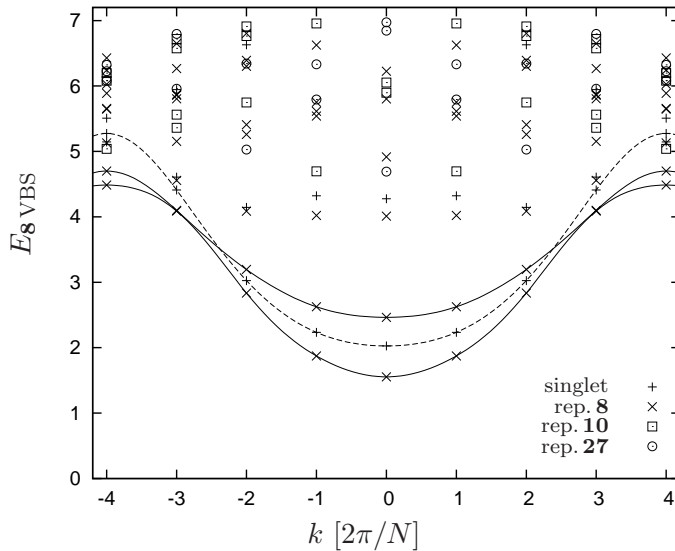
Figure 3.6: Spectrum of the **8** VBS Hamiltonian (3.50) for $N = 8$ sites obtained by exact diagonalization. (The lines are merely guides to the eye.) The "magnon" excitation transforming under rep. **8** of SU(3) has the lowest energy, followed by a singlet excitation, as expected from the discussion in the text. The well defined modes at low energies provide strong evidence of coloron–anti-coloron bound states as compared to deconfined domain walls, and hence support our conclusion that the **8** VBS exhibits a Haldane gap due to spinon confinement.

creation, which is specific to these models and not related to the universal Haldane gap stemming from confinement forces.

Most importantly, the spectrum provides strong evidence in favor of our assumption that the domain walls are not elementary excitations, but bound states of either two colorons or two anti-colorons, and hence that the lowest energy excitations of finite chains are coloron–anti-coloron bound states as illustrated in (3.53). The assumption is crucial for our conclusion that the model exhibits a Haldane gap. If the low energy sector of the model was determined by two deconfined domain walls, we would see a continuum of states in the spectrum, similar to the spectrum seen in spin $S = \frac{1}{2}$ chains of SU(2), see Fig. 3.1. The well defined low-energy modes in Fig. 3.6, however, look much more like the spinon–spinon bound state excitations seen in $S = 1$ chains or two-leg $S = \frac{1}{2}$ Heisenberg ladders. In particular, if we assume that the individual domain walls transform under reps. **6** and $\bar{\mathbf{6}}$, we expect excitations transforming under the representations contained in $\mathbf{6} \otimes \bar{\mathbf{6}} = \mathbf{1} \oplus \mathbf{8} \oplus \mathbf{27}$ to be approximately degenerate. Fig. 3.6 shows clearly that such a multiplet is not present a the lowest energies.

In the following sections, we generalize three of the models proposed for SU(3) spin chains, the trimer model, the symmetric representation **10** VBS, and the matrix product state **8** VBS to the case of SU(n) spin chains.

3.3.6 SU(4) tetramer chain and SU(n) generalization

After generalization of the MG model to SU(3), we ask for the SU(4) case. To build an SU(4) singlet, one has to antisymmetrize four SU(4) spins which transform according to the fundamental representation **4**. The four–fold degenerate *tetramer* states are in analogy to (3.18) given by

$$
\left| \psi_{\text{tetramer}}^{(\mu)} \right\rangle \;=\;
\begin{cases}
| \; \circ\!\!-\!\!\circ\!\!-\!\!\circ\!\!-\!\!\circ \;\; \circ\!\!-\!\!\circ\!\!-\!\!\circ\!\!-\!\!\circ \;\; \rangle \;\equiv\; \Psi^{(1)} \,|\,0\,\rangle, \\[4pt]
| \; \circ \;\; \circ\!\!-\!\!\circ\!\!-\!\!\circ\!\!-\!\!\circ \;\; \circ\!\!-\!\!\circ\!\!-\!\!\circ \;\; \rangle \;\equiv\; \Psi^{(2)} \,|\,0\,\rangle, \\[4pt]
| \; \circ\!\!-\!\!\circ \;\; \circ\!\!-\!\!\circ\!\!-\!\!\circ\!\!-\!\!\circ \;\; \circ\!\!-\!\!\circ \;\; \rangle \;\equiv\; \Psi^{(3)} \,|\,0\,\rangle, \\[4pt]
| \; \circ\!\!-\!\!\circ\!\!-\!\!\circ \;\; \circ\!\!-\!\!\circ\!\!-\!\!\circ\!\!-\!\!\circ \;\; \circ \;\; \rangle \;\equiv\; \Psi^{(4)} \,|\,0\,\rangle.
\end{cases}
\tag{3.54}
$$

The $\Psi^{(\mu)}$ are given by SU(4) Schwinger bosons and are the generalization of (3.34). Note that this formulation allows us directly to write down all SU(4) VBS states for totally symmetric representations.

$$
\Psi^{(i)} \Psi^{(j)} \,|\,0\,\rangle \qquad (i \neq j)
\tag{3.55}
$$

for $i, j \in \{1, 2, 3, 4\}$ are the six SU(4) representation **10** VBS state.

The Hamiltonian of the SU(4) tetramer chain [121] can be written as

$$
\mathcal{H}_{\text{tetramer}} = \sum_{i=1}^{N} \left(\left(\boldsymbol{J}_i^{(5)} \right)^2 - \frac{15}{8} \right) \left(\left(\boldsymbol{J}_i^{(5)} \right)^2 - \frac{39}{8} \right)
\tag{3.56}
$$

where $\boldsymbol{J}_i$ is now the 15-component SU(4) spin operator, see also Eq. 3.58. The same line of arguments as for the trimer model yields three antisymmetrically coupled representations **4** on consecutive sites as the elementary excitation, the SU(4) spinon carrying spin representation $\overline{\mathbf{4}}$. Thus we find again a situation where the spinons are just domain walls between the ground states, as illustrated below.

The generalization from SU(3) to SU(4) was trivial and, hence, we wish to treat the general problem for SU(n).

Consider an SU(n) spin chain with N sites, where N is a multiple of n, with a spin transforming according to the fundamental representation $\boldsymbol{n}$ of SU(n) at each lattice site,

$$
\boldsymbol{n} \;=\; (1, 0, \ldots, 0) \;=\; \square \;\,\hat{=}\;\, c_\sigma^\dagger \,|\,0\,\rangle,
\tag{3.57}
$$

where σ denotes a "flavor", $\sigma \in \{\mathrm{f}_1, \ldots, \mathrm{f}_n\}$, and $c_\sigma^\dagger$ creates a fermion of flavor σ.

The SU(n) generators at site i are in analogy to (3.19) defined as

$$
J_i^a = \frac{1}{2} \sum_{\sigma, \sigma' = \mathrm{f}_1, \ldots, \mathrm{f}_n} c_{i\sigma}^\dagger V_{\sigma\sigma'}^a c_{i\sigma'}, \quad a = 1, \ldots, n^2 - 1,
\tag{3.58}
$$

where the V^a denote the n^2-1 SU(n) Gell-Mann matrices [101]. The generators are normalized through the eigenvalue the quadratic Casimir operator takes in the adjoint representation, $\boldsymbol{J}^2 = \mathcal{C}^2_{\mathrm{SU}(n)}(1, 0, \ldots, 0, 1) = n$. The SU($n$) Heisenberg term for SU(n) is defined as $\boldsymbol{J}_i \boldsymbol{J}_j = \sum_{a=1}^{n^2-1} J_i^a J_j^a$.

To determine the eigenvalues of the quadratic Casimir for general representations of SU(n), a significant amount of representation theory is required [75]. We content ourselves here by providing the formulas up to $n = 6$ in App. B.2.

In analogy to the trimer states (3.19) and the tetramer states (3.54), we construct the n-mer states of an SU(n) spin chain by combining sets of n neighboring spins into a singlet,

$$\big|\psi_{n\text{-mer}}^{(\mu)}\big\rangle = \prod_{\substack{i \\ \left(\frac{i-\mu}{n}\text{ integer}\right)}} \Bigg(\sum_{\substack{(\sigma_1,\ldots,\sigma_n)= \\ \pi(\mathrm{f}_1,\ldots,\mathrm{f}_n)}} \mathrm{sign}(\pi) \prod_{\kappa=1}^{n} c^\dagger_{i-1+\kappa,\sigma_\kappa} \Bigg) |\,0\,\rangle, \tag{3.59}$$

where $\mu = 1, \ldots, n$ labels the n degenerate ground states, and i runs over the lattice sites subject to the constraint that $\frac{i-\mu}{n}$ is integer. The sum extends over all $n!$ permutations π of the n flavors $\mathrm{f}_1, \ldots, \mathrm{f}_n$.

In order to identify a parent Hamiltonian, consider the total SU(n) spin on $n+1$ neighboring sites for the n-mer states. Following the rules of combining representations labeled by Young tableaux (see e.g., [40, 54]), it is not difficult to see that the total spin will only contain representations given by tableaux with $n+1$ boxes and two columns, i.e., tableaux of the form

with $1 \leq \nu \leq \frac{n+1}{2}$. The eigenvalues of the quadratic Casimir operator for these representations are

$$f_n(\nu) = \frac{1}{2n}\Big(n^2(2\nu - 1) - 2n(\nu - 1)^2 - 1 \Big). \tag{3.60}$$

An educated guess for a parent Hamiltonian for the n-mer chain hence appears to be

$$H_{\mathrm{trial}} = \sum_{i=1}^{N} H_i \tag{3.61}$$

with

$$H_i = \prod_{\nu=1}^{\lfloor \frac{n+1}{2} \rfloor} \left(\left(\boldsymbol{J}_i^{(n+1)}\right)^2 - f_n(\nu) \right), \tag{3.62}$$

where $\lfloor \; \rfloor$ denotes the floor function, i.e., $\lfloor x \rfloor$ is the largest integer $l \leq x$, and we use the notation introduced in (3.21).

This construction yields the MG model [105] for SU(2), the trimer model (3.22) for SU(3), and the tetramer model (3.56) for SU(4). For $n \geq 5$, however, the decomposition of the tensor product $\boldsymbol{n}^{\otimes (n+1)}$ contains irreducible representations corresponding to Young tableaux with more than two columns, whose Casimirs are equal or smaller than a number of Casimirs included in the list $f_n(\nu)$, $\nu = 1, 2, \ldots, \lfloor \frac{n+1}{2} \rfloor$. If the Casimir of such an "undesired" representation not included in the list is smaller than an odd number of Casimirs included in the list, we obtain negative eigenvalues for H_i, and it is not a priori clear any more that the Hamiltonian (3.61) is positive semi-definite. An obvious cure to this problem is to write

$$H_{n\text{-mer}} = \sum_{i=1}^{N} H_i^2, \tag{3.63}$$

with H_i as in (3.62). This does, however, not cure potential problems arising from undesired representations which share the eigenvalues of the Casimir with one of the representations from the list, as it happens to be the case for $n = 5$. The Hamiltonian (3.63) likewise annihilates these representations, giving rise to a remote possibility that the n-mer states (3.59) are not the only ground states of (3.63). The potential relevance of these problems has to be investigated for each n separately.

3.3.7   Symmetric SU(n) VBS model

As a generalization of the AKLT model for SU(2) and the **10** VBS model for SU(3) discussed above, we now consider a VBS for an SU(n) chain of spins transforming under the symmetric representation

$$(n, 0, \ldots, 0) \;\; = \;\; \underbrace{\boxed{}}_{n \text{ boxes}} \;\; \hat{=} \;\; b_{\sigma_1}^{\dagger} b_{\sigma_2}^{\dagger} \ldots b_{\sigma_n}^{\dagger} \, | \, 0 \, \rangle,$$

where each $b_{\sigma}^{\dagger}$, $\sigma \in \{ \mathrm{f}_1, \ldots, \mathrm{f}_n \}$, is an SU($n$) Schwinger boson. The VBS state is obtained by combining n n-mer states (3.59), one for each $\mu = 1, \ldots, n$, in that the total spin on each lattice site is projected onto the symmetric representation $(n, 0, \ldots, 0)$. This yields

$$\big| \psi_{(n,0,\ldots,0)\,\mathrm{VBS}} \big\rangle = \prod_i \bigg(\sum_{\substack{(\sigma_1, \ldots, \sigma_n) = \\ \pi(\mathrm{f}_1, \ldots, \mathrm{f}_n)}} \mathrm{sign}(\pi) \prod_{\kappa=1}^{n} b_{i-1+\kappa, \sigma_\kappa}^{\dagger} \bigg) | \, 0 \, \rangle. \tag{3.64}$$

Let us now construct a parent Hamiltonian for the symmetric VBS (3.64). The total SU(n) spin of two neighboring sites of a representation $(n, 0, \ldots, 0)$ spin chain in general contains all the representations corresponding to Young tableaux with $2n$ boxes and at most two rows, i.e., all tableaux of the form

$$\underbrace{\boxed{}}_{n - \nu \text{ columns}} \underbrace{}_{2\nu \text{ boxes}}$$

The eigenvalues of the quadratic Casimir operator for these representations are given by

$$g_n(\nu) \equiv \mathcal{C}^2_{\mathrm{SU}(n)}(2\nu, n-\nu, 0, \ldots, 0) = 2n^2 - 4n + \nu(\nu+1). \qquad (3.65)$$

On the other hand, the total $\mathrm{SU}(n)$ spin of two neighboring sites of the representation $(n, 0, \ldots, 0)$ VBS (3.64) has to be contained in the product

$$\qquad (3.66)$$

As we project the spin on each lattice site onto the representation $(n, 0, \ldots, 0)$, only two these representations remain:

The eigenvalues of the quadratic Casimir operator are given by $g_n(0) = 2n(n-2)$ and $g_n(1) = 2(n-1)^2$, respectively. Hence, using $\boldsymbol{J}_i^2 = n(n-1)$, we obtain the parent Hamiltonian

$$H_{\mathrm{sym.VBS}} = \sum_{i=1}^{N} \left(\boldsymbol{J}_i \boldsymbol{J}_{i+1} + \frac{1}{2n-1} \big(\boldsymbol{J}_i \boldsymbol{J}_{i+1} \big)^2 + \frac{n(n-1)}{2n-1} \right). \qquad (3.67)$$

Since $g_n(0) \geq 0$ for $n \geq 2$ and $g_n(\nu)$ is a strictly increasing function of ν, the Hamiltonian (3.67) is positive semi-definite. For $n = 2$, we recover the AKLT model (3.17); for $n = 3$, we recover the **10** VBS model (3.46). It is worth mentioning that the whole discussion concerning spinon confinement in the AKLT model and in the representation **10** VBS model applies to the *symmetric SU(n) VBS model* for arbitrary n.

3.3.8 Adjoint SU(n) VBS model

In principle, a matrix product VBS can be formulated on all $\mathrm{SU}(n)$ chains with spins transforming under the symmetric combination of any representation $\boldsymbol{m}$ and its conjugate representation $\overline{\boldsymbol{m}}$. Unless the rep. $\boldsymbol{m}$ is self-conjugate, we obtain two inequivalent states, which transform into each other under space reflection. The construction of these is analogous to the **8** VBS introduced above, and likewise best illustrated as

$$\qquad (3.68)$$

The thick lines indicate that we combine pairs of neighboring representations $\boldsymbol{m}$ and $\overline{\boldsymbol{m}}$ into singlets. On each lattice site, we project onto the symmetric combination of $\boldsymbol{m}$ and $\overline{\boldsymbol{m}}$, as indicated. By "symmetric combination" we mean that

if representations $\boldsymbol{m}$ and $\overline{\boldsymbol{m}}$ of SU(n) have Dynkin coordinates $(\mu_1, \mu_2, \ldots, \mu_{n-1})$ and $(\mu_{n-1}, \mu_{n-2}, \ldots, \mu_1)$, respectively, we combine them into the representation with Dynkin coordinates $(\mu_1+\mu_{n-1}, \mu_2-\mu_{n-2}, \ldots, \mu_{n-1}+\mu_1)$. In other words, we align the columns of both tableaux horizontally, and hence obtain a tableau with twice the width, without ever adding a single box vertically to a column of the tableaux we started with. The states (3.68) we obtain are translationally invariant and we expect the parent Hamiltonians to involve nearest-neighbor interactions only.

In this subsection, we will formulate the simplest SU(n) model of this general family. We take $\boldsymbol{m}$ to be the representation formed by antisymmetrically combining $\kappa \leq \frac{n}{2}$ fundamental representations,

$$\boldsymbol{m} \ = \ [\kappa] \ \equiv \ (0, \ldots, 0, \underset{\kappa\text{-th entry}}{1}, 0, \ldots, 0) \ = \ \left.\begin{array}{c}\\\\\end{array}\right\} \kappa \text{ boxes} ,$$

which implies that we consider a model with the representation corresponding to a Young tableaux with a column with $n - \kappa$ boxes to the left of a column with κ boxes at each lattice site:

$$[\kappa, n-\kappa] \ \equiv \ \left.\begin{array}{c}\\\\\\\end{array}\right\} \kappa \text{ rows}$$

The construction of the parent Hamiltonian is similar to the n-mer model above. The total spin on two neighboring lattice sites can only assume representations contained in $\boldsymbol{m} \otimes \overline{\boldsymbol{m}}$, i.e., representations corresponding to tableaux of the form

$$[\nu, n - \nu] \ = \ \left.\begin{array}{c}\\\\\\\end{array}\right\} \nu \text{ rows}$$

with $0 \leq \nu \leq \kappa$. The eigenvalues of the quadratic Casimir operator for these representations are

$$h_n(\nu) = \nu\,(n - \nu + 1). \tag{3.69}$$

The obvious proposal for a parent Hamiltonian is hence

$$H = \sum_{i=1}^{N} H_i, \quad H_i = \prod_{\nu=0}^{\kappa} \left(\left(\boldsymbol{J}_i^{(2)} \right)^2 - h_n(\nu) \right). \tag{3.70}$$

This Hamiltonian singles out the matrix product state (3.68) as unique ground states for $n \leq 5$, but suffers from the same shortcomings as (3.61) with (3.62) for $n \geq 6$.

Now we restrict ourself to the special case $\kappa = 1$ which yields a spin chain with adjoint representation on each site. The adjoint representation is special as it has

the same dimensionality like the Lie algebra itself. The parent Hamiltonian can now be written (by use of $\boldsymbol{J}_i^2 = n$) as

$$\mathcal{H}_{\text{adj.VBS}} = \sum_{i=1}^{N} \left(\boldsymbol{J}_i \boldsymbol{J}_{i+1} + \frac{2}{3n} \left(\boldsymbol{J}_i \boldsymbol{J}_{i+1} \right)^2 + \frac{n}{3} \right). \qquad (3.71)$$

Note that the spin 1 representation is the adjoint representation of SU(2). Consequently, the model considered here should be an alternative generalization of the $S = 1$ AKLT model. And indeed, we recover for $n = 2$ the AKLT model (3.17) and for $n = 3$ the representation **8** VBS model. As for SU(2) and SU(3), the Hamiltonian (3.71) is valid for both even and odd number of sites. We further expect the spinon excitations to be confined in pairs. Note that the ground state of the SU(n) model is two–fold degenerate (spontaneously breakdown of parity) while for SU(2) the ground state becomes unique due to the fact that the fundamental representation of SU(2) is self–conjugate[11]. We wish to stress that the whole discussion of the AKLT model and the representation **8** VBS model concerning spinon confinement applies to the *adjoint SU(n) VBS model* for arbitrary n.

3.4   The Affleck–Lieb theorem

For the generic SU(2) spin chain, Haldane [67,68] identified the O(3) nonlinear sigma model as the effective low energy field theory of SU(2) spin chains, and argued that chains with integer spin possess a gap in the excitation spectrum, while a topological term renders half-integer spin chains gapless [8, 51]. The exact models for SU(2) spin chains we reviewed above, the MG and the AKLT chain, serve as paradigms to illustrate the general principle. Unfortunately, the effective field theory description of Haldane yielding the distinction between gapless half integer spin chains with deconfined spinons and gapped integer spin chains with confined spinons cannot be directly generalized to SU(n) chains, as there is no direct equivalent of the CP^1 representation used in Haldane's analysis.

Nonetheless, there is a rigorous and rather general result for antiferromagnetic chains of SU(n) spins transforming under a representation corresponding to a Young tableau with a number of boxes not divisible by n: Affleck and Lieb [13] showed that if the ground state is non-degenerate, and the Hamiltonian contains nearest-neighbor interactions only, than the gap in the excitation spectrum vanishes as $1/N$ (where N is the number of sites) in the thermodynamic limit. This result is fully consistent with the picture suggested by the models introduced above. Like the MG model, the trimer model and the representation **6** VBS have degenerate ground states and interactions which extend beyond the nearest neighbor, which implies that the theorem is not directly applicable.

On physical grounds, however, the statement that a given model is gapless (i.e., the excitation gap vanishes in the thermodynamic limit) implies that the spinons

---

[11]All SU(2) representations are self–conjugate. As a consequence, one can always couple two SU(2) representations S into a singlet, $\boldsymbol{S} \otimes \boldsymbol{S} = \boldsymbol{0} \oplus \boldsymbol{1} \oplus \cdots \oplus \boldsymbol{2S}$.

are deconfined. The reason is simply that if there was a confinement force between them, the zero-point energy associated with the quantum mechanical oscillator of the relative motion between the spinons would inevitably yield an energy gap. The MG, the trimer and the **6** VBS model constitute pedagogically valuable paradigms of deconfined spinons. Since the excitations in these models are literally domain walls between different ground states, no long-range forces can exist between them.

As Affleck and Lieb restricted their self to nearest neighbor interactions, the common interpretation [127] that *the half–integer spin S J_1-J_2 model is a nice paradigm to demonstrate the AL theorem* is not correct in our opinion. This interpretation is as follows: For a small ratio J_2/J_1 the model is in a gapless phase (as stated by the AL theorem) and undergoes for a certain ratio $J_{2,c}/J_1$ a phase transition to a dimerized phase with two–fold degenerate ground states (due to the ground state degeneracy, the AL theorem does not state anything anymore).

Our interpretation is different: The AL theorem means that for all representations where the number of boxes λ of the Young tableau is not divisible by n the models are gapless in the thermodynamic limit[12]. Additionally, there is a small number of representations, where the HM dimerizes already for nearest neighbor interactions. An example for that is the SU(4) representation **6** HM[13]. We think that the set of representations with models which already dimerizes for nearest neighbor interactions belongs to the set of representations for which we are unable to construct VBS states. In this sense, Affleck and Lieb's paper matches perfectly with our statements.

Affleck and Lieb do not make any statement about the spin chains with representations where λ/n is an integer. From the SU(2), SU(3), and SU(n) VBS models discussed above we have learned that the models with these representations are exactly the models exhibiting spinon confinement. In the following section, we will *prove* this statement in a somewhat exotic way.

3.5 General criterion for spinon confinement

The exact models we introduced above provide information about the models of SU(n) spin chains with representations corresponding to Young tableaux with a number of boxes divisible by n, i.e., models for which the Affleck–Lieb theorem is not applicable. We have studied two SU(3) models belonging to this family in Secs. 3.3.4 and 3.3.5, the rep. **10** VBS and the rep. **8** VBS, and found that both have confined spinons or colorons and hence display a Haldane-type gap in the spectrum.

In this section, we will argue that models of antiferromagnetic chains of SU(n) spins transforming under a representation corresponding to a Young tableau consisting of a number of boxes λ divisible by n generally possess a Haldane-type gap due to spinon confinement forces.

---

[12]Whether or not the model can be driven in a dimerized phase by applying a frustrating next–nearest neighbor interaction is beyond the scope of the AL theorem.

[13]This is one of the examples where our categorization is not applicable as we cannot construct a VBS. Our DMRG calculations show that the nearest neighbor HM is in a dimerized phase. The same results were obtained by Marston and Affleck [106] within the large-n approach.

We should caution immediately that our argument is based on several assumptions, which we consider reasonable, but which we are ultimately unable to prove.

The first, and also the most crucial, is the assumption that the question of whether a given model supports free spinon excitations can be resolved through study of the corresponding VBS state. This assumption definitely holds for SU(2) spin chains, where the MG model for $S = \frac{1}{2}$ indicates that the spinons are free, while the AKLT model for $S = 1$ serves as a paradigm for spinon confinement and hence the Haldane gap. The general conclusions we derived from our studies of the SU(3) VBSs above rely on this assumption. The numerical results we reported on the rep. **8** VBS provide evidence that this assumption holds at least for this model.

Let us consider an SU(n) spin chain with spins transforming under a representation corresponding to Young tableau consisting of L columns with $\kappa_1 \leq \kappa_2 \leq \ldots \leq \kappa_L < n$ boxes each,

$$[\kappa_1, \kappa_2, \ldots, \kappa_L] \equiv \quad \kappa_3^{\kappa_2 \kappa_1} \tag{3.72}$$

$$\kappa_L$$

with a total number of boxes

$$\lambda = \sum_{l=1}^{L} \kappa_l$$

divisible by n. We denote the Dynkin coordinates of this representation by $(\mu_1, \mu_2, \ldots, \mu_{n-1})$, which implies

$$\sum_{i=1}^{n-1} \mu_i = L.$$

Note that this representation is, by definition, given by the maximally symmetric component of the tensor product of the individual columns,

$$[\kappa_1, \kappa_2, \ldots, \kappa_L] = \mathcal{S}\big([\kappa_1] \otimes [\kappa_2] \otimes \ldots \otimes [\kappa_L]\big). \tag{3.73}$$

For convenience, we denote the $\binom{n}{\kappa}$ dimensional representation $[\kappa]$ in this subsection as $\boldsymbol{\kappa}_l \equiv [\kappa_l] = \textcircled{\scriptsize l}$.

Since λ is divisible by n, it will always be possible to obtain a singlet from the complete sequence of representations $\boldsymbol{\kappa}_1, \boldsymbol{\kappa}_2, \ldots, \boldsymbol{\kappa}_L$ by combining them antisymmetrically. To be precise, when we write that we combine representations $\boldsymbol{\kappa_1}$ and $\boldsymbol{\kappa_2}$ antisymmetrically, we mean we obtain a new representation $[\kappa_1 + \kappa_2]$ by stacking the two columns with κ_1 and κ_2 boxes on top of each other if $\kappa_1 + \kappa_2 < n$, and a new representation $[\kappa_1 + \kappa_2 - n]$ if $\kappa_1 + \kappa_2 \geq n$. In equations, we write this as

$$\mathcal{A}\big([\kappa_1] \otimes [\kappa_2]\big) \equiv \begin{cases} [\kappa_1 + \kappa_2] & \text{for } \kappa_1 + \kappa_2 < n \\ [\kappa_1 + \kappa_2 - n] & \text{for } \kappa_1 + \kappa_2 \geq n \end{cases} \tag{3.74}$$

Following the notation used above, we indicate the antisymmetric combination of representations $\boldsymbol{\kappa}_l$ by a line connecting them. In particular, we depict the singlet formed by combining $\boldsymbol{\kappa}_1, \boldsymbol{\kappa}_2, \ldots, \boldsymbol{\kappa}_L$ on different lattice sites as

$$①—②—③—\cdots—Ⓛ \tag{3.75}$$

The understanding here is that we combine them in the order indicated by the line, i.e., in (3.75) we first combine $\boldsymbol{\kappa}_1$ and $\boldsymbol{\kappa}_2$, then we combine the result with $\boldsymbol{\kappa}_3$, and so on. Depending on the order of the representations $\boldsymbol{\kappa}_l$ on the line, we obtain different, but not necessarily orthogonal, singlets. We assume that it is irrelevant whether we combine the representations starting from the left or from the right of the line, as the resulting state will not depend on it.

In general, it will be possible to construct a number $\leq \lambda/n$ of singlets out of various combinations of the $\boldsymbol{\kappa}$'s, one for each block of $\boldsymbol{\kappa}$'s for which the values of κ add up to n as we combine the representation in the order described above. In this case, we will be able to construct one VBS for each singlet, and subsequently combine them at each site symmetrically to obtain the desired representation (3.72). The argument for spinon confinement we construct below will hold for each of the individual VBSs, and hence for the combined VBS as well. It is hence sufficient for our purposes to consider situations where the entire sequence $\boldsymbol{\kappa}_1, \boldsymbol{\kappa}_2, \ldots, \boldsymbol{\kappa}_L$ is needed to construct a singlet.
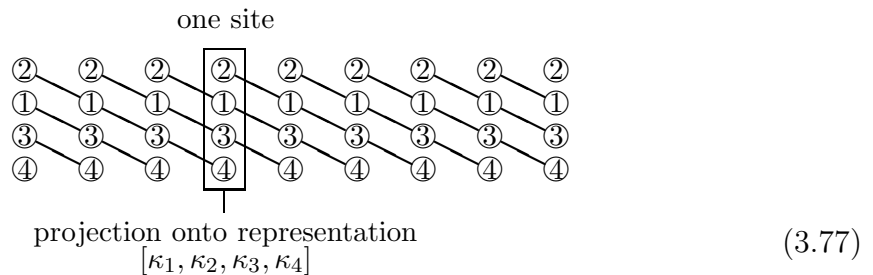
A possible VBS "ground state" for a representation corresponding to a Young tableau with $L = 4$ columns is depicted below.

one site

projection onto representation
$[\kappa_1, \kappa_2, \kappa_3, \kappa_4]$

$$\tag{3.76}$$
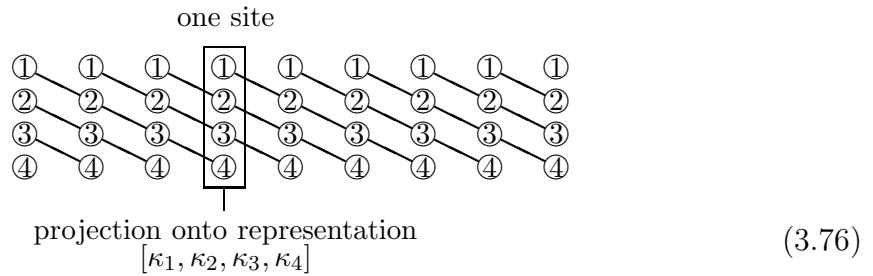
In general, there are as many inequivalent VBS "ground states" as there are inequivalent ways to order the representations $\boldsymbol{\kappa}_1, \boldsymbol{\kappa}_2, \ldots, \boldsymbol{\kappa}_L$, i.e., the number of inequivalent VBS "ground states" is given by

$$\frac{L!}{\mu_1! \cdot \mu_2! \cdot \ldots \cdot \mu_{n-1}!}.$$

To give an example, the following VBS

one site

projection onto representation
$[\kappa_1, \kappa_2, \kappa_3, \kappa_4]$

$$\tag{3.77}$$

is inequivalent to the one above if and only if $\kappa_1 \neq \kappa_2$. Note that all these VBS "ground states" states are translationally invariant. We expect some of these states, but not all of them, degenerate in energy for the appropriate parent Hamiltonian, and have accordingly written "ground states" in quotation marks. For example, if we form a SU(4) VBS with representation $[\kappa_1, \kappa_2, \kappa_3] = [1, 1, 2]$, the combination

$$①\!\!-\!\!-\!\!③\!\!-\!\!-\!\!②$$

might yield a state with a lower energy for the appropriate Hamiltonian than the state formed by combining

$$①\!\!-\!\!-\!\!②\!\!-\!\!-\!\!③·$$

Simple examples where we have only two inequivalent VBS ground states are provided by the matrix product states discussed in Secs. 3.3.5 and 3.3.8.

We will now argue that the elementary excitations of the corresponding VBS models are always confined. To this end, we first observe that any domain wall between translationally invariant "ground states" consists of a total of $m \cdot n$ representations $\boldsymbol{\kappa}_l$ (m integer). To illustrate this, consider a domain wall between the "ground states" depicted in (3.77) and (3.76):
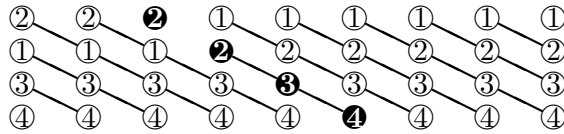
In the example, the domain wall consists of reps. $\boldsymbol{\kappa}_2$, $\boldsymbol{\kappa}_2$, $\boldsymbol{\kappa}_3$, and $\boldsymbol{\kappa}_4$. If the translationally invariant states on both sites are true ground states, the domain wall is likely to correspond to two elementary excitations: a rep. $\bar{\boldsymbol{\kappa}}_1$ spinon consisting of an antisymmetric combination of a $\boldsymbol{\kappa}_2$, a $\boldsymbol{\kappa}_3$, and a $\boldsymbol{\kappa}_4$, as indicated by the line in the drawing, and another rep. $\boldsymbol{\kappa}_2$ spinon. The reason we assume that $\boldsymbol{\kappa}_2$, $\boldsymbol{\kappa}_3$, and $\boldsymbol{\kappa}_4$ form a rep. $\bar{\boldsymbol{\kappa}}_1$ is simply that this combination is present in both ground states on either side, and hence bound to be the energetically most favorable combination. The second $\boldsymbol{\kappa}_2$, however, is not part of this elementary excitation, as combining it antisymmetrically with the others (i.e., the $\bar{\boldsymbol{\kappa}}_1$) would induce correlations which are not present in the ground state. We hence conclude that the second $\boldsymbol{\kappa}_2$ is an elementary excitation as well. The domain wall depicted above consists of a spinon transforming under rep. $\bar{\boldsymbol{\kappa}}_1$ and an anti-spinon transforming under rep. $\boldsymbol{\kappa}_2$.

The next step in our argument is to notice that the spinon and the complementary particle created simultaneously which may either be its anti-particle or some other spinon, are confined through a linear potential. To see this, we pull them apart and

look at the state in between:

$$\text{(3.78)}$$
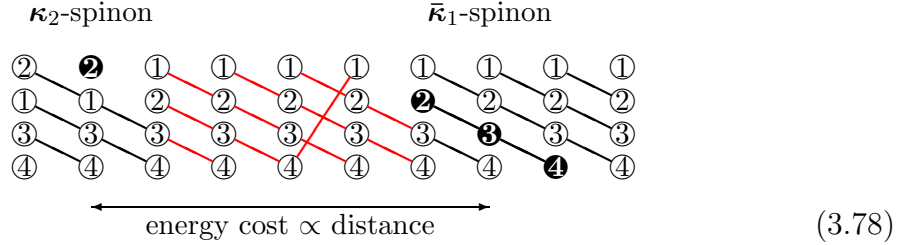
The state between spinon and anti-spinon is not translationally invariant. In the example, the unit cell of this state is depicted in red and consists of two regular bonds with three "singlet lines" between the sites, one stronger bond with four lines (which cross in the cartoon), and one weaker bond with only two lines. If we assume that the two states (3.77) and (3.76) on both sides are true ground states, it is clear that the irregularities in the strength of the bond correlations will cause the state between the spinon and anti-spinon to have a higher energy than either of them. This additional energy cost will induce a linear confinement potential between the spinons, and hence a linear oscillator potential for the relative motion of the particles. As in the models studied above, the Haldane gap corresponds to the zero-point energy of this oscillator.

If one of the "ground states" to the left or to the right of the domain wall is not a true ground state, but a translationally invariant state corresponding to a higher energy than the ground state, there will be a confining force between this domain wall and another domain wall which transforms the intermediate "ground state" with a higher energy back into a true ground state. This force will be sufficient to account for a Haldane gap, regardless of the strength or existence of a confinement force between the constituent particles of each domain wall.

The lowest-lying excitations of a representation $[\kappa_1, \kappa_2, \ldots, \kappa_L]$ spin chain, however, will in general not be domain walls, but spinons created by breaking up one of the singlets (3.75) in a ground state. This is illustrated below for the ground state (3.76):
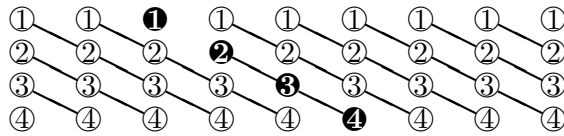
In the example, we have created a spinon transforming under rep. $\bar{\kappa}_1$ and its anti-particle, a spinon transforming under rep. κ_1. This is, however, irrelevant to the argument—we may break the singlet in any way we like. The important feature is that we obtain, by construction, at least two excitations, and that these are confined. In our specific example, the confining potential is equivalent to the confining potential

in (3.78) above:
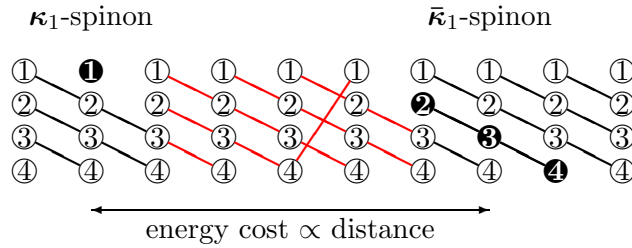
We leave it to the reader to convince him- or herself that the conclusions regarding confinement drawn from the simple examples studied here hold in general.

3.6 One step closer: Spinon confinement through next nearest neighbor interactions

Let us briefly summarize the results obtained. The $SU(n)$ models we have studied so far fall into two categories. The models belonging to the first—the trimer chain, the **6** VBS, and the n-mer chain—have n degenerate ground states, which break translational invariance up to translations by n lattice spacings. The Young tableaux describing the representations of $SU(n)$ at each site consist of a number of boxes λ which is smaller than n, and hence obviously not divisible by n. The models support deconfined spinon excitations, and hence do not possess a Haldane gap in the spectrum. The Hamiltonians of these models require interactions between $n+1$ neighboring sites along the chain. Even though the Affleck–Lieb theorem is not directly applicable to the models we constructed above, it is applicable to $SU(n)$ spin chains with spins transforming under the same representations. Like the VBS models, the theorem suggests that there is no Haldane gap in this family of models.

The models belonging to the second category—the **10** VBS, the **8** VBS, the symmetric $SU(n)$ VBS, and the adjoint $SU(n)$ VBS—have translationally invariant ground states. The ground states are unique for some models, like the **10** and the $(n, 0, \ldots, 0)$ VBS, and degenerate for others, like the **8** VBS. The Young tableaux describing the representations of $SU(n)$ at each site consist of a number of boxes λ which is divisible by n. The Affleck–Lieb theorem is not applicable to models of this category. The spinon excitations for this category of models are subject to confinement forces, which give rise to a Haldane gap. The parent Hamiltonians for these models require interactions between nearest-neighbor sites only.

At first glance, this classification might appear complete. Further possibilities arise, however, in $SU(n)$ spin chains where number of boxes λ the Young tableau consists of and n have a common divisor different from n, which obviously requires that n is not a prime number. In this case, it is possible to construct VBS models in which the ground state breaks translational invariance only up to translations by n/q lattice spacings, where q denotes the largest common divisor of λ and n such that $q < n$. This implies that the ground state of the appropriate, translationally invariant

Hamiltonian will be n/q-fold degenerate. In the examples we will elaborate on below, the parent Hamiltonians for these models require interactions between $\frac{n}{q} + 1$ sites, a feature we conjecture to hold in general. The spinon excitations of these models are confined, even though the Affleck–Lieb theorem states that the nearest-neighbor Heisenberg chain of $\mathrm{SU}(n)$ spins transforming under these representations is gapless. We will point out in Sec. 3.8.1 that this transition from a phase with deconfined to confined spinons by applying a next nearest neighbor interaction represents a new type of topological phase transition.

(We implicitly assume here that the ground states of the $\mathrm{SU}(n)$ nearest-neighbor Heisenberg chains are non-degenerate.) Let us illustrate the general features of this third category of models with a few simple examples.

(1) Consider an SU(4) chain with spins transforming under the 10-dimensional representation

$$(2,0,0) \; = \; \square\square \; .$$

Following the construction principle of the **6** VBS of SU(3), we find that the two degenerate VBS states $\Psi^{(1)}\Psi^{(3)}\,|\,0\,\rangle$ and $\Psi^{(2)}\Psi^{(4)}\,|\,0\,\rangle$ illustrated through

<div align="center">one site</div>

<div align="center">projection onto rep. $(2,0,0)$ (3.79)</div>

and the identical cartoon shifted by one lattice spacing to the right or the left, respectively, are exact zero-energy ground states of

$$H_{(2,0,0)\,\mathrm{VBS}} = \sum_{i=1}^{N} \left(\left(\boldsymbol{J}_i^{(3)}\right)^4 - 12\left(\boldsymbol{J}_i^{(3)}\right)^2 + \frac{135}{4} \right), \qquad (3.80)$$

which contains next-nearest neighbor interactions. The notation $\Psi^{(\mu)}\Psi^{(\nu)}$ was introduced in Eq. (3.55).

The example illustrates the general rule stated above. The largest common divisor of $n = 4$ and $\lambda = 2$ is $q = 2$. This implies $n/q = 2$ and hence two degenerate VBS states which break translational invariance up to translations by $n/q = 2$ lattice spacings. The parent Hamiltonian requires interaction between $1 + n/q = 3$ neighboring sites.

According to the Affleck–Lieb theorem, models of antiferromagnetic SU(4) chains of representation $(2,0,0)$ with nearest-neighbor Heisenberg interactions and non-degenerate ground states are gapless in the thermodynamic limit, which implies that the spinons are deconfined. In all the models we have studied in previous sections, the conclusions drawn from the Affleck–Lieb theorem were consistent with those drawn from our exact models. For the present model, however, they are not consistent.

Specifically, we strongly conjecture that the spinons in the $(2,0,0)$ VBS are confined. This conjecture is based on the reasonable assumption that the elementary excitations of the model transform as either the fundamental representation $\mathbf{4} = (1,0,0)$ of SU(4) or its conjugate representation $\bar{\mathbf{4}} = (0,0,1)$. This assumption implies that a

single domain wall in one of the 4-mer chains used to construct the VBS state (3.79) shifts this chain by one lattice spacing. If we assume a ground state to the left of the spinon, the state on to the right will have a higher energy for the next-nearest neighbor Hamiltonian (3.80), as illustrated below.


$$\text{energy cost} \propto \text{distance} \tag{3.81}$$
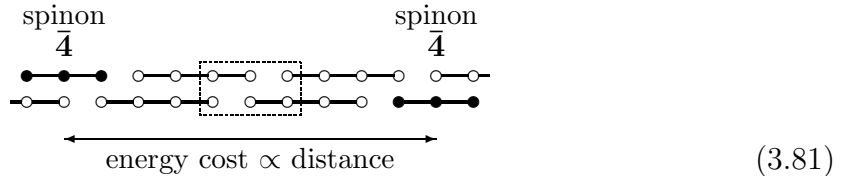
To recover the ground state, a second domain wall is required nearby, which is bound to the first by a linear potential.

Our conclusion is not in contradiction with the rigorous result of Affleck and Lieb, as they explicitly restrict themselves to models with nearest-neighbor interactions. If we had only nearest-neighbor interactions, the energy expectation value in the region between the domain walls would not be higher than in the ground state, as one can see easily from the cartoon above—the sequence of alternating links would merely shift from (strong, weak, strong, weak) to (strong, strong, weak, weak).

(2) The situation is similar for an SU(6) chain with spins transforming under the 56-dimensional representation

$$(3,0,0,0,0) \; = \; \square\square\square \; .$$

With $n = 6$ and $\lambda = 3$, we have again $\frac{n}{q} = 2$. Accordingly, we find that the two VBS states illustrated through

$$\text{projection onto rep. } (3,0,0,0,0) \tag{3.82}$$
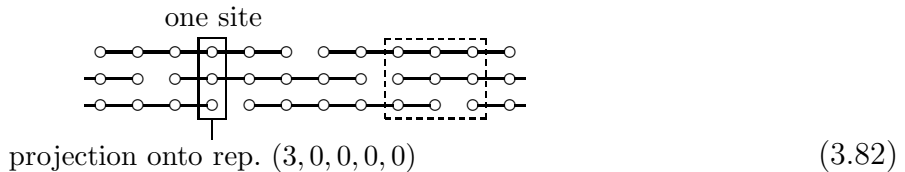
are exact ground states of a parent Hamiltonian containing up to next-nearest-neighbor interactions only, and that the spinon excitations are confined.

(3) As a third example, consider an SU(6) spin chain with spins transforming under the 21-dimensional representation

$$(2,0,0,0,0) \; = \; \square\square \; .$$

This implies $\frac{n}{q} = 3$. We find that the three VBS states illustrated by

$$\text{projection onto rep. } (2,0,0,0,0) \tag{3.83}$$
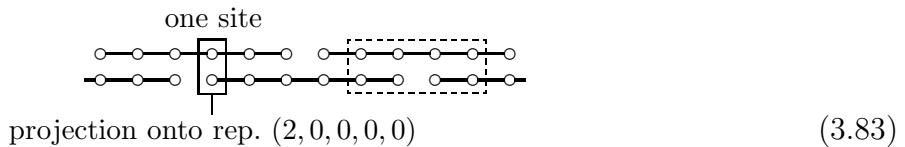
are exact ground states of a parent Hamiltonian involving the quadratic Casimir of total spin of four neighboring sites,

$$H_{(2,0,0,0,0)\,\text{VBS}} = \sum_{i=1}^{N} H_i \tag{3.84}$$

with

$$H_i = \left(\left(\boldsymbol{J}_i^{(4)}\right)^2 - \frac{32}{3}\right)\left(\left(\boldsymbol{J}_i^{(4)}\right)^2 - \frac{44}{3}\right)\left(\left(\boldsymbol{J}_i^{(4)}\right)^2 - \frac{50}{3}\right). \tag{3.85}$$

These VBS states break translational symmetry only up to translations by three lattice spacings. The spinons of this model are again confined through a linear potential, as illustrated below.

$$\text{energy cost} \propto \text{distance} \tag{3.86}$$

The conclusions we have drawn for this VBS model rest on the assumption that the quadratic Casimirs of the representations contained in the tensor product shown in the dashed box in (3.83) as well as in the tensor product one obtains if one shifts this box by one lattice spacing to the left or to the right are smaller than the largest Casimir contained in the tensor product shown in the dotted box in (3.86). We have verified the validity of this assumption for the (2,0,0,0,0) VBS model we considered here, but not shown it to hold for similar models with larger n or λ.

(4) Finally, consider an SU(6) spin chain with spins transforming under the 70-dimensional representation

$$(1, 1, 0, 0, 0) \;=\; \square\!\square \quad .$$

Thus we have once again $\frac{n}{q} = 2$. In a notation similar to the one introduced for the **8** VBS,

$$\square \;\hat{=}\; \circ, \quad \square\!\square \;\hat{=}\; \circ,$$

the two degenerate VBSs are illustrated by

$$\text{projection onto rep. } (1, 1, 0, 0, 0) \tag{3.87}$$

are exact ground states of a parent Hamiltonian involving the quadratic Casimir of the total spin of three neighboring sites,
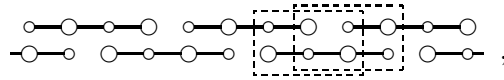
$$H_{(1,1,0,0,0)\,\text{VBS}} = \sum_{i=1}^{N} H_i \tag{3.88}$$

with

$$H_i = \left(\left(\boldsymbol{J}_i^{(3)}\right)^2 - 20\right)\left(\left(\boldsymbol{J}_i^{(3)}\right)^2 - 70\right)\left(\left(\boldsymbol{J}_i^{(3)}\right)^2 - 540\right). \tag{3.89}$$

The states (3.87) are not the only VBSs one can form. Other possibilities like

or

however, contain additional representations for the total SU(6) spin of three neighboring sites, and are hence expected to possess higher energies.

Spinon excitations transforming under the 6-dimensional rep. $(0, 0, 0, 0, 1)$ are linearly confined to spinons transforming under the 15-dimensional rep. $(0, 0, 0, 1, 0)$:

$$\tag{3.90}$$

The VBS configuration we have drawn between the two spinons in (3.90) constitutes just one of several possibilities. We expect, however, that this possibility corresponds to the lowest energy among them for the Hamiltonian (3.88). This concludes our list of examples.

The models introduced in this subsection are interesting in that they provide us with examples where spinon confinement, and with the confinement the existence of a Haldane gap, is caused by interactions extending beyond nearest neighbors. The conclusion drawn from the Affleck–Lieb theorem for SU(n) models with spins transforming under representations we have labeled here as the "third category" hence appear to hold for models with nearest-neighbor interactions only, to which the theorem is applicable. For these models, the theorem states that the spectrum is gapless, which according to our understanding implies that the models support deconfined spinon excitations. The examples we have studied, by contrast, suggest that models with longer-ranged interactions belonging to this category exhibit confinement forces between the spinon excitations and hence possess a Haldane gap.

It is worth noting that even though in the examples we elaborated here $\lambda < n$, we expect our conclusions to hold for models with $\lambda > n$ as well. To see this, let $m > 0$ be an integer such that $nm < \lambda < n(m + 1)$. We can now construct a first VBS with spinon confinement using nm boxes of the Young tableau and combine it with a second by projection on each side with a second VBS constructed from the remaining $\lambda' = \lambda - nm$ boxes. Since the spinons of the first VBS are always confined and hence gapped, the final VBS will support deconfined spinons if and only if the second VBS will support them, which in turn will depend on the largest common divisor q' of λ' and n as well as the range of the interaction. Since the largest common divisor q of n and λ is equal to q', there is no need to think in terms of λ' and q'. The conclusions regarding confinement and the Haldane gap will not depend on the distinction between λ and λ'.

3.7　Generalized Haldane scenario

In 1983 Haldane argued that there is a fundamental difference between integer and half–integer spin chains. Certain quantum antiferromagnets with integral spin –

including the isotropic Heisenberg chain – should have the following properties:

1. a unique ground state

2. a gap between the ground state and the first excited state

3. exponentially decaying static spin–spin correlations

This was called 'Haldane scenario' [87] and is in contrast to the behavior of the isotropic HM with half–integral spin which is expected to have no gap and algebraic decay of correlations. Our categorization is done by means of Young tableaux rather than the spin quantum number(s). The connection between spin S representations and Young tableaux is very easy: The Young tableaux of the SU(2) representations consist of only one row, and the number of columns (i.e., the number of boxes) is equal to $2S$:

$$\text{SU}(2): \quad \underset{S = 1/2}{\square} \qquad \underset{S = 1}{\square\square} \qquad \underset{S = 3/2}{\square\square\square} \qquad \underset{S = 2}{\square\square\square\square}$$

In the following section, we will categorize spin chains with arbitrary SU(n) spin representations. This categorization includes the SU(2) representations and, hence, Haldane's original conjecture. In Sec. 3.7.2, we formulate the *generalized Haldane scenario* for SU(n) spin chains.

3.7.1 Categorization of all SU(n) representations

In this section, we used the rules emerging from the numerous examples we studied to argue that models of SU(n) spin chains in general fall into three categories. The classification depends on the number of boxes λ of the Young tableau corresponding to the representation of the individual spins consists off, as follows:

1. If λ and n have no common divisor, the models will support free spin excitations and hence not exhibit a Haldane gap.

   The general reasoning here is simply that the VBS states in this category break translational invariance up to translations by n lattice spacings, and that there are (at least) n degenerate VBS ground states to each model. Spinons transforming under representations of Young tableaux with an arbitrary number of boxes can be accommodated in domain walls between these different ground states. Consequently, the spinons are deconfined.

2. If λ is divisible by n, the general argument we have constructed in Sec. 3.5 indicates that the model will exhibit spinon confinement and hence a Haldane gap.

3. If λ and n have a common divisor different from n, the examples studied in Sec. 3.6 suggest that the question of whether the spinons are confined or not depends on the details of the interactions. If q is the largest common divisor of λ and n, interactions ranging to the $\frac{n}{q}$-th neighbor were required for

spinon confinement in the models we studied. The Affleck-Lieb theorem [13], on the other hand, tells us that $SU(n)$ chains with nearest-neighbor Heisenberg interactions belonging to this category are gapless if the ground states are non-degenerate.

Note that the second category is really just the special case $q = n$ of the third: with $\frac{n}{q} = 1$, nearest-neighbor interactions are already sufficient for spinon confinement and a Haldane gap. The third category reduces for nearest neighbor interactions to the first one. Note that our categorization reduces for nearest neighbor interactions and $n = 2$ to Haldane's original conjecture.

The only restriction of our categorization is the that we allow representations only if one is able to construct a VBS state. The $SU(3)$ representation **8** VBS state, the adjoint VBS state, and the $SU(6)$ representation **70** VBS model are examples for models with representations where the corresponding Young tableau consists of more than one row. In principle, we are able to construct a VBS state for almost every representation, with only a few exceptions: totally antisymmetric and/or self–conjugate representations as e.g., the $SU(4)$ representation **6**, see also the footnote in Sec. 3.5.

3.7.2   The Haldane scenario for $SU(n)$ spin chains

In Sec. 3.7 we have listed the properties of $SU(2)$ models which exhibit a Haldane gap and support confined spinons: a unique ground state, a gap between ground state and excitation spectrum, and exponentially decaying correlations.

These conditions are fulfilled by the nearest neighbor Heisenberg models (HM) for integer S and the AKLT models. The generalization of VBS states to $SU(n)$ seems to violate this list of conditions. The $SU(3)$ representation **8** VBS state is two–fold degenerate, even though this model exhibits spinon confinement. We can fix this problem as follows: In the above list, the requirement of a unique ground state can be replaced by a translational invariant ground state. This holds for the representation **8** VBS state[14]. The next problem occurs with the third category of models, e.g., the $SU(4)$ representation **10** VBS state: this state was proposed to exhibit spinon confinement, but it breaks translational invariance (while translational symmetry by two lattice spacings is conserved). That means that also translational invariance might not be necessary for the *generalized* Haldane scenario. Only the gap in the excitation spectrum and exponentially decaying correlations are requirements for a Haldane–type gap. As long as we are considering VBS states, only the exponentially decaying correlations are significant for the decision whether or not a model has a Haldane–type gap because every VBS model is gapped by construction. This leads to the next problem: in a VBS state where the spinons are deconfined the correlations decay not exponentially but abruptly, i.e., faster than exponentially. In numerical studies on finite chains it might be difficult to distinguish between exponentially

---

[14]The degeneracy is due to spontaneous breaking of parity. For $SU(2)$ quantum spin chains, the requirements of translation symmetry of the ground state and uniqueness of the ground state are equivalent for isotropic spin interactions.

and abruptly decaying correlations. In the following section we describe a method to overcome this problem successfully. Therefore, we are able to formulate a generalized Haldane scenario. Certain quantum antiferromagnets which belong to the second or third category of Sec. 3.7.1 should have the following properties:

- a gap between the ground state(s) and the first excited state

- exponentially decaying static spin–spin correlations (even if translational symmetry is broken)

We conclude that $SU(n)$ spin chains with deconfined spinons have correlations with a power–law (Heisenberg models) or no correlations after a distance of more than n lattice sites (VBS models).

3.8   Exact results

In this section, we introduce the matrix product state representation of valence bond solids. When a state is written as a matrix product, one can calculate expectation values as well as correlation functions via the transfer matrix method. This method was used by Klümper *et al.* to evaluate ground state properties of the q–deformed $SU(2)$ model [85, 86]. In particular, they investigated the AKLT model and obtained the correlation length of spin–spin correlations. We will briefly review the evaluation of the correlation function of the AKLT state. After that, we apply the transfer matrix method to some of the introduced $SU(3)$ [65] and $SU(4)$ models.

SU(2) spin 1 AKLT model

The AKLT state

$$|\psi_{\mathrm{AKLT}}\rangle = \prod_i \left(a_i^\dagger b_{i+1}^\dagger - b_i^\dagger a_{i+1}^\dagger \right) |0\rangle \tag{3.91}$$

can also be written as a matrix product [85–87]. We first rewrite the valence bonds on sites i and $i+1$ as follows

$$a_i^\dagger b_{i+1}^\dagger - b_i^\dagger a_{i+1}^\dagger = \left(a_i^\dagger, b_i^\dagger \right) \begin{pmatrix} b_{i+1}^\dagger \\ -a_{i+1}^\dagger \end{pmatrix}. \tag{3.92}$$

and then use the outer product to combine the two vectors at each site into a matrix

$$
\begin{aligned}
M_i &\equiv \begin{pmatrix} b_i^\dagger \\ -a_i^\dagger \end{pmatrix} \left(a_i^\dagger, b_i^\dagger \right) |0\rangle_i \\
&= \begin{pmatrix} |1,0\rangle_i & \sqrt{2}\,|1,-1\rangle_i \\ -\sqrt{2}\,|1,1\rangle_i & -|1,0\rangle_i \end{pmatrix}.
\end{aligned} \tag{3.93}
$$

Assuming PBCs, (3.91) may then be written as the trace of the matrix product

$$|\psi_{\mathrm{AKLT}}\rangle = \mathrm{tr}\left(\prod_i M_i \right). \tag{3.94}$$

Now one has to introduce the transfer matrix R on every site which is defined as

$$R = R_{\alpha\beta} = R_{(\sigma\tau),(\sigma'\tau')} = \tilde{M}_{\sigma\sigma'} M_{\tau\tau'} \tag{3.95}$$

where $\tilde{M}$ is the complex conjugated of M without transposing the matrix. Additionally the transfer matrix for the spin operators can be introduced which allows to calculate quantities like $\langle S_i^z \rangle$ and $\langle \boldsymbol{S}_1 \boldsymbol{S}_r \rangle$. Details of the transfer matrix method are given in App. B.1. We will just give here the result for the AKLT model. The static spin–spin correlation function in the thermodynamic limit is given by [20]

$$\frac{\langle \psi_{\mathrm{AKLT}} | S_0^a S_j^b | \psi_{\mathrm{AKLT}} \rangle}{\langle \psi_{\mathrm{AKLT}} | \psi_{\mathrm{AKLT}} \rangle} = \delta_{ab} \frac{4}{3} (-1)^j \left(\frac{1}{3} \right)^j \sim e^{-j/\xi} \tag{3.96}$$

for $a, b = x, y, z$. The correlation length is $\xi = 1/\ln 3 \approx 0.91$. In principle, static spin–spin correlations can be evaluated within this method whenever a matrix product description is at hand. Let us emphasize that the obtained result is exact.

The main challenge is, hence, the formulation of the VBS states as matrix product states. In the following section, this is done for the representation **8** VBS state.

SU(3) representation 8 VBS model

In order to write down the states defined in (3.48) explicitly, it is convenient to formulate the corresponding state vectors as a matrix product. Taking (b,r,g) and (y,c,m) as bases for the reps. **3** and $\bar{\mathbf{3}}$, respectively, the singlet bonds in Ψ^{L} above can be written

$$\left(|\mathrm{b}\rangle_i |\mathrm{y}\rangle_{i+1} + |\mathrm{r}\rangle_i |\mathrm{c}\rangle_{i+1} + |\mathrm{g}\rangle_i |\mathrm{m}\rangle_{i+1} \right) = \left(|\mathrm{b}\rangle_i , |\mathrm{r}\rangle_i , |\mathrm{g}\rangle_i \right) \begin{pmatrix} |\mathrm{y}\rangle_{i+1} \\ |\mathrm{c}\rangle_{i+1} \\ |\mathrm{m}\rangle_{i+1} \end{pmatrix}.$$

We are hence led to consider matrices composed of the outer product of these vectors on each lattice site,

$$M_i^{\mathbf{1}\oplus\mathbf{8}} = \begin{pmatrix} |\mathrm{y}\rangle_i \\ |\mathrm{c}\rangle_i \\ |\mathrm{m}\rangle_i \end{pmatrix} \left(|\mathrm{b}\rangle_i , |\mathrm{r}\rangle_i , |\mathrm{g}\rangle_i \right).$$

In the case of the AKLT model reviewed above, the Schwinger bosons take care of the projection automatically, and we can simply assemble these matrices into a product state. For the **8** VBS, however, we need to enforce the projection explicitly. This is most elegantly accomplished using the Gell-Mann matrices, yielding the projected matrix

$$M_i = \frac{1}{2} \sum_{a=1}^{8} \lambda^a \operatorname{tr}\left(\lambda^a M_i^{\mathbf{1}\oplus\mathbf{8}} \right). \tag{3.97}$$

Here we have simply used the fact that the eight Gell-Mann matrices, supplemented by the unitary matrix, constitute a complete basis for the space of all complex 3×3

matrices. By omitting the unit matrix in the expansion (3.97), we effectively project out the singlet state. Written out explicitly, we obtain

$$M_i =$$

$$\begin{pmatrix} \frac{2}{3}|\mathrm{by}\rangle_i - \frac{1}{3}|\mathrm{rc}\rangle_i - \frac{1}{3}|\mathrm{gm}\rangle_i & |\mathrm{ry}\rangle_i & |\mathrm{gy}\rangle_i \\ |\mathrm{bc}\rangle_i & -\frac{1}{3}|\mathrm{by}\rangle_i + \frac{2}{3}|\mathrm{rc}\rangle_i - \frac{1}{3}|\mathrm{gm}\rangle_i & |\mathrm{gc}\rangle_i \\ |\mathrm{bm}\rangle_i & |\mathrm{rm}\rangle_i & -\frac{1}{3}|\mathrm{by}\rangle_i - \frac{1}{3}|\mathrm{rc}\rangle_i + \frac{2}{3}|\mathrm{gm}\rangle_i \end{pmatrix}.$$

$$(3.98)$$

Assuming PBCs, the **8** VBS state Ψ^{L} (illustrated in (3.48) on the left) is hence given by the trace of the matrix product

$$\left|\psi^{\mathrm{L}}_{\mathbf{8}\,\mathrm{VBS}}\right\rangle = \mathrm{tr}\left(\prod_i M_i\right). \qquad (3.99)$$

To obtain the state Ψ^{R} (illustrated on the right in (3.48)) we simply have to transpose the matrices in the product,

$$\left|\psi^{\mathrm{R}}_{\mathbf{8}\,\mathrm{VBS}}\right\rangle = \mathrm{tr}\left(\prod_i M_i^{\mathrm{T}}\right). \qquad (3.100)$$

Once we have obtained the matrix M_i we are able to calculate the transfer matrix of the representation **8** VBS state. Using the definition (3.95) we obtain the transfer matrix as well as the transfer matrix of the spin operators (for details see App. B.1). We find for the state (3.99) the static correlation function in the thermodynamic limit as

$$\frac{\left\langle \psi^{\mathrm{L}}_{\mathbf{8}\,\mathrm{VBS}}\right| J_1^a\, J_j^b \left|\psi^{\mathrm{L}}_{\mathbf{8}\,\mathrm{VBS}}\right\rangle}{\left\langle \psi^{\mathrm{L}}_{\mathbf{8}\,\mathrm{VBS}}\right| \psi^{\mathrm{L}}_{\mathbf{8}\,\mathrm{VBS}}\right\rangle} = \delta_{ab}\, F(j) = \delta_{ab}\frac{27}{16}\,(-1)^j\, 8^{-j} \propto e^{-j/\xi} \qquad (3.101)$$

where $\xi = 1/\ln 8 \approx 0.48$. The same result is obtained for the state (3.100). In the same way, one can show that for the adjoint SU(n) VBS model (3.71) the static spin–spin correlation function is in the thermodynamic limit $N \to \infty$

$$F^{\mathrm{SU}(n)}(j) = \delta_{ab}\frac{n^3}{2(n^2-1)}(-1)^{-j}(n^2-1)^{-j},$$

which simplifies for $n = 3$ to (3.101) and for $n = 2$ to the well–known result (3.96) of the AKLT chain. We note that the correlation length $\xi = 1/\ln(n^2-1)$ vanishes for the large–n limit $n \to \infty$.

In the following, we will show exemplarily how to obtain a matrix product state for VBSs which break translation symmetry. For this purpose, we revisit the construction of the representation **6** VBS (3.37) as matrix product state. It is the main idea thereby to reformulate the spin chain on *effective* sites such that the effective valence bonds connect only adjacent sites. One obtains, hence, a matrix product representation of the given state on an effective lattice which allows us to calculate correlation functions.
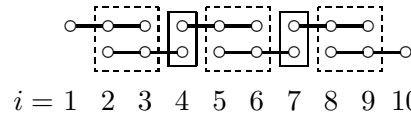
SU(3) representation 6 VBS model

We start with the representation **6** VBS state (3.37) which is depicted as a cartoon as follows,

one site
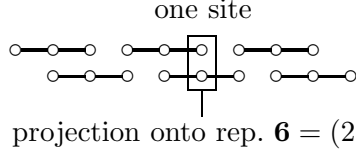
projection onto rep. **6** = (2, 0)   (3.102)

We now regroup the sites such that each pair of sites connected by two "singlet lines" becomes a single site in the new chain:

$i = 1 \quad 2 \quad 3 \quad 4 \quad 5 \quad 6 \quad 7 \quad 8 \quad 9 \quad 10$ (3.103)

Within each dashed box, we have representations

$$\bar{\mathbf{3}} \otimes \bar{\mathbf{3}} \; = \; \mathbf{3} \oplus \bar{\mathbf{6}}$$

form the two singlet lines coming in from the left and from the right. At the same time, as we have representations **6** on the original sites of the original SU(3) spin chain, we can only have representations

$$\mathbf{6} \otimes \mathbf{6} \; = \; \bar{\mathbf{6}} \oplus \mathbf{15} \oplus \mathbf{15'}.$$

Together, this implies that in each dashed box, we combine two representations $\bar{\mathbf{3}}$ symmetrically such that we obtain the representation $\bar{\mathbf{6}}$. In the re-grouped setting, we may hence picture the states as
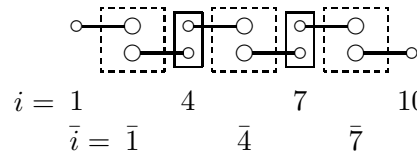
$$i = 1 \qquad 4 \qquad 7 \qquad 10$$
$$\bar{i} = \bar{1} \qquad \bar{4} \qquad \bar{7}$$

(3.104)

where each small circle ∘ represents a representation **3** and each large circle ○ a representation $\bar{\mathbf{3}}$.

The singlet bonds ∘——○ may hence in analogy to the bonds in the representation **8** VBS be written

$$\left(|b\rangle_i |y\rangle_{\bar{i}} + |r\rangle_i |c\rangle_{\bar{i}} + |g\rangle_i |m\rangle_{\bar{i}} \right) = \left(|b\rangle_i , |r\rangle_i , |g\rangle_i \right) \begin{pmatrix} |y\rangle_{\bar{i}} \\ |c\rangle_{\bar{i}} \\ |m\rangle_{\bar{i}} \end{pmatrix},$$

where $i = 1, 4, 7, \ldots$ for the state above, and $\bar{i}$ is the newly introduced "site" to the right of site i. The singlet bonds ○——∘ contracting the new site $\bar{i}$ with the site $i + 3$ to the right of it are given by

$$\left(|y\rangle_{\bar{i}} |b\rangle_{i+3} + |c\rangle_{\bar{i}} |r\rangle_{i+3} + |m\rangle_{\bar{i}} |g\rangle_{i+3} \right) = \left(|y\rangle_{\bar{i}} , |c\rangle_{\bar{i}} , |m\rangle_{\bar{i}} \right) \begin{pmatrix} |b\rangle_{i+3} \\ |r\rangle_{i+3} \\ |g\rangle_{i+3} \end{pmatrix}.$$

At each of the sites $i = 1, 4, 7, \ldots$, we have to combine two representations **3** symmetrically, i.e., project out the symmetric combination **6** from the matrix

$$M_i^{\bar{\mathbf{3}} \oplus \mathbf{6}} = \begin{pmatrix} |\mathrm{b}\rangle_i \\ |\mathrm{r}\rangle_i \\ |\mathrm{g}\rangle_i \end{pmatrix} \Big(|\mathrm{b}\rangle_i, |\mathrm{r}\rangle_i, |\mathrm{g}\rangle_i \Big).$$

This is most conveniently done with Schwinger bosons. We obtain

$$M_i = \begin{pmatrix} b_i^{\dagger 2} & b_i^\dagger r_i^\dagger & b_i^\dagger g_i^\dagger \\ b_i^\dagger r_i^\dagger & r_i^{\dagger 2} & r_i^\dagger g_i^\dagger \\ b_i^\dagger g_i^\dagger & r_i^\dagger g_i^\dagger & g_i^{\dagger 2} \end{pmatrix}. \tag{3.105}$$

Similarly, if we introduce a second set of Schwinger bosons for the complementary colors yellow, cyan, and magenta,

$$|\mathrm{y}\rangle = y^\dagger \,|\,0\,\rangle, \qquad |\mathrm{c}\rangle = c^\dagger \,|\,0\,\rangle, \qquad |\mathrm{m}\rangle = m^\dagger \,|\,0\,\rangle, \tag{3.106}$$

at each newly introduced site $\bar{i}$, we may write the matrices at these sites as

$$\overline{M}_{\bar{i}} = \begin{pmatrix} y_{\bar{i}}^{\dagger 2} & y_{\bar{i}}^\dagger c_{\bar{i}}^\dagger & y_{\bar{i}}^\dagger m_{\bar{i}}^\dagger \\ y_{\bar{i}}^\dagger c_{\bar{i}}^\dagger & c_{\bar{i}}^{\dagger 2} & c_{\bar{i}}^\dagger m_{\bar{i}}^\dagger \\ y_{\bar{i}}^\dagger m_{\bar{i}}^\dagger & c_{\bar{i}}^\dagger m_{\bar{i}}^\dagger & m_{\bar{i}}^{\dagger 2} \end{pmatrix}. \tag{3.107}$$

Assuming periodic boundary conditions (PBCs), the three representation **6** VBS states labeled by $\mu = 1, 2, 3$ may be written as matrix product states,

$$\left| \psi_{\mathbf{6}\,\mathrm{VBS}}^{(\mu)} \right\rangle = \mathrm{tr} \left[\prod_{\substack{i \\ \left(\frac{i-\mu}{3} \, \mathrm{integer} \right)}} M_i \overline{M}_{\bar{i}} \right]. \tag{3.108}$$

By use of the matrices M_i and $\overline{M}_i$, we are able to evaluate the static spin-spin correlation function between sites i and $i+3m$ (with m integer) and find for $N \to \infty$

$$\frac{\langle \psi_{\mathbf{6}\,\mathrm{VBS}}| \, J_0^a J_j^b \, |\psi_{\mathbf{6}\,\mathrm{VBS}}\rangle}{\langle \psi_{\mathbf{6}\,\mathrm{VBS}}|\psi_{\mathbf{6}\,\mathrm{VBS}}\rangle} = 0. \tag{3.109}$$

By building *effective* sites, it turned out that neighboring valence bonds are totally uncorrelated in the representation **6** VBS model. Thus we have found a situation as in the Majumdar–Ghosh model.

At this point, we emphasize again the meaning of the static spin–spin correlation functions. Within this framework, we are able to distinguish between abruptly decaying correlations (like in the MG model or the SU(3) representation **6** VBS model) and exponentially decaying correlations (like in the AKLT or SU(3) representation **8** VBS model).

Within this framework, we obtain no correlations at all for models which we expect to exhibit abruptly decaying correlations. For models with exponentially decaying correlations, we obtain a well–defined correlation length. We hypothesize that exponentially decaying correlations indicate spinon confinement.

SU(4) representation 10 VBS model

Now we turn to the SU(4) representation **10** VBS model which plays a key role for our generalization of Haldane's conjecture. The ground state of this model is two–fold degenerate due to spontaneous breaking of lattice translation symmetry. In our understanding, this model exhibits spinon confinement and is a paradigm for the third category of models, see Sect. 3.7.1. On the first view, this seems to be contradictory. So far, we have seen that all $SU(n)$ VBS states which breaks translational symmetry support deconfined spinons and have no exponentially decaying correlations. On the other side, all translational invariant $SU(n)$ VBS states have been proposed to exhibit spinon confinement and exponentially decaying correlations. In this sense, it is the crucial question whether or not the SU(4) representation **10** VBS state exhibits exponentially decaying correlations [122]. In order to force this issue we calculate the static spin–spin correlations explicitly.

Recall the state (3.79) as a cartoon,

one site

projection onto rep. $\mathbf{10} = (2, 0, 0)$
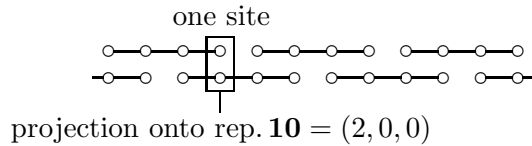
This state is two–fold degenerate as shifting by one lattice spacing to the right or the left, respectively, yields a new state. Both ground states are exact zero-energy ground states of the Hamiltonian (3.80) which involves next-nearest neighbor interactions.

We now regroup the sites such that each pair of sites connected by two "singlet lines" becomes a single site (dashed box) in the new chain:


$$i = 1 \quad 2 \quad 3 \quad 4 \quad 5 \quad 6 \quad 7 \quad 8 \quad 9 \quad 10 \quad 11 \quad 12 \tag{3.110}$$
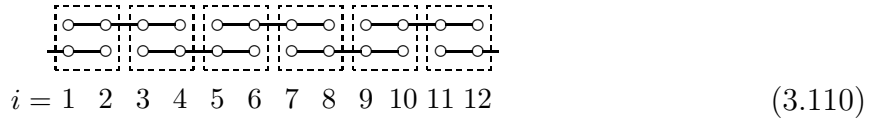
Within each dashed box, we have representations

$$\mathbf{6} \otimes \mathbf{6} \;=\; \mathbf{1} \oplus \mathbf{15} \oplus \mathbf{20}$$

form the two singlet lines coming in from the left and from the right. At the same time, as we have representations **10** on the original sites of the original SU(4) spin chain, we can only have representations

$$\mathbf{10} \otimes \mathbf{10} \;=\; \mathbf{20} \oplus \mathbf{35} \oplus \mathbf{45}.$$

Together, this implies that in each dashed box, we combine two representations **6** symmetrically such that we obtain a representation **20**. In the re-grouped setting, we may hence picture the states as

$$i = 1 \quad\quad 3 \quad\quad 5 \quad\quad 7 \quad\quad 9 \quad\quad 11$$

$$\tag{3.111}$$
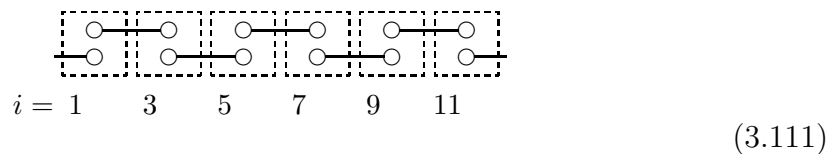
where each large circle $\circ$ represents a representation **6**.

In order to derive the matrix product representation we first rewrite the singlet $\circ\!\!\!-\!\!\!\circ$ on the bond $(i, i+2)$ as

$$b_{1,i}^\dagger b_{6,i+2}^\dagger - b_{2,i}^\dagger b_{5,i+2}^\dagger + b_{3,i}^\dagger b_{4,i+2}^\dagger + b_{4,i}^\dagger b_{3,i+2}^\dagger - b_{5,i}^\dagger b_{2,i+2}^\dagger + b_{6,i}^\dagger b_{1,i+2}^\dagger \,|\,0\,\rangle$$

$$= \left(b_{1,i}^\dagger \,,\, b_{2,i}^\dagger \,,\, b_{3,i}^\dagger \,,\, b_{4,i}^\dagger \,,\, b_{5,i}^\dagger \,,\, b_{6,i}^\dagger \right) \begin{pmatrix} b_{6,i+2}^\dagger \\ -b_{5,i+2}^\dagger \\ b_{4,i+2}^\dagger \\ b_{3,i+2}^\dagger \\ -b_{2,i+2}^\dagger \\ b_{1,i+2}^\dagger \end{pmatrix} |\,0\,\rangle \tag{3.112}$$

where we have chosen a local bosonic basis for the representation **6**. Second, at each second lattice site i we use the outer product to combine the two vectors originating from rewriting Eq. (3.112) on the bonds $(i-2, i)$ and $(i, i+2)$ into a matrix

$$M_i = \begin{pmatrix} b_{6,i}^\dagger \\ -b_{5,i}^\dagger \\ b_{4,i}^\dagger \\ b_{3,i}^\dagger \\ -b_{2,i}^\dagger \\ b_{1,i}^\dagger \end{pmatrix} \left(b_{1,i}^\dagger \,,\, b_{2,i}^\dagger \,,\, b_{3,i}^\dagger \,,\, b_{4,i}^\dagger \,,\, b_{5,i}^\dagger \,,\, b_{6,i}^\dagger \right) |\,0\,\rangle_i . \tag{3.113}$$

Assuming periodic boundary conditions the two–fold degenerate VBS state can then be written as the trace of the matrix product

$$\left| \psi_{\text{even}}^{\text{SU(4)rep.10}} \right\rangle = \text{tr}\left(\prod_{\substack{i=1 \\ i\,\text{even}}}^{N} M_i \right) \tag{3.114}$$

and

$$\left| \psi_{\text{odd}}^{\text{SU(4)rep.10}} \right\rangle = \text{tr}\left(\prod_{\substack{i=1 \\ i\,\text{odd}}}^{N} M_i \right). \tag{3.115}$$

In the following we use the state $\left| \psi_{\text{even}}^{\text{SU(4)rep.10}} \right\rangle$ only and write for convenience $|\psi_{\text{rep10}}\rangle$.

By means of the transfer matrix method we have calculated the static spin–spin correlation function with the result, that the correlations decay exponentially,

$$\frac{\langle \psi_{\text{rep10}} | J_1^a J_j^b | \psi_{\text{rep10}} \rangle}{\langle \psi_{\text{rep10}} | \psi_{\text{rep10}} \rangle} \propto \delta_{ab} \left(\frac{1}{7} \right)^j = e^{-j/\xi} \tag{3.116}$$

with the correlation length $\xi = 1/\ln 7 \approx 0.51$. For details of the calculation see App. B.1.

We have shown that the SU(4) representation **10** VBS state possesses exponentially decaying spin–spin correlations even though it breaks lattice translation symmetry. This exact result is evident for our conjecture that this state exhibits spinon confinement. In the following, we present another argument why spinon confinement is present in the SU(4) rep.**10** VBS model and, more generally, in all models belonging to the third category.

3.8.1   Effective mapping to translation invariant models

We wish to consider again the SU(4) representation **10** VBS model which we regrouped onto an effective lattice. Each effective site consists of two physical sites. The cartoon for the effective chain is similar to (3.111):

$$\alpha = \quad i \quad i+1 \quad i+2 \quad \cdots \qquad \text{projection onto rep.}\,\mathbf{20} = (0,2,0)$$

$$(3.117)$$

Each large circle $\circ$ denotes a representation **6** and we project onto each effective site α onto the symmetric representation $\mathbf{20} = \boxplus$. A parent Hamiltonian involving nearest neighbor interactions (on effective sites α) is easily given by

$$\mathcal{H}_{\text{rep.20}} = \sum_{\alpha=1}^{N/2} \left(\boldsymbol{J}_\alpha \boldsymbol{J}_{\alpha+1} + \frac{13}{54} \left(\boldsymbol{J}_\alpha \boldsymbol{J}_{\alpha+1} \right)^2 + \frac{1}{54} \left(\boldsymbol{J}_\alpha \boldsymbol{J}_{\alpha+1} \right)^3 + \frac{4}{3} \right). \qquad (3.118)$$

For several reasons, this model exhibits confined spinons:

1. the corresponding Young tableau consists of $\lambda = 4$ boxes

2. the ground state (defined on the effective lattice) is unique

3. the cartoon is AKLT-like

4. Affleck has shown [5,6] that the nearest neighbor Heisenberg model with representation **20** on each site has a unique ground state and a gap in the excitation spectrum. The VBS (3.118) is expected to be in the same phase as the HM. This is plausible as the prefactor of the biquadratic term in (3.118) is small (≈ 0.24) and the prefactor of the bicubic term is vanishing small (≈ 0.02).

Finally we can understand what the meaning of our "third category" is: in this category are all those representations which describe models which can be mapped (when considering $(1 + n/q)$–site interactions) to effective representations which belong to the second category. The fact, that the effective representations are placed on n/q neighboring (physical) sites, explains why the models of the third category can be expected to n/q–merize. The situation is, hence, totally different from that of common J_1–J_2 models (e.g., spin 1/2). This further gives a possible explanation why the phase transition occurs for such small values of $J_{2,c}$ as we will see in Sec. 3.9.9.

In common J_1–J_2 models the system is frustrated, a critical frustration has to be reached. In case of the models of the third category, the next–nearest neighbor coupling (in case of the SU(4) representation **10**) allows the system to build another effective spin representation which is energetically more favorable.

The same line of argument applies to the models (3.82), (3.83), and (3.87) of Sec. 3.6 and supports the drawn conclusion about the presence of spinon confinement.

3.9   Conjecture and its numerical confirmation

So far, we have introduced our approach how to decide which VBS states exhibit spinon confinement. We have categorized all VBS states into three categories which depend only on the given spin representation and, in case of the third category, on the range of interaction of the parent Hamiltonian. We have shown analytically that this categorization for valence bond solids is correct. Now we turn to the Heisenberg models which are the *generic* spin models and conjecture the following:

> **For any SU(n) spin representation for which we are able**
> **to construct a VBS state, the Heisenberg model falls**
> **into the same category as the VBS state.**

In case of the first category, we expect the nearest neighbor Heisenberg model to be gapless and to exhibit power–law spin–spin correlations since the spinons are deconfined. In case of the second category, we expect the nearest–neighbor Heisenberg model to have an energy gap between ground state and excitation spectrum, the correlations to decay exponentially since the spinons are confined. In case of the third category, the behavior of the Heisenberg model will depend on the range of interactions: the HM with interactions containing n/q neighboring sites will be gapless, whereas the HM with interactions containing more than n/q neighboring sites will exhibit confined spinons. As an example, we consider the SU(4) representation **10** HM. While the model with nearest–neighbor interactions is expected to be gapless, to possess a unique ground state and power–law correlations, the next–nearest neighbor Heisenberg model is expected to be gapped, should exhibit a degenerate ground state and exhibit exponentially decaying correlations. In particular, we propose that the transition from the critical phase to the Haldane phase will occur for abnormally small next–nearest neighbor coupling J_2. We notice that the next–nearest neighbor HM might break translational invariance as the corresponding VBS does. We will see below that there are clear indications, that this breaking of translational symmetry is different from the known frustration effect in J_1–J_2 models.

In order to prove this conjecture, we present numerical results for all discussed Heisenberg models with SU(3) and SU(4) spin symmetry. Before we will discuss one representation after the other, we start with a brief review of the SU(2) Heisenberg models in order to introduce the numerical method and discuss these results in the context of known models.

As numerical method, we use the density matrix renormalization group [152] (DMRG)[15] in order to investigate the Heisenberg models and figure out their properties. In particular, we are interested in the following questions:

- Is the model gapped or gapless?

- Is the ground state degenerate?

- Is the ground state translational invariant?

- How do the correlations decay?

To cover all these questions, one has to calculate at least the two lowest energies in the spectrum (in case of degeneracy more than two), to detect correlation functions, and perhaps dimer–dimer correlations. All things we mentioned are standard tools within DMRG. Computing these quantities correctly can be very expensive: for each quantity we want to look at, one has to do many calculations with varying number of kept states in order to extrapolate the converged system. This has to be repeated for different system sizes in order to extrapolate the thermodynamic limit. As already mentioned, this has to be done for every quantity we wish to look at. As we are interested in many systems with different spin representations, we had to compute innumerable DMRG–calculations. Furthermore, the higher–dimensional representations of SU(3) and SU(4) turn out to exhibit a very slow convergence behavior. The above described procedure might fail for these representations due to restrictions in computer time and computer memory.

To avoid these problems, we are looking for more modern quantities: the entanglement entropy and the bond entropy. By partitioning an extended quantum system into two blocks, the entanglement entropy is defined as the von Neumann entropy of the reduced density matrix ρ_A of one of the two blocks,

$$S_A = -\text{tr}(\rho_A \ln \rho_A) \ .$$

The success of this quantity can be understood because it is a single number able to capture the main features of the scaling behavior. In fact, in one–dimensional critical ground states, when the block A is a segment of length ℓ in an infinite system, the entanglement entropy diverges with the logarithm of the block size as [38, 149]

$$S_A = \frac{c}{3} \ln \ell + c_1' \tag{3.119}$$

where c is the central charge of the associated conformal field theory (CFT) and c_1' a non–universal constant. Away from the critical point (i.e., when the gap opens up) S_A saturates to a constant value [149] proportional to the logarithm of the correlation length [38]. It is one of the main advantages of the entanglement entropy, that we have a finite–size formula available [38]. Eq. (3.119) becomes for a chain of length L

$$S_{\ell,L} = \frac{c}{3} \ln \left[\left(\frac{L}{\pi} \right) \sin \left(\frac{\pi \ell}{L} \right) \right] + c_1 \tag{3.120}$$

---

[15]Recommendable reviews are Refs. [70, 112, 129]. For a specific discussion about critical SU(n) spin chains and the DMRG method see Ref. [52].

where c_1 is again a non–universal constant. We will see later, that (3.120) will allow us to figure out the corresponding CFT for very small systems. We further notice, that the entanglement entropy of a gapless system must have a sine–shape. In case, we find for a converged system derivations from the sine shape, this might indicate the opening of the energy gap. The breaking of lattice translational symmetry can also be detected by the entanglement entropy. In the following we use the terms entanglement entropy and *block* entropy synonymously.

The other quantity we look at is the bond entropy. This is nothing but the two–site entanglement entropy, i.e., the von Neumann entropy of the reduced density matrix where all sites are traced out except of site α and $\alpha-1$. It measures, hence, the entanglement of the sites α and $\alpha-1$ with the remainder of the whole system. This quantity is helpful in order to detect the breaking of lattice translational symmetry.

We wish to emphasize that these quantities have a huge advantage: Both quantities can be determined for finite system lengths which save pains to extrapolate the thermodynamic limit. The quantities themselves give a measure of the convergence of the calculations, i.e., sometimes it is sufficient to compute a given DMRG–calculation only once. As a third advantage we can notice that the entanglement and the bond entropy comes out quite naturally from the DMRG, as it is the underlying concept to calculate the reduced density matrix for each DMRG step.

Conformal field theory and the central charge

In the following, we wish to establish the connection between the entanglement entropy and the corresponding CFT.

The SU(n) Wess–Zumino–Witten (WZW) models have been found to capture the low energy behavior of a family of critical quantum spin chains [10]. WZW models are conformal field theories, meaning that the Lagrangians are invariant under conformal mappings. These are all combinations of translation, rotation, and dilatation in two–dimensional space-time. For field theories with conformal invariance, it suffices to specify the scaling of the fields or rather the scaling of their correlation functions to characterize the theory completely [42]. As such, once a CFT is identified, there is no immediate need to work with the associated Lagrangian. As a general structure, a WZW model consists of a non-linear sigma model term and k times a topological Wess-Zumino term, where k is a non-zero positive integer [42]. The SU(n) WZW model of level k (denoted SU(n)$_k$ WZW in the following) can be characterized by the central charge.

The central charge c is defined in the framework of the Virasoro algebra of the CFT [42]. Alternatively, c is also named conformal anomaly number. It appears in the correlation function of the energy momentum tensor $T(z)$ of the theory, where z denotes a complex space-time variable. This correlation has a singularity as $z \to 0$, with a prefactor proportional to c, $\langle T(z)T(0)\rangle \sim \frac{c/2}{z^4}$. For the SU($n$)$_k$ WZW, c is given by

$$c = \frac{k(n^2 - 1)}{k + n}.$$
(3.121)

The for our purposes relevant feature of the central charge is that c appears as a

universal scaling factor in the microscopically accessible entanglement entropy [89], see (3.119) and (3.120).

3.9.1 SU(2) spin 1/2 Heisenberg model

To begin with, we consider the spin 1/2 nearest–neighbor Heisenberg model (3.1). The output which is paradigmatic for a critical spin chain is shown in Fig. 3.7. We
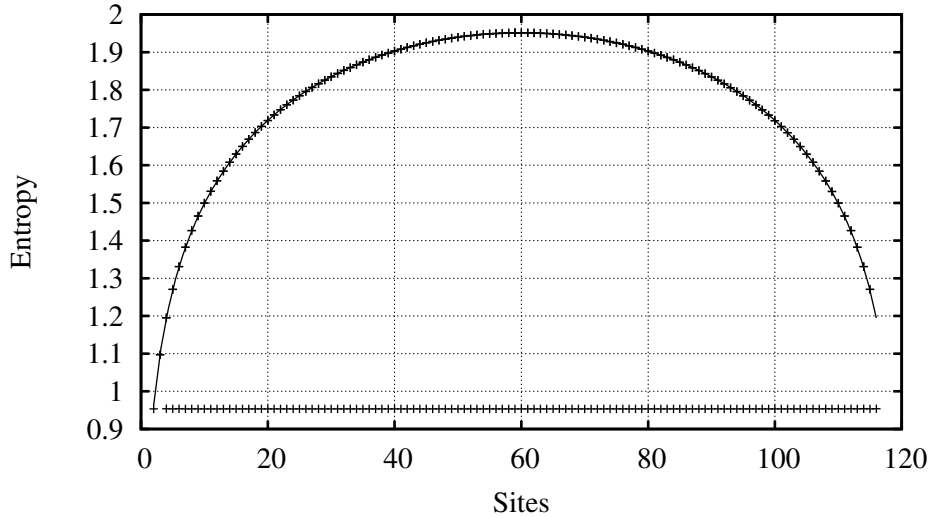

Figure 3.7: DMRG output of the spin 1/2 Heisenberg model shows a smooth bond entropy indicating a translational invariant ground state. The sine shape of the entanglement entropy clearly detects a gapless system. We have fitted the central charge $c = 1.00 \pm 0.00$.

have fitted the DMRG data (obtained for the HM with $L = 120$) with Eq. (3.120) and find in very high accuracy the central charge $c = 1.00$. Note that all errors are fitting errors. Errors due to discarding states in the reduced density matrix are considered in the quantity called *discarded entropy*. By means of Eq. (3.121) we detect the $SU(2)_1$ WZW model as corresponding CFT. This first example shows that we can successfully use entanglement and bond entropy to classify the HM: here we have found that the ground state is unique and translational invariant and the spectrum is gapless. Additionally, we have identified the corresponding CFT.

Now we add to the Hamiltonian (3.1) a next–nearest neighbor Heisenberg interaction

$$\mathcal{H}(J_2) = J_2 \sum_i \boldsymbol{S}_i \boldsymbol{S}_{i+2} \tag{3.122}$$

and investigate what happens for different values of J_2. Note that we have set the prefactor J_1 of the nearest–neighbor Heisenberg term to unity throughout the thesis unless otherwise stated explicitly.

In Fig. 3.8 we have shown the entanglement entropy for five different values of J_2 ($J_2 \equiv V_2$). For $J_2 = 0.35$ we find the sine shape which indicates criticality
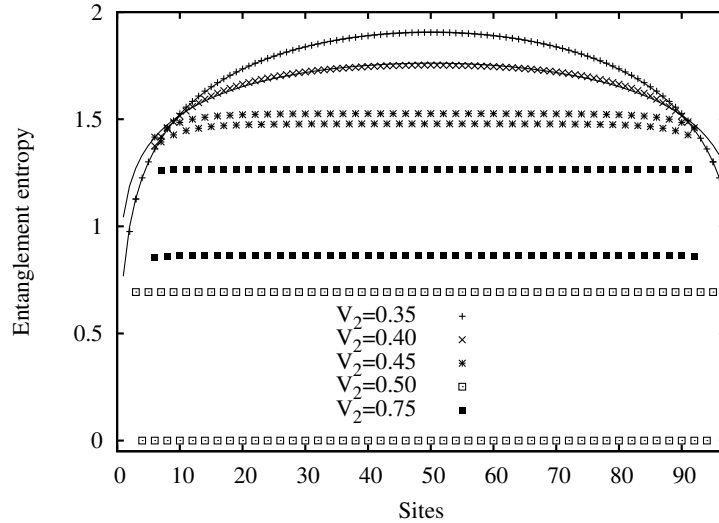
Figure 3.8: The entanglement entropy of the J_1–J_2 model for several values of J_2 is plotted. The system size of all considered models is 100 sites. The different curves are discussed in the text.

of the system. The central charge is fitted to $c = 0.98$. Due to the fact, that the central charge is underestimated by the DMRG (presumed convergence of the DMRG *calculation*) this is a hint for the careful physicist that something might have changed qualitatively in contrast to the $J_2 = 0$ case. For $J_2 = 0.4$, one sees that the fitted sine shape does not match perfectly anymore. This might indicate the opening of a gap. Moreover, the fitted value for the central charge is now $c = 0.62$. According to Eq. (3.121) a value smaller than 1 is impossible for the central charge of an $SU(n)_k$ WZW model[16]. We conclude that we have reached a gapped phase. For the value $J_2 = 0.45$ the entanglement entropy saturates after a few sites to a constant value what is typical for a gapped phase. We further see the breaking of translational invariance clearly indicated by the alternating of the entropy. This alternating has a period of two sites. We conclude that the system is still invariant under translations by two lattice sites. The gapped phase must be a dimerized phase. At the MG point $J_2 = 0.5$, the entanglement entropy oscillates between 0 and 0.7. As discussed at the very beginning of this thesis, at the MG point neighboring dimers are completely uncorrelated with its environment. This results in an entanglement entropy with value 0 on every second site. Note that the dimerization causes a degeneracy of the ground state. For $J_2 = 0.75$ the system is still in a strong dimer phase, but the dimerization is not exact anymore. One might think of that as a superposition of the MG state and a liquid state.

In Fig. 3.9 we have plotted the bond entropy for the same values of J_2 as in Fig. 3.8. In this plot, we can also see the breaking of translational invariance with increasing J_2. For $J_2 = 0.35$ and $J_2 = 0.4$ the bond entropy still indicates a unique

---

[16]In general, critical $SU(n)$ invariant quantum spin chains must correspond to an $SU(n)_k$ WZW model as effective low–energy theory. Hence, the central charge must be $c \geq 1$ according to (3.121).

ground state, for $J_2 = 0.45$, however, the ground state is degenerate. At the MG point, the bond entropy is oscillating from 0 to 1.4 and behaves qualitatively as the entanglement entropy. At $J_2 = 0.75$ the bond entropy has still a strong oscillatory behavior.
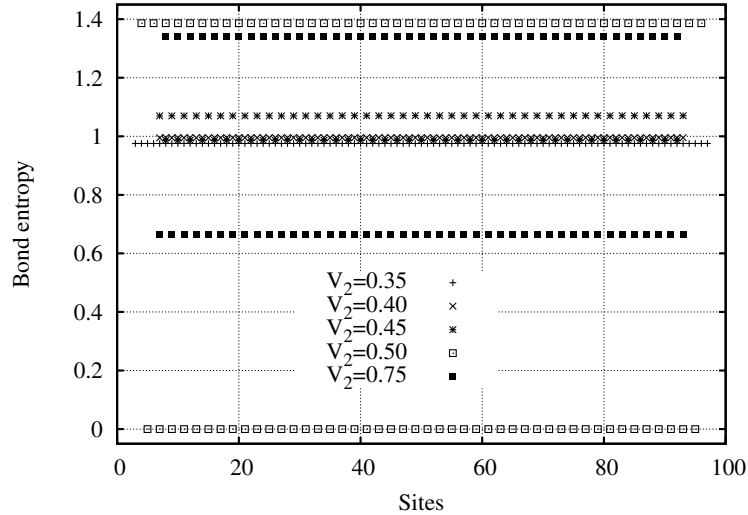

Figure 3.9: The bond entropy of the J_1–J_2 model for several values of J_2 is plotted. The system size of all considered models is 100 sites. The bond entropies are discussed in the text.

The J_1–J_2 model was very well studied within various techniques and we have, hence, a good understanding of the phase diagram. In fact, the model undergoes at $J_{2,c} = 0.2411$ a continuous phase transition to a dimerized phase, reaches the MG point where the dimerization becomes exact. At $J_{2,max} = 0.57$ the maximum dimerization is reached, i.e., that the dimer order parameter reaches its maximum value. We realize that we overestimate the critical coupling $J_{2,c}$ when we proceed as illustrated. To find phase transitions in higher accuracy, one has to compute the system for several chain lengths L with open boundary conditions rather than periodic ones and then to extrapolate $L \to \infty$. As we are only interested in the qualitative behavior of a given model this proceeding is sufficient for our purposes.

3.9.2   SU(2) spin 1 Heisenberg model

The spin 1 Heisenberg model was the first model proposed by Haldane to possess an energy gap. As mentioned above, the AKLT model which is just the HM plus an additional biquadratic Heisenberg term is the most important toy model in order to study and understand Haldane–phase antiferromagnets. As a consequence, the whole phase diagram for arbitrary values of the bilinear and biquadratic Heisenberg term was studied intensively. For convenience, we consider the most general isotropic
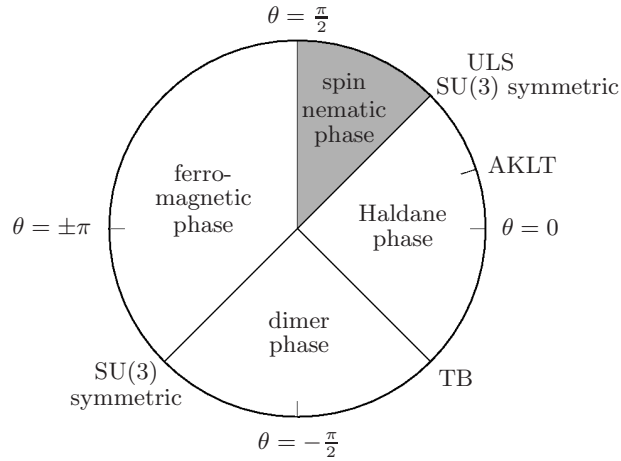
Figure 3.10: Phase diagram of Hamiltonian (3.123) as a function of θ.

spin Hamiltonian with nearest–neighbor interactions,

$$\mathcal{H}_{S=1} = \sum_i \left(\cos\theta \, \boldsymbol{S}_i\boldsymbol{S}_{i+1} + \sin\theta \, (\boldsymbol{S}_i\boldsymbol{S}_{i+1})^2 \right). \tag{3.123}$$

The phase diagram of the model (3.123) as a function of θ has been investigated by numerous authors [49, 77, 88, 95, 130, 140] and is by now well understood.

The point $\theta = 0$ on the circle shown in Fig. 3.10, the antiferromagnetic Heisenberg point, is embedded in the so–called Haldane phase ($-\pi/4 < \theta < \pi/4$) which is characterized by a unique ground state, exponentially decaying correlations, and a gap between the ground state and the excited states. The Haldane phase includes at $\theta_{\mathrm{VBS}} = \arctan(1/3)$ the valence bond solid (VBS) or AKLT model. The AKLT Hamiltonian shares the most properties of the isotropic Heisenberg Hamiltonian but, in contrast to the isotropic Heisenberg model, possesses a ground state which can be written out explicitly, see Eq. (3.16).

Above the Haldane phase in Fig. (3.10), there is a critical phase ($\pi/4 < \theta < \pi/2$) with spin nematic correlations [95]. The phase transition at $\theta_{\mathrm{ULS}} = \pi/4$ was proposed to be of Kosterlitz–Thouless type [49, 77]. At the transition point, the Hamiltonian (3.123) reduces to the Uimin–Lai–Sutherland (ULS) model [91, 142, 148] which exhibits explicit SU(3) symmetry. The ULS model is a sum of permutation operators and exactly solvable via the nested Bethe ansatz.

At $\theta = \pi/2$, the Hamiltonian (3.123) becomes ferromagnetic with gapless excitations. It reaches the ferromagnetic Heisenberg point at $\theta = \pm\pi$ and undergoes a first order phase transition to a dimerized phase at $\theta = -3\pi/4$ where (3.123) is again SU(3) symmetric and has a highly degenerate ground state [24]. Close to this point there was a long–standing discussion regarding the possible existence of a small spin nematic phase. Recently, this was ruled out by numerical and analytical arguments [66, 95]. In the dimerized phase ($-3\pi/4 < \theta < -\pi/4$), the excitations are gaped. At the Takhtajan–Babudjan point $\theta_{\mathrm{TB}} = -\pi/4$, the gap closes and the model is again exactly solvable via the nested Bethe ansatz [23, 143], has gapless

excitations, and a unique ground state. Finally, the phase transition to the Haldane phase at $\theta = -\pi/4$ is of second order [3,6].
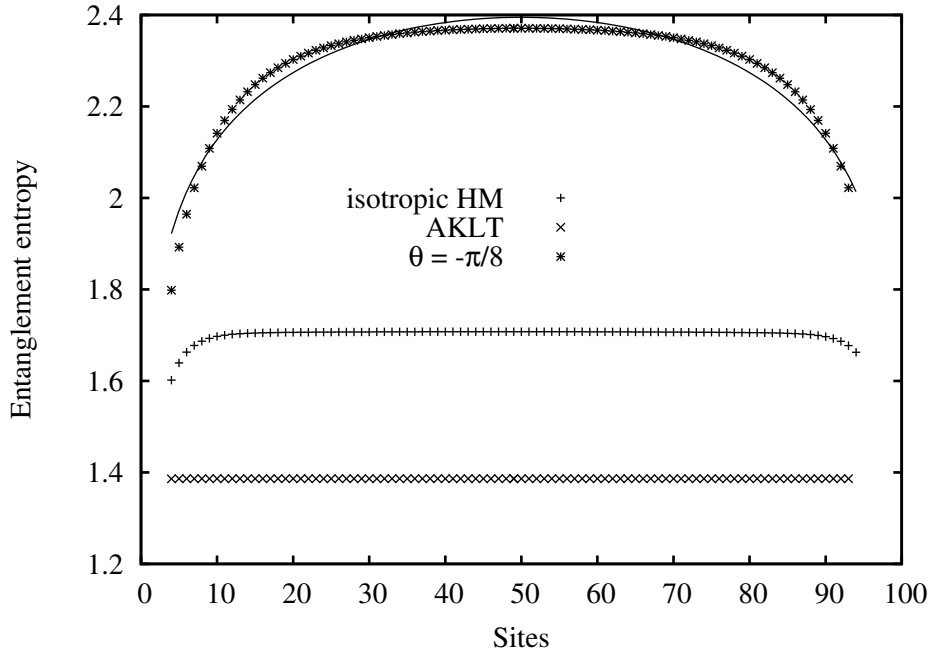

Figure 3.11: Entanglement and bond entropy of models with different values of θ. The isotropic HM ($\theta = 0$), the AKLT model ($\theta = \arctan 1/3$), and another model inside the Haldane phase ($\theta = -\pi/8$). The chain length is 100 sites.

In the following, we investigate the Haldane and the dimer phase as well as ULS and TB point. In Fig. 3.11 we have plotted the entropies for models with three different values of θ inside the Haldane phase. The first model is the isotropic HM ($\theta = 0$) which corresponds to the curve in the middle of Fig. 3.11. The entanglement entropy increases on the first ten sites and saturates then to a constant value. This is the typical behavior of the entanglement entropy of a gaped system [149]. The number of sites until reaching the saturation is related to the correlation length. The lower curve in Fig. 3.11 shows the entanglement entropy of the AKLT model. Obviously the correlation length in this model is so short that the saturation is reached after a few sites. As the entanglement entropy is computed starting at the fifth site, we see a homogenous entropy. The upper curve in Fig. 3.11 corresponds to the Hamiltonian (3.123) with $\theta = -\pi/8$. The entanglement entropy is very close to the sine shape which is shown for comparison in the figure. It is distinguishable from a critical model, but the gap in the spectrum must be small and the correlation length very large. We can conclude that it might be difficult to distinguish between spin chains with tiny gap (as the $S = 3$ Heisenberg model) and a critical model. The explanation is simple: in case the gap is smaller than the finite–level splitting, the gap cannot be detected. In such a case, one has to consider larger system lengths in order to decrease the finite level splitting. We notice that tiny energy gaps in the excitation spectrum are difficult to detect, but the problem is controllable.

At the upper boundary of the Haldane phase in Fig. 3.10, at the Uimin–Lai–Sutherland (ULS) point, the entanglement entropy shows the typical sine shape and the central charge is found to be $c = 2.00$ which clearly indicates the $SU(3)_1$ WZW being the corresponding CFT. The critical phase above the Haldane phase, i.e., the spin nematic phase, can easily be detected, while the central charge is $c = 2$ or slightly above $c = 2.00$. The critical phase was investigated by means of CFT by Itoi and Kato [77]. At the lower boundary of the Haldane phase in Fig. 3.10, at the Takhtajan–Babudjan (TB) point, the entanglement entropy shows again the typical sine shape but the central charge is found to be $c = 3/2$. According to (3.121) we identify the $SU(2)_2$ WZW model as corresponding CFT. The phase between TB point and ferromagnetic phase is known to be a dimer phase. In Fig. 3.12 we have plotted the entanglement entropy of (3.123) for $\theta = -\pi/2$. In this plot, the entanglement entropy does not fit the sine. The discrepancy is small. There might be two reasons: either the entanglement entropy "feels" the opening of a gap or the DMRG calculation is not converged. A second look to the bond entropy shows a flickering. This might indicate the spontaneous breaking of translation symmetry (i.e., the presence of a dimer phase) or a non–converged system. In our first attempt, we had kept 1500 DMRG states only and saw a similar output. We repeated, hence, this calculation with 2500 kept DMRG states resulting in a truncation error smaller
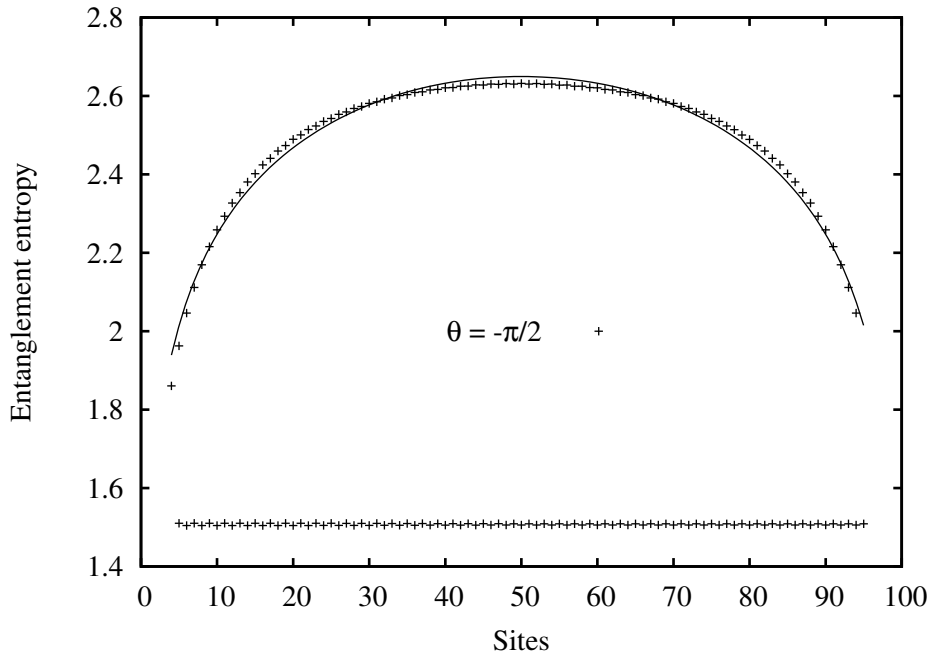

Figure 3.12: Entanglement and bond entropy of the model (3.123) in the dimer phase at $\theta = -\pi/2$. The plot does not fit the sine shape perfectly. Moreover, the bond entropy is flickering. This might indicate a spontaneous breaking of translation symmetry. The chain length is 100 sites and we have kept 2500 DMRG states. Due to the large number of kept DMRG states the truncation error is smaller than 10^{-5} indicating convergence of the system.

than 10^{-5}. The flickering in the bond entropy has remained. We conclude that our entropy quantities feel the presence of a dimerized phase.

We have seen that the entanglement entropy as the quantity we look at provides us in principle a qualitatively good understanding of the phase diagram. We have seen, however, that this way of investigating a phase diagram hides some dangers.

3.9.3   SU(2) spin 3/2 Heisenberg model

While the phase diagram of the spin 1/2 chain with next–nearest neighbor interactions and the spin 1 chain with bilinear and biquadratic Heisenberg term is very well understood we have only little knowledge about the phase–diagram of the antiferromagnetic spin 3/2 Heisenberg chain with next nearest neighbor interactions[17] As a further demonstration of the usefulness of the entropy quantities for investigating a phase diagram, we start to discover the spin 3/2 J_1–J_2 model. Again we set $J_1 = 0$ and vary J_2. We start at the isotropic Heisenberg point, $J_2 = 0$, and find a critical model with a central charge slightly above $c = 1$. As discussed in the 1980s by several authors, there are logarithmic corrections present which vanishes in the thermodynamic limit. For the finite system, these corrections cause an increased central charge. The system remains critical up to $J_2 = 0.33$ where the flickering of the bond entropy indicates the breaking of translation symmetry, see Fig. 3.13. The central charge at $J_2 = 0.33$ is fitted to $c = 0.986$. In case of convergence, this
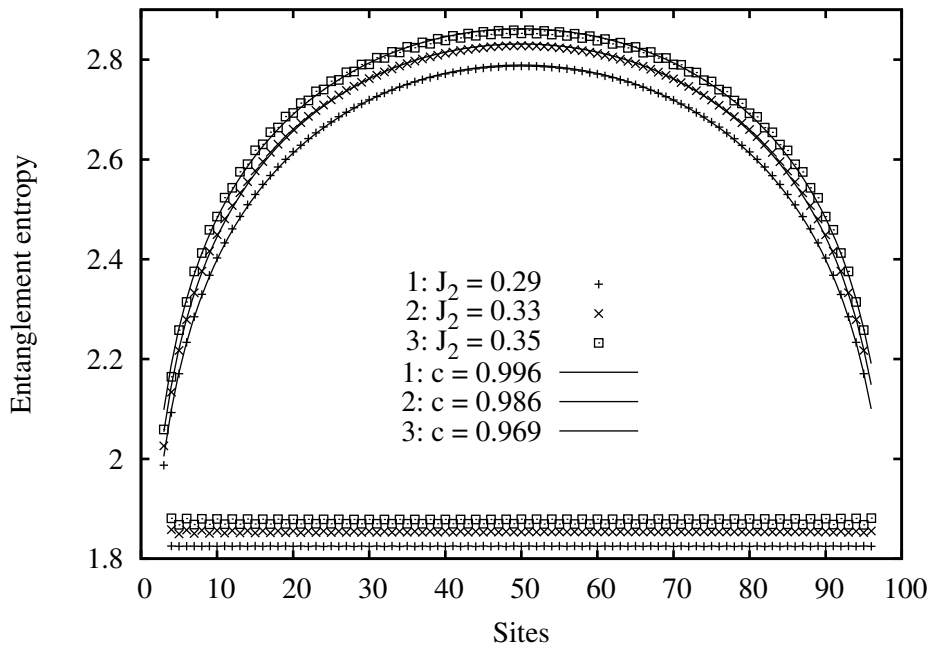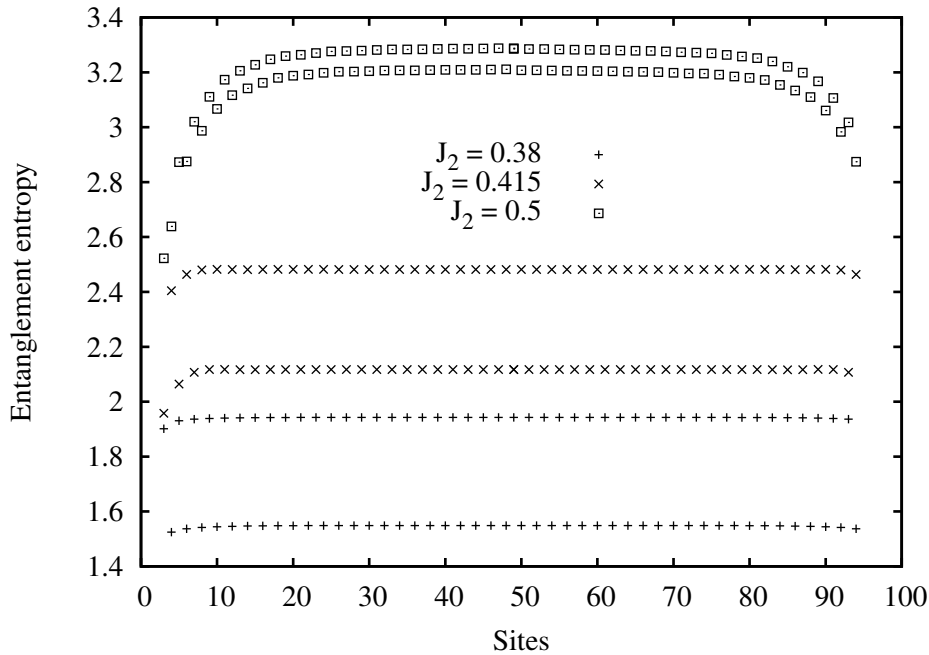

Figure 3.13: Entanglement and bond entropy of the spin 3/2 J_1–J_2 model. Data for $J_2 = 0.29$, 0.33, and 0.35 is shown.

---

[17]Note that the phase diagram of the nearest neighbor HM with bilinear, biquadratic, and bicubic interactions is unknown so far.

indicates the opening of a gap. Even though, the entanglement entropy fits the sine very well up to $J_2 = 0.35$, the value of the central charge decreased below $c = 1.0$ as well as the increasing alternation of the bond entropy shows that we have reached a dimerized phase. For $J_2 = 0.38$, we find already a strong oscillation between two values in the bond and entanglement entropy. This oscillation in the entropies, i.e., the dimerization, reaches its maximum at $J_2 = 0.415$ and decreases for larger values of J_2. For $J_2 = 0.38$, $J_2 = 0.415$, and $J_2 = 0.5$, the entanglement entropy is plotted in Fig. 3.14.

Figure 3.14: Entanglement and bond entropy of the spin $3/2$ J_1–J_2 model. Data for $J_2 = 0.38$, 0.415, and 0.5 is shown.

A further increase of J_2 causes the vanishing of the dimerization. For $J_2 = 0.6$, the entanglement entropy indicates the presence of an energy gap, the dimerization effect is, however, absent. Also the bond entropy for $J_2 = 0.6$ is homogenous and clearly indicates a translational invariant ground state. We notice that the system with 1000 kept DMRG states converges well for $0 < J_2 < 0.6$, for larger values this is not the case anymore. We find for $J_2 = 0.75$ a bond entropy which indicates that the system is not converged. We have plotted the bond and entanglement entropy of the spin $3/2$ J_1–J_2 model for $J_2 = 0.6$ and $J_2 = 0.75$ in Fig. 3.15. To ensure the validity of our results for $J_2 = 0.75$, we had to repeat the calculation with more kept DMRG states.

The "little knowledge" about the phase diagram (we have mentioned above) is due to the work by Roth and Schollwöck [127]. They investigated the phase diagram of the next nearest neighbor model within DMRG. They used a *conventional* dimer order parameter to detect the dimerization, the gap was measured by extrapolating the difference between the two lowest energies in the spectrum. Their results of
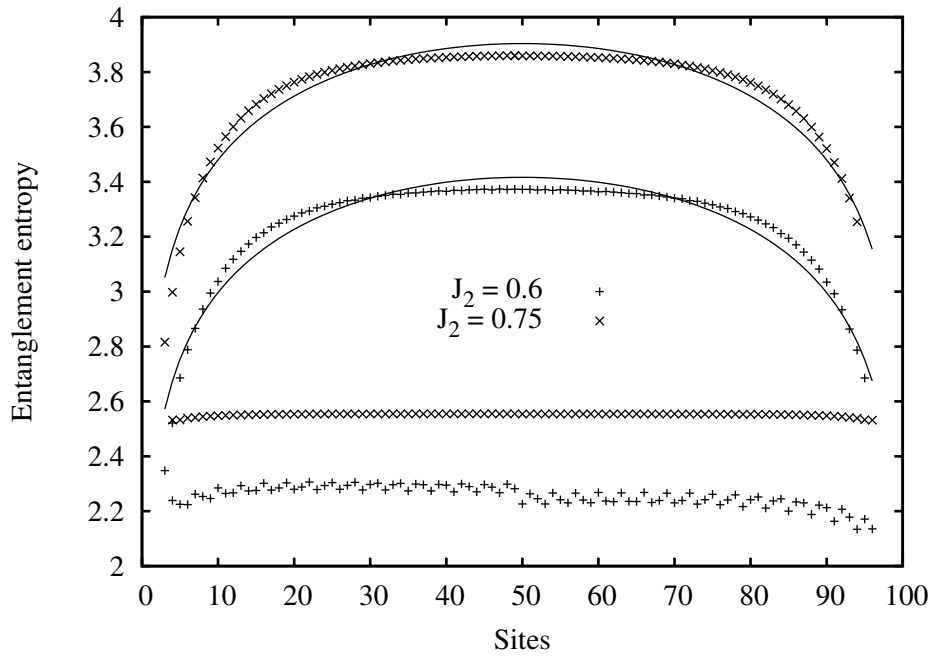
Figure 3.15: Entanglement and bond entropy of the spin 3/2 J_1–J_2 model. Data for $J_2 = 0.38$, 0.6, and 0.75 is shown.
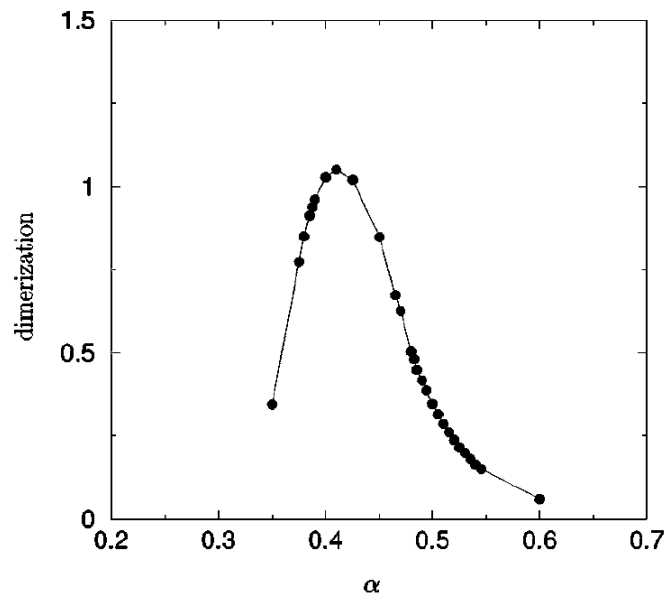

Figure 3.16: Numerical results for the dimer order parameter obtained by Roth and Schollwöck [127] within DMRG. The phase transition from the spin liquid phase to the dimer phase is found at $\alpha = J_2/J_1 = 0.33$. The dimerization reaches its maximum at $\alpha = 0.415$ and vanishes above $\alpha \approx 0.6$. The figure is taken from Ref. [127].

the dimer order parameter coincides with our findings obtained by the entanglement entropy. The plot of the dimer order parameter from Ref. [127] is shown in Fig. 3.16. At this point, we end with the demonstration of the usefulness of the entanglement and bond entropy in order to investigate phase diagrams. We wish to emphasize that this method is restricted as we can only distinguish between gapless and non–gapless phases as well as between translation invariant and non–invariant states. In the following, we start to test our conjecture for the SU(3) and SU(4) Heisenberg models.

3.9.4   SU(3) representation 3 Heisenberg model

We start our investigation of SU(n) HM with the SU(3) HM with fundamental representation. The Hamiltonian reads

$$\mathcal{H}^{\mathrm{HM}} \;=\; \sum_i \boldsymbol{S}_i \boldsymbol{S}_{i+1}$$

where the representation of the spin operator $\boldsymbol{S}_i$ corresponds to the considered Young tableau. Here, in case of the fundamental representation of SU(3), the Young tableau consists of one single box, $\lambda = 1$:

$$\square$$

This model is expected to be gapless since the spinons are deconfined as they are in the trimer model, see Sec. 3.3.2. In fact, the HM is gapless and the corresponding CFT is SU(3)$_1$ WZW. As we mentioned in the section about the spin 1 chain, at the ULS point the bilinear–biquadratic Heisenberg model exhibits SU(3) symmetry.
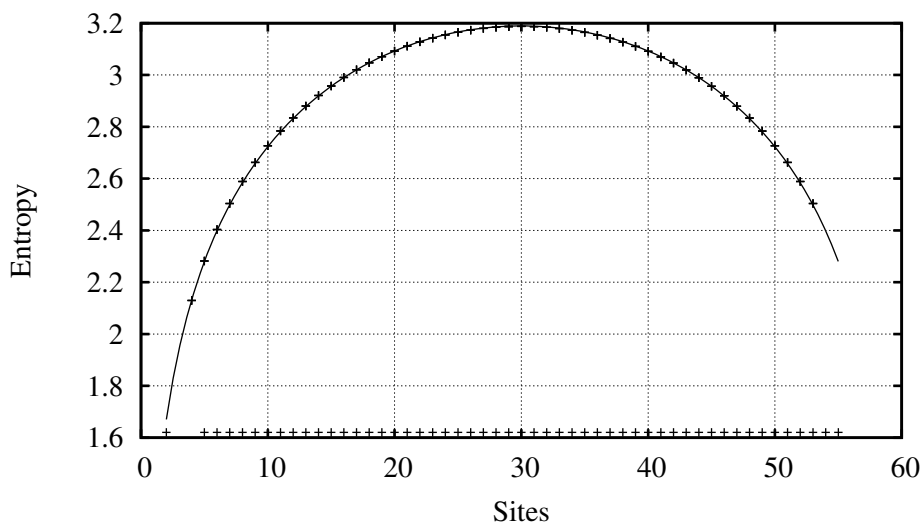

Figure 3.17: Entanglement and bond entropy of the SU(3) Heisenberg model with nearest neighbor interactions. We have fitted a central charge $c = 2.00$ which corresponds to the SU(3)$_1$ WZW model as corresponding CFT. The chain length is 60 sites.

In this sense, the ULS model can be understood as the SU(3) HM. The difference
is only in the description of both models: while the internal structure of the ULS
model is characterized by the quantum number S^z, the internal structure of the
SU(3) HM is characterized by the quantum numbers J^3 and J^8. The entanglement
entropy of the SU(3) HM is shown in Fig. 3.17. The entanglement entropy fits the
sine very well; we have fitted a central charge $c = 2.00$ with high accuracy which
identifies by use of Eq. (3.121) the $SU(3)_1$ WZW model as underlying field theory.
The bond entropy of the model is unique and indicates translation invariance. Very
recently, it was pointed out by Corboz *et al.* [39] that the SU(3) HM with next
nearest neighbor interactions undergoes a phase transition into a trimerized phase
for $J_2 > J_{2,c} = 0.45$. That means, translation symmetry is broken while translation
symmetry modulo three lattice spacings is conserved. We have tested the results of
Corboz *et al.* for $J_2 = J_1 = 1.0$. Our results are in agreement with their findings. We
find a $2 - 1 - 2 - 1$–alternation in both entanglement and bond entropy. The output
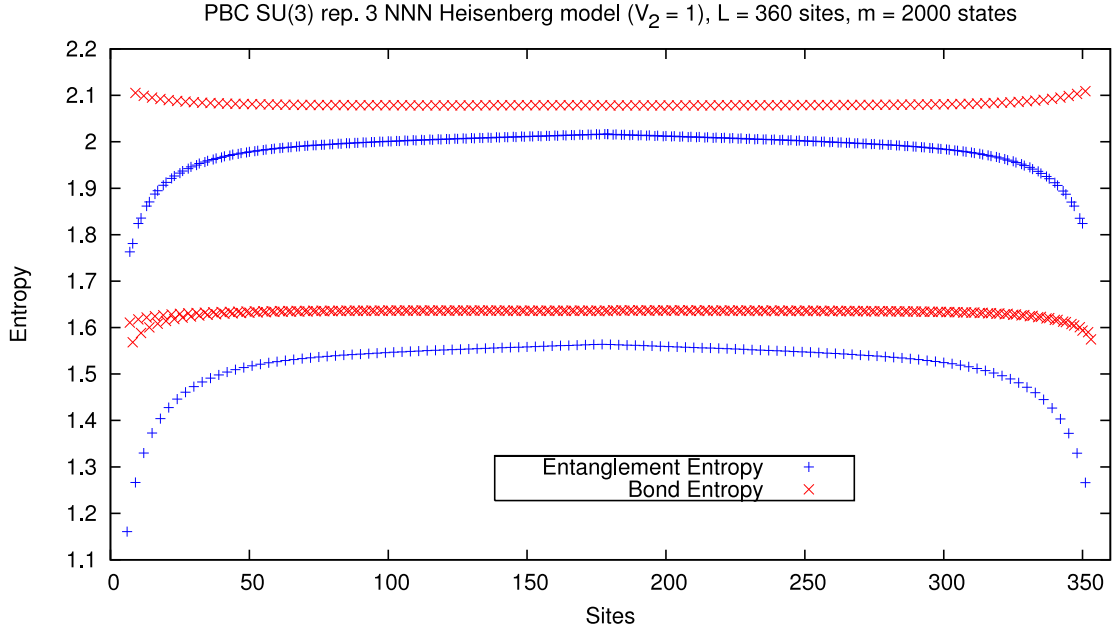of the entanglement entropy is shown in Fig. 3.18.

Figure 3.18: Entanglement and bond entropy of the SU(3) Heisenberg model with
nearest and next nearest neighbor interactions ($J_1 = J_2 = 1.0$). Both entanglement
and bond entropy show the $2 - 1 - 2 - 1$–alternation clearly indicating the broken
translation symmetry. The system remains invariant under translations by three
lattice sites. The system is in a trimerized phase. The chain length is 360 sites.

3.9.5   SU(3) representation 6 Heisenberg model

In this section we investigate the HM for the first higher dimensional representation of SU(3), the totally symmetric representation **6**. The Young tableau which corresponds to this representation consists of two boxes, $\lambda = 2$:

The study of the SU(3) representation **6** VBS model yields the result that the spinons are deconfined. We expect, hence, the corresponding HM with nearest–neighbor interactions to be gapless. The entanglement entropy of this model has the typical sine shape of a critical model and bond entropy indicates translation invariance. The fitted value of the central charge is in the interval $2 < c < 3$. Increasing the system length decreases the central charge. We can assume that the central charge reaches the value $c = 2.0$ in the thermodynamic limit. The corresponding CFT is, hence, a $SU(3)_1$ WZW model. This might imply, that we have found the analogous situation to SU(2). All gapless nearest neighbor Heisenberg models with SU(3) symmetry correspond to the Wess–Zumino–Witten σ model with topological coupling $k = 1$. The higher WZW models, i.e., with coupling $k = 2, 3, \ldots$ are realized by additional terms containing higher powers of the Heisenberg terms. These models are referred to as Andrei–Johannesson models in the literature [19,52,80] and represent the SU(n) generalizations of the Takhtajan–Babudjan series [23, 143]. The DMRG output for the SU(3) representation **6** HM is shown in Fig. 3.19.
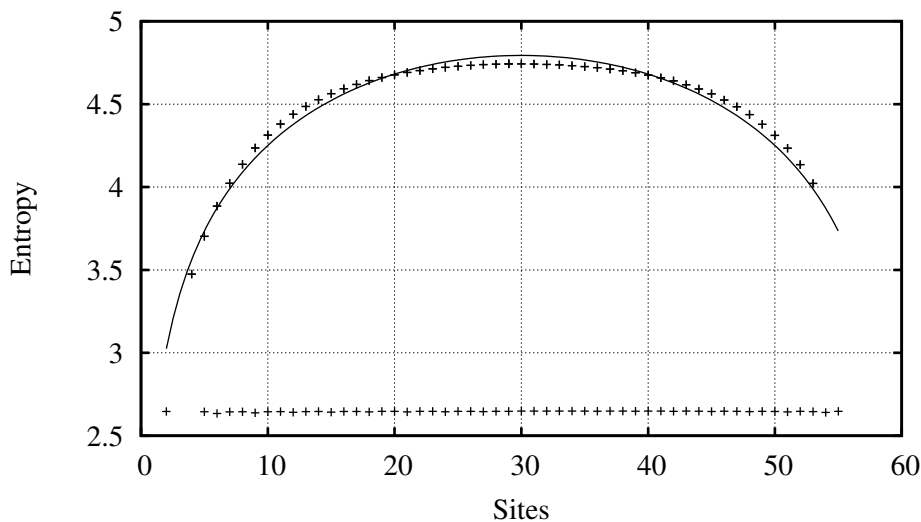

Figure 3.19: Entanglement and bond entropy of the SU(3) representation **6** HM. The sine shape indicates the critical behavior of the model. The chain length is 60 sites. Even though we have kept 5000 DMRG states, the system is not fully converged as it can be seen by the discrepancy between sine and data points.

3.9.6 SU(3) representation 10 Heisenberg model

Now we consider the SU(3) representation **10** HM. The representation **10** is totally symmetric and the corresponding Young tableau consists of three boxes, $\lambda = 3$:

$$\square\square\square$$

The HM is predicted to exhibit spinon confinement as $\lambda = 3$ and $n = 3$. Their ratio is integer. Hence, we are looking for a unique ground state separated by a gap from the excitation spectrum. For the corresponding VBS model, there is no doubt that the model is a direct generalization of the AKLT model. As the VBS model is nothing but a bilinear HM with additional biquadratic term, the situation should be clear for the nearest–neighbor HM. In Fig. 3.20, we show the entanglement entropy for the representation **10** VBS model and the HM. Both models have a unique ground state. The entanglement entropy of the VBS reaches the saturation much faster than the HM. We further note that the VBS model (3.46) converges much faster and behaves as the AKLT model. From a computational point of view the representation **10** VBS state is really a generalization of the AKLT model. The entanglement entropy of both models equals the one of the $S = 1$ HM or AKLT chain. For the ten–dimensional SU(3) representation, the conjecture is clearly fulfilled.
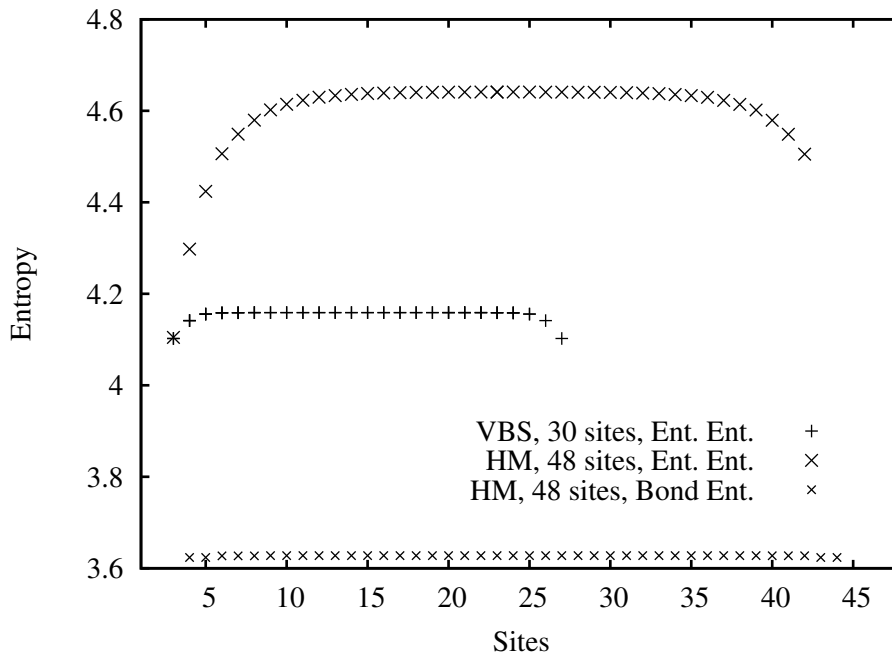

Figure 3.20: Entanglement of the SU(3) representation **10** HM and VBS model is shown. Additionally, the bond entropy of the HM is shown. The VBS was calculated on a chain with 30 sites, while the HM on a chain with 48 sites. The essence can be seen: both models saturate after a few sites. The VBS seems to exhibit a shorter correlation length. The situation is, hence, analogous to the spin 1 HM and AKLT model.

3.9.7 SU(3) representation 8 Heisenberg model

Now we consider the SU(3) representation **8** HM. Note that the eight–dimensional representation of SU(3) is the adjoint representation. As a consequence, the ground state of the representation **8** chain can be reached for both even and odd chain length. The Young tableau which corresponds to the this representation consists of three boxes, $\lambda = 3$:

Here we have a situation where we expect spinon confinement as $n = 3$, $\lambda = 3$, and their ratio is integer. For this representation, we have no DMRG calculations available. Due to the degeneracy of the point $(J^3, J^8) = (0, 0)$ in the weight diagram, we could not implement the representation **8** in the DMRG code. Instead, we present in Fig. 3.21 the gap size of chains with finite length obtained via exact diagonalization (PBCs). The fits shown in Fig. 3.21 indicate the existence of a finite energy gap for both the HM and VBS model in thermodynamic limit. For the HM, we are restricted to the four data points shown in Fig. 3.21. As the gap size is very small, more elaborate calculations have to be done in order to verify the gap size. Nonetheless, the results of Fig. 3.21 are very plausible. The VBS has as usual a "huge" energy gap, $\Delta_{\mathrm{VBS}} = 1.34 \pm 0.04$. Decreasing the biquadratic Heisenberg term $\beta(\boldsymbol{J}_i \boldsymbol{J}_{i+1})^2$ from $\beta_{\mathrm{VBS}} = 2/9 = 0.222$ to $\beta_{\mathrm{HM}} = 0$ decreases the gap size. The gap size at the isotropic Heisenberg point, $\Delta_{\mathrm{HM}} = 0.10 \pm 0.06$, seems to be realistic. The errors are fitting errors. Even though we cannot present extensive DMRG studies, the conjecture seems to be valid for the representation **8** HM.
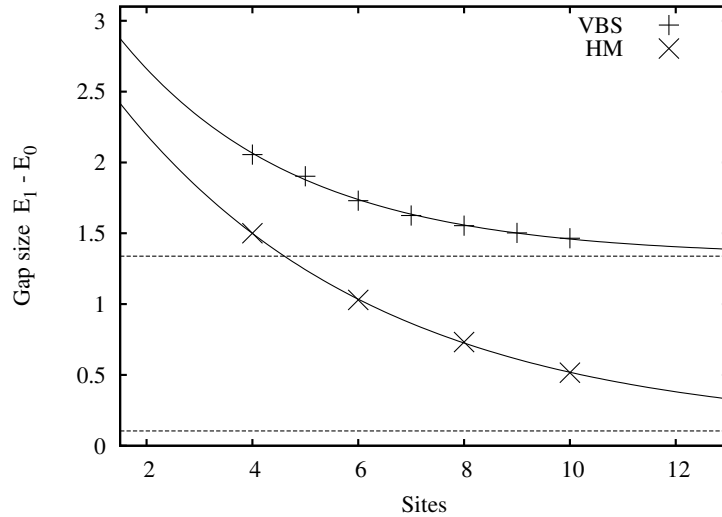

Figure 3.21: Gap sizes from the representation **8** HM and VBS model. The data points are obtained within exact diagonalization imposing periodic boundary conditions. The extrapolated gap sizes are for the VBS $\Delta_{\mathrm{VBS}} = 1.34 \pm 0.04$ and for the HM $\Delta_{\mathrm{HM}} = 0.10 \pm 0.06$.

3.9.8   SU(4) representation 4 Heisenberg model

Now we consider the SU(4) HM. The fundamental representation of SU(4) is four–dimensional. The Young tableau which corresponds to this representation consists of a single box, $\lambda = 1$:

$$\square$$

As for all fundamental representations of SU(n), the ratio $\lambda/n = 1/n$ cannot be integer and the HM must exhibit gapless excitations. The DMRG output which is presented in Fig. 3.22 shows for the entanglement entropy the sine shape of a critical model, the unique value of the bond entropy indicated a translation invariant ground state. A closer look to the entanglement entropy shows a discrepancy between the plot and the fitting curve. We have kept 8000 DMRG states for the shown calculation. Nevertheless, the system is not perfectly converged as indicated by this discrepancy in the entanglement entropy. The fitted value of the central charge $c = 2.95$ is very close to the predicted value $c = 3.0$. The DMRG output is shown in Fig. 3.22. For a more detailed discussion concerning this issue see Ref. [52]. Within a very small error we identify the SU(4)$_1$ WZW model as the underlying CFT.
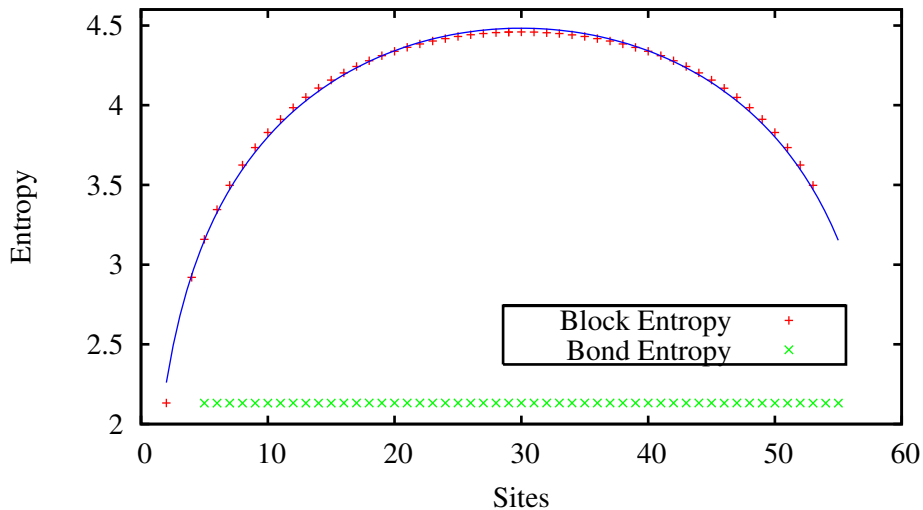

Figure 3.22: Entanglement and bond entropy of the SU(4) HM with fundamental representation. One can see that the DMRG is not yet fully converged even though we have kept 8000 DMRG states. Nevertheless, the fit of the central charge yields $c = 2.95$. This is very close to the expected value $c = 3$. The length of the system is 60 sites.

The reader may notice that the SU(n) HM with fundamental representation must be critical also from a mathematical point of view. The reason is that the Heisenberg term can be rewritten as the permutation operator as defined in Eq. (3.23). This ensures criticality [84, 142].

3.9.9   SU(4) representation 10 Heisenberg model

Finally we consider the SU(4) representation **10** Heisenberg model. The Young tableau that corresponds to this representation consists of two boxes, $\lambda = 2$:

$$\square\square$$

This representation allows us to test our conjecture concerning the third category of representations since $\lambda = 2$ and $n = 4$ have a largest common divisor $q = 2$. We expect, hence, spinon confinement through $(1 + n/q)$–site, i.e., next–nearest neighbor, interactions. The ten–dimensional representation is the highest $SU(n)$ representation which is numerically accessible[18]. Hence, this will be the only numerical test available. First we consider the nearest neighbor Heisenberg model. Due to our approach as well as due to the Affleck–Lieb theorem [13] the model is expected to be gapless and possesses a unique ground state. Although we cannot rigorously rule out the existence of a dimerization phase, it would not fit in the general understanding of $SU(n)$ representations: so far nearest neighbor Heisenberg models with totally symmetric representation possess a unique ground state. Our DMRG calculations of the nearest–neighbor model indicate criticality as it converges worse than all other models ever considered. Note that the $S = 3/2$ chain converges much slower than the $S = 1/2$ chain in case of SU(2). Moreover, the SU(3) representation **6** chain converged much slower than the representation **3** chain. We are expecting, hence, that the SU(4) representation **10** HM converges much slower than the SU(4) representation **4** HM for which 8000 kept DMRG states turned out to be not sufficient[19]. Even though we cannot reach perfect convergence, we tried to fit the central charge by best means. The result is to be handled with care (as a non–converged DMRG calculation can yield results which are completely nonsense), but the fitted central charge is above 3. For higher dimensional representations of $SU(n)$ the formula (3.121) has to be modified by inverse logarithmic corrections $\sim \mathcal{O}(\ln L^3)$ due to the appearance of marginally irrelevant operators. This effectively yields a central charge larger than the "quantized" value if one makes use of the formula (3.120). A central charge $c \gtrsim 3$, hence, indicates correspondence to the $SU(4)_1$ WZW model.

Now we come to the model which plays the key role in this thesis chapter: the SU(4) representation **10** Heisenberg model with next–nearest neighbor interactions. Following our conjecture, this model should exhibit confined spinons. Spinon confinement must yield gapped excitations. Furthermore, the possibility of a broken translation symmetry cannot be ruled out as the VBS model breaks the symmetry itself. To begin with, we investigate the model for the value $J_2 = 0.5$ as in this case

---

[18]At least, within the DMRG method we are at the limit regarding memory and computational time. The next higher–dimensional representations of SU(3) and SU(4) are both 15–dimensional which is illusive to calculate for adequate system length. To implement the fundamental representation of SU(5) is possible but we have seen that it was almost impossible to bring the fundamental representation of SU(4) to convergence. Moreover, we do not expect something *exciting* for the fundamental representation of SU(5).

[19]For a detailed discussion of convergence within DMRG, critical $SU(n)$ spin models, and boundary conditions see Ref. [52].

the next–nearest neighbor HM approximates the VBS model (3.80) best possible,

$$
\tilde{H}_{(2,0,0)\,\text{VBS}} = \sum_{i=1}^{N} \frac{1}{60} \left(\left(\boldsymbol{J}_i + \boldsymbol{J}_{i+1} + \boldsymbol{J}_{i+2} \right)^2 - \frac{9}{2} \right) \left(\left(\boldsymbol{J}_i + \boldsymbol{J}_{i+1} + \boldsymbol{J}_{i+2} \right)^2 - \frac{15}{2} \right)
$$

$$
= \sum_{i=1}^{N} \left(\boldsymbol{J}_i \boldsymbol{J}_{i+1} + \frac{1}{2} \boldsymbol{J}_i \boldsymbol{J}_{i+2} + \frac{2}{15} \left(\boldsymbol{J}_i \boldsymbol{J}_{i+1} \right)^2 + \frac{1}{15} \left(\boldsymbol{J}_i \boldsymbol{J}_{i+2} \right)^2 + \dots \right)
$$

$$
\approx \sum_{i=1}^{N} \boldsymbol{J}_i \boldsymbol{J}_{i+1} + \frac{1}{2} \boldsymbol{J}_i \boldsymbol{J}_{i+2} \, .
$$

The ellipses in the middle line represent three terms consisting of four spin operators which appear with the same prefactor as the biquadratic nearest neighbor term. In fact, the DMRG output for $J_2 = 0.5$ shows the behavior of a system where the ground state dimerizes as expected from the VBS state. The entanglement entropy is shown in Fig. 3.23.

At this point, we wish to summarize our results obtained so far. In Sec. 3.3 we have presented several models and found a criterion which allows us to decide whether or not the spinons are confined in a given model. Then we conjectured,

Figure 3.23: Entanglement and bond entropy of the SU(4) representation **10** HM with next–nearest neighbor interactions and $J_2/J_1 = 0.5$. The chain length is 100 sites. Both entropy quantities show a strong alternation between neighboring sites. The plot corresponds to what we expect for the SU(4) representation **10** VBS model which we approximated by the choice of $J_2/J_1 = 0.5$. This supports our conjecture clearly.

that the HM will fall into the same category as the corresponding VBS model. For all HM considered so far this turned out to be true. Now, in case of the SU(4) representation **10** HM, we have found the nearest neighbor model to be gapless while the next–nearest neighbor model behaves like the VBS model which was shown to exhibit spinon confinement. We conclude that the nearest–neighbor HM must exhibit confined spinons as well and, hence, our conjecture turns out to be true (at least for all representations which are numerically achievable).

3.9.10 J_1–J_2 models with and without spinon confinement

Now we want to consider J_1–J_2 models in more detail in order to give another argument that a Haldane–type gap is present in the SU(4) representation **10** J_1–J_2 model.

First we summarize our knowledge about SU(n) J_1–J_2 models. The SU(2) spin 1/2 model undergoes a second order phase transition at $J_{2,c}^{1/2} = 0.2411$ [44, 115] to a dimerized phase, the spin 3/2 model at $J_{2,c}^{3/2} = 0.33$ [127]. Recently, it was shown that the SU(3) representation **3** model undergoes the phase transition at $J_{2,c}^{\text{rep.}3} = 0.45$ [39] to a trimerized phase, for the SU(3) representation **6** model we know at least that it starts to trimerize although we do not know for which J_2 the transition occurs. More important, the SU(4) representation **4** model undergoes a phase transition into a tetramerized phase. At least for $J_2 = 1$ this was shown within a level spectroscopy of exact diagonalization data [94] and within DMRG [121]. In all the mentioned SU(n) J_1–J_2 models the frustration caused by the next–nearest neighbor coupling drives the model into an n–merized phase, see also Tab. 3.3. The exact values of the

Critical couplings of J_1–J_2 models				
	□	□□	□□□	□□□□
SU(2), dimer phase	0.2411	H	0.33	H
SU(3), trimer phase	0.45	?	H	—
SU(4), tetramer phase	> 0.6	<0.1 dimer	—	H

Table 3.3: The critical couplings $(J_2/J_1)_c$ of several J_1–J_2 models are shown. The "H" denotes the "Haldane phase", i.e., the models are gapped (and remain gapped for a next–nearest neighbor interaction, see e.g., [88]) and have a translation invariant ground state. The critical coupling of SU(3) representation **6** is so far unknown while the coupling for the SU(4) representation **4** J_1–J_2 model is a preliminary result which have to be confirmed [122]. The SU(3) model with the $\lambda = 4$ and the SU(4) model with $\lambda = 3$ are numerically not accessible.

critical couplings $J_{2,c}$ of all models listed in the table suggest for SU(4) representation **10** model that such a transition into a tetramerized phase should occur for a critical coupling which is at least $\tilde{J}_{2,c} \approx 0.5$. This suggestion is, however, wrong:

- The SU(4) representation **10** model dimerizes rather than tetramerizes.

- The phase transition into this dimerized phase occurs for an abnormally small $J_{2,c}^{\text{rep.10}} < 0.1$ as we will see below.

We wish to stress that the dimerization as well as the abnormally small critical coupling $J_{2,c}$ cannot be explained in the context of a frustration effect in J_1–J_2 models. In particular, it is worth mentioning that the dimerization in a chain with representation **10** on each site is surprising as it is impossible to couple two neighboring sites into a singlet, $\mathbf{10} \otimes \mathbf{10} = \mathbf{20}^\star \oplus \mathbf{35} \oplus \mathbf{45}$. The effect of dimerization can only be understood in the context of the VBS model (3.79) and, hence, in the context of spinon confinement.

We have investigated the phase transition of the J_1–J_2 model more carefully. Going away from the approximate VBS–point $J_{2,\text{VBS}} = 0.5$ to larger values of J_2, the dimerization remains. Going to smaller values of J_2, the system is still in a dimer phase. But the dimerization effect and the gap size decrease with decreasing J_2. To obtain meaningful DMRG results, we have to consider much longer system sizes. In Fig. 3.24 we have plotted the entanglement entropy for $J_2 = 0.15$ on a 200 site chain where the dimerization can be well seen in the entanglement entropy. The reader may notice that we are numerically at the limit concerning computer memory and computing time. It is very difficult to obtain converged calculations. Nonetheless, preliminary results for $J_2 = 0.1$ on a 250 site chain show still the oscillatory behavior,
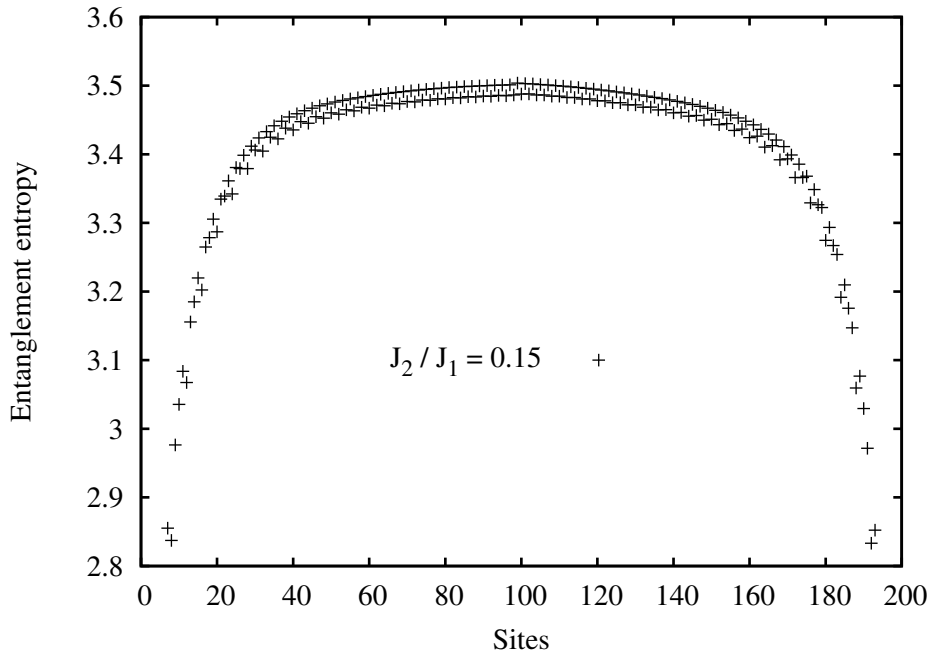

Figure 3.24: Entanglement and bond entropy of the SU(4) representation **10** HM with next–nearest neighbor interactions and $J_2/J_1 = 0.15$. The shown plot is only a preliminary result.

i.e., dimerization, in the entanglement entropy. As stressed in Sec. 3.8.1, in our thinking the next nearest neighbor interaction allows the system to group effective sites with the higher dimensional representation **20** which clearly falls into the category of Haldane-gap models. This assumption explains many things. First, the abnormally small critical coupling can be understood since it is energetically favorable to build these effective sites and reach the gapped phase. That means, it is only relevant that the next–nearest neighbor coupling is present and not that it exceeds a critical value. Second, we can understand why this system dimerizes rather than tetramerizes. The model on the effective sites is translation invariant. Due to the fact, that each effective site consists of two physical sites, the model dimerizes as there are two possibilities to place the effective sites onto the physical sites. Third, it provides an additional reason that spinon confinement is present since the effective model with representation **20** exhibits confined spinons as well. We conclude that the conjecture is valid also for the SU(4) representation **10** Heisenberg models.

3.10 Conclusion

In this Thesis, we have presented a new picture in which the physical mechanism behind the Haldane gap can be understood. We have further presented an approach which allows us to decide whether or not a spin chain is critical. We have extended our investigation to $SU(n)$ spin chains. Their rising relevance from an experimentalists point of view has been discussed. By applying our approach to $SU(n)$ spin chains, our results directly lead to the following observation: If for a given $SU(n)$ spin representation (represented by a Young tableau with λ boxes) the ratio λ/n is integral then the nearest–neighbor Heisenberg model is in a massive phase. If the ratio λ/n is not integral when the nearest neighbor Heisenberg model is critical and the corresponding CFT is supposed to be $SU(n)_1$ WZW. Applying a next–nearest neighbor interaction leads for a certain parameter regime J_2/J_1 to n–merization, i.e., lattice translational symmetry is broken while the ground states are invariant under translations by n lattice spacings. For the cases, where λ and n have a common divisor different from n, the model with $(1 + n/q)$–site interactions undergoes a new type of topological phase transition from a phase with deconfined spinons into a n/q–merized phase with confined spinons. For the cases, where $n/q > 2$, we expect first a phase transition into a n–merized phase by applying a next–nearest neighbor interaction. Applying then additional $(1 + n/q)$–site interactions drives the model into the n/q–merized phase where the spinons are confined. We wish to stress that this phase transition is not a frustration effect but of topological origin. The critical phase is characterized by deconfined spinons, while the gapped, n/q–merized phase by confined spinons. We suggest that this transition occurs due to an effective change of the spin representation. The original spin representation supports deconfined spinons, while the effective representation favors a Haldane–gap phase. Finally, we think that the open problem of generalizing Haldane's conjecture to $SU(n)$ should hereby be solved.

Appendix A

Cold bosonic atoms in a π–flux lattice

A.1 Useful sums

For evaluating the norm, the single particle density matrix, and the number fluctuations of the exact wave functions, the following formulas might be helpful.

$$0) \qquad S(0, M) = \sum_{n=0}^{M} \binom{2n}{n} \binom{2(M-n)}{M-n} \; = \; 4^M$$

$$1) \qquad S(1, M) = \sum_{n=0}^{M} \binom{2n}{n} \binom{2(M-n)}{M-n} n \; = \; 4^M \frac{M}{2}$$

$$2) \qquad S(2, M) = \sum_{n=0}^{M} \binom{2n}{n} \binom{2(M-n)}{M-n} n^2 \; = \; 4^M \frac{M}{2} \frac{3M+1}{4}$$

$$3) \qquad S(3, M) = \sum_{n=0}^{M} \binom{2n}{n} \binom{2(M-n)}{M-n} n^3 \; = \; 4^M \frac{M}{2} (5M+3) \frac{M}{8}$$

The general formula $S(k, M)$ can also be evaluated [93] by means of the Stirling numbers of the second kind $S2(k, p) = \frac{1}{p!} \sum_{j=0}^{p} (-1)^{p-j} \binom{p}{j} j^k$,

$$S(k, M) = \sum_{n=0}^{M} \binom{2n}{n} \binom{2(M-n)}{M-n} n^k \; = \; 4^M \sum_{p=0}^{\min(M,k)} \binom{M}{p} \frac{(2p-1)!!}{2^p} S2(k, p) \; .$$

A.2   Bogoliubov calculation

In this appendix, we present the Bogoliubov approach applied to bosons in a π-flux lattice. We start with a brief review of Bogoliubov's original work from 1947 [31]. He considered a dilute gas of atoms obeying Bose statistics and interacting via an inter-atomic interaction, which is weakly repulsive. The main idea was to replace the creation and annihilation operators at $\boldsymbol{k} = 0$ by their averages. He argued that these averages are equal to the square root of the occupation number of the $\boldsymbol{k} = 0$ state. The remaining effective Hamiltonian (neglecting interactions of "excited particles" with each other – or with other words, neglecting four–body interactions) can be diagonalized by means of what is nowadays called a Bogoliubov transformation. Then we repeat the calculation in the grand–canonical ensemble for bosonic atoms loaded into an optical lattice (with arbitrary spatial dimension) and show that we find qualitatively the same results. After reviewing the Bose gas and the Bose lattice gas, we apply the Bogoliubov approach to the π-flux lattice scenario. The main challenge is to "prepare" the Hamiltonian in such a basis, that we find at $\boldsymbol{k} = 0$ either the c–condensate or the d–condensate and not a superposition of both condensates, i.e., that the ground state is not a Schrödinger–cat state. Once the Hamiltonian is expressed in this c– and d–operators, we can follow Bogoliubov's original work straight forwardly. Finally we also discuss the Bogoliubov spectrum in presence of attractive interactions, i.e., then the system exhibits a fragmented condensate. In both cases, we find a gapless Goldstone mode which is linear in $\boldsymbol{k}$ for small momentum $\boldsymbol{k}$. The critical velocities of the repulsive and the attractive superfluid are, however, different.

A.2.1   Bogoliubov's original calculation for the Bose gas in the canonical ensemble

Bogoliubov[1] considered a weakly interacting Bose gas with repulsive interaction $U > 0$. *Weakly interacting* means that the gas is dilute and, hence, the relation $U = 4\pi a/m$, where a is the scattering length, is approximately valid. The many body Hamiltonian is defined as

$$\mathcal{H} = \mathcal{H}_0 + \mathcal{H}_{\text{int}} = \sum_{\boldsymbol{k}} \frac{\boldsymbol{k}^2}{2m} a_{\boldsymbol{k}}^\dagger a_{\boldsymbol{k}} + \frac{U}{2V} \sum_{\boldsymbol{k},\boldsymbol{k}',\boldsymbol{q}} a_{\boldsymbol{k}+\boldsymbol{q}}^\dagger a_{\boldsymbol{k}'-\boldsymbol{q}}^\dagger a_{\boldsymbol{k}'} a_{\boldsymbol{k}} \tag{A.1}$$

where V is the volume of the gas, m the mass of the atoms, and $\hbar \equiv 1$ throughout the section. The creation and annihilation operators fulfill the bosonic commutation relation

$$\left[a_{\boldsymbol{k}}, a_{\boldsymbol{k}'}^\dagger \right] = \delta_{\boldsymbol{k},\boldsymbol{k}'}. \tag{A.2}$$

Formally we apply now perturbation theory to this Hamiltonian. Note that in the ground state of ideal Bose gas all particles are condensed – or, equivalently, occupy

---

[1]Bogoliubov's calculation which can be considered as the beginning of the *many body problem* is illustrated in many textbooks. Nonetheless, we refer the reader to the classical textbooks of Landau [98] and Abrikosov, Gorkov, and Dzyaloshinski [2].

the condensed state. The condensed state is a state with vanishing energy. The occupation number is $N_{\boldsymbol{k}=0} \equiv N_0 = N$ and $N_{\boldsymbol{k}\neq 0} = 0$. In a weakly interacting Bose gas the situation changes slightly: $N_0 \lesssim N$ and $N_{\boldsymbol{k}\neq 0} \gtrsim 0$. In particular, $N_{\boldsymbol{k}\neq 0} \ll N_0$ and, hence, we are able to write $a_0^\dagger a_0 = N_0 \approx N$. The commutator $a_0 a_0^\dagger - a_0^\dagger a_0 = 1$ is much smaller than the operators $a_0^\dagger$ and a_0 itself. That means, one can replace these operators by their averages and neglect the operator character.

$$a_0^\dagger \to \sqrt{N_0} \quad \text{and} \quad a_0 \to \sqrt{N_0} \tag{A.3}$$

Applying perturbation theory is equivalent to the expansion of the sum in $\mathcal{H}_{\text{int}}$ in powers of the small quantities $a_{\boldsymbol{k}\neq 0}^\dagger$, $a_{\boldsymbol{k}\neq 0}$. The zeroth order is given by

$$a_0^\dagger a_0^\dagger a_0 a_0 = N_0^2. \tag{A.4}$$

The first order vanishes since it is impossible to conserve momentum for terms like $a_{\boldsymbol{k}\neq 0}^\dagger a_0^\dagger a_0 a_0$. The second order is given by

$$N_0 \sum_{\boldsymbol{k}\neq 0} \left(a_{\boldsymbol{k}}^\dagger a_{-\boldsymbol{k}}^\dagger + a_{\boldsymbol{k}} a_{-\boldsymbol{k}} + 4 a_{\boldsymbol{k}}^\dagger a_{\boldsymbol{k}} \right). \tag{A.5}$$

Since we are calculating in the canonical ensemble we have to replace N_0 by the total particle number N. N is, say, in the experiment given by the system, a parameter, while N_0 is a non–fixed number and not a sensible physical quantity to express other quantities. The exact relation between N and N_0 is

$$N = N_0 + \sum_{\boldsymbol{k}\neq 0} a_{\boldsymbol{k}}^\dagger a_{\boldsymbol{k}}. \tag{A.6}$$

Thus we have terms of order $\mathcal{O}(N)$ and $\mathcal{O}(N^2)$ and are allowed to neglect terms of order $\mathcal{O}(N^0)$. This means that we can replace $N_0 \approx N$ and $N_0^2 \approx N^2 - 2N \sum_{\boldsymbol{k}\neq 0} a_{\boldsymbol{k}}^\dagger a_{\boldsymbol{k}}$ if we restrict ourself to the second order.

Substituting all these assumptions and considerations in the Hamiltonian (A.1) we obtain the Bogoliubov mean field Hamiltonian

$$\mathcal{H}^{\text{Bogo}} = \frac{UN^2}{2V} + \frac{1}{2} \sum_{\boldsymbol{k}\neq 0} \left[\left(\frac{\boldsymbol{k}^2}{2m} + \frac{UN}{V} \right) \left(a_{\boldsymbol{k}}^\dagger a_{\boldsymbol{k}} + a_{-\boldsymbol{k}}^\dagger a_{-\boldsymbol{k}} \right) + \frac{UN}{V} \left(a_{\boldsymbol{k}}^\dagger a_{-\boldsymbol{k}}^\dagger + a_{\boldsymbol{k}} a_{-\boldsymbol{k}} \right) \right]. \tag{A.7}$$

The second term in (A.7) is not diagonal. To diagonalize it, we could carry out a linear transformation of the operators $a_{\boldsymbol{k}}^\dagger$ and $a_{\boldsymbol{k}}$ and follow the path as described in the textbook by Abrikosov, Gorkov, and Dzyaloshinski [2] or Landau and Lifshitz [98], respectively. Here we are presenting another way we find more elegant. We write

the Hamiltonian (A.7) as a matrix equation by use of the commutation relations.

$$\mathcal{H}^{\text{Bogo}} = \frac{UN^2}{2V} - \frac{1}{2} \sum_{\boldsymbol{k} \neq 0} \left(\frac{\boldsymbol{k}^2}{2m} - \frac{UN}{V} \right)$$

$$+ \frac{1}{2} \sum_{\boldsymbol{k} \neq 0} \left(a_{\boldsymbol{k}}^\dagger, \, a_{-\boldsymbol{k}} \right) \begin{pmatrix} \epsilon_{\boldsymbol{k}} + \frac{UN}{V} & \frac{UN}{V} \\ \frac{UN}{V} & \epsilon_{\boldsymbol{k}} + \frac{UN}{V} \end{pmatrix} \begin{pmatrix} a_{\boldsymbol{k}} \\ a_{-\boldsymbol{k}}^\dagger \end{pmatrix}$$

$$= \frac{\kappa N}{2} - \frac{1}{2} \sum_{\boldsymbol{k} \neq 0} \left(\frac{\boldsymbol{k}^2}{2m} - \kappa \right) + \frac{1}{2} \sum_{\boldsymbol{k} \neq 0} \left(a_{\boldsymbol{k}}^\dagger, \, a_{-\boldsymbol{k}} \right) \left[(\epsilon_{\boldsymbol{k}} + \kappa) \, \mathbf{1} + \kappa \sigma^x \right] \begin{pmatrix} a_{\boldsymbol{k}} \\ a_{-\boldsymbol{k}}^\dagger \end{pmatrix}$$

Here we introduced the shortcut $\epsilon_{\boldsymbol{k}} = \frac{\boldsymbol{k}^2}{2m}$ and σ^x is the first Pauli matrix. We further introduced in the second line the so-called *microscopic coupling* $\kappa = \frac{UN}{V}$. The bosonic Bogoliubov approximation can now be done via the operator $\mathcal{U} = \exp\left(\sigma^x \theta_{\boldsymbol{k}}\right)$. Note that $\mathcal{U}^{-1} = e^{-\sigma^x \theta_{\boldsymbol{k}}}$ and $\mathcal{U}\mathcal{U}^{-1} = \mathcal{U}^{-1}\mathcal{U} = 1$ and $\left(\mathcal{U}^{-1}\right)^2 = \exp\left(-2\sigma^x \theta_{\boldsymbol{k}}\right) = \cosh(2\theta_{\boldsymbol{k}})\mathbf{1} + \sinh(2\theta_{\boldsymbol{k}})\sigma^x$. Thus we obtain

$$\mathcal{H}^{\text{Bogo}} = \text{const.} + \frac{1}{2} \sum_{\boldsymbol{k} \neq 0} \left(a_{\boldsymbol{k}}^\dagger, \, a_{-\boldsymbol{k}} \right) \mathcal{U}\mathcal{U}^{-1} \left[\, \dots \, \right] \mathcal{U}^{-1}\mathcal{U} \begin{pmatrix} a_{\boldsymbol{k}} \\ a_{-\boldsymbol{k}}^\dagger \end{pmatrix} \tag{A.8}$$

with new operators $\left(a_{\boldsymbol{k}}^\dagger, \, a_{-\boldsymbol{k}} \right) \mathcal{U} = \left(\alpha_{\boldsymbol{k}}^\dagger, \, \alpha_{-\boldsymbol{k}} \right)$. The transformed matrix becomes

$$\mathcal{U}^{-1} \left[(\epsilon_{\boldsymbol{k}} + \kappa) \, \mathbf{1} + \kappa \sigma^x \right] \mathcal{U}^{-1}$$

$$= \left[\cosh(2\theta_{\boldsymbol{k}})\mathbf{1} + \sinh(2\theta_{\boldsymbol{k}})\sigma^x \right] \left[(\epsilon_{\boldsymbol{k}} + \kappa) \, \mathbf{1} + \kappa \sigma^x \right]$$

$$= \left(\cosh(2\theta_{\boldsymbol{k}})(\epsilon_{\boldsymbol{k}} + \kappa) + \sinh(2\theta_{\boldsymbol{k}})\kappa \right) \mathbf{1} + \left(\cosh(2\theta_{\boldsymbol{k}})\kappa + \sinh(2\theta_{\boldsymbol{k}})(\epsilon_{\boldsymbol{k}} + \kappa) \right) \sigma^x$$

In order to diagonalize the Hamiltonian we set the off–diagonal terms (i.e., the terms $\propto \sigma^x$) to zero, determine $\theta_{\boldsymbol{k}}$ for this equation and after doing so we substitute $\theta_{\boldsymbol{k}}$ into the diagonal part of the Hamiltonian (i.e., the terms $\propto \mathbf{1}$). Finally we obtain the Bogoliubov quasi–particle spectrum for the new operators $\alpha_{\boldsymbol{k}}^\dagger$ and $\alpha_{\boldsymbol{k}}$,

$$\mathcal{H}^{\text{Bogo}} = \frac{\kappa N}{2} - \frac{1}{2} \sum_{\boldsymbol{k} \neq 0} \left(\epsilon_{\boldsymbol{k}} + \kappa - \sqrt{(\epsilon_{\boldsymbol{k}} + \kappa)^2 - \kappa^2} \right)$$
$$+ \sum_{\boldsymbol{k} \neq 0} \sqrt{(\epsilon_{\boldsymbol{k}} + \kappa)^2 - \kappa^2} \, \alpha_{\boldsymbol{k}}^\dagger \alpha_{\boldsymbol{k}} \, . \tag{A.9}$$

The expression (A.9) consists of three terms. The sum of the first two terms is a certain constant. The third term represents a diagonal operator which can be written in the form

$$\sum_{\boldsymbol{k} \neq 0} \varepsilon_{\boldsymbol{k}} n_{\boldsymbol{k}} \tag{A.10}$$

where $n_{\boldsymbol{k}}$ is the occupation number of the operator $\alpha_{\boldsymbol{k}}$. The smallest value of the energy is obtained when all the $n_{\boldsymbol{k}}$ equal zero, and therefore (A.10) is the energy of the excitation. This expression has the same form as the energy of a system of noninteracting particles. It follows that the weakly excited states of a dilute Bose gas can be described by using the model of elementary excitations, with an energy spectrum

$$\varepsilon_{\boldsymbol{k}} = \sqrt{\left(\frac{\boldsymbol{k}^2}{2m} + \frac{UN}{V}\right)^2 - \left(\frac{UN}{V}\right)^2} = \sqrt{\frac{\kappa}{m}}\, k\, \sqrt{1 + \boldsymbol{k}^2\left(\frac{V}{2UN}\right)^2}. \qquad \text{(A.11)}$$

which is plotted in Fig. A.1. Note that in Bogoliubov's original work there is no trace
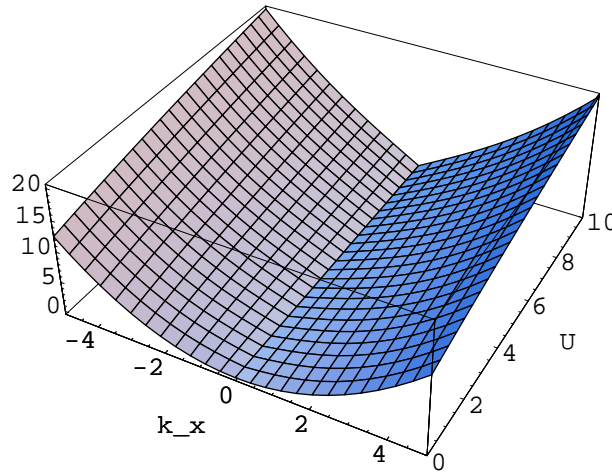
Figure A.1: Quasi–particle spectrum of the dilute Bose gas in two dimensions. At the x-axes we have plotted k, since the spectrum is in momentum space rotationally invariant. At the y-axes we have plotted the repulsive interaction U. At $U = 0$ we see the spectrum for free particles, and for $U > 0$ the Bogoliubov quasi-particle spectrum. Around $k = 0$ for $U > 0$ we see the linear slope representing the sound mode of the superfluid.

of the second, "roton" branch of the excitation spectrum postulated by Landau. Since we are only interested in the critical velocity v_c of the superfluid we conclude this chapter with a brief discussion of the spectrum and with the determination of v_c.

From the right-hand side of equation (A.11) we can directly read the critical velocity $v_c = \sqrt{\kappa/m}$. That means for small momenta $\boldsymbol{k}$ the dispersion (A.11) reduces to the phonon spectrum $\varepsilon = v_c|\boldsymbol{k}|$ with speed of sound v_c which is usually referred to as the critical velocity in case of the superfluid. This phonon–like mode appears due to the spontaneously broken U(1) symmetry and is a consequence of Goldstone's theorem. The formal definition of the critical velocity is given by

$$v_c = \left.\frac{\partial \varepsilon_{\boldsymbol{k}}}{\partial \boldsymbol{k}}\right|_{\boldsymbol{k}\to 0} \overset{\text{Bose gas}}{=} \sqrt{\frac{UN}{mV}}\ . \qquad \text{(A.12)}$$

If we consider large momenta $\boldsymbol{k}$, it is convenient to consider the left–hand side of (A.11). For large momenta the term $\left(\frac{\boldsymbol{k}^2}{2m}\right)^2$ dominates and the spectrum is that of free particles.

A.2.2 Bogoliubov approach for bosons on the lattice in the grand canonical ensemble

In this section we briefly repeat the calculation of the previous section in the grand canonical ensemble and in the presence of a lattice. Since the calculation, particularly the diagonalization procedure, is the same as in the canonical ensemble, we concentrate on the discussion of the difference between both ensembles and the determination of the chemical potential μ. The difference between the Bose gas and the Bose lattice model, is for the Bogoliubov calculation irrelevant. We only assume that the single particle spectrum $\epsilon_{\boldsymbol{k}}$ vanishes for the condensed state, $\epsilon_0 = 0$. We further mention that the calculation is not influenced by the number of spatial dimensionality d of the system.

Bosons on a d-dimensional lattice are most conveniently described by the Bose–Hubbard model (BHM) [50], a tight–binding model plus a repulsive contact interaction for lattice bosons,

$$\mathcal{H} = -t \sum_{\langle i,j \rangle} c_i^\dagger c_j - \mu \sum_i c_i^\dagger c_i + \frac{U}{2} \sum_i c_i^\dagger c_i^\dagger c_i c_i \qquad (A.13)$$

We stress that we consider now the "non–magnetic" case, i.e., there is no artificial vector potential. The BHM in momentum space reads

$$\mathcal{H} = \sum_{\boldsymbol{k}} \left[\underbrace{2t\left(d - \sum_{j=1}^{d} \cos\left(k_j a\right)\right)}_{=:\epsilon_{\boldsymbol{k}}} - \mu \right] a_{\boldsymbol{k}}^\dagger a_{\boldsymbol{k}} + \frac{U a^d}{2 N_{\mathrm{s}}} \sum_{\boldsymbol{k},\boldsymbol{k}',\boldsymbol{q}} a_{\boldsymbol{k}+\boldsymbol{q}}^\dagger a_{\boldsymbol{k}'-\boldsymbol{q}}^\dagger a_{\boldsymbol{k}'} a_{\boldsymbol{k}}, \qquad (A.14)$$

where a is the lattice spacing, N_{s} the number of sites (i.e., $V = N_{\mathrm{s}} a^d$), and the kinetic energy was shifted by $+2td$ in order to have a vanishing single particle energy in the condensed state, $\epsilon_0 = 0$. Note that the summation over $\boldsymbol{k}$ is restricted to the first Brioullin zone. For the rest of this section we set the lattice spacing $a \equiv 1$.

In the canonical ensemble, there is no chemical potential and the particle number N is fixed, i.e., N is an exterior parameter that can be chosen in an experiment. In the grand canonical ensemble, N is not fixed anymore. Instead of N, the chemical potential μ is the fixed quantity and plays the role of an exterior parameter. For the Bogoliubov approximation, we determine the chemical potential in (A.14) by the requirement that the linear contribution to the fluctuations in the condensate has to be zero.

We replace the creation and annihilation operators of the condensed state by their averages plus fluctuations,

$$a_0^\dagger \rightarrow \sqrt{N_0} + \delta a_0^\dagger \quad \text{and} \quad a_0 \rightarrow \sqrt{N_0} + \delta a_0. \qquad (A.15)$$

The terms of the Hamiltonian for $\boldsymbol{k} = 0$ are

$$
\begin{aligned}
\overline{H} = & -\mu\, a_0^\dagger a_0 + \frac{U}{2N_\mathrm{s}} a_0^\dagger a_0^\dagger a_0 a_0 \\
\to & -\mu \left(\sqrt{N_0} + \delta a_0^\dagger \right) \left(\sqrt{N_0} + \delta a_0 \right) + \frac{U}{2N_\mathrm{s}} \left(\sqrt{N_0} + \delta a_0^\dagger \right)^2 \left(\sqrt{N_0} + \delta a_0 \right)^2 \\
= & -\mu N_0 + \frac{U N_0}{2N_\mathrm{s}} + \left(-\mu + \frac{U}{N_\mathrm{s}} N_0 \right) \sqrt{N_0} \left(\delta a_0^\dagger + \delta a_0 \right) + \text{ second order terms.}
\end{aligned}
\tag{A.16}
$$

The requirement that the terms linear in the fluctuations must be zero is fulfilled by

$$
\mu = \frac{U}{N_\mathrm{s}} N_0.
\tag{A.17}
$$

More precise, we have not determined the chemical potential but the occupation number of the condensate as a function of the chemical potential, $N_0 = N_\mathrm{s}/U\mu$. For our purposes we wish to express μ through N_0.

Following the line of derivation of the previous chapter, we obtain the mean field Hamiltonian

$$
\mathcal{H}^{\mathrm{Bogo}} = \left(-\mu + \frac{U n_0}{2} \right) N_0 + \sum_{\boldsymbol{k} \neq 0} (\epsilon_{\boldsymbol{k}} - \mu)\, a_{\boldsymbol{k}}^\dagger a_{\boldsymbol{k}} + \frac{1}{2} U n_0 \sum_{\boldsymbol{k} \neq 0} \left(a_{\boldsymbol{k}}^\dagger a_{-\boldsymbol{k}}^\dagger + a_{\boldsymbol{k}} a_{-\boldsymbol{k}} + 4 a_{\boldsymbol{k}}^\dagger a_{\boldsymbol{k}} \right),
$$

where we introduced the shortcut $n_0 = N_0/N_\mathrm{s}$. Making use of commutation relations and substituting equation (A.17), the Hamiltonian becomes as a matrix equation

$$
\mathcal{H}^{\mathrm{Bogo}} = -\frac{1}{2} U n_0 N_0 =
$$

$$
\frac{1}{2} \sum_{\boldsymbol{k} \neq 0} (\epsilon_{\boldsymbol{k}} + U n_0) + \frac{1}{2} \sum_{\boldsymbol{k} \neq 0} \left(a_{\boldsymbol{k}}^\dagger,\, a_{\boldsymbol{k}} \right) \begin{pmatrix} \epsilon_{\boldsymbol{k}} + U n_0 & U n_0 \\ U n_0 & \epsilon_{\boldsymbol{k}} + U n_0 \end{pmatrix} \begin{pmatrix} a_{\boldsymbol{k}} \\ a_{-\boldsymbol{k}}^\dagger \end{pmatrix}.
$$

Again we diagonalize the Hamiltonian by a Bogoliubov approximation and obtain the quasi–particle spectrum

$$
\varepsilon_{\boldsymbol{k}} = \sqrt{\epsilon_{\boldsymbol{k}}^2 + 2 U n_0 \epsilon_{\boldsymbol{k}}}.
\tag{A.18}
$$

For two dimensions, we have plotted the quasi-particle spectrum as a function of U in Fig. A.2. For small momenta there is the Goldstone mode with dispersion $\varepsilon = v_c |\boldsymbol{k}|$ with the critical velocity

$$
v_c \overset{\mathrm{Bose\,latt.}}{=} \sqrt{\frac{2 U N_0 t}{N_\mathrm{s}}}\,.
\tag{A.19}
$$

The approximation in the grand canonical calculation for bosons on the lattice and the discussion whether or not Bogoliubov's approach can describe the quantum phase transition from a superfluid to a Mott–Insulator [50, 59, 78] can be found in the nice paper by van Oosten *et al.* [116].
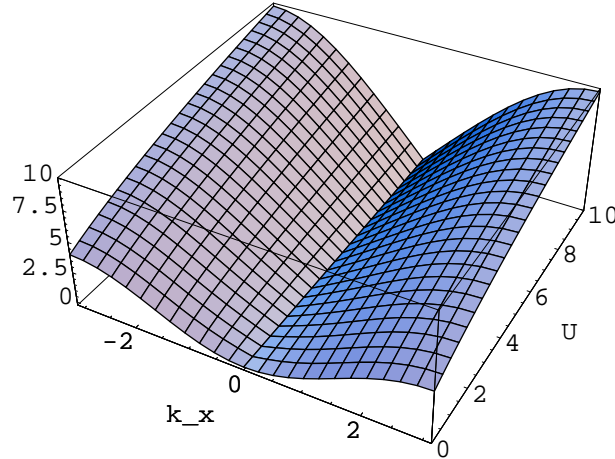
Figure A.2: Quasi–particle spectrum for the BHM in two dimensions. The spectrum is rotationally invariant in the k_x-k_y-plane. Therefore at the x-axes we plotted $k_x = |\boldsymbol{k}| \in [-\pi, \pi]$, at the y-axes the interaction U is plotted. For $U = 0$ the spectrum corresponds to the single particle spectrum and has the pure cosinus form. For $U \neq 0$ around $\boldsymbol{k} = 0$ the spectrum has the phonon-like behavior, $\varepsilon \propto |\boldsymbol{k}|$.

A.2.3 Bogoliubov approach for bosons in the π-flux lattice

Naively, one could assume to start with the magnetic BHM in lower band approximation as defined in Eq. (2.33). As the ground state of this Hamiltonian is a superposition of the c– and d–condensate for which we wish to obtain the critical velocities and quasi–particle spectra, the straight ansatz of Bogoliubov might fail. Instead, we have to rewrite the magnetic Bose–Hubbard model in the basis where the ground state is either represented by the c–condensate or by the d–condensate.

As a first step, we have to enlarge the primitive unit cell to four sites in order to contain a whole plaquette and to respect our new knowledge about the broken $\mathbb{Z}_2$ symmetry. The enlarged unit cell corresponds to a reduced Brioullin zone which is only a quarter of the original unit cell. The kinetic energy term is then given by

$$\mathcal{H}_{\mathrm{kin}} = {\sum_{\boldsymbol{k}}}' \left(c_{\boldsymbol{k},1}^\dagger, c_{\boldsymbol{k},2}^\dagger, c_{\boldsymbol{k},3}^\dagger, c_{\boldsymbol{k},4}^\dagger \right) \mathcal{X}^{\mathrm{t}} \mathcal{P}^\dagger \mathcal{P} \mathcal{X} H_{\boldsymbol{k}} \mathcal{X}^{\mathrm{t}} \mathcal{P}^\dagger \mathcal{P} \mathcal{X} \begin{pmatrix} c_{\boldsymbol{k},1} \\ c_{\boldsymbol{k},2} \\ c_{\boldsymbol{k},3} \\ c_{\boldsymbol{k},4} \end{pmatrix} \tag{A.20}$$

with the matrix

$$H_{\boldsymbol{k}} = \begin{pmatrix} 0 & 0 & \cos k_x & \cos k_y \\ 0 & 0 & \cos k_y & -\cos k_x \\ \cos k_x & \cos k_y & 0 & 0 \\ \cos k_y & -\cos k_x & 0 & 0 \end{pmatrix}. \tag{A.21}$$

The unitary matrix $\mathcal{X}$ transforms the crystal momentum operators to the band operators, similarly as the matrix $\mathcal{U}$ as defined in App. ?? does. The difference is,

that the bands in the interval $[(\frac{\pi}{2}, -\frac{\pi}{2}), (\frac{3\pi}{2}, \frac{\pi}{2})]$ are now identified with the interval $[(-\frac{\pi}{2}, -\frac{\pi}{2}), (\frac{\pi}{2}, \frac{\pi}{2})]$. That means, we have two lower and two upper bands in the reduced Brioullin zone. Finally, the transformation $\mathcal{P}$ rotates the basis such that the two–fold degenerate single particle states at $\boldsymbol{k} = 0$ corresponds to the states $c^\dagger \,|\,0\,\rangle$ and $d^\dagger \,|\,0\,\rangle$, respectively. We repeat this step:

$$\mathcal{P}\mathcal{X} \begin{pmatrix} c_{\boldsymbol{k},1} \\ c_{\boldsymbol{k},2} \\ c_{\boldsymbol{k},3} \\ c_{\boldsymbol{k},4} \end{pmatrix} = \mathcal{P} \begin{pmatrix} \alpha_{\boldsymbol{k},-} \\ \gamma_{\boldsymbol{k},-} \\ \alpha_{\boldsymbol{k},+} \\ \gamma_{\boldsymbol{k},+} \end{pmatrix} = \begin{pmatrix} \alpha_{\boldsymbol{k},-} - i\gamma_{\boldsymbol{k},-} \\ \alpha_{\boldsymbol{k},-} + i\gamma_{\boldsymbol{k},-} \\ \alpha_{\boldsymbol{k},+} - i\gamma_{\boldsymbol{k},+} \\ \alpha_{\boldsymbol{k},+} + i\gamma_{\boldsymbol{k},+} \end{pmatrix} = \begin{pmatrix} c_{\boldsymbol{k},-} \\ d_{\boldsymbol{k},-} \\ c_{\boldsymbol{k},+} \\ d_{\boldsymbol{k},+} \end{pmatrix} \qquad \text{(A.22)}$$

In this notation, $c^\dagger_{\boldsymbol{k}=0,-} \,|\,0\,\rangle \equiv c^\dagger \,|\,0\,\rangle$ and $d^\dagger_{\boldsymbol{k}=0,-} \,|\,0\,\rangle \equiv d^\dagger \,|\,0\,\rangle$. Now we consider the Hubbard interaction which we have already transformed to momentum space:

$$\mathcal{H}_{\text{int}} = \frac{2U}{N_{\text{s}}} {\sum_{\boldsymbol{k},\boldsymbol{k}',\boldsymbol{q}}}' \sum_{\alpha=1}^{4} c^\dagger_{\boldsymbol{k}+\boldsymbol{q},\alpha} c^\dagger_{\boldsymbol{k}'-\boldsymbol{q},\alpha} c_{\boldsymbol{k}',\alpha} c_{\boldsymbol{k},\alpha} \; . \qquad \text{(A.23)}$$

Now we transform also the interaction to the new operators $c_{\boldsymbol{k},-}$ and $d_{\boldsymbol{k},-}$, we neglect again the upper bands represented by the operators $c_{\boldsymbol{k},+}$ and $d_{\boldsymbol{k},+}$. The transformations read

$$c_{\boldsymbol{k},1} = \frac{+i\cos k_x + \cos k_y}{2\sqrt{\cos^2 k_x + \cos^2 k_y}} c_{\boldsymbol{k},-} + \frac{-i\cos k_x + \cos k_y}{2\sqrt{\cos^2 k_x + \cos^2 k_y}} d_{\boldsymbol{k},-} + \text{``upper bands''} \; ,$$

$$c_{\boldsymbol{k},2} = \frac{-\cos k_x + i\cos k_y}{2\sqrt{\cos^2 k_x + \cos^2 k_y}} c_{\boldsymbol{k},-} + \frac{-\cos k_x - i\cos k_y}{2\sqrt{\cos^2 k_x + \cos^2 k_y}} d_{\boldsymbol{k},-} + \text{``upper bands''} \; ,$$

$$c_{\boldsymbol{k},3} = \frac{i}{2} c_{\boldsymbol{k},-} - \frac{i}{2} d_{\boldsymbol{k},-} + \text{``upper bands''} \; ,$$

$$c_{\boldsymbol{k},4} = \frac{1}{2} c_{\boldsymbol{k},-} + \frac{1}{2} d_{\boldsymbol{k},-} + \text{``upper bands''} \; .$$

Now we have to substitute these transformations into the interaction term (A.23). This causes a lot of book keeping. In the transformed interaction term, we neglect all terms describing interactions between "excited states" as Bogoliubov did. So we obtain the interaction term of the Bogoliubov mean field Hamiltonian for the π–flux lattice:

$$\mathcal{H}_{\text{int}}^{\text{eff}} = \frac{U}{2N_{\text{s}}} \left(c_0^\dagger c_0^\dagger c_0 c_0 + 4 c_0^\dagger c_0 d_0^\dagger d_0 + d_0^\dagger d_0^\dagger d_0 d_0 \right) \tag{A.24}$$

$$+ \frac{U}{4N_{\text{s}}} \sum_{\boldsymbol{k}\neq0}' \left(8 c_{\boldsymbol{k}}^\dagger c_{\boldsymbol{k}} c_0^\dagger c_0 + 8 c_{\boldsymbol{k}}^\dagger c_{\boldsymbol{k}} d_0^\dagger d_0 + 8 d_{\boldsymbol{k}}^\dagger d_{\boldsymbol{k}} c_0^\dagger c_0 + 8 d_{\boldsymbol{k}}^\dagger d_{\boldsymbol{k}} d_0^\dagger d_0 \right.$$

$$+ \frac{(4-4i)(\cos k_x - \cos k_y)}{\cos k_x + i \cos k_y} c_{\boldsymbol{k}}^\dagger d_{\boldsymbol{k}} c_0^\dagger d_0$$

$$+ \frac{(4+4i)(\cos k_x + \cos k_y)}{\cos k_x + i \cos k_y} c_{\boldsymbol{k}}^\dagger d_{\boldsymbol{k}} d_0^\dagger c_0$$

$$+ \frac{(4+4i)(\cos k_x - \cos k_y)}{\cos k_x - i \cos k_y} d_{\boldsymbol{k}}^\dagger c_{\boldsymbol{k}} d_0^\dagger c_0$$

$$+ \frac{(4-4i)(\cos k_x + \cos k_y)}{\cos k_x - i \cos k_y} d_{\boldsymbol{k}}^\dagger c_{\boldsymbol{k}} c_0^\dagger d_0$$

$$+ \left[\left(\mathcal{B}(0,0,\boldsymbol{k}) + 1 \right) c_{\boldsymbol{k}}^\dagger c_{-\boldsymbol{k}}^\dagger c_0 c_0 + \left(\mathcal{P}(0,0,\boldsymbol{k}) + 1 \right) d_{\boldsymbol{k}}^\dagger d_{-\boldsymbol{k}}^\dagger d_0 d_0 \right.$$

$$+ \left(\mathcal{D}(0,0,\boldsymbol{k}) + 1 \right) c_{\boldsymbol{k}}^\dagger c_{-\boldsymbol{k}}^\dagger d_0 d_0 + \left(\mathcal{M}(0,0,\boldsymbol{k}) + 1 \right) d_{\boldsymbol{k}}^\dagger d_{-\boldsymbol{k}}^\dagger c_0 c_0$$

$$\left. + 4 c_{\boldsymbol{k}}^\dagger d_{-\boldsymbol{k}}^\dagger c_0 d_0 + 4 d_{\boldsymbol{k}}^\dagger c_{-\boldsymbol{k}}^\dagger c_0 d_0 \ + \ \text{h.c.} \right] \right)$$

Note that $\mathcal{D}(0,0,\boldsymbol{k}) = -\mathcal{B}(0,0,\boldsymbol{k})$ and $\mathcal{M}(0,0,\boldsymbol{k}) = -\mathcal{P}(0,0,\boldsymbol{k})$. Both $\mathcal{B}$ and $\mathcal{P}$ consists of cosine-terms in a non–trivial way.

A.2.4   Result for the repulsive model

When we concentrate on the repulsive model, the ground state is given by the macroscopic occupation of the c–condensate or the d–condensate, respectively. Without loss of generality, we assume the Bose liquid to be condensed in the single particle state $c_0^\dagger | 0 \rangle$. Consequently, we can assume that the single particle state $d_0^\dagger | 0 \rangle$ is not occupied (at least, not macroscopically occupied):

$$c_0^\dagger \approx c_0 \approx \sqrt{N_c^{(0)}} \equiv \sqrt{N_c} \tag{A.25}$$

and

$$d_0^\dagger \approx d_0 \approx 0 \tag{A.26}$$

When we find the following mean field Hamiltonian[2],

$$
\begin{aligned}
\mathcal{H}^{\text{eff}} &= -\mu c_0^\dagger c_0 + \frac{2U}{N_{\text{s}}} c_0^\dagger c_0^\dagger c_0 c_0 + {\sum_{\boldsymbol{k} \neq 0}}' (\xi_{\boldsymbol{k}} - \mu) \left(c_{\boldsymbol{k}}^\dagger c_{\boldsymbol{k}} + d_{\boldsymbol{k}}^\dagger d_{\boldsymbol{k}} \right) \\
&\quad + {\sum_{\boldsymbol{k} \neq 0}}' \frac{U}{4N_{\text{s}}} \Bigg\{ 8 N_c c_{\boldsymbol{k}}^\dagger c_{\boldsymbol{k}} + 8 N_c d_{\boldsymbol{k}}^\dagger d_{\boldsymbol{k}} + (\mathcal{B}(0,0,\boldsymbol{k}) + 1) \, N_c c_{\boldsymbol{k}}^\dagger c_{-\boldsymbol{k}}^\dagger + \text{h.c.} \\
&\quad + (\mathcal{P}(0,0,\boldsymbol{k}) + 1) \, N_c d_{\boldsymbol{k}}^\dagger d_{-\boldsymbol{k}}^\dagger + \text{h.c.} \Bigg\}
\end{aligned}
$$

We determine the chemical potential as done in Sec. A.2.2 and find the result

$$
\mu = \frac{U N_c}{N_{\text{s}}} \; . \tag{A.27}
$$

We finally obtain the Hamiltonian in matrix form (neglecting additive constants) as

$$
\mathcal{H}^{\text{eff}} = \frac{1}{2} {\sum_{\boldsymbol{k} \neq 0}}' \left(c_{\boldsymbol{k}}^\dagger, c_{-\boldsymbol{k}}, d_{\boldsymbol{k}}^\dagger, d_{-\boldsymbol{k}} \right)
\begin{pmatrix}
\xi_{\boldsymbol{k}} + \kappa_c & \frac{\kappa_c}{2}(\mathcal{B} + 1) & 0 & 0 \\
\frac{\kappa_c}{2}(\mathcal{B} + 1) & \xi_{\boldsymbol{k}} + \kappa_c & 0 & 0 \\
0 & 0 & \xi_{\boldsymbol{k}} + \kappa_c & \frac{\kappa_c}{2}(\mathcal{P} + 1) \\
0 & 0 & \frac{\kappa_c}{2}(\mathcal{P} + 1) & \xi_{\boldsymbol{k}} + \kappa_c
\end{pmatrix}
\begin{pmatrix}
c_{\boldsymbol{k}} \\
c_{-\boldsymbol{k}}^\dagger \\
d_{\boldsymbol{k}} \\
d_{-\boldsymbol{k}}^\dagger
\end{pmatrix}
$$

where the microscopic coupling $\kappa_c = \frac{U N_c}{N_{\text{s}}}$ and $\xi_{\boldsymbol{k}} = -2t \left(\sqrt{\cos^2 k_x + \cos^2 k_y} + \sqrt{2} \right)$ is the single particle spectrum which is shifted such that $\xi_{\boldsymbol{k}=0} = 0$. In the limit $\boldsymbol{k} \to 0$, the prefactors $\mathcal{B}(0,0,\boldsymbol{k}) \to 1$ and $\mathcal{P}(0,0,\boldsymbol{k}) \to 1$. We eventually obtain the Bogoliubov quasi particle spectrum

$$
\begin{aligned}
\epsilon_{\boldsymbol{k}} &= \sqrt{\xi_{\boldsymbol{k}}^2 + 2\kappa_c \xi_{\boldsymbol{k}}} \\
&\stackrel{\boldsymbol{k} \to 0}{=} |\boldsymbol{k}| \sqrt{\sqrt{2} t a^2 \kappa_c} \sqrt{1 + \frac{1}{2\sqrt{2}} \frac{t a^2}{\kappa_c} |\boldsymbol{k}|^2} \; .
\end{aligned} \tag{A.28}
$$

The critical velocity is given by

$$
v_c \stackrel{\text{rep.flux latt}}{=} \sqrt{\sqrt{2} t \kappa_c} = \sqrt{\frac{\sqrt{2} t \, U \, N_c}{N_{\text{s}}}} \equiv \sqrt{\frac{t^{\text{flux}} \, U \, N_c}{N_{\text{s}}}} \tag{A.29}
$$

This result is very plausible, as we find the same result as for the Bose liquid without flux when replacing t by $t^{\text{flux}} = t/\sqrt{2}$. Note that the quasi particle spectrum does not

---

[2]We consider the magnetic BHM in the grand–canoncial ensemble.

change qualitatively when considering the prefactors $\mathcal{B}$ and $\mathcal{P}$ correctly. In particular, the critical velocity is not influenced. When we consider the prefactors $\mathcal{B}$ and $\mathcal{P}$, the quasi particle spectrum becomes

$$\epsilon_{\boldsymbol{k}} = \sqrt{\xi_{\boldsymbol{k}}^2 + 2\kappa_c\xi_{\boldsymbol{k}} + \frac{\kappa_c^2(\cos k_x - \cos k_y)^2}{2(\cos^2 k_x + \cos^2 k_y)}} \ . \tag{A.30}$$

A.2.5 Result for the attractive model

Now we concentrate on the attractive model, the ground state is fragmented, i.e., both single particle ground states, $c_0^\dagger|0\rangle$ and $d_0^\dagger|0\rangle$, are occupied macroscopically:

$$c_0^\dagger \approx c_0 \approx \sqrt{N_c} \tag{A.31}$$

and

$$d_0^\dagger \approx d_0 \approx \sqrt{N_d} \ . \tag{A.32}$$

We further assume that $N_c \approx N_d \approx N_0/2$ which is justified when considering the solution of the effective model, see Sec. 2.4.1. Applying all these assumptions to the Hamiltonian (A.24), we again obtain a matrix equation for the Hamiltonian (neglecting additive constants):

$$\mathcal{H}^{\text{eff}} = \frac{1}{2}\sideset{}{'}\sum_{\boldsymbol{k}\neq 0}\left(c_{\boldsymbol{k}}^\dagger, c_{-\boldsymbol{k}}, d_{\boldsymbol{k}}^\dagger, d_{-\boldsymbol{k}}\right)\begin{pmatrix} \xi_{\boldsymbol{k}}+\frac{\kappa_0}{2} & \frac{\kappa_0}{2} & \kappa_0 & \kappa_0 \\ \frac{\kappa_0}{2} & \xi_{\boldsymbol{k}}+\frac{\kappa_0}{2} & \kappa_0 & \kappa_0 \\ \kappa_0 & \kappa_0 & \xi_{\boldsymbol{k}}+\frac{\kappa_0}{2} & \frac{\kappa_0}{2} \\ \kappa_0 & \kappa_0 & \frac{\kappa_0}{2} & \xi_{\boldsymbol{k}}+\frac{\kappa_0}{2} \end{pmatrix}\begin{pmatrix} c_{\boldsymbol{k}} \\ c_{-\boldsymbol{k}}^\dagger \\ d_{\boldsymbol{k}} \\ d_{-\boldsymbol{k}}^\dagger \end{pmatrix}$$

The microscopic coupling is now given by $\kappa_0 = \frac{UN_0}{N_{\rm s}} \equiv -\frac{|U|N_0}{N_{\rm s}}$. We eventually find the Bogoliubov quasi particle spectrum for the fragmented condensate as

$$\epsilon_{\boldsymbol{k}}^{\text{attr.}} = \sqrt{\xi_{\boldsymbol{k}}^2 + |\kappa_0|\xi_{\boldsymbol{k}}}$$

$$\overset{\boldsymbol{k}\to 0}{=} |\boldsymbol{k}|\sqrt{ta^2\frac{1}{\sqrt{2}}|\kappa_0|}\sqrt{1 + \frac{ta^2}{\sqrt{2}|\kappa_0|}|\boldsymbol{k}|^2} \ , \tag{A.33}$$

the critical velocity is now given by

$$v_c \overset{\text{attr. flux latt}}{=} \sqrt{\frac{t}{\sqrt{2}}|\kappa_0|} = \sqrt{\frac{t\,|U|\,N_0}{\sqrt{2}\,N_{\rm s}}} \ . \tag{A.34}$$

Appendix B

Spinon confinement

B.1 Transfer matrix method

In the following we briefly show a sketch of the calculations for the correlations of the SU(3) representation **8** VBS state, for the SU(3) representation **6** VBS state as well as for the SU(4) representation **10** VBS state. The results were already presented in Sec. 3.8.

B.1.1 SU(3) representation 8 VBS state

We begin with the matrix product representation of the states which we obtained in Sec. 3.8. Actually, we only need the knowledge of the matrix M_i which was introduced in Eq. (3.107),

$$M_i = \begin{pmatrix} \frac{2}{3}\left|\text{by}\right\rangle_i - \frac{1}{3}\left|\text{rc}\right\rangle_i - \frac{1}{3}\left|\text{gm}\right\rangle_i & \left|\text{ry}\right\rangle_i & \left|\text{gy}\right\rangle_i \\ \left|\text{bc}\right\rangle_i & -\frac{1}{3}\left|\text{by}\right\rangle_i + \frac{2}{3}\left|\text{rc}\right\rangle_i - \frac{1}{3}\left|\text{gm}\right\rangle_i & \left|\text{gc}\right\rangle_i \\ \left|\text{bm}\right\rangle_i & \left|\text{rm}\right\rangle_i & -\frac{1}{3}\left|\text{by}\right\rangle_i - \frac{1}{3}\left|\text{rc}\right\rangle_i + \frac{2}{3}\left|\text{gm}\right\rangle_i \end{pmatrix}$$

We follow the calculation of the static correlation function in the q-deformed SU(2) model studied by Klümper, Schadschneider, and Zittartz [86]. We wish to calculate

$$\frac{\left\langle \psi^{\text{L}}_{\mathbf{8}\,\text{VBS}}\right| J^a_i\, J^b_j \left|\psi^{\text{L}}_{\mathbf{8}\,\text{VBS}}\right\rangle}{\left\langle \psi^{\text{L}}_{\mathbf{8}\,\text{VBS}}\middle| \psi^{\text{L}}_{\mathbf{8}\,\text{VBS}}\right\rangle} = \delta_{ab}\, F(j - i), \tag{B.1}$$

in the thermodynamic limit. Due to SU(3) invariance the correlation function (B.1) is proportional to δ_{ab} and does not depend on a. Therefore we can choose a diagonal operator J^a, say J^8. Here

$$\left\langle \psi^{\text{L}}_{\mathbf{8}\,\text{VBS}}\right| = \text{tr}\left(\prod_i \tilde{M}_i\right), \tag{B.2}$$

where

$$\tilde{M}_i = \begin{pmatrix} \frac{2}{3}\left\langle\text{by}\right|_i - \frac{1}{3}\left\langle\text{rc}\right|_i - \frac{1}{3}\left\langle\text{gm}\right|_i & \left\langle\text{ry}\right|_i & \left\langle\text{gy}\right|_i \\ \left\langle\text{bc}\right|_i & -\frac{1}{3}\left\langle\text{by}\right|_i + \frac{2}{3}\left\langle\text{rc}\right|_i - \frac{1}{3}\left\langle\text{gm}\right|_i & \left\langle\text{gc}\right|_i \\ \left\langle\text{bm}\right|_i & \left\langle\text{rm}\right|_i & -\frac{1}{3}\left\langle\text{by}\right|_i - \frac{1}{3}\left\langle\text{rc}\right|_i + \frac{2}{3}\left\langle\text{gm}\right|_i \end{pmatrix}$$

First we calculate the norm of the state (we assume a chain with N sites):

$$\langle \psi^{\mathrm{L}}_{\mathbf{8}\,\mathrm{VBS}} | \psi^{\mathrm{L}}_{\mathbf{8}\,\mathrm{VBS}} \rangle \;=\; \tilde{M}^{b_1 b_2}_1 \, M^{a_1 a_2}_1 \, \tilde{M}^{b_2 b_3}_2 \, M^{a_2 a_3}_2 \cdots \tilde{M}^{b_N b_1}_N \, M^{a_N a_1}_N \tag{B.3}$$

$$\;=\; R^{b_1 b_2}_{a_1 a_2} \, R^{b_2 b_3}_{a_2 a_3} \cdots R^{b_N b_1}_{a_N a_1} = \mathrm{tr}\!\left(R^N \right), \tag{B.4}$$

where

$$R = \begin{pmatrix}
\frac{2}{3} & 0 & 0 & 0 & 1 & 0 & 0 & 0 & 1 \\
0 & -\frac{1}{3} & 0 & 0 & 0 & 0 & 0 & 0 & 0 \\
0 & 0 & -\frac{1}{3} & 0 & 0 & 0 & 0 & 0 & 0 \\
0 & 0 & 0 & -\frac{1}{3} & 0 & 0 & 0 & 0 & 0 \\
1 & 0 & 0 & 0 & \frac{2}{3} & 0 & 0 & 0 & 1 \\
0 & 0 & 0 & 0 & 0 & -\frac{1}{3} & 0 & 0 & 0 \\
0 & 0 & 0 & 0 & 0 & 0 & -\frac{1}{3} & 0 & 0 \\
0 & 0 & 0 & 0 & 0 & 0 & 0 & -\frac{1}{3} & 0 \\
1 & 0 & 0 & 0 & 1 & 0 & 0 & 0 & \frac{2}{3}
\end{pmatrix}$$

and we use the notation for tensor products as given e.g., in Ref. [90]. R can be diagonalized using

$$U = \begin{pmatrix}
\frac{1}{\sqrt{3}} & \frac{1}{\sqrt{2}} & \frac{1}{\sqrt{6}} & 0 & 0 & 0 & 0 & 0 & 0 \\
0 & 0 & 0 & 1 & 0 & 0 & 0 & 0 & 0 \\
0 & 0 & 0 & 0 & 1 & 0 & 0 & 0 & 0 \\
0 & 0 & 0 & 0 & 0 & 1 & 0 & 0 & 0 \\
\frac{1}{\sqrt{3}} & -\frac{1}{\sqrt{2}} & \frac{1}{\sqrt{6}} & 0 & 0 & 0 & 0 & 0 & 0 \\
0 & 0 & 0 & 0 & 0 & 0 & 1 & 0 & 0 \\
0 & 0 & 0 & 0 & 0 & 0 & 0 & 1 & 0 \\
0 & 0 & 0 & 0 & 0 & 0 & 0 & 0 & 1 \\
\frac{1}{\sqrt{3}} & 0 & -\frac{2}{\sqrt{6}} & 0 & 0 & 0 & 0 & 0 & 0
\end{pmatrix}$$

i.e.,

$$D = U^\dagger R U = \frac{1}{3}\,\mathrm{diag}\!\left(8, -1, -1, -1, -1, -1, -1, -1, -1 \right).$$

This yields

$$\langle \psi^{\mathrm{L}}_{\mathbf{8}\,\mathrm{VBS}} | \psi^{\mathrm{L}}_{\mathbf{8}\,\mathrm{VBS}} \rangle = \mathrm{Tr}\!\left(R^N \right) = \mathrm{Tr}\!\left(D^N \right) = \frac{1}{3^N}\left(8^N + (-1)^N \, 7 \right) \rightarrow \left(\frac{8}{3} \right)^N.$$

As a second step we need to evaluate

$$\langle \psi^{\mathrm{L}}_{\mathbf{8}\,\mathrm{VBS}} | \, J^8_i \, J^8_j \, | \psi^{\mathrm{L}}_{\mathbf{8}\,\mathrm{VBS}} \rangle = \mathrm{tr}\!\left(\tilde{J} \, R^{j-i-1} \, \tilde{J} \, R^{N+i-j-1} \right),$$

where

$$\tilde{J} = \left(J^8\right)^{b_1 b_2}_{a_1 a_2} = \tilde{M}^{b_1 b_2}_i \, J^8_i \, M^{a_1 a_2}_i$$

$$= \frac{\sqrt{3}}{2} \, \tilde{M}^{b_1 b_2}_i \begin{pmatrix} 0 & 0 & -\,|\mathrm{gy}\rangle \\ 0 & 0 & -\,|\mathrm{gc}\rangle \\ |\mathrm{bm}\rangle & |\mathrm{rm}\rangle & 0 \end{pmatrix}$$

$$= \frac{\sqrt{3}}{2} \begin{pmatrix} 0 & 0 & 0 & 0 & 0 & 0 & 0 & 0 & -1 \\ 0 & 0 & 0 & 0 & 0 & 0 & 0 & 0 & 0 \\ 0 & 0 & 0 & 0 & 0 & 0 & 0 & 0 & 0 \\ 0 & 0 & 0 & 0 & 0 & 0 & 0 & 0 & 0 \\ 0 & 0 & 0 & 0 & 0 & 0 & 0 & 0 & -1 \\ 0 & 0 & 0 & 0 & 0 & 0 & 0 & 0 & 0 \\ 0 & 0 & 0 & 0 & 0 & 0 & 0 & 0 & 0 \\ 0 & 0 & 0 & 0 & 0 & 0 & 0 & 0 & 0 \\ 1 & 0 & 0 & 0 & 1 & 0 & 0 & 0 & 0 \end{pmatrix}.$$

This yields

$$\left\langle \psi^{\mathrm{L}}_{\mathbf{8}\,\mathrm{VBS}} \right| J^8_i \, J^8_k \left| \psi^{\mathrm{L}}_{\mathbf{8}\,\mathrm{VBS}} \right\rangle = \mathrm{tr}\left(U^\dagger \tilde{J} U \, D^{j-i-1} \, U^\dagger \tilde{J} U \, D^{N+i-j-1} \right)$$

$$= \left(\frac{8}{3}\right)^N \frac{27}{16} \left[(-1)^{j-i}\, 8^{-j+i} + \frac{(-1)^{N+i-j}}{8^{N+i-j}} \right].$$

This yields for the correlation function

$$\frac{\left\langle \psi^{\mathrm{L}}_{\mathbf{8}\,\mathrm{VBS}} \right| J^a_i \, J^b_j \left| \psi^{\mathrm{L}}_{\mathbf{8}\,\mathrm{VBS}} \right\rangle}{\left\langle \psi^{\mathrm{L}}_{\mathbf{8}\,\mathrm{VBS}} \middle| \psi^{\mathrm{L}}_{\mathbf{8}\,\mathrm{VBS}} \right\rangle} = \delta_{ab}\, \frac{27}{16} \frac{(-1)^{j-i}\, 8^{-j+i} + \frac{(-1)^{N+i-j}}{8^{N+i-j}}}{1 + 7\frac{(-1)^N}{8^N}}.$$

Hence, taking $i = 0$ and $N \to \infty$ we find

$$F(j) = \frac{27}{16}\,(-1)^j\, 8^{-j} \propto e^{-j/\xi}, \tag{B.5}$$

where $\xi = 1/\ln 8 \approx 0.48$. The same result is obtained for $\left|\psi^{\mathrm{R}}_{\mathbf{8}\,\mathrm{VBS}}\right\rangle$.

In the same way one can show for the adjoint SU(n) VBS model (3.71) that the correlation function (B.1) is in the thermodynamic limit $N \to \infty$

$$\delta_{ab}\, \frac{n^3}{2(n^2-1)}\,(-1)^{-k}\,(n^2-1)^{-k},$$

which simplifies for $n = 3$ to Eq. (B.5) and for $n = 2$ to the SU(2) result [11]

$$\frac{\left\langle \psi_{\mathrm{AKLT}} \right| S^a_0 \, S^b_k \left| \psi_{\mathrm{AKLT}} \right\rangle}{\left\langle \psi_{\mathrm{AKLT}} \middle| \psi_{\mathrm{AKLT}} \right\rangle} = \delta_{ab}\, \frac{4}{3}\,(-1)^{-k}\, 3^{-k}.$$

B.1.2 SU(3) representation **6** VBS state

Again we start with the matrix product representation of the SU(3) rep.**6** VBS state (see Sec. 3.8),

$$|\psi_{\mathbf{6}\,\text{VBS}}\rangle = \text{tr}\left(\prod_\alpha M_\alpha \bar{M}_\alpha\right) = M_1^{a_1 b_1}\, \bar{M}_1^{b_1 a_2}\, M_2^{a_2 b_2}\, \bar{M}_2^{b_2 a_3} \ldots M_{N/3}^{a_{N/3} b_{N/3}}\, \bar{M}_{N/3}^{b_{N/3} a_1},$$

where $\alpha = 1, \ldots, N/3$ is an artificial index which stands for groups of three lattice sites, i.e., $\alpha = 3$ represents the lattice sites $i = 7, 8, 9$. The matrices are given by

$$M_\alpha = \begin{pmatrix} |\text{bb}\rangle_i & |\text{br}\rangle_i & |\text{bg}\rangle_i \\ |\text{br}\rangle_i & |\text{rr}\rangle_i & |\text{rg}\rangle_i \\ |\text{bg}\rangle_i & |\text{rg}\rangle_i & |\text{gg}\rangle_i \end{pmatrix}, \tag{B.6}$$

where $i = 3(\alpha - 1) + 1$, and

$$\bar{M}_\alpha = \begin{pmatrix} |\text{yy}\rangle_{\bar{i}} & |\text{yc}\rangle_{\bar{i}} & |\text{ym}\rangle_{\bar{i}} \\ |\text{yc}\rangle_{\bar{i}} & |\text{cc}\rangle_{\bar{i}} & |\text{cm}\rangle_{\bar{i}} \\ |\text{ym}\rangle_{\bar{i}} & |\text{cm}\rangle_{\bar{i}} & |\text{mm}\rangle_{\bar{i}} \end{pmatrix}, \tag{B.7}$$

where $\bar{i}$ stands for the coupled lattice sites $3(\alpha - 1) + 2$ and $3(\alpha - 1) + 3$. We wish to calculate

$$\frac{\langle\psi_{\mathbf{6}\,\text{VBS}}|\, J_0^a\, J_k^b\, |\psi_{\mathbf{6}\,\text{VBS}}\rangle}{\langle\psi_{\mathbf{6}\,\text{VBS}}|\, \psi_{\mathbf{6}\,\text{VBS}}\rangle}, \tag{B.8}$$

in the thermodynamic limit. Here

$$\langle\psi_{\mathbf{6}\,\text{VBS}}^{\text{L}}| = \text{tr}\left(\prod_\alpha \tilde{M}_\alpha \tilde{\bar{M}}_\alpha\right),$$

where the matrices $\tilde{M}_\alpha$ and $\tilde{\bar{M}}_\alpha$ are obtained from (B.6) and (B.7) by replacing the kets by bras. First we calculate the norm of the state (we assume a chain with $N = 3m$ sites):

$$\begin{aligned} \langle\psi_{\mathbf{6}\,\text{VBS}}|\, \psi_{\mathbf{6}\,\text{VBS}}\rangle &= \tilde{M}_1^{c_1 d_1}\, M_1^{a_1 b_1}\, \tilde{\bar{M}}_1^{d_1 c_2}\, \bar{M}_1^{b_1 a_2}\, \tilde{M}_2^{c_2 d_2}\, M_2^{a_2 b_2}\, \tilde{\bar{M}}_2^{d_2 c_3}\, \bar{M}_2^{b_2 a_3} \\ &\quad \cdots \tilde{M}_{N/3}^{c_{N/3} d_{N/3}}\, M_{N/3}^{a_{N/3} b_{N/3}}\, \tilde{\bar{M}}_{N/3}^{d_{N/3} c_1}\, \bar{M}_{N/3}^{b_{N/3} a_1} \\ &= R_{a_1 b_2}^{c_1 d_1}\, \bar{R}_{b_1 a_2}^{d_1 c_2}\, R_{a_2 b_2}^{c_2 d_2}\, \bar{R}_{b_2 a_3}^{d_2 c_3} \cdots R_{a_{N/3} b_{N/3}}^{c_{N/3} d_{N/3}}\, \bar{R}_{b_{N/3} a_1}^{d_{N/3} c_1} \\ &= S_{a_1 a_2}^{c_1 c_2}\, S_{a_2 a_3}^{c_2 c_3} \cdots S_{a_{N/3} a_1}^{c_{N/3} c_1} = \text{Tr}\left(S^{N/3}\right), \end{aligned}$$

where

$$R = \bar{R} = \begin{pmatrix} 1 & 0 & 0 & 0 & 1 & 0 & 0 & 0 & 1 \\ 0 & 0 & 0 & 1 & 0 & 0 & 0 & 0 & 0 \\ 0 & 0 & 0 & 0 & 0 & 0 & 1 & 0 & 0 \\ 0 & 1 & 0 & 0 & 0 & 0 & 0 & 0 & 0 \\ 1 & 0 & 0 & 0 & 1 & 0 & 0 & 0 & 1 \\ 0 & 0 & 0 & 0 & 0 & 0 & 0 & 1 & 0 \\ 0 & 0 & 1 & 0 & 0 & 0 & 0 & 0 & 0 \\ 0 & 0 & 0 & 0 & 0 & 1 & 0 & 0 & 0 \\ 1 & 0 & 0 & 0 & 1 & 0 & 0 & 0 & 1 \end{pmatrix}$$

and

$$S = R\bar{R} = \begin{pmatrix} 3 & 0 & 0 & 0 & 3 & 0 & 0 & 0 & 3 \\ 0 & 1 & 0 & 0 & 0 & 0 & 0 & 0 & 0 \\ 0 & 0 & 1 & 0 & 0 & 0 & 0 & 0 & 0 \\ 0 & 0 & 0 & 1 & 0 & 0 & 0 & 0 & 0 \\ 3 & 0 & 0 & 0 & 3 & 0 & 0 & 0 & 3 \\ 0 & 0 & 0 & 0 & 0 & 1 & 0 & 0 & 0 \\ 0 & 0 & 0 & 0 & 0 & 0 & 1 & 0 & 0 \\ 0 & 0 & 0 & 0 & 0 & 0 & 0 & 1 & 0 \\ 3 & 0 & 0 & 0 & 3 & 0 & 0 & 0 & 3 \end{pmatrix}$$

S can be diagonalized using

$$U = \begin{pmatrix} \frac{1}{\sqrt{3}} & 0 & 0 & 0 & \frac{1}{\sqrt{2}} & 0 & 0 & 0 & \frac{1}{\sqrt{6}} \\ 0 & 1 & 0 & 0 & 0 & 0 & 0 & 0 & 0 \\ 0 & 0 & 1 & 0 & 0 & 0 & 0 & 0 & 0 \\ 0 & 0 & 0 & 1 & 0 & 0 & 0 & 0 & 0 \\ \frac{1}{\sqrt{3}} & 0 & 0 & 0 & -\frac{1}{\sqrt{2}} & 0 & 0 & 0 & \frac{1}{\sqrt{6}} \\ 0 & 0 & 0 & 0 & 0 & 1 & 0 & 0 & 0 \\ 0 & 0 & 0 & 0 & 0 & 0 & 1 & 0 & 0 \\ 0 & 0 & 0 & 0 & 0 & 0 & 0 & 1 & 0 \\ \frac{1}{\sqrt{3}} & 0 & 0 & 0 & 0 & 0 & 0 & 0 & -\frac{2}{\sqrt{6}} \end{pmatrix}$$

i.e.,

$$D = U^{\dagger} S U = \text{diag}\big(9, 1, 1, 1, 0, 1, 1, 1, 0\big).$$

This yields

$$\langle \psi_{\mathbf{6}\,\text{VBS}} | \psi_{\mathbf{6}\,\text{VBS}} \rangle = \text{Tr}\Big(D^{N/3}\Big) = 9^{N/3} + 6 \to 9^{N/3}.$$

Due to SU(3) invariance the correlation function (B.8) is proportional to δ_{ab} and does not depend on a, i.e.,

$$\frac{\langle \psi_{\mathbf{6}\,\text{VBS}} | J_0^a J_k^b | \psi_{\mathbf{6}\,\text{VBS}} \rangle}{\langle \psi_{\mathbf{6}\,\text{VBS}} | \psi_{\mathbf{6}\,\text{VBS}} \rangle} = \delta_{ab} \, F(k).$$

Therefore we can choose a diagonal operator J^a, say J^3. We find

$$\langle \psi_{\mathbf{6}\,\text{VBS}} | J_i^3 J_k^3 | \psi_{\mathbf{6}\,\text{VBS}} \rangle = \text{Tr}\Big(\tilde{J} S^{k-i-1} \tilde{J} S^{N/3+i-k-1} \Big),$$

where

$$J^3 = \left(J^3\right)^{cd}_{ab} = \tilde{M}^{cd}_i J^3_i M^{ab}_i$$

$$= \tilde{M}^{cd}_i \begin{pmatrix} |\text{bb}\rangle_i & 0 & \frac{1}{2}|\text{bg}\rangle_i \\ 0 & -|\text{rr}\rangle_i & -\frac{1}{2}|\text{rg}\rangle_i \\ \frac{1}{2}|\text{bg}\rangle_i & -\frac{1}{2}|\text{rg}\rangle_i & 0 \end{pmatrix}$$

$$= \begin{pmatrix} 1 & 0 & 0 & 0 & 0 & 0 & 0 & 0 & 1/2 \\ 0 & 0 & 0 & 0 & 0 & 0 & 0 & 0 & 0 \\ 0 & 0 & 0 & 0 & 0 & 0 & 1/2 & 0 & 0 \\ 0 & 0 & 0 & 0 & 0 & 0 & 0 & 0 & 0 \\ 0 & 0 & 0 & 0 & -1 & 0 & 0 & 0 & -1/2 \\ 0 & 0 & 0 & 0 & 0 & 0 & 0 & -1/2 & 0 \\ 0 & 0 & 1/2 & 0 & 0 & 0 & 0 & 0 & 0 \\ 0 & 0 & 0 & 0 & 0 & -1/2 & 0 & 0 & 0 \\ 1/2 & 0 & 0 & 0 & -1/2 & 0 & 0 & 0 & 0 \end{pmatrix}$$

and

$$\tilde{J} = U^\dagger J^3 \bar{R} U = \begin{pmatrix} 0 & 0 & 0 & 0 & 0 & 0 & 0 & 0 & 0 \\ 0 & 0 & 0 & 0 & 0 & 0 & 0 & 0 & 0 \\ 0 & 0 & 1/2 & 0 & 0 & 0 & 0 & 0 & 0 \\ 0 & 0 & 0 & 0 & 0 & 0 & 0 & 0 & 0 \\ 3\sqrt{3/2} & 0 & 0 & 0 & 0 & 0 & 0 & 0 & 0 \\ 0 & 0 & 0 & 0 & 0 & -1/2 & 0 & 0 & 0 \\ 0 & 0 & 0 & 0 & 0 & 0 & 1/2 & 0 & 0 \\ 0 & 0 & 0 & 0 & 0 & 0 & 0 & -1/2 & 0 \\ 0 & 0 & 0 & 0 & 0 & 0 & 0 & 0 & 0 \end{pmatrix}.$$

This yields (we keep only the leading term)

$$\langle \psi_{\mathbf{6}\,\text{VBS}}| \, J^3_i J^3_k \, |\psi_{\mathbf{6}\,\text{VBS}}\rangle = 1.$$

Hence, taking $i = 0$ and $N \to \infty$ we find

$$F(k) = 0,$$

i.e., there are no correlations between more than three neighboring sites. The situation is, hence, similar to the one in the Majumdar–Ghosh model where neighboring dimers (or valence bonds) are uncorrelated.

B.1.3   SU(4) representation 10 VBS state

The matrix product representation of the SU(4) representation **10** VBS state was in Sec. 3.8 derived as

$$
M_i = \begin{pmatrix}
b_6^\dagger b_1^\dagger & b_6^\dagger b_2^\dagger & b_6^\dagger b_3^\dagger & b_6^\dagger b_4^\dagger & b_6^\dagger b_5^\dagger & b_6^\dagger b_6^\dagger \\
-b_5^\dagger b_1^\dagger & -b_5^\dagger b_2^\dagger & -b_5^\dagger b_3^\dagger & -b_5^\dagger b_4^\dagger & -b_5^\dagger b_5^\dagger & -b_5^\dagger b_6^\dagger \\
b_4^\dagger b_1^\dagger & b_4^\dagger b_2^\dagger & b_4^\dagger b_3^\dagger & b_4^\dagger b_4^\dagger & b_4^\dagger b_5^\dagger & b_4^\dagger b_6^\dagger \\
b_3^\dagger b_1^\dagger & b_3^\dagger b_2^\dagger & b_3^\dagger b_3^\dagger & b_3^\dagger b_4^\dagger & b_3^\dagger b_5^\dagger & b_3^\dagger b_6^\dagger \\
-b_2^\dagger b_1^\dagger & -b_2^\dagger b_2^\dagger & -b_2^\dagger b_3^\dagger & -b_2^\dagger b_4^\dagger & -b_2^\dagger b_5^\dagger & -b_2^\dagger b_6^\dagger \\
b_1^\dagger b_1^\dagger & b_1^\dagger b_2^\dagger & b_1^\dagger b_3^\dagger & b_1^\dagger b_4^\dagger & b_1^\dagger b_5^\dagger & b_1^\dagger b_6^\dagger
\end{pmatrix}_i |0\rangle_i .
$$

Assuming periodic boundary conditions the two–fold degenerate VBS state can then be written as the trace of the matrix product

$$
\left|\psi_{\text{even}}^{\text{SU(4)rep.10}}\right\rangle = \text{tr}\left(\prod_{\substack{i=1 \\ i\,\text{even}}}^{N} M_i \right)
$$

and

$$
\left|\psi_{\text{odd}}^{\text{SU(4)rep.10}}\right\rangle = \text{tr}\left(\prod_{\substack{i=1 \\ i\,\text{odd}}}^{N} M_i \right).
$$

In the following we use the state $\left|\psi_{\text{even}}^{\text{SU(4)rep.10}}\right\rangle$ only and write for convenience $|\psi_{\text{rep10}}\rangle$.

Now we wish to calculate

$$
\frac{\langle \psi_{\text{rep10}}| J_1^3 J_j^3 |\psi_{\text{rep10}}\rangle}{\langle \psi_{\text{rep10}}|\psi_{\text{rep10}}\rangle} = F(j) \tag{B.9}
$$

and introduce the 36×36 transfer matrix R at any lattice site as

$$
R_{\alpha\beta} = R_{(\sigma\tau),(\sigma'\tau')} = \tilde{M}_{\sigma\sigma'} M_{\tau\tau'}
$$

where we have introduced the complex conjugated matrix $\tilde{M}$ according to $\tilde{M}_{\sigma\sigma'} = M_{\sigma\sigma'}^\star$, i.e., by simply taking the complex conjugate of each matrix element in Eq. (3.113) without transposing the matrix. The order of the indices is $\alpha, \beta = 1, 2, \ldots, 36 \leftrightarrow (11), (12), \ldots, (66)$. The reader may notice that we do not explicitly write out the 36×36 transfer matrices due to the page restrictions of this thesis. The evaluation of these matrices, however, is equivalent to the previous cases and goes without problems. The norm of the VBS state is now given by

$$
\langle \psi_{\text{rep10}}|\psi_{\text{rep10}}\rangle = \text{tr}\left(R^M\right) = 7^M + 15(-1)^M + 20
$$

where we have evaluated the trace by diagonalization of R. M is half the number of lattice sites, $M = N/2$. In the second step we calculate the expectation value

$\langle \psi_{\text{rep10}}| J_1^3 J_j^3 |\psi_{\text{rep10}}\rangle$. We introduce the transfer–matrix representation of the spin operator J^3 defined as

$$\hat{J}_{\alpha\beta} = \hat{J}_{(\sigma,\tau),(\sigma',\tau')} = \tilde{M}_{\sigma\sigma'} J^3 M_{\tau\tau'}.$$

Here the operator J^3 acts on the elements of M as

$$J^3 b_1^\dagger = J^3 b_6^\dagger = 0, \quad J^3 b_2^\dagger = -\frac{1}{2} b_2^\dagger, \quad J^3 b_3^\dagger = \frac{1}{2} b_3^\dagger, \quad J^3 b_4^\dagger = -\frac{1}{2} b_4^\dagger, \quad J^3 b_5^\dagger = \frac{1}{2} b_5^\dagger,$$

as J^3 can defined in the bosonic basis as

$$J^3 = 1/2 \left(-b_2^\dagger b_2 + b_3^\dagger b_3 - b_4^\dagger b_4 + b_5^\dagger b_5 \right) \ .$$

This yields

$$\langle \psi_{\text{rep10}}| J_1^3 J_j^3 |\psi_{\text{rep10}}\rangle = \text{tr}\big(J_1 R^{j-2} J_j R^{M-j} \big)$$

which can be evaluated by diagonalization of R. Finally we arrive at

$$\langle J_1^a J_j^b \rangle = \frac{\langle \psi_{\text{rep10}}| J_1^a J_j^b |\psi_{\text{rep10}}\rangle}{\langle \psi_{\text{rep10}}\rangle \psi_{\text{rep10}}}$$

$$= \delta_{ab} \frac{7^{-j}\left(-\frac{1}{144} - \frac{31}{3}(-1)^j\right) - \frac{1}{7^M}\left(\frac{7^j}{7056} - \frac{1}{144} + \frac{65}{12}(-1)^j + (-1)^{M+j}\left(\frac{65}{12} + \frac{31}{147}7^j\right)\right)}{1 + \frac{1}{7^M}\left(20 + 15(-1)^M\right)}$$

$$\overset{M\to\infty}{\longrightarrow} (-1)^{j-1}\frac{31}{3}\frac{1}{7^j} - \frac{1}{144}\frac{1}{7^j} \sim \frac{1}{7^j} \sim e^{-j/\xi}$$

with the correlation length $\xi = 1/\ln 7 \approx 0.51$.

B.2   Representation theory of SU(n) for pedestrians

Young tableaux and representations of SU(2)

Figure B.1: Tensor product of two $S = \frac{1}{2}$ spins with Young tableaux and weight diagrams of the occurring SU(2) representations. S^z is the diagonal generator.

Let us begin with a review of Young tableaux and the representations of SU(2). The group SU(2) has three generators S^a, $a = 1, 2, 3$, which obey the algebra (3.2) The representations of SU(2) are classified by the spin S, which takes integer or half-integer values. The fundamental representation of SU(2) has spin $S = \frac{1}{2}$, it contains the two states $|\uparrow\rangle$ and $|\downarrow\rangle$. Higher-dimensional representations can be constructed as tensor products of fundamental representations, which is conveniently accomplished using Young tableaux (see *e.g.* [76]). These tableaux are constructed as follows (see Figs. B.1 and B.2 for examples). For each of the N spins, draw a box numbered consecutively from left to right. The representations of SU(2) are obtained by putting the boxes together such that the numbers assigned to them increase in each row from left to right and in each column from top to bottom. Each tableau indicates symmetrization over all boxes in the same row, and antisymmetrization over all boxes in the same column. This implies that we cannot have more than two boxes on top of each other. If κ_i denotes the number of boxes in the ith row, the spin is given by $S = \frac{1}{2}(\kappa_1 - \kappa_2)$.

To be more explicit, let us consider the tensor product $\frac{1}{2} \otimes \frac{1}{2} \otimes \frac{1}{2}$ depicted in

Figure B.2: Tensor product of three $S = \frac{1}{2}$ spins with Young tableaux. For SU(n) with $n > 2$, the tableau with three boxes on top of each other exists as well.
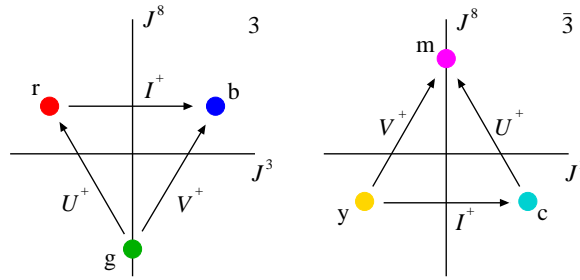
Figure B.3: (Color online) a) Weight diagram of the fundamental SU(3) representation $\mathbf{3} = (1,0)$. b) Weight diagram of the complex conjugate representation $\bar{\mathbf{3}} = (0,1)$. J^3 and J^8 denote the diagonal generators, I^+, U^+, and V^+ the raising operators.

Fig. B.2 in detail. We start with the state $\left|\frac{3}{2}, \frac{3}{2}\right\rangle = |\uparrow\uparrow\uparrow\rangle$, and hence find

$$\left|\tfrac{3}{2}, \tfrac{1}{2}\right\rangle = \frac{1}{\sqrt{3}} S^- \left|\tfrac{3}{2}, \tfrac{3}{2}\right\rangle = \frac{1}{\sqrt{3}}\big(|\uparrow\uparrow\downarrow\rangle + |\uparrow\downarrow\uparrow\rangle + |\downarrow\uparrow\uparrow\rangle\big). \tag{B.10}$$

The two states with $S = S^z = \frac{1}{2}$ must be orthogonal to (B.10). A convenient choice of basis is

$$\left|\tfrac{1}{2}, \tfrac{1}{2}, +\right\rangle = \frac{1}{\sqrt{3}}\big(|\uparrow\uparrow\downarrow\rangle + \omega\,|\uparrow\downarrow\uparrow\rangle + \omega^2\,|\downarrow\uparrow\uparrow\rangle\big),$$
$$\left|\tfrac{1}{2}, \tfrac{1}{2}, -\right\rangle = \frac{1}{\sqrt{3}}\big(|\uparrow\uparrow\downarrow\rangle + \omega^2\,|\uparrow\downarrow\uparrow\rangle + \omega\,|\downarrow\uparrow\uparrow\rangle\big), \tag{B.11}$$

where $\omega = \exp\!\big(i\frac{2\pi}{3}\big)$. The tableaux tell us primarily that two such basis states exist, not what a convenient choice of orthonormal basis states may be.

The irreducible representations of SU(2) can be classified through the eigenvalues of the Casimir operator given by the square of the total spin $\mathbf{S}^2$. The special feature of $\mathbf{S}^2$ is that it commutes with all generators S^a and is hence by Schur's lemma [40] proportional to the identity for any finite-dimensional irreducible representation. The eigenvalues are given by

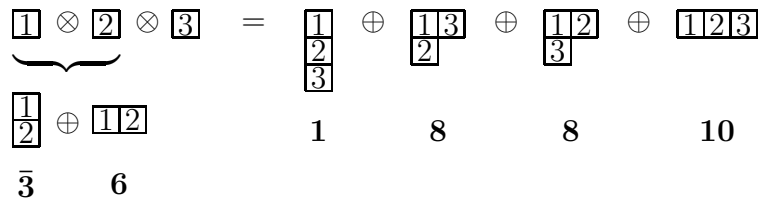$$\mathbf{S}^2 = \mathcal{C}^2_{\mathrm{SU}(2)} = S(S+1).$$

Figure B.4: Tensor product $\mathbf{3} \otimes \mathbf{3} \otimes \mathbf{3}$ with Young tableaux.

$$\underbrace{}_{\mu_2 \text{ columns}} \underbrace{}_{\mu_1 \text{ boxes}}$$
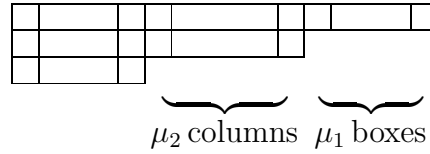
Figure B.5: Dynkin coordinates (μ_1, μ_2) for a given Young tableau. The columns containing three boxes represent additional SU(3) singlet factors, which yield equivalent representations and hence leave the Dynkin coordinates (μ_1, μ_2) unchanged.

B.2.1   Representation theory of SU(3)

The group SU(3) has eight generators J^a, $a = 1, \ldots, 8$, which obey the algebra

$$\left[J^a, J^b \right] = f^{abc} J^c, \tag{B.12}$$

where the structure constants f^{abc} are given in App. B.2.4. For SU(3) we have two diagonal generators, usually chosen to be J^3 and J^8, and six generators which define the ladder operators $I^{\pm} = J^1 \pm i J^2$, $U^{\pm} = J^6 \pm i J^7$, and $V^{\pm} = J^4 \pm i J^5$, respectively. An explicit realization of (B.12) is, for example, given by the J^a's as expressed in terms of Gell-Mann matrices in (3.19). This realization defines the fundamental representation **3** of SU(3) illustrated in Fig. B.3a. It is three-dimensional, and we have chosen to label the basis states by the colors blue (b), red (r), and green (g). The weight diagram depicted in Fig. B.3a instructs us about the eigenvalues of the diagonal generators as well as the actions of the ladder operators on the basis states.

All other representations of SU(3) can be constructed by taking tensor products of reps. **3**, which is again most conveniently accomplished using Young tableaux (see Fig. B.4 for an example). The antisymmetrization over all boxes in the same column implies that we cannot have more than three boxes on top of each other. Each tableaux stands for an irreducible representation of SU(3), which can be uniquely labeled by their highest weight or Dynkin coordinates (μ_1, μ_2) [40, 54] (see Fig. B.5). For example, the fundamental representation **3** has Dynkin coordinates (1,0). Note that all columns containing three boxes are superfluous, as the antisymmetrization of three colors yields only one state. In particular, the SU(3) singlet has Dynkin coordinates (0,0). In general, the dimension of a representation (μ_1, μ) is given by $\frac{1}{2}(\mu_1 + 1)(\mu_2 + 1)(\mu_1 + \mu_2 + 2)$. The labeling using bold numbers refers to the dimensions of the representations alone. Although this labeling is not unique, it will mostly be sufficient for our purposes. A representation $\boldsymbol{m}$ and its conjugated counterpart $\overline{\boldsymbol{m}}$ are related to each other by interchange of their Dynkin coordinates.

B.2.2   Examples of representations of SU(3)

We now consider some specific representations of SU(3) in detail. As starting point we use the fundamental representation **3** spanned by the states $|b\rangle$, $|r\rangle$, and $|g\rangle$. The second three-dimensional representation $\overline{\mathbf{3}}$ is obtained by antisymmetrically coupling two reps. **3**. The Dynkin coordinates of the rep. $\overline{\mathbf{3}}$ are (0,1), i.e., the reps. **3** and $\overline{\mathbf{3}}$ are complex conjugate of each other. An explicit basis of the rep. $\overline{\mathbf{3}}$ is given by the
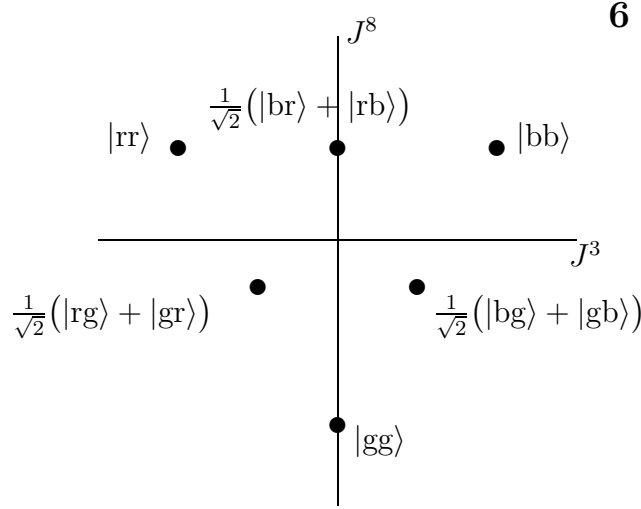
Figure B.6: Weight diagram of the representation $\mathbf{6} = (2,0)$. The weight diagram of the conjugate representation $\bar{\mathbf{6}} = (0,2)$ is obtained by reflection at the origin [40].

colors yellow (y), cyan (c), and magenta (m),

$$
\begin{aligned}
|y\rangle &= \frac{1}{\sqrt{2}}\big(|rg\rangle - |gr\rangle\big), \\
|c\rangle &= \frac{1}{\sqrt{2}}\big(|gb\rangle - |bg\rangle\big), \\
|m\rangle &= \frac{1}{\sqrt{2}}\big(|br\rangle - |rb\rangle\big).
\end{aligned}
\tag{B.13}
$$

The weight diagram is shown in Fig. B.3.b. The generators are given by (3.19) with λ^a replaced by $-(\lambda^a)^*$, where * denotes complex conjugation of the matrix elements [54]. In particular, we find $I^+ |y\rangle = - |c\rangle$, $U^+ |c\rangle = - |m\rangle$, and $V^+ |y\rangle = - |m\rangle$.

The six-dimensional representation $\mathbf{6}$ has Dynkin coordinates (2,0), and can hence be constructed by symmetrically coupling two reps. $\mathbf{3}$. The basis states of the rep. $\mathbf{6}$ are shown in Fig. B.6. The conjugate representation $\bar{\mathbf{6}}$ can be constructed by symmetrically coupling two reps. $\bar{\mathbf{3}}$.

Let us now consider the tensor product $\mathbf{3} \otimes \bar{\mathbf{3}} = \mathbf{1} \oplus \mathbf{8}$. The weight diagram of the so-called adjoint representation $\mathbf{8} = (1,1)$ is shown in Fig. B.7. The states can be constructed starting from the highest weight state $|bm\rangle$, yielding $I^- |bm\rangle = |rm\rangle$, $U^- |bm\rangle = - |bc\rangle$, $V^- |bm\rangle = |gm\rangle - |by\rangle$, and so on. This procedure yields two linearly independent states with $J^3 = J^8 = 0$. The representation $\mathbf{8}$ can also be obtained by coupling of the reps. $\mathbf{6}$ and $\mathbf{3}$, as can be seen from the Young tableaux in Fig. B.4. On a more abstract level, the adjoint representation is the representation we obtain if we consider the generators J^a themselves basis vectors. In the weight diagram shown in Fig. B.7, the generators J^3 and J^8 correspond to the two states at the origin, whereas the ladder operators $I^\pm$, $U^\pm$, and $V^\pm$ correspond to the states at the six surrounding points. In the notation of Fig. B.7, the singlet orthogonal to $\mathbf{8}$ is given by $\frac{1}{\sqrt{3}}\big(|by\rangle + |rc\rangle + |gm\rangle\big)$.
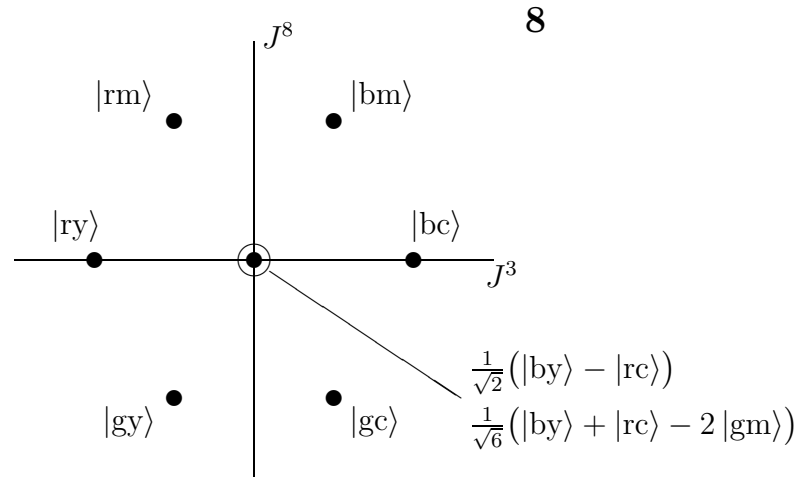
Figure B.7: Weight diagram of the adjoint representation $\mathbf{8} = (1,1)$. The state with $J^3 = J^8 = 0$ is doubly degenerate [40]. Note that two reps. $\mathbf{8}$ can be constructed by combining three fundamental reps. $\mathbf{3}$ (colors), just as two reps. $\frac{1}{2}$ can be constructed by combining three SU(2) spins (cf. (B.11)). The states in the diagram span a basis for one of these representations.

The weight diagrams of four other representations relevant to our purposes below are shown in Figs. B.8 to B.10.

It is known that the physical properties of SU(2) spin chains crucially depend on whether on the lattice sites are integer or half-integer spins. A similar distinction can be made for SU(3) chains, as elaborated in Sec. **??**. The distinction integer or half-integer spin for SU(2) is replaced by a distinction between three families of irreducible representations of SU(3): either the number of boxes in the Young tableau is divisible by three without remainder (e.g., $\mathbf{1}$, $\mathbf{8}$, $\mathbf{10}$, $\mathbf{27}$), with remainder one (e.g., $\mathbf{3}$, $\bar{\mathbf{6}}$, $\mathbf{15}$, $\mathbf{15'}$), or with remainder two (e.g., $\bar{\mathbf{3}}$, $\mathbf{6}$, $\overline{\mathbf{15}}$, $\overline{\mathbf{15}}'$).

While SU(2) has only one Casimir operator, SU(3) has two. The quadratic
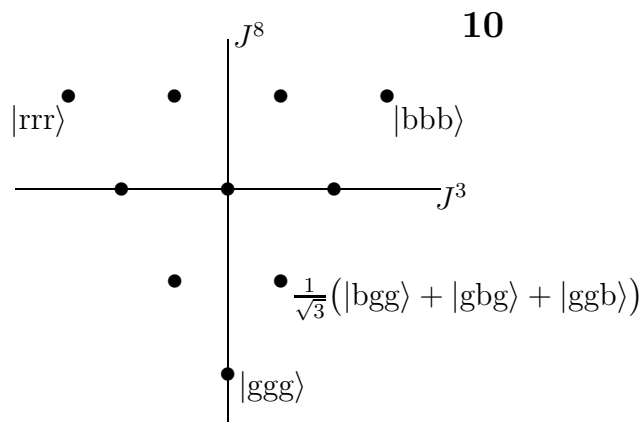

Figure B.8: Weight diagram of the representation $\mathbf{10} = (3,0)$. The weight diagram of the conjugate representation $\overline{\mathbf{10}} = (0,3)$ is obtained by reflection at the origin [40].
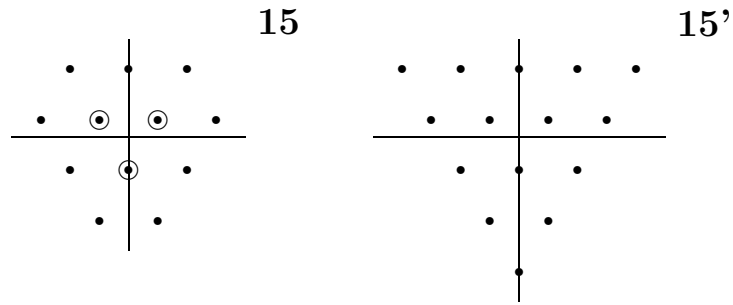
Figure B.9: Weight diagram of the representations $\mathbf{15} = (2,1)$ and $\mathbf{15'} = (4,0)$.

Casimir operator is defined as

$$\boldsymbol{J}^2 = \sum_{a=1}^{8} J^a J^a, \tag{B.14}$$

where the J^a's are the generators of the representation. As $\boldsymbol{J}^2$ commutes with all generators J^a it is proportional to the identity for any finite-dimensional irreducible representation. The eigenvalue in a representation with Dynkin coordinates (μ_1, μ_2) is [40]

$$\boldsymbol{J}^2 = \mathcal{C}^2_{\mathrm{SU}(3)}(\mu_1, \mu_2) = \frac{1}{3}\big(\mu_1^2 + \mu_1\mu_2 + \mu_2^2 + 3\mu_1 + 3\mu_2\big). \tag{B.15}$$

We have chosen the normalization in (B.15) according to the convention

$$\mathcal{C}^2_{\mathrm{SU}(n)}(\text{adjoint representation}) = n,$$

which yields $\mathcal{C}^2_{\mathrm{SU}(3)}(1,1) = 3$ for the representation $\mathbf{8}$. Note that the quadratic Casimir operator cannot be used to distinguish between a representation and its conjugate. This distinction would require the cubic Casimir operator [40], which we will not need for our purposes.
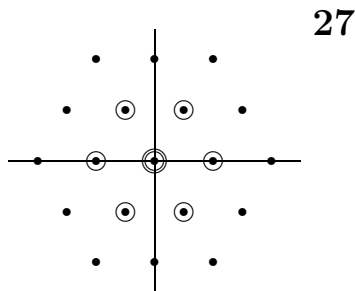

Figure B.10: Weight diagram of the self-conjugate representation $\mathbf{27} = (2,2)$. The state with $J^3 = J^8 = 0$ is three-fold degenerate [40].

B.2.3   Representation theory of SU(4) and examples of SU(4) representations

The group SU(4) has fifteen generators V^a, $a = 1, \ldots, 15$. The three diagonal generators are V^3, V^8, and V^{15} (SU(n) has $n - 1$ diagonal generators). The twelve remaining generators form the ladder operators as in the SU(3) case. The weight diagrams are now three–dimensional, the SU(4) Young tableaux consists of up to three rows, and the representations can be labeled by three Dynkin labels (μ_1, μ_2, μ_3). The weight diagram of the fundamental representation of SU(4) is shown in Fig. B.11. All
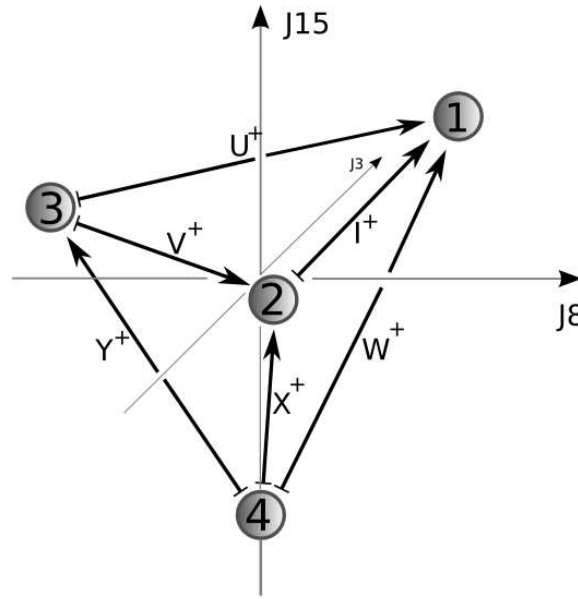
Figure B.11: Weight diagram of the fundamental representation of SU(4). The action of the six ladder operators I^+, U^+, V^+, W^+, X^+, and Y^+ are also shown.

other representations of SU(4) can be constructed by taking tensor products of representations **4**, which is again most conveniently accomplished by Young tableaux, e.g.,

$$\mathbf{4} \otimes \mathbf{4} \; = \; \mathbf{10} \; \oplus \; \mathbf{6} \; .$$

We have obtained a totally symmetric representation $\mathbf{10} = (2, 0, 0)$ and and totally anti–symmetric representation $\mathbf{6} = (0, 1, 0)$. Note that the rep.**6** is self–conjugate,

$$\mathbf{6} \; \otimes \; \mathbf{6} \; = \; \text{singlet} \; \oplus \; \ldots \; . \tag{B.16}$$

The totally symmetric representation **10** is shown in Fig. B.12.

One can imagine the weight diagram of the rep.**10** as the combination of four tetrahedra. All corners are the states in its weight diagram, see Fig. B.12. The inner "free" space forms an octahedron. Its corners form the states of the totally anti–symmetric representation **6** of SU(4). The corresponding phase diagram of the representation **6** is shown in Fig. B.13.
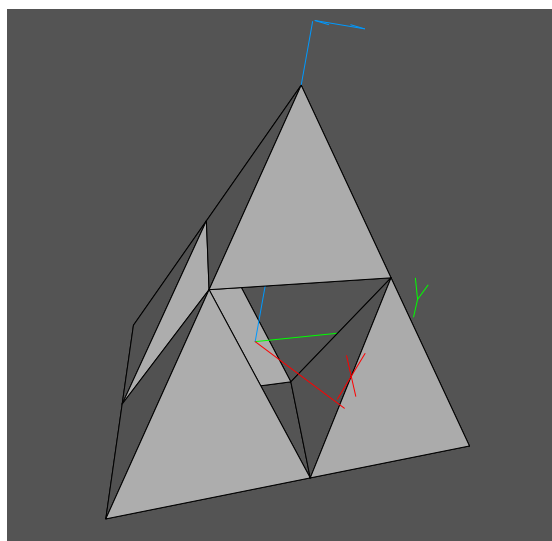
Figure B.12: Weight diagram of the ten–dimensional representation **10** of SU(4). The corners of the "small" tetrahedra form the ten states of the rep. **10**.
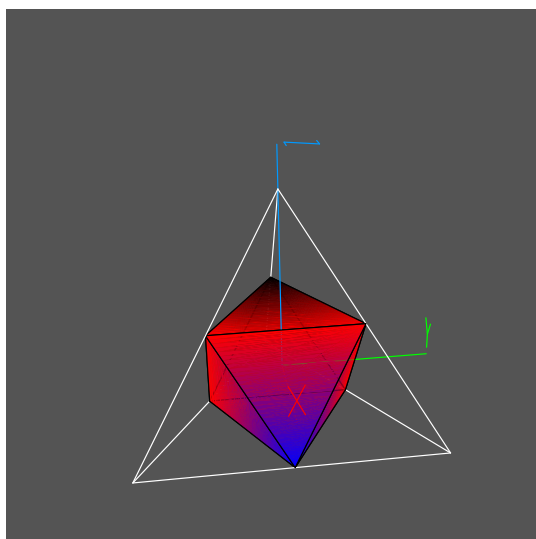

Figure B.13: Weight diagram of the six–dimensional representation **6** of SU(4). The inner octahedron forms the weight diagram of the rep.**6**.

The origin in the weight diagrams which are shown in Figs. B.11, B.12, and B.13 corresponds to the singlet. Thus we can see, that it is impossible to form a singlet with two fundamental representation as well as with two representations **10**. For the representation **6**, however, it is possible to form the singlet as stressed in Eq. (B.16).

B.2.4   SU(3) Gell-Mann matrices

The Gell-Mann matrices are given by [40, 54]

$$\lambda^1 = \begin{pmatrix} 0 & 1 & 0 \\ 1 & 0 & 0 \\ 0 & 0 & 0 \end{pmatrix}, \quad \lambda^2 = \begin{pmatrix} 0 & -i & 0 \\ i & 0 & 0 \\ 0 & 0 & 0 \end{pmatrix}, \quad \lambda^3 = \begin{pmatrix} 1 & 0 & 0 \\ 0 & -1 & 0 \\ 0 & 0 & 0 \end{pmatrix},$$

$$\lambda^4 = \begin{pmatrix} 0 & 0 & 1 \\ 0 & 0 & 0 \\ 1 & 0 & 0 \end{pmatrix}, \quad \lambda^5 = \begin{pmatrix} 0 & 0 & -i \\ 0 & 0 & 0 \\ i & 0 & 0 \end{pmatrix}, \quad \lambda^6 = \begin{pmatrix} 0 & 0 & 0 \\ 0 & 0 & 1 \\ 0 & 1 & 0 \end{pmatrix},$$

$$\lambda^7 = \begin{pmatrix} 0 & 0 & 0 \\ 0 & 0 & -i \\ 0 & i & 0 \end{pmatrix}, \quad \lambda^8 = \frac{1}{\sqrt{3}} \begin{pmatrix} 1 & 0 & 0 \\ 0 & 1 & 0 \\ 0 & 0 & -2 \end{pmatrix}.$$

They are normalized as $\mathrm{tr}\left(\lambda^a \lambda^b\right) = 2\delta_{ab}$ and satisfy the commutation relations $\left[\lambda^a, \lambda^b\right] = 2f^{abc}\lambda^c$. The structure constants f^{abc} are totally antisymmetric and obey Jacobi's identity

$$f^{abc} f^{cde} + f^{bdc} f^{cae} + f^{dac} f^{cbe} = 0.$$

Explicitly, the non-vanishing structure constants are given by $f^{123} = i$, $f^{147} = f^{246} = f^{257} = f^{345} = -f^{156} = -f^{367} = i/2$, $f^{458} = f^{678} = i\sqrt{3}/2$, and 45 others obtained by permutations of the indices.

B.2.5   SU(4) Gell-Mann matrices

The SU(4) Gell-Mann matrices are given by [54]

$$V^1 = \begin{pmatrix} 0 & 1 & 0 & 0 \\ 1 & 0 & 0 & 0 \\ 0 & 0 & 0 & 0 \\ 0 & 0 & 0 & 0 \end{pmatrix} \qquad V^2 = \begin{pmatrix} 0 & -i & 0 & 0 \\ i & 0 & 0 & 0 \\ 0 & 0 & 0 & 0 \\ 0 & 0 & 0 & 0 \end{pmatrix} \qquad V^3 = \begin{pmatrix} 1 & 0 & 0 & 0 \\ 0 & -1 & 0 & 0 \\ 0 & 0 & 0 & 0 \\ 0 & 0 & 0 & 0 \end{pmatrix}$$

$$V^4 = \begin{pmatrix} 0 & 0 & 1 & 0 \\ 0 & 0 & 0 & 0 \\ 1 & 0 & 0 & 0 \\ 0 & 0 & 0 & 0 \end{pmatrix} \qquad V^5 = \begin{pmatrix} 0 & 0 & -i & 0 \\ 0 & 0 & 0 & 0 \\ i & 0 & 0 & 0 \\ 0 & 0 & 0 & 0 \end{pmatrix} \qquad V^6 = \begin{pmatrix} 0 & 0 & 0 & 0 \\ 0 & 0 & 1 & 0 \\ 0 & 1 & 0 & 0 \\ 0 & 0 & 0 & 0 \end{pmatrix}$$

$$V^7 = \begin{pmatrix} 0 & 0 & 0 & 0 \\ 0 & 0 & -i & 0 \\ 0 & i & 0 & 0 \\ 0 & 0 & 0 & 0 \end{pmatrix} \qquad V^8 = \frac{1}{\sqrt{3}} \begin{pmatrix} 1 & 0 & 0 & 0 \\ 0 & 1 & 0 & 0 \\ 0 & 0 & -2 & 0 \\ 0 & 0 & 0 & 0 \end{pmatrix} \qquad V^9 = \begin{pmatrix} 0 & 0 & 0 & 1 \\ 0 & 0 & 0 & 0 \\ 0 & 0 & 0 & 0 \\ 1 & 0 & 0 & 0 \end{pmatrix}$$

$$V^{10} = \begin{pmatrix} 0 & 0 & 0 & -i \\ 0 & 0 & 0 & 0 \\ 0 & 0 & 0 & 0 \\ i & 0 & 0 & 0 \end{pmatrix} \quad V^{11} = \begin{pmatrix} 0 & 0 & 0 & 0 \\ 0 & 0 & 0 & 1 \\ 0 & 0 & 0 & 0 \\ 0 & 1 & 0 & 0 \end{pmatrix} \quad V^{12} = \begin{pmatrix} 0 & 0 & 0 & 0 \\ 0 & 0 & 0 & -i \\ 0 & 0 & 0 & 0 \\ 0 & i & 0 & 0 \end{pmatrix}$$

$$V^{13} = \begin{pmatrix} 0 & 0 & 0 & 0 \\ 0 & 0 & 0 & 0 \\ 0 & 0 & 0 & 1 \\ 0 & 0 & 1 & 0 \end{pmatrix} \quad V^{14} = \begin{pmatrix} 0 & 0 & 0 & 0 \\ 0 & 0 & 0 & 0 \\ 0 & 0 & 0 & -i \\ 0 & 0 & i & 0 \end{pmatrix} \quad V^{15} = \frac{1}{\sqrt{6}} \begin{pmatrix} 1 & 0 & 0 & 0 \\ 0 & 1 & 0 & 0 \\ 0 & 0 & 1 & 0 \\ 0 & 0 & 0 & -3 \end{pmatrix}$$

.

B.2.6 Eigenvalues of the quadratic Casimir operator

The eigenvalues of the quadratic Casimir operator for representations of SU(n), $\mathcal{C}^2_{\mathrm{SU}(n)}(\mu_1, \mu_2, \ldots, \mu_{n-1})$, up to $n = 6$ are given by:

$$\mathcal{C}^2_{\mathrm{SU}(2)}(\mu) = \tfrac{1}{4}\left(\mu^2 + 2\mu\right) = \tfrac{\mu}{2}\left(\tfrac{\mu}{2} + 1\right)$$

$$\mathcal{C}^2_{\mathrm{SU}(3)}(\mu_1, \mu_2) = \tfrac{1}{3}\left(\mu_1^2 + \mu_1\mu_2 + \mu_2^2 + 3\mu_1 + 3\mu_2\right)$$

$$\mathcal{C}^2_{\mathrm{SU}(4)}(\mu_1, \mu_2, \mu_3) = \tfrac{1}{8}\,(3\mu_1^2 + 4\mu_2^2 + 3\mu_3^2 + 4\mu_1\mu_2$$
$$+ 2\mu_1\mu_3 + 4\mu_2\mu_3 + 12\mu_1 + 16\mu_2 + 12\mu_3)$$

$$\mathcal{C}^2_{\mathrm{SU}(5)}(\mu_1, \mu_2, \mu_3, \mu_4) = \tfrac{1}{5}\,(2\mu_1^2 + 3\mu_2^2 + 3\mu_3^2 + 2\mu_4^2$$
$$+ 3\mu_1\mu_2 + 4\mu_2\mu_3 + 3\mu_3\mu_4 + 2\mu_1\mu_3 + \mu_1\mu_4$$
$$+ 2\mu_2\mu_4 + 10\mu_1 + 15\mu_2 + 15\mu_3 + 10\mu_4)$$

$$\mathcal{C}^2_{\mathrm{SU}(6)}(\mu_1, \mu_2, \mu_3, \mu_4, \mu_5) =$$
$$\tfrac{1}{12}\,(5\mu_1^2 + 8\mu_2^2 + 9\mu_3^2 + 8\mu_4^2 + 5\mu_5^2$$
$$+ 8\mu_1\mu_2 + 12\mu_2\mu_3 + 12\mu_3\mu_4 + 8\mu_4\mu_5$$
$$+ 4\mu_1\mu_4 + 6\mu_1\mu_3 + 8\mu_2\mu_4 + 6\mu_3\mu_5$$
$$+ 4\mu_2\mu_5 + 2\mu_1\mu_5 + 30\mu_1 + 48\mu_2$$
$$+ 54\mu_3 + 48\mu_4 + 30\mu_5)$$

The general method to obtain these and further eigenvalues for $n > 6$ requires a discussion of representation theory [75] at a level which is beyond the scope of this thesis.

The dimensionality of a representation $(\mu_1, \mu_2, \ldots, \mu_{n-1})$ is determined by the so-called Hook formula [40]

$$\dim = \frac{\prod_{i<j}^{n}\left(\lambda_i - \lambda_j + j - i\right)}{\prod_{i<j}^{n}\left(j - i\right)}, \tag{B.17}$$

where $\lambda_i = \sum_{j=i}^{n-1} \mu_j$ for $i = 1, \ldots, n$. In particular, it yields for $n = 2, 3, 4$:

$$\dim_{\text{SU}(2)}(\mu) = \mu + 1$$

$$\dim_{\text{SU}(3)}(\mu_1, \mu_2) = \tfrac{1}{2}(\mu_1 + 1)(\mu_2 + 1)(\mu_1 + \mu_2 + 2)$$

$$\dim_{\text{SU}(4)}(\mu_1, \mu_2, \mu_3) = \tfrac{1}{12}(\mu_1 + 1)(\mu_2 + 1)(\mu_3 + 1)$$
$$(\mu_1 + \mu_2 + 2)(\mu_2 + \mu_3 + 2)(\mu_1 + \mu_2 + \mu_3 + 3)$$

Bibliography

[1] J. R. Abo-Shaeer, C. Raman, J. M. Vogels, and W. Ketterle, *Observation of vortex lattices in Bose-Einstein condensates*, Science **292**, 476 (2001).

[2] A. A. Abrikosov, L. P. Gorkov, and I. E. Dzyaloshinski, *Methods of Quantum Field Theory in Statistical Physics* (Dover, New York, 1975).

[3] I. Affleck, *Critical behavior of two-dimensional systems with continuous symmetries*, Phys. Rev. Lett. **55**, 1355 (1985).

[4] —, *Large-n limit of SU(n) quantum "spin" chains*, Phys. Rev. Lett. **54**, 966 (1985).

[5] —, *The quantum Hall effects, σ-models at* $\Theta = \pi$ *and quantum spin chains*, Nucl. Phys. B **257**, 397 (1985).

[6] —, *Exact critical exponents for quantum spin chains, non-linear σ-models at* $\theta = \pi$ *and the quantum hall effect*, Nucl. Phys. B **265**, 409 (1986).

[7] —, *Mass generation by merons in quantum spin chains and the O(3) σ model*, Phys. Rev. Lett. **56**, 408 (1986).

[8] —, *Field theory methods and quantum critical phenomena*, in E. Brézin and J. Zinn-Justin, eds., *Fields, strings and critical phenomena*, volume XLIX of *Les Houches lectures* (Elsevier, Amsterdam, 1990).

[9] —, *Soliton confinement and the excitation spectrum of spin-peierls antiferromagnets*, in A. T. Skjeltorp and D. Sherrington, eds., *Dynamical Properties of Unconventional Magnetic Systems*, Kluwer Academic (Dordrecht, 1998). Available at cond-mat/9705127.

[10] I. Affleck and F. D. M. Haldane, *Critical theory of quantum spin chains*, Phys. Rev. B **36**, 5291 (1987).

[11] I. Affleck, T. Kennedy, E. H. Lieb, and H. Tasaki, *Rigorous results on valence-bond ground states in antiferromagnets*, Phys. Rev. Lett. **59**, 799 (1987).

[12] —, *Valence bond ground states in isotropic quantum antiferromagnets*, Commun. Math. Phys. **115**, 477 (1988).

[13] I. Affleck and E. H. Lieb, *A proof of part of Haldane's conjecture on spin chains*, Lett. Math. Phys. **12**, 57 (1986).

[14] Y. Ajiro, T. Goto, H. Kikuchi, T. Sakakibara, and T. Inami, *High-field magnetization of a quasi-one-dimensional S=1 antiferromagnet $Ni(C_2H_8N_2)_2NO_2(ClO_4)$: Observation of the Haldane gap*, Phys. Rev. Lett. **63**, 1424 (1989).

[15] M. Albiez, R. Gati, J. Fölling, S. Hunsmann, M. Christiani, and M. K. Oberthaler, *Direct observation of tunneling and nonlinear self-trapping in a single bosonic Josephson junction*, Phys. Rev. Lett. **95**, 010402 (2005).

[16] J. F. Allen and A. D. Misener, *Flow of liquid helium II*, Nature **141**, 75 (1938).

[17] B. P. Anderson and M. A. Kasevich, *Macrosopic quantum interference from atomic tunnel arrays*, Science **282**, 1686 (1998).

[18] M. H. Anderson, J. R. Ensher, M. R. Matthews, C. E. Wieman, and E. A. Cornell, *Observation of Bose-Einstein condensation in a dilute atomic vapor*, Science **269**, 198 (1995).

[19] N. Andrei and H. Johannesson, *Higher dimensional representations of the SU(N) Heisenberg model*, Phys. Lett. **104A**, 370 (1984).

[20] D. P. Arovas, A. Auerbach, and F. D. M. Haldane, *Extended Heisenberg models of antiferromagnetism: Analogies to the fractional quantum hall effect*, Phys. Rev. Lett. **60**, 531 (1988).

[21] A. Auerbach, *Interacting electrons and quantum magnetism* (Springer, New York, 1994).

[22] D. Augier, D. Poilblanc, E. Sørensen, and I. Affleck, *Dynamical effects of phonons on soliton binding in spin-peierls systems*, Phys. Rev. B **58**, 9110 (1998).

[23] H. M. Babudjan, Phys. Lett. **90A**, 479 (1982).

[24] C. D. Batista, G. Ortiz, and J. E. Gubernatis, Phys. Rev. B **65**, 180402(R) (2002).

[25] G. Baym and C. J. Pethick, *Ground-state properties of magnetically trapped Bose-condensed rubidium gas*, Phys. Rev. Lett. **76**, 6 (1996).

[26] H. Bethe, *Zur Theorie der Metalle I. Eigenwerte und Eigenfunktionen der linearen Atomkette*, Z. Phys. **71**, 205 (1931). Translated in D. C. Mattis, ed., *The Many-Body Problem* (World Scientific, Singapore, 1993).

[27] R. Bhat, M. J. Holland, and L. D. Carr, *Bose-Einstein condensates in rotating lattices*, Phys. Rev. Lett. **96**, 060405 (2006).

[28] R. Bhat, M. Krämer, J. Cooper, and M. J. Holland, *Hall effects in Bose-Einstein condensates in a rotating optical lattice*, Phys. Rev. A **76**, 043601 (2007).

[29] R. Bhat, B. M. Peden, B. T. Seaman, M. Krämer, L. D. Carr, and M. J. Holland, *Quantized vortex states of strongly interacting bosons in a rotating optical lattice*, Phys. Rev. A **74**, 063606 (2006).

[30] I. Bloch, J. Dalibard, and W. Zwerger, *Many-body physics with ultracold gases*, Rev. Mod. Phys. **80**, 885 (2008).

[31] N. N. Bogoliubov, *On the theory of superfluidity*, Izv. Akad. Nauk SSSR, Ser. Fiz. **11**, 77 (1947).

[32] S. N. Bose, Z. Phys. **26**, 178 (1924).

[33] P. Bouwknegt and K. Schoutens, *The $SU(n)_1$ WZW models: Spinon decomposition and Yangian structure*, Nucl. Phys. B **482**, 345 (1996).

[34] C. C. Bradley, C. A. Sackett, and R. G. Hulet, *Bose-Einstein condensation of lithium: Observation of limited condensate number*, Phys. Rev. Lett. **78**, 985 (1997).

[35] C. C. Bradley, C. A. Sackett, J. J. Tollet, and R. G. Hulet, *Evidence of Bose-Einstein condensation in an atomic gas with attractive interactions*, Phys. Rev. Lett. **75**, 1687 (1995).

[36] S. Brehmert, A. K. Kolezhuk, H.-J. Mikeska, and U. Neugebauer, *Elementary excitations in the gapped phase of a frustrated $S = 1/2$ spin ladder: from spinons to the Haldane triplet*, J. Phys.: Condens. Matter **10**, 1103 (1998).

[37] W. J. L. Buyers, R. M. Morra, R. L. Armstrong, M. J. Hogan, P. Gerlach, and K. Hirakawa, *Experimental evidence for the Haldane gap in a spin-1 nearly isotropic, antiferromagnetic chain*, Phys. Rev. Lett. **56**, 371 (1986).

[38] P. Calabrese and J. Cardy, *Entanglement entropy and quantum field theory*, J. Stat. Mech. , P06002 (2004).

[39] P. Corboz, A. M. Läuchli, K. Totsuka, and H. Tsunetsugu, *Spontaneous trimerization in a bilinear-biquadratic $S = 1$ zig-zag chain*, Phys. Rev. B **76**, 220404(R) (2007).

[40] J. F. Cornwell, *Group theory in physics*, volume II (Academic Press, London, 1984).

[41] K. B. Davis, M.-O. Mewes, M. R. Andrews, N. J. van Druten, D. S. Durfee, D. M. Kurn, and W. Ketterle, *Bose-Einstein Condensation in a gas of sodium atoms*, Phys. Rev. Lett. **75**, 3969 (1995).

[42] P. Di Francesco, P. Mathieu, and D. Sénéchal, *Conformal Field Theory* (Springer, New York, 1997).

[43] P. A. M. Dirac, in *Proc. R. Soc. A*, volume 123, 714 (1929).

[44] S. Eggert, *Numerical evidence for multiplicative logarithmic corrections from marginal operators*, Phys. Rev. B **54**, R9612 (1996).

[45] A. Einstein, Sitzungsber. Kgl. Preuss. Akad. Wiss. **1924**, 261 (1924).

[46] —, Sitzungsber. Kgl. Preuss. Akad. Wiss. **1925**, 3 (1925).

[47] L. Faddeev, *Integrable models in 1+1-dimensional quantum field theory*, in J.-B. Zuber and R. Stora, eds., *Recent advances in field theory and statistical mechanics*, volume XXXIX of *Les Houches lectures* (Elsevier, Amsterdam, 1982).

[48] L. D. Faddeev and L. A. Takhtajan, *What is the spin of a spin wave?*, Phys. Lett. A **85**, 375 (1981).

[49] G. Fáth and J. Sólyom, Phys. Rev. B **47**, 872 (1993).

[50] M. P. A. Fisher, P. B. Weichman, G. Grinstein, and D. S. Fisher, *Boson localization and the superfluid-insulator transition*, Phys. Rev. B **40**, 546 (1989).

[51] E. Fradkin, *Field Theories of Condensed Matter Systems*, number 82 in Frontiers in Physics (Westview Press, Bouler, 1991).

[52] M. Führinger, S. Rachel, R. Thomale, M. Greiter, and P. Schmitteckert, *DMRG studies of critical SU(N) spin chains*, Ann. Phys. (Berlin) , (2008).

[53] R. Gati, B. Hemmerling, J. Frölling, M. Albiez, and M. K. Oberthaler, *Noise thermometry with two weakly coupled Bose-Einstein condensates*, Phys. Rev. Lett. **96**, 130404 (2006).

[54] H. Georgi, *Lie Algebras in Particle Physics* (Addison-Wesley, Redwood City, 1982).

[55] J. M. Gerton, D. Strekalov, I. Prodan, and R. G. Hulet, *Direct observation of growth and collapse of Bose-Einstein condensate with attractive interactions*, Nature **408**, 692 (2000).

[56] T. Giamarchi, *Quantum Physics in One Dimension* (Oxford University Press, Oxford, 2004).

[57] M. Girardeau, *Weak-coupling expansion for the ground-state energy of a many-boson system*, Phys. Rev. **115**, 1090 (1959).

[58] A. Görlitz, T. L. Gustavson, A. E. Leanhardt, R. Löw, , A. P. Chikkatur, S. Gupta, S. Inouye, D. E. Pritchard, and W. Ketterle, *Sodium Bose-Einstein condensates in the F=2 state in a large-volume optical trap*, Phys. Rev. Lett. **90**, 090401 (2003).

[59] M. Greiner, O. Mandel, T. Esslinger, T. W. Hänsch, and I. Bloch, *Quantum phase transition from a superfluid to a Mott insulator in a gas of ultracold atoms*, Nature **415**, 39 (2002).

[60] M. Greiter, *Fictitious flux confinement: Magnetic pairing in coupled spin chains or planes*, Phys. Rev. B **66**, 054505 (2002).

[61] —, *S=1 spin liquids: Broken discrete symmetries restored*, J. Low Temp. Phys. **126**, 1029 (2002).

[62] M. Greiter and S. Rachel, *Valence bond solids for SU(n) spin chains: Exact models, spinon confinement, and the Haldane gap*, Phys. Rev. B **75**, 184441 (2007).

[63] —, *Ultracold bosons in a π–flux lattice: a superfluid with orbital antiferromagnetic order* (2008), To be submitted to Phys. Rev. Lett.

[64] M. Greiter, S. Rachel, and D. Schuricht, *Exact results for SU(3) spin chains: Trimer states, valence bond solids, and their parent Hamiltonians*, Phys. Rev. B **75**, 060401(R) (2007).

[65] —, *Exact spin–spin correlation functions of SU(3) valence bond solid states* (2008), Manuscript in preparation.

[66] T. Grover and T. Senthil, Phys. Rev. Lett. **98**, 247202 (2007).

[67] F. D. M. Haldane, *Contiuum dynamics of the 1-D Heisenberg antiferromagnet: Identification with the O(3) nonlinear sigma model*, Phys. Lett. **93 A**, 464 (1983).

[68] —, *Nonlinear field theory of large-spin Heisenberg antiferromagnets: Semiclassically quantized solitons of the one-dimensional easy-axis Néel state*, Phys. Rev. Lett. **50**, 1153 (1983).

[69] P. C. Haljan, I. Coddington, P. Engels, and E. A. Cornell, *Driving Bose–Einstein–Condensate vorticity with a rotating normal cloud*, Phys. Rev. Lett. **87**, 210403 (2001).

[70] K. Hallberg, *New trends in density matrix renormalization*, Adv. Phys. **55**, 477 (2006).

[71] W. Heisenberg, *Über den anschaulichen Inhalt der quantentheoretischen Kinematik und Mechanik*, Z. Phys. **43**, 172 (1927).

[72] E. Hodby, G. Hechenblaikner, S. A. Hopkins, O. M. Marago, and C. J. Foot, *Vortex nucleation in Bose–Einstein condensates in an oblate, purely magnetic potential*, Phys. Rev. Lett. **88**, 010405 (2002).

[73] D. R. Hofstadter, *Energy levels and wave functions of bloch electrons in rational and irrational magnetic fields*, Phys. Rev. B **14**, 2239 (1976).

[74] J. H. Huckans, J. R. Williams, E. L. Hazlett, R. W. Stites, and K. M. O'Hara, *Effect of resonant interactions on the stability of a three-state Fermi gas* (2008), ArXiv:0810.3288.

[75] J. E. Humphreys, *Introduction to Lie Algebras and Representation Theory* (Springer, New York, 1987).

[76] T. Inui, Y. Tanabe, and Y. Onodera, *Group Theory and Its Applications in Physics* (Springer, Berlin, 1996).

[77] C. Itoi and M.-H. Kato, Phys. Rev. B **55**, 8295 (1997).

[78] D. Jaksch, C. Bruder, J. I. Cirac, C. W. Gardiner, and P. Zoller, *Cold bosonic atoms in optical lattices*, Phys. Rev. Lett. **81**, 3108 (1998).

[79] D. Jaksch and P. Zoller, *Creation of effective magnetic fields in optical lattices: the Hofstadter butterfly for cold neutral atoms*, New J. Phys. **5**, 56 (2003).

[80] H. Johannesson, *The structure of low-lying excitations in a new integrable quantum chain model*, Nucl. Phys. B , (1986).

[81] Y. Kagan, G. V. Shlyapnikov, and J. T. M. Walraven, *Bose-Einstein condensation in trapped atomic gases*, Phys. Rev. Lett. **76**, 2670 (1996).

[82] P. Kapitza, *Viscosity of liquid helium below the λ-point*, Nature **141**, 74 (1938).

[83] K. Katsumata, H. Hori, T. Takeuchi, M. Date, A. Yamagishi, and J. P. Renard, *Magnetization process of an $S = 1$ linear-chain Heisenberg antiferromagnet*, Phys. Rev. Lett. **63**, 86 (1989).

[84] A. Klümper (2008), private communication.

[85] A. Klümper, A. Schadschneider, and J. Zittartz, *Equivalence and solution of anisotropic spin-1 models and generalized $t - j$ fermion models in one dimension*, J. Phys. A **24**, L955 (1991).

[86] —, *Groundstate properties og a generalized VBS-model*, Z. Phys. B **87**, 281 (1992).

[87] —, *Matrix product ground states for one-dimensional spin-1 quantum antiferromagnets*, Europhys. Lett. **24**, 293 (1993).

[88] A. Kolezhuk, R. Roth, and U. Schollwöck, *First order transition in the frustrated antiferromagnetic Heisenberg $S = 1$ quantum spin chain*, Phys. Rev. Lett. **77**, 5142 (1996).

[89] V. E. Korepin, *Universality of entropy scaling in one dimensional gapless models*, Phys. Rev. Lett. **92**, 096402 (2004).

[90] V. E. Korepin, N. M. Bogoliubov, and A. G. Izergin, *Quantum Inverse Scattering Method and Correlation Functions* (Cambridge University Press, Cambridge, 1997).

[91] C. K. Lai, J. Math. Phys. **15**, 1675 (1970).

[92] L. D. Landau, *Theory of superfluidity of helium II*, Phys. Rev. **60**, 356 (1941).

[93] W. Lang (2008), private communication.

[94] A. Läuchli (2008), Private communication.

[95] A. Läuchli, G. Schmid, and S. Trebst, *Spin nematics correlations in bilinear-biquadratic $S = 1$ spin chains*, Phys. Rev. B **74**, 144426 (2006).

[96] T. D. Lee, K. Huang, and C. N. Yang, *Eigenvalues and eigenfunctions of a Bose system of hard spheres and its low-temperature properties*, Phys. Rev. **106**, 1135 (1957).

[97] A. J. Leggett, *Quantum Liquids* (Oxford University Press, 2006).

[98] E. M. Lifshitz and L. P. Pitaevskii, *Statistical Physics, Part 2* (Butterworth-Heinemann, Oxford, 1980).

[99] F. London, *The λ-phenomenon of liquid helium and the Bose-Einstein degeneracy*, Nature **141**, 643 (1938).

[100] S. Ma, C. Broholm, D. H. Reich, B. J. Sternlieb, and R. W. Erwin, *Dominance of long-lived excitations in the antiferromagnetic spin-1 chain NENP*, Phys. Rev. Lett. **69**, 3571 (1992).

[101] A. J. Macfarlane, A. Sudbery, and P. H. Weisz, *On gell-mann's λ-matrices, d- and f-tensors, octets, and parametrizations of su(3)*, Commum. Math. Phys. **11**, 77 (1968).

[102] K. W. Madison, C. F. Bharucha, P. R. Morrow, S. R. Wilkinson, Q. Niu, B. Sundaram, and M. G. Raizen, *Quantum tranport of ultracold atoms in an accelerating optical potential*, Appl. Phys. B: Lasers Opt. **65**, 693 (1997).

[103] K. W. Madison, F. Chevy, W. Wohlleben, and J. Dalibard, *Vortex formation in a stirred Bose–Einstein condensate*, Phys. Rev. Lett. **84**, 806 (2000).

[104] C. K. Majumdar and D. K. Ghosh, *On next-nearest-neighbor interaction in linear chain. I*, J. Math. Phys. **10**, 1388 (1969).

[105] —, *On next-nearest-neighbor interaction in linear chain. II*, J. Math. Phys. **10**, 1399 (1969).

[106] J. B. Marston and I. Affleck, *Large-n limit of the Hubbard-Heisenberg model*, Phys. Rev. B **39**, 11538 (1989).

[107] R. A. Molina, J. Dukelsky, and P. Schmitteckert, *Crystallization of trions in SU(3) cold atom gases trapped in optical lattices* (2008), ArXiv:0807.1886.

[108] E. J. Mueller, *Superfluidity and mean-field energy loops: Hysteretic behavior in Bose-Einstein condensates*, Phys. Rev. A **66**, 063603 (2002).

[109] —, *Artificial electromagnetism for neutral atoms: Escher staircase and Laughlin liquids*, Phys. Rev. A **70**, 041603 (2004).

[110] E. J. Mueller, T.-L. Ho, M. Ueda, and G. Baym, *Fragmentation of Bose–Einstein condensates*, Phys. Rev. A **74**, 033612 (2006).

[111] C. J. Myatt, E. A. Burt, R. W. Ghrist, E. A. Cornell, and C. E. Wieman, *Production of two overlapping Bose-Einstein condensates by sympathetic cooling*, Phys. Rev. Lett. **78**, 586 (1997).

[112] R. M. Noack and S. R. Manmana, *Diagonalization- und numerical renormalization-group-based methods for interacting quantum systems*, volume 789 of *Conf. Proc.*, 93 (AIP, Melville, 2005).

[113] P. Noziéres, *in Bose-Einstein Condensation* (Cambridge University Press, Cambridge, England, 1995).

[114] P. Noziéres and D. Saint James, *Particle vs. pair condensation in attractive Bose liquids*, J. de Physique (Paris) **43**, 1133 (1982).

[115] K. Okamoto and K. Nomura, *Fluid-dimer critical point in $S = \frac{1}{2}$ antiferromagnetic Heisenberg chain with next nearest neighbor interactions*, Phys. Lett. A **169**, 433 (1992).

[116] D. v. Oosten, P. v. d. Straten, and H. T. C. Stoof, *Quantum phases in an optical lattice*, Phys. Rev. A **63**, 053601 (2001).

[117] K. Osterloh, M. Baig, L. Santos, P. Zoller, and M. Lewenstein, *Cold atoms in non-abelian gauge potentials: From the Hofstadter "moth" to lattice gauge theory*, Phys. Rev. Lett. **95**, 010403 (2005).

[118] T. B. Ottenstein, T. Lompe, M. Kohnen, A. N. Wenz, and S. Jochim, *Collisional stability of a three-component degenerate Fermi gas*, Phys. Rev. Lett. **101**, 203202 (2008).

[119] O. Penrose and L. Onsager, *Bose-Einstein condensation and liquid helium*, Phys. Rev. **104**, 576 (1956).

[120] L. P. Pitaevskii, *Dynamics of collapse of a confined Bose gas*, Phys. Lett. A , (1996).

[121] S. Rachel and M. Greiter, *Exact models for trimerization and tetramerization in spin chains*, Phys. Rev. B **78**, 134415 (2008).

[122] S. Rachel, R. Thomale, M. Führinger, D. Schuricht, P. Schmitteckert, and M. Greiter, *Spinon confinement as origin of Haldane's gap* (2008), Manuscript in preparation.

[123] C. A. Regal, *Experimental realization of BCS-BEC crossover physics with a Fermi gas of atoms*, Ph.D. thesis, University of Colorado, Boulder (2006).

[124] — (2008), private communication.

[125] J. P. Renard, M. Verdaguer, L. P. Regnault, W. A. C. Erkelens, J. Rossat-Mignod, and W. G. Stirling, *Presumption for a quantum energy gap in the quasi-one-dimensional S=1 Heisenberg antiferromagnet*, Europhys. Lett. **3**, 945 (1987).

[126] J. L. Roberts, N. R. Claussen, S. L. Cornish, E. A. Donley, E. A. Cornell, and C. E. Wieman, *Controlled collapse of a Bose–Einstein condensate*, Phys. Rev. Lett. **86**, 4211 (2001).

[127] R. Roth and U. Schollwöck, *Frustrated antiferromagnetic quantum spin chains for spin length $S > 1$*, Phys. Rev. B **58**, 9264 (1998).

[128] P. A. Ruprecht, M. Edwards, K. Burnett, and C. W. Clark, *Probing the linear and nonlinear excitations of Bose-condensed neutral atoms in a trap*, Phys. Rev. A **54**, 4178 (1996).

[129] U. Schollwöck, *The density-matrix renormalization group*, Rev. Mod. Phys. **77**, 259 (2005).

[130] U. Schollwöck, T. Jolicoeur, and T. Garel, *Onset of incommensurability at the valence-bond-solid point in the $S = 1$ quantum spin chain*, Phys. Rev. B **53**, 3304 (1996).

[131] E. Schrödinger, *Quantisierung als Eigenwertproblem*, Ann. d. Physik **81**, 109 (1926).

[132] D. Schuricht and M. Greiter, *Complementary colors of colorons: The elementary excitations of the SU(3) Haldane–Shastry model*, Europhys. Lett. **71**, 987 (2005).

[133] —, *Coloron excitations of the SU(3) Haldane–Shastry model*, Phys. Rev. B **73**, 235105 (2006).

[134] D. Schuricht and S. Rachel, *Valence bond solid states with symplectic symmetry*, Phys. Rev. B **78**, 014430 (2008).

[135] V. Schweikhard (2007), private communication.

[136] J. Schwinger, in L. Biedenharn and H. van Dam, eds., *Quantum Theory of Angular Momentum* (Academic Press, New York, 1965).

[137] E. V. Shuryak, *Metastable Bose condensate made of atoms with attractive interaction*, Phys. Rev. A **54**, 3151 (1996).

[138] A. S. Sørensen, E. Demler, and M. D. Lukin, *Fractional quantum hall states of atoms in optical lattices*, Phys. Rev. Lett. **94**, 086803 (2005).

[139] E. Sørensen, I. Affleck, D. Augier, and D. Poilblanc, *Soliton approach to spin-peierls antiferromagnets: Large-scale numerical results*, Phys. Rev. B **58**, R14701 (1998).

[140] E. S. Sørensen and A. P. Young, *Correlation length of the biquadratic spin-1 chain*, Phys. Rev. B **42**, 754 (1990).

[141] J. Stenger, S. Inouye, D. M. Stamper-Kurn, H.-J. Miesner, A. P. Chikkatur, and W. Ketterle, *Spin domains in ground-state Bose-Einstein condensates*, Nature **396**, 345 (1998).

[142] B. Sutherland, *Model for a multicomponent quantum system*, Phys. Rev. B **12**, 3795 (1975).

[143] L. A. Takhtajan, Phys. Lett. **87A**, 479 (1982).

[144] L. Tisza, *Transport phenomena in helium II*, Nature **141**, 913 (1938).

[145] H.-H. Tu, G.-M. Zhang, , and T. Xiang, *Class of exactly solvable SO(n) symmetric spin chains with matrix product ground states*, Phys. Rev. B **78**, 094404 (2008).

[146] S. Tung, V. Schweikhard, and E. A. Cornell, *Observation of vortex pinning in Bose-Einstein condensates*, Phys. Rev. Lett. **97**, 240402 (2006).

[147] M. Ueda and A. J. Leggett, *Ground-state properties of a rotating Bose-Einstein condensate with attractive interaction*, Phys. Rev. Lett. **83**, 1489 (1999).

[148] G. V. Uimin, Sov. Phys. JETP **12**, 225 (1970).

[149] G. Vidal, J. I. Latorre, E. Rico, and A. Kitaev, *Entanglement in quantum critical phenomena*, Phys. Rev. Lett. **90**, 227902 (2003).

[150] F. Wang and A. Vishvanath, *A Z_2 spin-orbital liquid state in the square lattice Kugel-Khomskii model* (2008), arXiv:0806.1743.

[151] G. H. Wannier, *Dynamics of band electrons in electric and magnetic fields*, Rev. Mod. Phys. **34**, 645 (1962).

[152] S. R. White, *Density matrix formulation for quantum renormalization groups*, Phys. Rev. Lett. **69**, 2863 (1992).

[153] N. K. Wilkin, J. M. F. Gunn, and R. A. Smith, *Do attractive bosons condense?*, Phys. Rev. Lett. **80**, 2265 (1998).

[154] C. Wu, *Hidden symmetry and quantum phases in spin-3/2 cold atomic system*, Mod. Phys. Lett. B **20**, 1707 (2006).

[155] C. N. Yang, *Some exact results for the many-body problem in one dimension with repulsive delta-function interaction*, Phys. Rev. Lett. **19**, 1312 (1967).

[156] P. Zoller and M. Greiter (2005), private communication.

[157] M. W. Zwierlein, J. R. Abo-Shaeer, A. Schirotzek, C. H. Schunck, and W. Ketterle, *Vortices and superfluidity in a strongly interacting Fermi gas*, Nature **435**, 1047 (2005).

[158] M. W. Zwierlein, C. A. Stan, C. H. Schunck, S. M. F. Raupach, S. Gupta, Z. Hadzibabic, and W. Ketterle, *Observation of Bose–Einstein condensation of molecules*, Phys. Rev. Lett. **25**, 250401 (2003).